Title
Contact Mechanics Modeling of Homogeneous and Layered Elastic-Plastic Media: Surface Roughness and Adhesion Effects

Author
Song, Zhichao

Publication Date
2012

Peer reviewed|Thesis/dissertation

Contact Mechanics Modeling of Homogeneous and Layered Elastic-Plastic Media: Surface Roughness and Adhesion Effects

By

Zhichao Song

A dissertation submitted in partial satisfaction of the

requirements for the degree of

Doctor of Philosophy

in

Engineering – Mechanical Engineering

in the

Graduate Division

of the

University of California, Berkeley

Committee in charge:

Professor Kyriakos Komvopoulos, Chair

Professor David Bogy

Professor Robert Ritchie

Fall 2012

Contact Mechanics Modeling of Homogeneous and Layered Elastic-Plastic Media: Surface Roughness and Adhesion Effects

By

Zhichao Song

Abstract

Contact Mechanics Modeling of Homogeneous and Layered Elastic-Plastic Media: Surface Roughness and Adhesion Effects

by

Zhichao Song

Doctor of Philosophy in Engineering-Mechanical Engineering

University of California, Berkeley

Professor Kyriakos Komvopoulos, Chair

The main objective of this dissertation was to analyze surface contact interaction at different length scales and to elucidate the effects of material properties (e.g., adhesion and mechanical properties), normal and shear (friction) surface tractions, and topography parameters (e.g., roughness) on contact deformation. To accomplish this objective, a surface adhesion model based on an interatomic potential was incorporated into finite element contact models of rough surfaces exhibiting multi-scale roughness described by statistical and fractal geometry models.

The problem of a rigid sphere in contact with an elastic-plastic half-space was first examined in the light of finite element simulations. Four post-yield deformation regimes were identified and the boundaries of neighboring regimes were obtained by curve-fitting of finite element results. Material hardness was shown to significantly deviate from the similarity solution with decreasing elastic modulus-to-yield strength ratio and the logarithmic dependence of the mean contact pressure on the indentation depth was found to hold only when the plastic zone was completely surrounded by elastic material. Constitutive equations were first derived for elastic-perfectly plastic half-spaces from curve-fitting finite element results and were then extended to isotropic, power-law hardening half-spaces, using the concept of the effective strain, which correlates the indentation depth with the indenter size. Finite element simulations of unloading process and repetitive normal contact were used to correlate the residual indentation depth and the dissipated plastic energy with the maximum indentation depth. Elastic shakedown, plastic shakedown, and ratcheting were identified by tracking the accumulation of plasticity for different values of maximum contact load and elastic modulus-to-yield strength ratio. The semi-infinite half-space was characterized by three different regions, named ratcheting region, shakedown region and elastic region, as the distance to contact surface increases. The obtained results have direct implication in material property measurements obtained with indentation method, particularly for materials exhibiting strain hardening behavior, and provide insight into the accumulation of plasticity due to repetitive contact loading, which is important in the understanding of the contact fatigue life of contact-mode devices.

Sliding contact between a rigid fractal surface exhibiting multi-scale roughness and an elastic-plastic half-space was examined to elucidate rough-surface deformation due to small-amplitude reciprocating sliding (fretting). Stick-slip at the asperity scale was analyzed based on Mindlin's theory and a friction model that accounts for both adhesion and plowing effects. Numerical results yield insight into the effects of surface roughness, contact pressure, oscillation amplitude, elastic modulus-to-yield strength ratio, and interfacial adhesion on the friction force, slip index, and energy dissipation. The results of this study illustrate the important role of the contact load and surface topography on the energy dissipation and fretting wear of small-amplitude oscillatory contacts.

Surface adhesion modeled as surface traction obeying the Lennard-Jones (LJ) potential was incorporated into the contact analysis of a rigid sphere indenting an elastic half-space to study contact instabilities associated with instantaneous surface contact (jump-in) and detachment (jump-out). This surface traction was introduced into a finite element contact model in the form of nonlinear spring elements and the jump-in/jump-out condition obtained analytically was confirmed by finite element results. Then, adhesive contact between a rigid sphere and an elastic-plastic half-space was analyzed and the effect of plasticity on the pull-off force and the commencement of contact instabilities was interpreted in terms of a modified Tabor parameter. The developed finite element model with nonlinear spring elements representing adhesive surface interaction provides a physics-based, computationally-efficient technique for studying adhesive contacts. The obtained results provide explanation for the contact instabilities encountered during surface probing with microprobe tips and stiction (permanent adhesion) in contact-mode microdevices.

Adhesive contact between a rigid sphere and a layered medium analyzed with the finite element method shed light into adhesion-induced contact deformation. Two modes of surface detachment were observed for perfect bonding of the film to the substrate – brittle- and ductile-like surface detachment. Simulation results illustrate the effects of the maximum surface separation, film thickness, film-to-substrate elastic property mismatch, and substrate yield strength on the mode of surface detachment and residual deformation. Introducing a cohesive model that allows for crack formation and growth along the film/substrate interface in the previous finite element model, a residual cohesive zone was found at the crack tip after complete unloading. Contact instabilities and interface delamination were interpreted by the competing effects of surface adhesion and interfacial cohesion. Crack closure and crack-tip opening displacement (CTOD) were studied by performing a parametric study of the cohesive strength, interfacial energy, surface energy, surface adhesive strength, substrate yield strength, and initial defect size. The obtained results can be used to explain thin-film failure in contact systems due to the effect of adhesion and to improve the endurance of thin-film media subjected to surface tractions.

Adhesive contact of two elastic rough surfaces was analyzed by integrating asperity-scale constitutive equations into the model of Greenwood and Williamson (1966) to account for the effect of contact instabilities at asperity level on the macroscopic contact response. The strength of adhesion was found to be mostly affected by the Tabor parameter and the surface roughness. The widely used adhesion parameter of Fuller and Tabor (1977) was shown to be appropriate only for contact systems characterized by a high Tabor parameter. Therefore, a new adhesion

parameter that governs the strength of adhesion of contact systems with a low Tabor parameter was introduced. Finally, a generalized adhesion parameter was derived by using the concept of the effective interatomic separation, defined as the ratio of the elastic stretch due to adhesion and the equilibrium interatomic distance.

The research carried out in this dissertation provides fundamental understanding of the evolution of the stress and strain fields in contacting surfaces, the evolution of plasticity in indentation, the development of friction and dissipation of energy in fretting contacts, the occurrence of adhesion-induced contact instabilities and interfacial delamination, and the factors affecting the strength of adhesion for rough surfaces in normal contact. The results of this thesis have direct implications in various technologies, including high-efficiency gas turbines, magnetic storage devices, and microelectromechanical systems.

Dedications

To my father, mother and girlfriend
for their support, encouragement and unselfish love

Table of Contents

List of Figures.....v

List of Tables.....xiv

Acknowledgements.....xv

Chapter 1 ***Introduction***.....1

Chapter 2 ***Elastic-plastic spherical indentation: deformation regimes, evolution of plasticity and hardening effect***.....6

2.1 Introduction.....6

2.2 Method of analysis.....8

2.2.1 Problem definition.....8

2.2.2 Finite element model.....8

2.2.3 Constitutive material model......10

2.3 Results and discussion.....11

2.3.1 Deformation regimes of elastic-plastic indentation.....11

2.3.2 Constitutive contact equations.....14

2.3.3 Evolution of plasticity.....16

2.3.4 Hardening effect.....18

2.4 Conclusions.....20

Chapter 3 ***Unloading of an elastic-plastic half-space indented by a rigid sphere and the evolution of plasticity due to repetitive normal load***.....22

3.1 Introduction.....22

3.2 Contact model of loading-unloading cycle.....23

3.3 Results and discussion.....24

3.3.1 Universal loading-unloading behavior.....24

3.3.2 Residual indentation depth and dissipated plastic energy.....25

3.3.3 Unloading constitutive equations.....27

3.3.4 Effect of strain hardening.....27

3.3.5 Evolution of plastic zone in multiple loading-unloading cycles.....29

3.4 Conclusions.....34

Chapter 4 ***A fretting contact analysis of fractal surfaces***.....35

4.1 Introduction.....35

4.2 Friction model.....36

4.3 Surface description.....37

4.4 Contact mechanics analysis.....38

4.4.1 Normal contact of a rigid rough (fractal) surface and a deformable half-space.....38

4.4.2 Tangential contact of a rigid rough (fractal) surface and a deformable half-space.....39

4.5 Numerical results and discussion....42
4.5.1 Effect of surface roughness....42
4.5.2 Effect of nominal contact pressure....43
4.5.3 Effect of fretting amplitude....45
4.5.4 Effect of elastic modulus-to-yield strength ratio....46
4.5.5 Effect of interfacial condition parameter....47
4.6 Conclusions....49

Chapter 5 ***Adhesion-induced instabilities in elastic and elastic-plastic contacts during single and repetitive normal loading....51***
5.1 Introduction....51
5.2 Analytical model of adhesive contact....53
5.3 Finite element model of adhesive contact....57
5.4 Results and discussion....58
5.4.1 Elastic adhesive contact....58
5.4.2 Elastic-plastic adhesive contact....60
5.5 Conclusions....66

Chapter 6 ***Adhesive contact of elastic-plastic layered media: effective Tabor parameter and Mode of surface separation....68***
6.1 Introduction....68
6.2 Finite element model....70
6.3 Results and discussion....71
6.3.1 Substrate effect and effective Tabor parameter....71
6.3.2 Effect of plasticity parameter....74
6.3.3 Effect of layer-to-substrate elastic modulus ratio....77
6.3.4 Effect of layer thickness....80
6.3.5 Effect of cyclic contact loading....80
6.4 Conclusions....82

Chapter 7 ***Delamination of an elastic film from elastic-plastic substrate during adhesive contact loading and unloading....84***
7.1 Introduction....84
7.2 Contact model....85
7.3 Results and discussion....87
7.3.1 Effect of minimum surface separation....89
7.3.2 Effect of substrate yield strength....92
7.3.3 Effect of interface work of adhesion....93
7.3.4 Effect of cohesive strength....95
6.3.5 Effect of preexisting crack....97
7.4 Conclusions....99

Chapter 8 ***Contact mechanics of elastic rough surfaces in the presence of adhesion: contact instabilities and strength of adhesion....101***
8.1 Introduction....101

8.2 Analysis of single adhesive contacts.....103
8.2.1 Constitutive relations for surface separation range of dominant attractive force.....106
8.2.1.1 Elastic adhesive contact without jump-in instability.....106
8.2.1.2 Elastic adhesive contact with jump-in instability.....109
8.2.2 Constitutive relations for surface separation range of dominant repulsive force.....110
8.3 Contact analysis of elastic rough surfaces.....111
8.3.1 Rough surface model.....111
8.3.2 Constitutive contact relations for rough elastic surfaces without jump-in instabilities.....112
8.3.3 Constitutive contact relations for rough elastic surfaces with jump-in instabilities.....113
8.4 Results and discussion.....114
8.4.1 Effect of adhesion-induced instabilities at the asperity level on rough surface contact behavior.....114
8.4.2 Effect of surface roughness on strength of adhesion.....115
8.4.3 Effect of Tabor parameter on strength of adhesion.....117
8.4.4 A new adhesion parameter and effective separation.....117
8.5 Conclusions.....118

Chapter 9 *Conclusion*.....120

Bibliography.....124

Appendix A *Surface traction distribution due to Lennard-Jones potential*.....133

***Appendix B Contact area at maximum adhesion force derived from the JKR theory*.....135**

List of Figures

Figure 2.1 Schematic of a deformable half-space indented by a rigid sphere.

Figure 2.2 Finite element model of a half-space and a spherical indenter.

Figure 2.3 Variation of mean contact pressure $\bar{p}_m$ with indentation depth $\bar{\delta}$ in the elastic deformation regime.

Figure 2.4 Variation of mean contact pressure $\bar{p}_m$ with indentation depth $\bar{\delta}$ for an elastic-perfectly plastic half-space with E^*/Y = 55. Boundaries between various deformation regimes are represented by vertical dashed lines.

Figure 2.5 Variation of mean contact pressure $\bar{p}_m$ with indentation depth $\bar{\delta}$ for elastic-perfectly plastic half-spaces with E^*/Y = 11–2200. Solid lines represent boundaries between deformation regimes.

Figure 2.6 Variation of hardness H/Y with effective elastic modulus-to-yield strength ratio E^*/Y for elastic-perfectly plastic half-spaces.

Figure 2.7 Variation of contact area $\bar{a}$ with indentation depth $\bar{\delta}$ for elastic-perfectly plastic half-spaces with E^*/Y = 11–2200. Solid lines represent boundaries between deformation regimes.

Figure 2.8 Evolution of plastic zone in the nonlinear elastic-plastic (NLEP) deformation regime of an elastic-perfectly plastic half-space with (a) E^*/Y = 2200 and (b) E^*/Y = 11.

Figure 2.9 Variation of elastic core height $\bar{h}$ and radius $\bar{r}$ with indentation depth $\bar{\delta}$ in the nonlinear elastic-plastic (NLEP) deformation regime of an elastic-perfectly plastic half-space with E^*/Y = 2200.

Figure 2.10 Variation of (a) mean contact pressure $\bar{p}_m$ and (b) contact area $\bar{a}$ with indentation depth $\bar{\delta}$ for elastic-plastic half-spaces with E^*/Y = 11 and n = 0–0.5.

Figure 2.11 (a) Effective strain ε^* versus indentation depth $\bar{\delta}$ for elastic-plastic half-spaces with E^*/Y = 11 and n = 0.2–0.5 and (b) mean contact pressure $\bar{p}_m^*$ (normalized by the effective yield strength Y^*) versus indentation depth $\bar{\delta}$ for elastic-plastic half-spaces with E^*/Y = 11 and n = 0–0.5.

Figure 3.1 (a) schematic of the loading half-cycle and (b) the unloading half-cycle of elastic-plastic half-space in normal contact with a rigid spherical indenter

Figure 3.2 (a) Dimensionless normal force $\bar{P}$ and (b) contact area $\bar{A}$ verse dimensionless indentation depth $\bar{\delta}$, for elastic-perfectly plastic half-space of E^*/Y =110, 220, 550 and 1100

Figure 3.3 Dimensionless residual indentation depth $\tilde{\delta}_{res}$ verse dimensionless maximum indentation depth $\bar{\delta}_{max}$

Figure 3.4 Dimensionless dissipated plastic energy $\tilde{E}_P$ verse dimensionless maximum indentation depth $\bar{\delta}_{max}$

Figure 3.5 (a) Dimensionless normal force $\tilde{P}$ and (b) contact area $\tilde{A}$ verse dimensionless unloading indentation depth $\tilde{\delta}$ (comparison of simulation results and curve fitted equations)

Figure 3.6 Dimensionless residual indentation depth $\tilde{\delta}_{res}$ vs. strain hardening exponent n (unloading from $\bar{\delta}_{max}$= 110)

Figure 3.7 Distribution of equivalent plastic strain $\bar{\varepsilon}_P$ in elastic-plastic half-space of E^*/Y = 550, subjected to repetitive normal load $\bar{P}_{max}$ = 500, after 1st (a) loading and (b) unloading half-cycle

Figure 3.8 Distribution of equivalent plastic strain $\bar{\varepsilon}_P$ in elastic-plastic half-space of E^*/Y = 550, subjected to repetitive normal load $\bar{P}_{max}$ = 500, after 2nd (a) loading and (b) unloading half-cycle

Figure 3.9 Dimensionless dissipated plastic energy $\bar{E}_P$ verse the number of cycles N after each loading and unloading half-cycle for elastic-plastic half-space of E^*/Y = 550, subjected to repetitive normal load $\bar{P}_{max}$ = 500

Figure 3.10 Distribution of equivalent plastic strain $\bar{\varepsilon}_P$ in elastic-plastic half-space of E^*/Y = 55, subjected to repetitive normal load $\bar{P}_{max}$ = 500, after 1st (a) loading and (b) unloading half-cycle

Figure 3.11 Distribution of equivalent plastic strain $\bar{\varepsilon}_P$ in elastic-plastic half-space of E^*/Y = 55, subjected to repetitive normal load $\bar{P}_{max}$ = 500, after 2nd (a) loading and (b) unloading half-cycle

Figure 3.12 Dimensionless dissipated plastic energy $\bar{E}_P$ verse the number of cycles N after each loading and unloading half-cycle for elastic-plastic half-space of E^*/Y = 55, subjected to repetitive normal load $\bar{P}_{max}$ = 500

Figure 3.13 Evolution of equivalent plastic strain $\bar{\varepsilon}_P$ along (a) the axis of symmetry in depth direction (z-axis) and (b) contact surface in radial direction (r-axis) with the number of cycles

Figure 3.14 Distribution of effective stress σ_V for elastic-plastic half-space, described by a combined isotropic/kinematic strain hardening behavior half-space, subjected to repetitive normal load of $\bar{P}_{max}$ = 500, after (a) 1st, (b) 2nd , (c) 3rd and (d) 4th unloading half-cycle

Fig. 4.1 Typical three dimensional fractal rough surface generated from Eq. (3) with M= 20, γ = 1.5, L = 10 mm, L_s = 5nm, G = 50 nm and D = 2.5.

Fig. 4.2 Schematic of fretting loop for (a) partial slip and (b) full slip at at maximum fretting amplitude

Fig. 4.3 (a) Dimensionless tangential force $\bar{Q}$ vs. dimensionless tangential displacement $\bar{s}$ for rough surfaces of fractal roughness $\bar{G} = 10^{-7}$ (RMS roughness $\sigma/L = 6.9 \times 10^{-6}$), 5×10^{-7} ($\sigma/L = 1.6 \times 10^{-5}$), 2×10^{-6} ($\sigma/L = 3.1 \times 10^{-5}$), and 10^{-5} ($\sigma/L = 7.2 \times 10^{-5}$), in fretting contact with an elastic-plastic half-space of E^*/Y = 440, subjected to nominal contact pressure $\bar{p}$ = 0.3, fretting amplitude $\bar{s}_{max} = 5 \times 10^{-4}$ and interfacial adhesion parameter m = 0.5. (b) The drop of tangential force $\Delta\bar{Q}$ =$\Delta Q/Q_{max}$ vs. fractal roughness $\bar{G}$.

Fig. 4.4 (a) maximum tangential force $\bar{Q}_{max}$ and fretting energy dissipation $\Delta\bar{W}$ vs. fractal roughness $\bar{G}$ (b) Elastic contact area $\bar{S}_e$ and plastic contact area $\bar{S}_p$ vs. fractal roughness $\bar{G}$ for rough surfaces in fretting contact with an elastic-plastic half-space of E^*/Y = 440, subjected to nominal contact pressure $\bar{p}$ = 0.3, fretting amplitude $\bar{s}_{max} = 5 \times 10^{-4}$ and interfacial adhesion parameter m = 0.5.

Fig. 4.5 Tangential force $\bar{Q}$ vs. tangential displacement $\bar{s}$ for fractal rough surfaces $\bar{G} = 2 \times 10^{-6}$ in fretting contact with an elastic-plastic half-space of E^*/Y = 440, subjected to nominal contact pressure $\bar{p}$ = 0.1, 0.6 and 1.5, fretting amplitude $\bar{s}_{max} = 5 \times 10^{-4}$ μm and interfacial adhesion parameter m = 0.5.

Fig. 4.6 (a) maximum friction force $\bar{Q}_{max}$and fretting energy dissipation $\Delta\bar{W}$ vs. nominal contact pressure $\bar{p}$ and (b) fraction of plastic contact force $F_p/(F_e + F_p)$ and plastic contact area $S_p/(S_e + S_p)$ vs. nominal contact pressure $\bar{p}$ for fractal rough surfaces $\bar{G} = 2 \times 10^{-6}$ in fretting contact with an elastic-plastic half-space of E^*/Y = 440, subjected to fretting amplitude $\bar{s}_{max} = 5 \times 10^{-4}$ μm and interfacial adhesion parameter m = 0.5.

Fig. 4.7 (a) Tangential force $\bar{Q}$ vs. tangential displacement $\bar{s}$ for fractal rough surfaces $\bar{G} = 2 \times 10^{-6}$ in fretting contact with an elastic-plastic half-space of E^*/Y = 440, subjected to nominal contact pressure $\bar{p}$ = 0.3, fretting amplitude $\bar{Q}_{max} = 5 \times 10^{-5}$, 10^{-4}, 2×10^{-4} and 10^{-3} and interfacial adhesion parameter m = 0.5. (b) Fretting energy dissipation $\Delta\bar{W}$ vs. fretting amplitude s_{max}.

Fig. 4.8(a) Tangential force $\bar{Q}$ vs. tangential displacement $\bar{s}$ for fractal rough surfaces $\bar{G} = 2 \times 10^{-6}$ in fretting contact with an elastic-plastic half-space of E^*/Y = 110, 220, 440 and 660, subjected to nominal contact pressure $\bar{p}$ = 0.3, fretting amplitude $\bar{s}_{max} = 5 \times 10^{-4}$ and interfacial adhesion parameter m = 0.5. (b) Slip index θ vs. elastic modulus-to-yield strength ratio E^*/Y.

Fig. 4.9(a) maximum friction force $\bar{Q}_{max}$ vs. elastic modulus-to-yield strength ratio E^*/Y. (b) fretting energy dissipation $\Delta\bar{W}$ vs. elastic modulus-to-yield strength ratio E^*/Y for fractal

rough surfaces $\bar{G} = 2 \times 10^{-6}$ in fretting contact with an elastic-plastic half-space, subjected to nominal contact pressure $\bar{p}$ = 0.3, fretting amplitude $\bar{s}_{max} = 5 \times 10^{-4}$ and interfacial adhesion parameter m = 0.5.

Fig. 4.10(a) maximum friction force $\bar{Q}_{max}$vs. interfacial adhesion parameter m for fractal rough surfaces $\bar{G} = 2 \times 10^{-6}$, 10^{-5}, 5×10^{-5} in fretting contact with an elastic-plastic half-space of E^*/Y = 220, subjected to nominal contact pressure $\bar{p}$ = 0.3 and fretting amplitude $\bar{s}_{max} = 5 \times 10^{-4}$. (b) fretting energy dissipation $\Delta\bar{W}$ vs. interfacial adhesion parameter m for G = 2, 10 and 50nm.

Fig. 4.11 Slip index θ vs. interfacial adhesion parameter m for fractal rough surfaces $\bar{G} = 2 \times 10^{-6}$, 10^{-5}, 5×10^{-5} in fretting contact with an elastic-plastic half-space of E^*/Y = 220, subjected to nominal contact pressure $\bar{p}$ = 0.3 and fretting amplitude $\bar{s}_{max} = 5 \times 10^{-4}$

Figure 5.1. Equivalent model of a rigid sphere in close proximity with an elastic half-space. The pile-up at the half-space surface is due to the effect of adhesion.

Figure 5.2. Schematics of a rigid sphere in proximal distance with an elastic half-space: (a) relatively large gap (no surface deformation), (b) pile-up formation due to adhesive interaction, and (c) sudden surface contact (jump-in).

Figure 5.3. Critical central gap at the instant of jump instabilities versus Tabor parameter.

Figure 5.4. Critical central gap at the instant of the jump-in instability versus Tabor parameter.

Figure 5.5. Finite element model of a rigid sphere in close proximity with a deformable half-space. Surface adhesion is modeled by nonlinear springs (shown by serrated lines) with a force-distance relationship governed by the L-J potential.

Figure 5.6. Pull-off force versus Tabor parameter.

Figure 5.7. Surface gap error versus radial distance for μ = 2.1.

Figure 5.8. Central gap versus displacement for (a) μ = 2.1, (b) μ = 1.14, (c) μ = 0.72, and (d) μ = 0.16.

Figure 5.9. (a) Normal load and (b) central gap versus displacement for μ = 1.14, β = 1.67, and $\bar{\delta}_{max}$ = 6.67.

Figure 5.10. Normal load and central gap versus displacement for (a, b) μ = 0.45, β = 1.67, $\bar{\delta}_{max}$ = 6.67 and (c, d) μ = 1.14, β = 2.78, $\bar{\delta}_{max}$ = 0.

Figure 5.11. Schematics of (a) residual impression and (b) necking produced during surface approach and surface retraction, respectively.

Figure 5.12. Normal load versus displacement for μ = 1.14, β = 1.67, and $\bar{\delta}_{max}$ = 0, 6.67, and 13.33.

Figure 5.13. Pull-off force versus maximum normal displacement for μ = 1.14 and β = 1.67.

Figure 5.14. Normal load versus displacement for four complete approach-retraction cycles: (a) μ = 1.14, β = 1.67, $\bar{\delta}_{max}$ = 6.67, (b) μ = 0.45, β = 1.67, $\bar{\delta}_{max}$ = 6.67, and (c) μ = 1.14, β = 2.78, $\bar{\delta}_{max}$ = 0.

Figure 5.15. Contours of equivalent plastic strain in the subsurface of an elastic-plastic half-space for μ = 1.14 and $\bar{\delta}_{max}$ = 0: (a) β = 1.67, (b) β = 2.78, and (c) β = 4.17. Contours in (a) and (b) are at the instant of surface separation (jump-out), whereas contours in (c) are due to stretching of a neck strongly adhered to the retracting rigid sphere.

Figure 6.1 (a) Schematic showing a rigid sphere of radius R in close proximity with a layered medium consisting of an elastic layer of thickness t and an elastic-plastic substrate (center deflection h_o is due to an adhesion (attractive) surface force) and (b) finite element mesh of the layered medium, showing the nonlinear spring elements used to model interfacial adhesion.

Figure 6.2 Pull-off force $\bar{P}_{off}$ versus layer thickness $\bar{t}$ for a layered medium consisting of an elastic layer of E_l = 20 GPa and a rigid substrate.

Figure 6.3 Center deflection before surface separation $\bar{h}_o$ versus Tabor parameter μ for homogeneous elastic half-space.

Figure 6.4 Substrate effect θ versus layer thickness $\bar{t}$ for elastic layered medium with E_l/E_s in the range of 2.5–40.

Figure 6.5 Substrate effect θ versus center layer deflection ξ for elastic layered medium having a wide range of E_l/E_s.

Figure 6.6 (a) Surface force $\bar{P}$ versus surface separation $\bar{\delta}$ during loading (solid lines) and unloading (dashed lines) and (b) residual surface height $\bar{h}_r$ versus radial distance $\bar{r}$ for elastic-plastic layered medium, E_l/E_s = 10, β = 33.3, $\bar{t}$ = 8, and $\bar{\delta}_{max}$= 3.33, 10, and 16.7. (Pull-off force $\bar{P}_{off}$ and separation force $\bar{P}_{sep}$ are defined in (a).)

Figure 6.7 (a) Surface force $\bar{P}$ versus surface separation $\bar{\delta}$ during loading (solid lines) and unloading (dashed lines) and (b) residual surface height $\bar{h}_r$ versus radial distance $\bar{r}$ for elastic-plastic layered medium, E_l/E_s = 10, β = 6.67, $\bar{t}$ = 8, and $\bar{\delta}_{max}$= 3.33, 10, and 16.7.

Figure 6.8 Residual center height $\bar{h}_{o,r}$ versus maximum surface separation $\bar{\delta}_{max}$ for elastic-plastic layered medium, E_l/E_s = 10, β = 3.33–33.3, and $\bar{t}$ = 8.

Figure 6.9 (a) Surface force $\bar{P}$ versus surface separation $\bar{\delta}$ during loading (solid lines) and unloading (dashed lines) and (b) residual surface height $\bar{h}_r$ versus radial distance $\bar{r}$ for elastic-plastic layered medium, E_l/E_s = 10, β = 1.67, 6.67, and 33.3, $\bar{t}$ = 8, and $\bar{\delta}_{\max}$= 10.

Figure 6.10 (a) Surface force $\bar{P}$ versus surface separation $\bar{\delta}$ during loading (solid lines) and unloading (dashed lines) and (b) residual surface height $\bar{h}_r$ versus radial distance $\bar{r}$ for elastic-plastic layered medium, E_l/E_s = 2.5, 10, and 40, β = 33.3, $\bar{t}$ = 8, and $\bar{\delta}_{\max}$= 10.

Figure 6.11 Contours of equivalent plastic strain $\bar{\varepsilon}_p$ after complete unloading for elastic-plastic layered medium, E_l/E_s = 2.5, 10, and 40, β = 33.3, $\bar{t}$ = 8, and $\bar{\delta}_{\max}$= 10.

Figure 6.12 (a) Surface force $\bar{P}$ versus surface separation $\bar{\delta}$ during loading (solid lines) and unloading (dashed lines) and (b) residual surface height $\bar{h}_r$ versus radial distance $\bar{r}$ for elastic-plastic layered medium, E_l/E_s = 10, β = 33.3, $\bar{t}$ = 4, 8, and 16, and $\bar{\delta}_{\max}$= 10.

Figure 6.13 Surface force $\bar{P}$ versus surface separation $\bar{\delta}$ during loading (solid lines) and unloading (dashed lines) for four consecutive loading cycles, elastic-plastic layered medium, E_l/E_s = 10, (a) β = 6.67 and (b) 33.3, $\bar{t}$ = 8, and $\bar{\delta}_{\max}$= 10.

Figure 6.14 Depth distributions of equivalent plastic strain $\bar{\varepsilon}_p$ along the axis of symmetry ($\bar{r}$ = 0) for four consecutive loading/unloading cycles, elastic-plastic layered medium, E_l/E_s = 10, β = 6.67 and 33.3, $\bar{t}$ = 8, and $\bar{\delta}_{\max}$= 10.

Figure 6.15 Radial distributions of equivalent plastic strain $\bar{\varepsilon}_p$ along the layer/substrate interface ($\bar{z}$ = –8) for four consecutive loading/unloading cycles, elastic-plastic layered medium, E_l/E_s = 10, β = 6.67 and 33.3, $\bar{t}$ = 8, and $\bar{\delta}_{\max}$= 10.

Figure 7.1 Model of a rigid sphere in close proximity with a layered medium consisting of an elastic film and a semi-infinite elastic-plastic substrate.

Figure 7.2 Schematic representation of traction versus film-substrate separation constitutive law of a bilinear cohesive zone. Surface separation larger than h^* leads to either partial damage (point C) or full damage (point B), accompanied by a decrease in cohesive strength σ_c.

Figure 7.3 Schematics of deformed layered medium (a) before and (b) after complete separation (jump-out) of the elastic film from the rigid sphere. Formation of a crack and a cohesive zone (gray region), partial closure of the cohesive zone (blue region), and high tensile stresses (red region) can be encountered at the film/substrate interface during a full load-unload cycle, depending on the material properties and minimum surface separation (maximum compressive force).

Figure 7.4 (a) Surface force $\bar{P}$ and (b) corresponding film-substrate separation below the center of contact $\bar{\Delta}_o$ versus surface separation $\bar{\delta}$ for $\bar{\Gamma}$ = 0.125, $\bar{Y}$ = 0.4, $\bar{\sigma}_c$ = 0.075, and $\bar{\delta}_{\min}$= –

0.5, –1.0, and –1.5 (loading = solid lines; unloading = dashed lines). Characteristic points are shown for $\bar{\delta}_{\min} = -1.5$.

Figure 7.5 (a) Contours of residual $\bar{\sigma}_{zz}^{\text{res}}$ stress and (b) variation of residual film deflection at the center of contact $\bar{\delta}^{\text{res}}$ with minimum surface separation $\bar{\delta}_{\min}$ for $\bar{\Gamma} = 0.125$, $\bar{Y} = 0.4$, and $\bar{\sigma}_c = 0.075$.

Figure 7.6 Crack-tip opening displacement β and film deflection at the crack-tip location $\bar{\Delta}_f$ versus minimum surface separation $\bar{\delta}_{\min}$ for $\bar{\Gamma} = 0.125$, $\bar{Y} = 0.4$, and $\bar{\sigma}_c = 0.075$.

Figure 7.7 (a) Surface force $\bar{P}$ and (b) corresponding film-substrate separation below the center of contact $\bar{\Delta}_o$ versus surface separation $\bar{\delta}$ for $\bar{\Gamma} = 0.125$, $\bar{Y} = 0.1$, 1.0, and 10, $\bar{\sigma}_c = 0.075$, and $\bar{\delta}_{\min} = -1.0$ (loading = solid lines; unloading = dashed lines).

Figure 7.8 Interfacial surface separation $\bar{\Delta}$ before (dashed lines) and after (solid lines) jump-out versus radial distance $\bar{r}$ for $\bar{\Gamma} = 0.125$, $\bar{Y} = 0.1$, 1.0, and 10, $\bar{\sigma}_c = 0.075$, and $\bar{\delta}_{\min} = -1.0$.

Figure 7.9 (a) Surface force $\bar{P}$ and (b) corresponding film-substrate separation at the center of contact $\bar{\Delta}_o$ versus surface separation $\bar{\delta}$ for $\bar{\Gamma} = 0.125$, 0.25, and 0.5, $\bar{Y} = 0.4$, $\bar{\sigma}_c = 0.075$, and $\bar{\delta}_{\min} = -1.0$ (loading = solid lines; unloading = dashed lines). Characteristic points are shown for $\bar{\Gamma} = 0.125$.

Figure 7.10 (a) Radius of fictitious crack $\bar{a}_{fc}$ and residual fictitious crack $\bar{a}_{fc}^{\text{res}}$ and (b) closure of residual fictitious crack c versus interface work of adhesion $\bar{\Gamma}$ for $\bar{Y} = 0.4$, $\bar{\sigma}_c = 0.075$, and $\bar{\delta}_{\min} = -1.0$.

Figure 7.11 Crack-tip opening displacement β and film deflection at the crack-tip location $\bar{\Delta}_f$ versus interface work of adhesion $\bar{\Gamma}$ for $\bar{Y} = 0.4$, $\bar{\sigma}_c = 0.075$, and $\bar{\delta}_{\min} = -1.0$.

Figure 7.12 (a) Surface force $\bar{P}$ and (b) corresponding film-substrate separation at the center of contact $\bar{\Delta}_o$ versus surface separation $\bar{\delta}$ for $\bar{\Gamma} = 0.125$, $\bar{Y} = 0.4$, $\bar{\sigma}_c = 0.015$, 0.075, and 0.2, and $\bar{\delta}_{\min} = -1.0$ (loading = solid lines; unloading = dashed lines). Characteristic points are shown for $\bar{\sigma}_c = 0.075$ and 0.2.

Figure 7.13 (a) Radius of fictitious crack $\bar{a}_{fc}$ and residual fictitious crack $\bar{a}_{fc}^{\text{res}}$ and (b) closure of residual fictitious crack c versus cohesive strength $\bar{\sigma}_c$ for $\bar{\Gamma} = 0.125$, $\bar{Y} = 0.4$, and $\bar{\delta}_{\min} = -1.0$.

Figure 7.14 Crack-tip opening displacement β and film deflection at the crack-tip location $\bar{\Delta}_f$ versus cohesive strength $\bar{\sigma}_c$ for $\bar{\Gamma} = 0.125$, $\bar{Y} = 0.4$, and $\bar{\delta}_{\min} = -1.0$.

Figure 7.15 (a) Surface force $\bar{P}$ and (b) corresponding film-substrate separation at the center of contact $\bar{\Delta}_o$ versus surface separation $\bar{\delta}$ for $\bar{\Gamma} = 0.125$, $\bar{Y} = 0.4$, $\bar{\sigma}_c = 0.075$, $\bar{\delta}_{\min} = -1.0$, and $\bar{a}_i = 1$, 4, and 8 (loading = solid lines; unloading = dashed lines).

Figure 7.16 Surface separation at jump-in $\bar{\delta}_{\text{in}}$ and jump-out $\bar{\delta}_{\text{out}}$ versus initial crack radius $\bar{a}_i$ for $\bar{\Gamma} = 0.125$, $\bar{Y} = 0.4$, $\bar{\sigma}_c = 0.075$, and $\bar{\delta}_{\text{min}} = -1.0$.

Figure 8.1 Equivalent model of a rigid sphere of reduced radius of curvature R and an elastic half-space of effective elastic modulus E^*.

Figure 8.2 Schematics of interfacial force and contact area versus minimum surface separation for smooth ($\mu < 0.5$) and discontinuous ($\mu > 0.5$) surface approach and retraction.

Figure 8.3 Critical contact radius $\bar{a}_c$ at the instant of maximum adhesive force versus Tabor parameter μ. Discrete data points represent numerical data obtained with a previous finite element model of adhesive contact (Song and Komvopoulos, 2011). The solid curve is a best fit through the numerical data.

Figure 8.4 Critical surface separation $\bar{\delta}_{oc}$ versus Tabor parameter μ for single contacts that do not exhibit jump-in instability ($\mu < 0.5$). Discrete data points represent numerical data obtained with a previous finite element model of adhesive contact (Song and Komvopoulos, 2011). The solid line is a best fit through the numerical data.

Figure 8.5 Comparison of analytical solutions (Eq. (9)) and numerical results obtained with the model of a previous FEM study (Song and Komvopoulos, 2011) of interfacial force $\bar{P}$ versus minimum surface separation $\bar{\delta}_o$ for Tabor parameter μ equal to (a) 0.091, (b) 0.145, (c) 0.23, and (d) 0.425.

Figure 8.6 Critical central gap $\bar{x}_{oc}$ for jump-in instability versus Tabor parameter μ. Discrete data points represent numerical data obtained with a previous finite element model of adhesive contact (Song and Komvopoulos, 2011). The solid curve is a best fit through the numerical data.

Figure 8.7 Comparison of analytical solutions (Hertz analysis) and FEM results obtained with a previous finite element model of adhesive contact (Song and Komvopoulos, 2011): (a) interfacial force $(P - P_{\text{max}})/(4E^*R^2/3)$ versus minimum surface separation $(\delta_{oc} - \delta_o)/R$ after the occurrence of maximum adhesive force and (b) contact area $(A - \pi a_c^2)/\pi R^2$ versus minimum surface separation $(\delta_o^* - \delta_o)/R$ after the establishment of contact for Tabor parameter μ = 0.091–1.971.

Figure 8.8 Schematic of equivalent rough-surface contact model comprising a rigid rough surface and an elastic half-space.

Figure 8.9 (a) Interfacial force $\bar{F}$ and (b) contact area $\bar{S}$ versus mean surface separation $\bar{d}$ for fixed surface roughness (σ = 2 nm) and Tabor parameter μ = 0.5–46.9. The inset in (a) is a magnified plot of the interfacial force for $\mu = 10$.

Figure 8.10 Strength of adhesion $\bar{F}_{\text{max}}$ versus surface roughness σ for Tabor parameter $\mu =$ $0.1, 1.0,$ and 10.

Figure 8.11 Strength of adhesion $\bar{F}_{\max}$ versus Tabor parameter μ for surface roughness $\sigma = 0.5$, 1.0, and 2.0 nm.

Figure 8.12 (a) Strength of adhesion $\bar{F}_{\max}$ and (b) relative strength of adhesion χ versus surface roughness σ for adhesion parameter $\theta = 0.2$, 1.0, and 5.0.

Figure 8.13 Relative strength of adhesion χ versus surface roughness σ for adhesion parameter $\zeta = 0.2$, 0.5, and 1.0.

List of Tables

Table 5.1 Comparison of analytical and finite element method (FEM) results of dimensionless critical central gap at the instant of jump-in for different values of Tabor parameter.

Acknowledgements

I would like to express my most sincere gratitude to my advisor and dissertation committee chair Professor Kyriakos Komvopoulos for his guidance, support and encouragement throughout my five-year graduate study at Berkeley. The detail-orientated working attitude, creative and critical thinking, and independent learning skills I learned from him will definitely benefit my entire career and life.

I am also very grateful to the members of my dissertation committee, Prof. David Bogy and Prof. Robert Ritchie, for providing many valuable suggestions and comments to this dissertation. My appreciation also goes to the members of my Ph.D. qualify exam committee members, Prof. Hari, Dharan, Prof. David Bogy, Prof. David Steigmann and Prof. Ronald Gronsky, for their helpful comments and discussions on my research and coursework.

This work was partially supported by Siemens Energy Inc., and I am very thankful to Dr. Marc Mittelbach and Dr. Sachin Shinde at Gas Turbine Department, Siemens Energy Inc, for many stimulating and constructive discussions through regular quarterly meetings and several on-campus visits.

I wish to thank all my friends and colleagues, Dr. Heng Pan, Dr. Haifei Cheng, Dr. Hanshen Zhang, Dr. Xi Yin, Dr. Qian Cheng, Dr. Huaming Xu, Mr. Mehrzad Tartibi, Mr. Taekown Jee, Ms. Hua Xiang for their invaluable discussion in research projects and coursework, as well as the mental support through the tough time. I will remember all the fun moments we shared and your friendship is as prestigious and meaningful as the Ph.D. degree to me.

I would like to thank my girlfriend, Feifei Shi for her unselfish love, patience and support. You are always able to cheers me up when I am frustrated and calm me down when I am inpatient.

Last but not least, I would like to my father Mr. Changyin Song and mother Ms. Lanling Lu. Your unconditional love, absolute trust and effortless support throughout the twenty-eight years of my life are always the most important reasons for any accomplishment I have ever made. As the Only child, I have never been blamed or complained for leaving home so many years, but I know exactly how much you miss me, because I miss you too. I hope this is my first step to fulfill the wishes of my family members and I promise to spend more time with you in future.

CHAPTER 1

Introduction

Contact mechanics is an important branch of solid mechanics, dealing with stresses and deformation of two or more bodies undergoing intimate surface interactions, as a result of internal and/or external loads. It has been a powerful tool in various industries across scales, including the automobile industry, where the macroscopic contacts of gears, bearings and brakes have to be appropriately designed in order to fulfill the desired functionality; the gas turbine industry, where the fretting wear at diaphragm-shroud interface could be a critical issue that affects the energy transfer efficiency and gas turbine lifetime; the hard-disk industry, where the microscopic contacts at head-disk interface (HDI) may affects data storage capability and product reliability significantly and the micro-electronic-mechanical system (MEMS) industry, where the contact surfaces has to be optimized in terms of geometry, material and surface treatment, in order to avoid mechanical failure like sticition and wear during high frequency contact. It also provides insights and theoretical foundation in scientific research, such as interpretation of the contact probe-based measurements (e.g. indentation and atomic force microscope (AFM)).

The pioneering work on contact mechanics dates back to Hertz (1882), who published the classical paper "On the contact of elastic solids", in which he showed that an ellipsoidal, Hertzian distribution of contact pressure would produce elastic displacements in the two bodies which were compatible with proposed elliptical contact area. The Hertz theory was strictly restricted to frictionless contact of perfectly elastic solids until the second half of the 20^{th} century, when these restrictions were removed by proper treatment of friction, stick-slip phenomenon and development of plasticity and linear viscoelasticity theories.

With the emergence of high performance computers and advances in numerical method, particularly finite element method, around forty years ago, numerical simulation has been extensively used to analyze the elastic-plastic contact mechanics, which provides important insights of the transition from elastic-dominated to plastic-dominated contact behavior, and also validates the classical Hertz theory of elastic contact, and slip line method and similarity solution for fully plastic contact.

Mechanical failures may occur in different ways, including excessive plastic flow, fracture, cyclic fatigue and wear. Hard coating has been widely used on contacting surfaces, in order to enhance the tribological performance, and product reliability and durability. As a result, tremendous research attentions have been drawn into the contact problems of layered media. Despite of limited analytical solution obtained for perfectly bonded elastic layered media, these contact problems are in general complex and have to rely on numerical simulation, considering the elastic-plastic deformation of layer/substrate material and potential interface delamination.

Driven by the development of modern engineering technologies, particularly in the hard-disk and MEMS industries, contact mechanics at micro/nanoscale has attracted significant

interests recently. The main challenges arise from two aspects: first, even the macroscopically smooth surfaces exhibit multi-scale surface roughness and it is essential to establish a multi-scale contact mechanics model that correlates macroscopic contact loads and the real surface topography, in order for an accurate real contact area, stresses and coefficient of friction; second, surface adhesion plays an important role in contact formulation as contact surfaces scale down and surface forces exceed bulk forces, as evidenced by numerous experimental observations (i.g. stiction failure in MEMS devices; contact instabilities in nanoindentation and AFM), therefore, an appropriate implementation of surface adhesion in contact mechanics model is desired for accurate predictions of micro/nanoscale contact behavior.

The traditional ways to characterize rough surfaces are to use statistical parameters, such as surface height variance, skewness and kurtosis. The most widely used statistical rough surface model is Greenwood-Williamson (GW) model, evidenced by the 3000+ citations of their original paper (1966) and general acceptance in industry for its good agreement with experimental observation. GW model characterizes rough surfaces by three independent parameters: areal density of asperity, radius of curvature at the summit of asperities and standard deviation of surface height. The simple expression of GW model allows itself to be implemented into numerical programs easily and efficiently. However, a major drawback of these statistical approaches, including GW model, is the use of scale-dependent statistical parameters. Recently, many engineering surfaces have been found to exhibit random and self-affinity features; consequently, the scale-invariant fractal geometry (Menderbrot, 1973) has been widely used in contact mechanics analysis.

Among the first attempts to incorporate surface adhesion in contact mechanics were the Johnson-Kendall-Roberts (JKR) model (1971) and Derjaguin-Muller-Toporov (DMT) model (1975), which yield different prediction of the pull-off force. These two contradictory arguments were later accommodated by introducing a dimensionless parameter, known as Tabor parameter (1977) and a smooth transition between the two models were obtained analytically using Dugdale assumption (Maugis, 1992) and numerically by assigning a specific surface traction-separation law (i.g. Lennard-Jones potential) (Muller et al., 1980). However, aforementioned work are restricted to adhesive contact of elastic solids and recently, surface traction-separation law has been implemented into finite element model, thus allows the modeling of elastic-plastic adhesive contact.

The main objectives of this dissertation were to develop contact mechanics models at asperity and rough surface scales and analyze the effects of bulk and surface material properties, surface topography and loading history on elastic and elastic-plastic contact behaviors, with particular emphasis on constitutive modeling of spherical indentation (loading) and retraction (unloading), rough surface contact, adhesion-induced contact instabilities for homogeneous and layered media and interface delamination in layered media. This dissertation is organized into nine chapters as following.

Chapter 2 presented a finite element analysis of spherical indentation on homogeneous elastic-plastic half-space. Four different post-yielding deformation regimes were identified, which correspond to different stages in evolution of the plastic zone. The boundaries of neighboring deformation regimes were obtained by curve fitting the simulation results, and a

deformation map was formulated. It was shown that the mean contact pressure does not reach its maximum (hardness, H) at the inception of transient fully-plastic deformation regime (TFP), but continues to increase until steady-state fully-plastic deformation regime (SSFP). Two distinct modes of plastic zone evolution were observed: for low effective elastic modulus-to-yield strength ratio (E^*/Y) value, plastic zone initiated at subsurface propagates in vertical direction uniformly to the surface; while for high E^*/Y values, subsurface plastic zone first propagates to the edge of contact region, forming a residual elastic core; then toward the center, until the residual elastic core disappears. Mean contact pressure and contact area constitutive equations were derived by curve fitting the simulation results of elastic-perfectly plastic half-space and extended to strain hardening half-space, by introducing an effective strain ε^* that characterizes the average indentation depth and effective yield strength accordingly.

Chapter 3 was focused on constitutive modeling of unloading behavior of an indented elastic-plastic half-space and the accumulation of plasticity in half-space due to repetitive normal contact. Residual indentation depth and dissipated plastic energy were given in a dimensionless form by curve fitting the finite element simulation results and the unloading constitutive equations were derived for elastic-perfectly plastic half-space, and extended to strain hardening half-space. Adopting the concept of effective strain introduced in chapter 2, residual indentation depth of strain hardening half-space was derived. Under multiple loading-unloading cycles, half-space of high and low E^*/Y values stabilized to elastic and plastic shakedown/ratcheting respectively. Based on the accumulation of equivalent plastic strain, the half-space of low E^*/Y value was further divided into elastic region, shakedown region and ratcheting region, as the distance to contact surface decreases.

In chapter 4, a multi-scale contact mechanics model was established to analyze the fretting contact between two rough (fractal) surfaces exhibiting fractal behavior. Contact load was distributed among the discrete contact spots by calculating the mean surface separation iteratively. A uniform tangential displacement (fretting amplitude) was imposed on individual asperities in contact and Mindlin's theory (1953) was applied to determine stick-slip status and the tangential force accordingly. Instead of a predefined, constant friction coefficient (Columb's friction coefficient), the adhesion friction force was determined by the real contact area and interfacial stress, which is dependent on the interfacial condition, but independent of the normal contact pressure and deformation mode. In addition to adhesion friction force, plowing friction component was considered for fully plastically deformed asperities in gross slip. In contrast to fretting contact analysis based on Greenwood-Williamson (GW) rough surface mode in previous literatures, present chapter showed more plastically deformed asperities were in gross slip range and contributed to frictional energy dissipation, while more elastically deformed asperities fell into the stick range and controlled the tangential stiffness of the system. Effect of fractal roughness, effective elastic modulus-to-yield strength ratio, mean contact pressure and fretting amplitude were discussed in context of numerical simulation results. Adhesion-dominant fretting and plowing-dominant fretting contact were identified.

Chapter 5 developed an elastic-plastic contact mechanics model in presence of surface adhesion, which was represented by a traction-separation relationship governed by the Lennard-Jones (LJ) potential. Adhesion-induced contact instabilities were analyzed by the theory of elasticity and a critical Tabor parameter was determined to be $\mu^* = 0.5$, above which contact and

separation of surfaces occur in an unstable way. A finite element model was used to simulate the adhesive contact of a rigid sphere and an elastic-plastic half-space, in which the LJ potential governed surface adhesion was implemented by nonlinear spring elements. The contact behavior was controlled by three key parameters: Tabor parameter μ, plasticity parameter β and maximum normal displacement δ_{max}. Simulation results showed that in the presence of plastic deformation, pull-off force may be significantly higher than the value predicted by the JKR and DMT model. Contact instabilities were also influenced by necking and residual impression due to excessive plastic deformation and could be interpreted by a modified Tabor parameter. Multiple loading-unloading cycles of adhesive contact was analyzed and it was shown that high Tabor parameter and low plasticity parameter resulted in elastic shakedown, whereas low Tabor parameter and high plasticity parameter led to plastic shakedown.

Chapter 6 extended finite element model developed in chapter 5 to simulate the adhesive contact of a rigid sphere and a layered medium that consists of a stiff elastic layer and a compliant elastic-plastic substrate. An effective Tabor parameter was derived as a function of layer thickness t, layer and substrate Tabor parameter μ_f and μ_s, respectively. It was shown that surface separation (detachment) during unloading was not encountered at the instant of maximum adhesion (pull-off) force, but as the layered medium continued to be stretched by rigid sphere, until jump-out instability occured. Brittle and ductile separation modes were identified from the residual deformation after complete unloading and a map of separation mode was constructed with respect to the maximum surface separation $\delta_{\max}$ and substrate plasticity parameter β. For high β values, the unloading process is more ductile with larger $\delta_{\max}$, evidenced by the increase of pile-up height; while for small β values, the separation is more brittle with larger $\delta_{\max}$, illustrated by the increase of residual impression depth. Multiple loading-unloading cycles of adhesive contact was analyzed and incremental plasticity (ratcheting) in the substrate was found the most likely steady-state deformation mechanicsm. In subsequent approach cycles, adhesion force was larger (smaller) and critical surface separation for jump-in instability was smaller (larger) than that of the 1^{st} cycle, for low (high) β value, which was interpreted by residual impression (permanent pile-up) after the 1^{st} cycle.

Chapter 7 continued to study the mechanical response of layered media subjected to contact load in the presence of surface adhesion. Instead of being assumed perfectly bonded (chapter 6), the layer-substrate interface was modeled by a bilinear cohesive zone law, which was characterized by cohesive strength and interface work of adhesion, and allowed the crack initiation and growth along the interface. It was shown that the unloading response comprises five sequential stages: elastic recovery, interface damage (crack) initiation, damage evolution (delamination), film bending, and abrupt surface separation (jump-out), with plastic deformation in the substrate occurring only during damage initiation. Accumulation of plasticity in the substrate produced partial closure of the cohesive zone upon full unloading (jump-out), residual tensile stresses at the front of the crack tip, and downward deflection of the elastic film. The interface work of adhesion affected the contact behavior only during unloading. In particular, both surface force and contact stiffness were influenced by the evolution of interfacial damage during unloading only in the case of relatively low interface work of adhesion. Increasing the interface work of adhesion promotes crack closure and increases the crack-tip opening displacement after full unloading (jump-out). Both crack closure and crack-tip opening displacement after full unloading increase with the decrease of cohesive strength due to the increase in cohesive zone closure and critical surface separation at failure, respectively; an

unstable crack initiation was observed for layer-substrate interface of high cohesive strength. The maximum interface delamination was observed for substrate of intermediate yield strength: when substrate yield strength is low, the substrate undergoes excessive plastic deformation during unloading, conforming the deflected elastic layer; for high yield strength substrate, plastic deformation during loading is negligible, thus the adhesion-induced delamination is completely closed after jump-out. The effect of preexisting crack at interface was found to be significant only during the unloading process. Above a critical crack size, surface separations at the instances of jump-in and jump-out instabilities exhibited a linear dependence on crack size; while below which, crack size showed no influence on contact instabilities. The results of this study provide insight into the interdependence of contact instabilities and evolution of interfacial damage (cracking) in layered media during adhesive contact loading and unloading.

Analytical and numerical (FEM) model of elastic adhesive contact developed in chapter 5 was extended in chapter 8 to study the elastic adhesive contact behavior of rough surface. Based on the instability criteria derived in chapter 5, two sets of constitutive equations were developed for single asperity contacts demonstrating smooth ($\mu < 0.5$) and abrupt ($\mu < 0.5$) contacts. These constitutive equations were incorporated into a Greenwood-Williamson (GW) (1966) rough surface model, and the evolution of contact force and contact area were obtained with respect to mean surface separation. The evolution of contact area exhibited a three-stage behavior and particularly, the rapid nonlinear increase of contact area in the second stage was attributed to the asperity-scale jump-in instabilities. The maximum adhesive force (strength of adhesion) was shown to decrease with surface roughness and increases with Tabor parameter. The adhesion parameter θ defined by Fuller and Tabor (1975) was shown to be governing parameter of the strength of adhesion, only for contact surfaces of high μ values; a new adhesion parameter ζ, defined as the ratio of surface roughness to equilibrium interatomic separation ε, was proposed and confirmed by numerical simulation to control the strength of adhesion for low μ values. To accommodate the two different adhesion parameters, an effective surface separation was introduced, as the sum of the effective adhesion force range (characterized by ε) and adhesion-induced asperity elastic deformation (characterized by $\mu\varepsilon$). The effective surface separation represents a critical separation between two countering asperities, above which the adhesion force is secondary. A general adhesion parameter ξ is defined as the ratio of surface roughness to the effective surface separation, with θ and ζ as two asymptotes in for the high and low Tabor parameter values, respectively.

Finally, chapter 9 concludes the dissertation with a summary of main findings and implications reported in chapter 2-8.

Chapter 2

Elastic-plastic spherical indentation: deformation regimes, evolution of plasticity, and hardening effect

2.1. Introduction

Indentation-induced plasticity is a fundamental problem in contact mechanics with direct implications in a broad range of engineering applications, including materials hardness measurement, load-carrying capacity of bearings and gears, and wear of plastically deformed micro/macroscopic contacts, such as those formed between magnetic recording heads and hard disks (Komvopoulos, 2000) and gas-turbine blades and shrouds (Cowles, 1996), respectively. One of the earliest indentation studies aimed to evaluate the hardness of metals is attributed to Tabor (1951). This work motivated numerous subsequent analytical and experimental studies dealing with the evolution of plasticity in half-spaces due to compression by rigid indenters of various shapes. Ishlinsky (1944) used the slip-line theory of plasticity (Hill, 1967) to analyze indentation of a rigid-perfectly plastic half-space by a rigid sphere and found that the hardness is equal to three times the yield strength of the material. A similar result was obtained by Hill et al. (1989) and Biwa and Storåkers (1995), who used flow theory to obtain a similarity solution of rigid-plastic and elastic-plastic indentation, respectively. Johnson (1985) showed that the overall deformation behavior of indented elastic-perfectly plastic materials is characterized by the sequential evolution of elastic, elastic-plastic, and fully plastic deformation below the rigid indenter and that the material hardness is reached at the inception of fully plastic deformation.

Although elastic and fully plastic deformation due to indentation loading can be studied analytically by the Hertz theory and the slip-line theory of plasticity or similarity approach, respectively, analytical treatment of indentation-induced elastic-plastic deformation is cumbersome because both elastic and plastic deformation play important roles on the overall deformation behavior. Samuels and Mulhearn (1957) observed that compression of a half-space by a blunt indenter produces subsurface displacements approximately in the radial direction from initial contact and argued that deformation can be represented by approximately hemi-spherical isostrain contours. Motivated by this observation, Johnson (1985) derived a simple constitutive relation between the mean contact pressure p_m in spherical indentation normalized by the material yield strength Y and a strain parameter E^*r/YR, where $E^* = E/(1-\nu^2)$ is the effective elastic modulus (E and ν denote elastic modulus and Poisson's ratio, respectively), r is the contact radius, and R is the radius of curvature of the spherical indenter.

Difficulties in analyzing the complex elastic-plastic deformation due to indentation loading were overcome with the enhancement of computational capability and implementation of numerical methods, such as the finite element technique. One of the first finite element studies of elastic-plastic indentation is attributed to Hardy et al. (1971), who observed a change in contact pressure distribution from elliptical (Hertzian) to rectangular and a trend for the stresses along the axis of symmetry to become constant with increasing contact load. Follansbee and Sinclair

(1984) analyzed elastic-plastic indentation with a constant-strain-triangle finite element code, and using a grid expansion technique to improve the computation efficiency they obtained numerical results that are in excellent agreement with the classical (Hertzian) elastic solution and experimental results for small and large indentation depths, respectively. Giannakopoulos et al. (1994) performed a finite element analysis of Vickers indentation and obtained constitutive relations of the indentation load and depth for elastic and elastic-plastic material behaviors, respectively. Komvopoulos and Ye (2001) derived a dimensionless constitutive equation for indentation of elastic-perfectly plastic half-spaces by a rigid sphere that is in good agreement with the constitutive model obtained by Johnson (1985) and found that $H = 2.9\,Y$. Kogut and Komvopoulos (2004) showed that the slip-line solution $H = 3\,Y$ is suitable for half-spaces exhibiting high E^*/Y values (i.e., materials demonstrating negligible elastic deformation during indentation), whereas the hardness of half-spaces characterized by low E^*/Y values can be much less than 3Y. They also E^*/Y and δ/r', where r'or is the radius of the truncated contact area, as independent parameters to derive constitutive models that were shown to yield more accurate predictions than that of Johnson (1985) based on a single strain parameter (E^*r/YR). Park and Pharr (2004) showed that elastic-plastic deformation due to indentation can be divided into elastic- and plastic-dominant regimes, characterized by insignificant and significant hardening effect, respectively. Mesarovic and Fleck (1999) observed a decrease in p_m at large indentation depths δ, which they attributed to failure of the assumptions used to derive the similarity solution, specifically infinitesimal strain kinematics and boundary condition of uniform normal velocity. Indentation mechanics models have also been used to characterize the mechanical behavior of layered medium (Bhattacharya and Nix, 1988; Ye and Komvopoulos, 2003), interpret the elastic modulus and hardness of thin films measured by the nanoindentation technique (Knapp et al., 1999), study the effect of repetitive contact loading on stress and strain accumulation (Kral et al., 1993), explore the role of surface adhesion in indentation response (Mesarovic and Johnson, 2000), and study multi-scale roughness effects in contact mechanics of real surfaces (Komvopoulos and Yan, 1998).

Despite significant insight into elastic-plastic deformation of indented half-space media derived from aforementioned analytical and numerical investigations, insight into the evolution of different deformation behaviors in the post-yield response of elastic-plastic materials, measurement of the true material hardness, and role of strain hardening in indentation requires further comprehensive study. Understanding of deformation response due to indentation loading requires knowledge of the evolution of plasticity of global deformation parameters. Consequently, the objective of this chapter was to examine the post-yield indentation behavior of elastic-plastic half-spaces for a wide range of material properties and identify the deformation regimes arising from the onset of yielding to the commencement of steady-state fully plastic behavior. Equations for the boundaries between different deformation regimes were obtained numerically and constitutive relationships of the mean contact pressure and contact area were extracted from finite element results. Two different deformation modes of the evolution of the residual elastic core between the indenter and the plastic zone are observed by tracking the development of the plastic zone with increasing indentation depth. An effective strain accounting for the increase in yield strength due to the hardening effect is used to provide a general description of the indentation behavior of elastic-plastic half-spaces possessing different strain hardening characteristics. General constitutive equations of the mean contact pressure and contact area are given for both elastic-perfectly plastic and hardening materials.

2.2. Method of analysis

2.2.1. Problem definition

Figure 2.1 shows a schematic of an elastic-plastic half-space indented by a rigid sphere of radius R. The radius of the truncated area and the real contact area is denoted by r' and r, respectively. For small indentation depths ($\delta << R$), deformation is purely elastic and the mean contact pressure p_m and real contact area a are given by (Johnson, 1985)

$$p_m = \frac{P}{\pi r^2} = \frac{4\sqrt{2}}{3\pi}\left(\frac{E^*\delta}{r'}\right) \tag{2.1}$$

$$a = 0.5a' = \pi\delta(R - 0.5\delta) \tag{2.2}$$

where P is the normal load and $a' = \pi(r')^2 = \pi\delta(2R - \delta)$ is the truncated contact area.

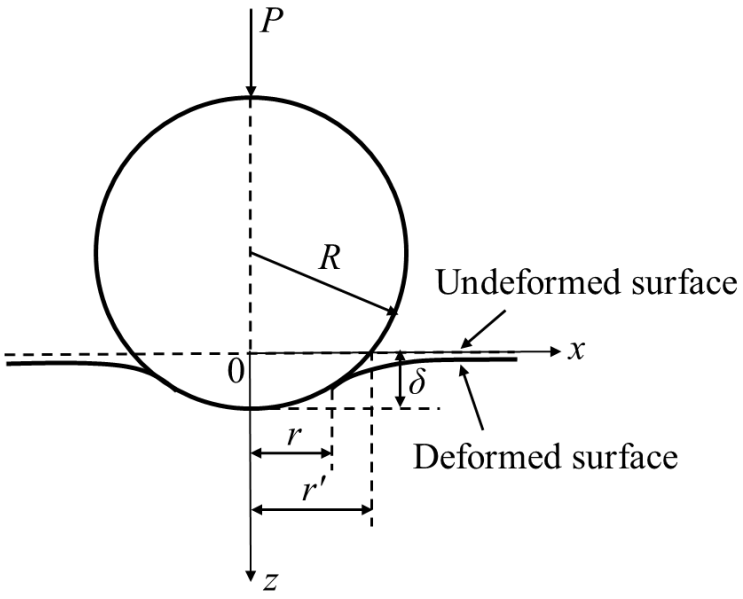

Figure 2.1 Schematic of a deformable half-space indented by a rigid sphere.

Yielding is first encountered on the axis of symmetry ($x = 0$) at depth $z = 0.48r$, and the corresponding indentation depth and mean contact pressure are given by $\delta_c = 1.78r'/(E^*/Y)$ and $p_m = 1.1Y$, respectively. Increasing further the indentation depth ($\delta > \delta_c$) leads to elastic-plastic deformation and the deviation of p_m and a from Eqs. (2.1) and (2.2), respectively. The maximum mean contact pressure $p_m^{\max}$, referred to as the material hardness, is reached at the inception of fully plastic deformation and remains constant with further increasing the indentation depth (load).

2.2.2. Finite element model

Figure 2.2 shows the finite element model used in this study. The spherical indenter was modeled as a rigid surface, while the half-space was represented by a mesh consisting of 39,650 axisymmetric, linear, isoperimetric elements comprising 40,270 nodes. Contact between the rigid sphere and the deformable medium was assumed to be frictionless. Nodes on the symmetry axis and bottom boundary of the mesh were constrained against displacement in the horizontal (radial) and vertical directions, respectively. The distance between two neighboring nodes of the refined mesh adjacent to the contact interface is equal to $0.0008R$.

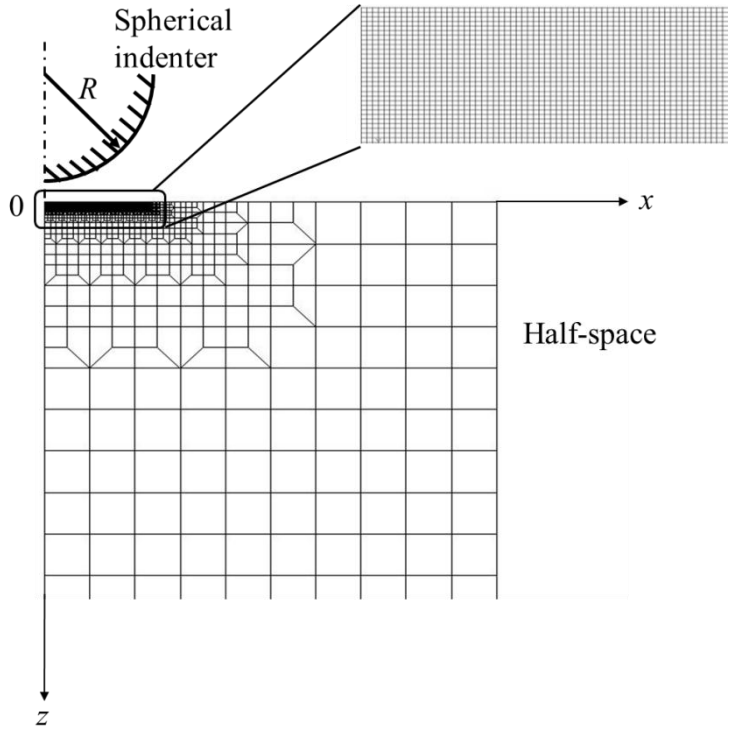

Figure 2.2 Finite element model of a half-space and a spherical indenter.

Numerical results are presented in terms of dimensionless parameters, such as mean contact pressure $\bar{p}_m = p_m/Y$, contact area $\bar{a} = a/a'$, indentation depth $\bar{\delta} = \delta/r'$, and effective elastic modulus-to-yield strength ratio E^*/Y. Figure 2.3 shows the variation of $\bar{p}_m$ with $\bar{\delta}$ in the elastic deformation regime ($\delta < \delta_c$). Finite element results are compared with the analytical solution obtained from Hertz theory (Eq. (2.1)). The close agreement between numerical and analytical results validates the modeling assumptions and verifies the suitability of the adopted finite element mesh. All simulations were performed with the multi-purpose finite element code ABAQUS/Standard (Implicit) (version 6.6.3).

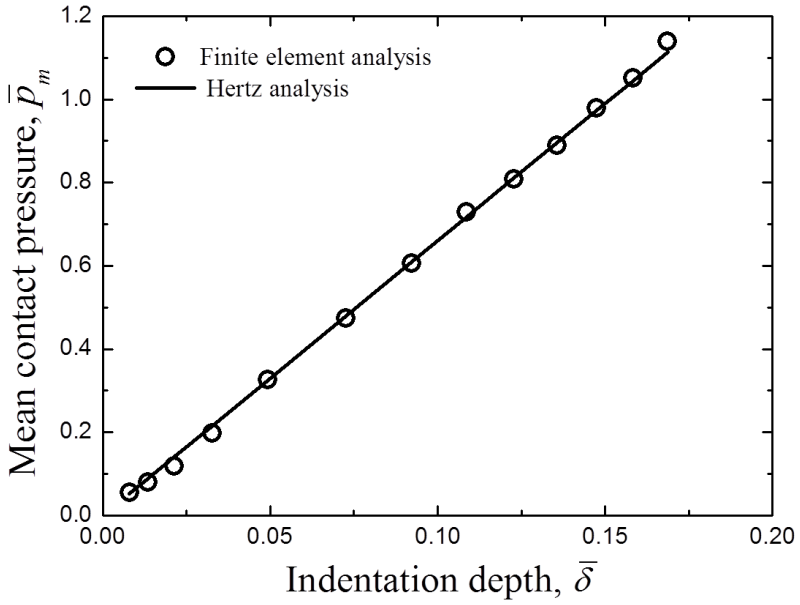

Figure 2.3 Variation of mean contact pressure $\bar{p}_m$ with indentation depth $\bar{\delta}$ in the elastic deformation regime.

2.2.3. Constitutive material model

Deformation in the elastic-plastic half-space was described by the following stress-strain constitutive equations:

$$\sigma = E^* \varepsilon \quad (\sigma < Y) \tag{2.3a}$$

$$\sigma = Y(\varepsilon/\varepsilon_Y)^n \quad (\sigma \geq Y) \tag{2.3b}$$

where σ is the stress, ε is the strain, $\varepsilon_Y = Y/E^*$ is the yield strain, and n is the strain hardening exponent.

Yielding was determined by the von Mises yield criterion, expressed as

$$\sigma_{eq} = \sqrt{\frac{3}{2} S_{ij} S_{ij}} = Y \tag{2.4}$$

where σ_{eq} is the von Mises equivalent stress and S_{ij} represents components of the deviatoric stress tensor.

The evolution of plasticity in the indented half-space was tracked by the equivalent plastic strain $\bar{\varepsilon}_p$, defined as

$$\bar{\varepsilon}_p = \int_\Omega \sqrt{\frac{2}{3} d\varepsilon_{ij}^p d\varepsilon_{ij}^p} \tag{2.5}$$

where $d\varepsilon_{ij}^{p}$ denotes increments of plastic strain and Ω is the strain path used to track the accumulation of plasticity.

2.3. Results and discussion

2.3.1. Deformation regimes of elastic-plastic indentation

Figure 2.4 shows representative finite element results of the mean contact pressure $\bar{p}_m$ as a function of indentation depth $\bar{\delta}$ for an elastic-perfectly plastic half-space with $E^*/Y = 55$. Contrary to classical contact mechanics showing the post-yield behavior comprising elastic-plastic and fully plastic deformation regimes (Johnson, 1985), the present analysis shows that the post-yield response consists of four deformation regimes – linear elastic-plastic (LEP), nonlinear elastic-plastic (NEP), transient fully plastic (TFP), and steady-state fully plastic (SSFP). The post-yield deformation regimes shown in Figure 2.4 were identified by tracking the evolution of the plastic zone and variation of mean contact pressure with the increase of the indentation depth $\bar{\delta}$, as discussed below.

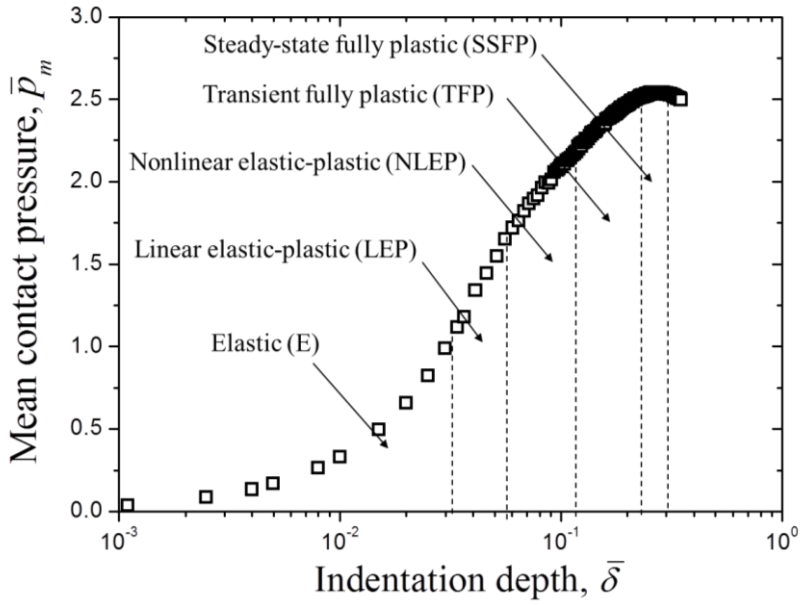

Figure 2.4 Variation of mean contact pressure $\bar{p}_m$ with indentation depth $\bar{\delta}$ for an elastic-perfectly plastic half-space with $E^*/Y = 55$. Boundaries between various deformation regimes are represented by vertical dashed lines.

Linear elastic-plastic (LEP): The lower and upper bounds of the LEP regime correspond to the inception of yielding and the instant that the plastic zone reaches the surface, respectively. Because the plastic zone is completely surrounded by elastic material, the contact behavior in this regime is controlled by elastic deformation. The mean contact pressure exhibits a semi-logarithmic dependence on indentation depth, used to derive constitutive relations of elastic-plastic indentation by curve fitting finite element results (Ye and Komvopoulos, 2003; Kogut and

Komvopoulos, 2004). However, Figure 2.4 shows that this semi-logarithmic relationship holds only in the LEP deformation regime, where the plastic zone is fully confined into the subsurface.

Nonlinear elastic-plastic (NLEP): A transition from elastic- to plastic-dominant deformation behavior occurs in the NLEP regime where the elastic core between the rigid indenter and the plastic zone shrinks and ultimately disappears. Figure 2.4 shows that as soon as the plastic zone reaches the surface, the contact stiffness decreases and the semi-logarithmic dependence of $\bar{p}_m$ on $\bar{\delta}$ observed in the LEP regime no longer holds.

Transient fully plastic (TFP): In contrast to earlier studies (Hill et al., 1989; Mesarovic and Fleck, 1999; Komvopoulos and Ye, 2001; Park and Pharr, 2004; Kogut and Komvopoulos, 2004), Figure 2.4 shows that $\bar{p}_m^{\max}$ is not encountered at the inception of fully-plastic deformation, i.e., upon the disappearance of the elastic core (termination of the NLEP regime). Instead, $\bar{p}_m$ continues to increase with more plasticity accumulating in the subsurface until $\bar{p}_m^{\max}$ is ultimately reached. This regime is referred to as the TFP regime.

Steady-state fully plastic (SSFP): A further increase in indentation depth produces a plateau of $\bar{p}_m^{\max}$ that characterizes the SSFP deformation regime and corresponds to the true material hardness, predicted by the similarity solution and slip-line plasticity theory. The trend for $\bar{p}_m$ to decrease at very large indentation depths is attributed to the increase of the contact area due to pile-up formation, and is in agreement with the breakdown of infinitesimal strain kinematics and boundary condition of uniform normal velocity used in the similarity solution (Mesarovic and Fleck, 1999).

Figure 2.5 shows the variation of the mean contact pressure $\bar{p}_m$ with the indentation depth $\bar{\delta}$ for E^*/Y in the range of 11–2200. Boundaries between different deformation regimes are shown by solid lines. The boundary curves were obtained by fitting the numerical data at the transition between neighboring deformation regimes for different E^*/Y values. For E^*/Y = 2200, representing a material of extremely low yield strain (ε_Y = 0.0004), i.e., negligible contribution of elastic deformation, $\bar{p}_m^{\max}$ = 2.89, which is close to the similarity solution ($\bar{p}_m^{\max}$ = 3.0) obtained for a rigid perfectly-plastic material. However, for E^*/Y = 11, the effect of elastic deformation is significant and $\bar{p}_m^{\max}$ = 2.09, which is significantly less than the similarity solution.

From curve fitting the numerical results corresponding to the boundary between the TFP and SSFP deformation regimes shown in Figure 2.5, the following hardness and corresponding indentation depth relationships were obtained:

$$\frac{H}{Y} = 2.96\left[1 - \left(\frac{E^*}{Y}\right)^{-1/2}\right] \tag{2.6}$$

$$\bar{\delta} = \frac{1}{0.053\left(\frac{E^*}{Y}\right)+0.82} \tag{2.7}$$

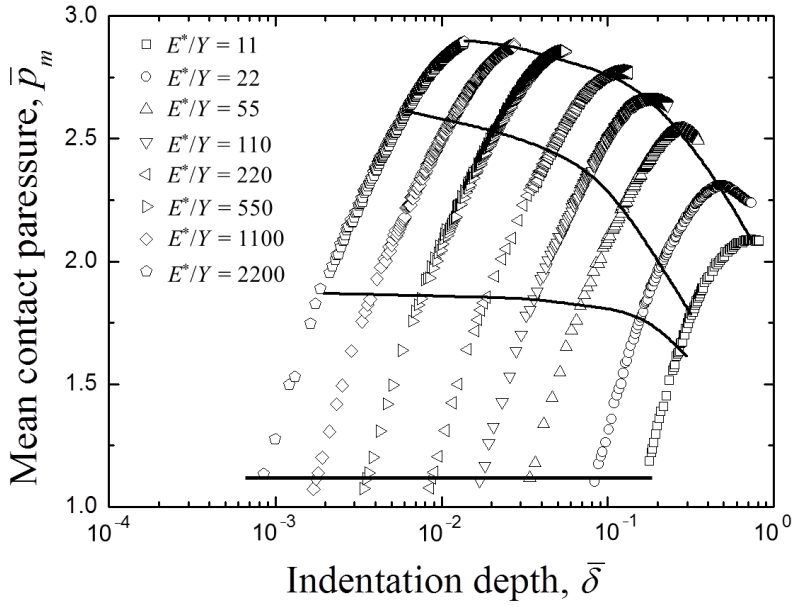

Figure 2.5 Variation of mean contact pressure $\bar{p}_m$ with indentation depth $\bar{\delta}$ for elastic-perfectly plastic half-spaces with E^*/Y = 11–2200. Solid lines represent boundaries between deformation regimes.

Figure 2.6 shows a best-fit curve (Eq. (2.6)) and finite element results of the hardness H/Y as a function of E^*/Y. Solutions from previous studies are also included for comparison. Although all solutions demonstrate a similar trend, significant differences exist for high E^*/Y values, which may be attributed to differences in mesh refinement and/or the smaller E^*/Y range examined in those earlier studies. The convergence of Eq. (2.6) to H/Y =3 with increasing E^*/Y is validated by indentation experiments (Marsh, 1964). It is noted that Eq. (2.6) may not hold for very low E^*/Y values, because the very large indentation depth needed to initiate plastic deformation in these cases exceeded the current simulation capability. However, Eq. (2.6) is applicable for most engineering materials.

Using a similar curve fitting approach, relationships were obtained for the other deformation boundaries shown in Figure 2.5. For the boundary of the LEP and NLEP deformation regimes,

$$\bar{p}_m = 1.85\left[1 - \left(\frac{E^*}{Y}\right)^{-0.93}\right] \tag{2.8}$$

$$\bar{\delta} = \frac{1}{0.25\left(\frac{E^*}{Y}\right)+0.54} \tag{2.9}$$

and for the boundary of the NLEP and TEP deformation regimes,

$$\bar{p}_m = 2.7\left[1 - \left(\frac{E^*}{Y}\right)^{-0.44}\right] \tag{2.10}$$

$$\bar{\delta} = \frac{1}{0.11\left(\frac{E^*}{Y}\right)+1.99} \tag{2.11}$$

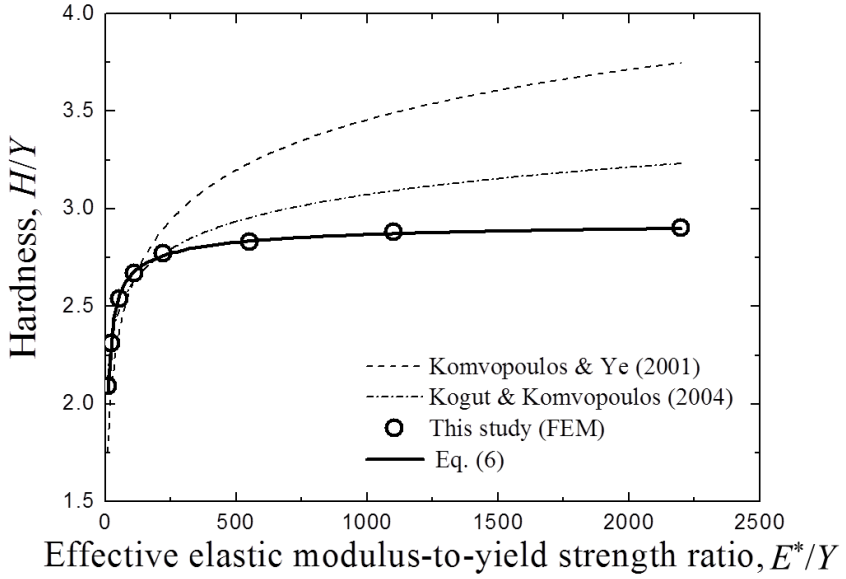

Figure 2.6 Variation of hardness H/Y with effective elastic modulus-to-yield strength ratio E^*/Y for elastic-perfectly plastic half-spaces.

2.3.2. Constitutive contact equations

As mentioned earlier, the indentation behavior in the elastic deformation regime is characterized by the linear dependence of $\bar{p}_m$ on $\bar{\delta}$ (Eq. (2.1)), while in the SSFP deformation regime the mean contact pressure reaches a maximum corresponding to the material hardness (Eq. (2.6)).

In the LEP deformation regime ($1.78/(E^*/Y) \le \bar{\delta} \le [0.54 + 0.25(E^*/Y)]^{-1}$), curve fitting of the finite element results yields the following semi-logarithmic relation of $\bar{p}_m$ in terms of $\bar{\delta}$:

$$\bar{p}_m = 1.03 + \log\left[\bar{\delta}^{2.23}\left(\frac{E^*}{Y}\right)^{2.08}\right] + \frac{\log\bar{\delta}}{0.04\log\left(\frac{E^*}{Y}\right)+2.16} = 1.03 + 2.08\log\left(\frac{E^*}{Y}\right) + \left\{2.23 + \left[0.04\log\left(\frac{E^*}{Y}\right) + 2.16\right]^{-1}\right\}\log\bar{\delta} \tag{2.12}$$

Contrary to previous studies (e.g., Ye and Komvopoulos, 2003; Kogut and Komvopoulos, 2004), the second expression of Eq. (2.12) indicates that the slope of the $\bar{p}_m$ versus $\log\bar{\delta}$ plot is a function of E^*/Y.

Similarly, curve fitting of finite element results corresponding to the NLEP and TFP deformation regimes ($[0.54 + 0.25(E^*/Y)]^{-1} \le \bar{\delta} \le [0.82 + 0.553(E^*/Y)]^{-1}$) gives

$$\bar{p}_m = 2.13\left[\log\left(\frac{E^*}{Y}\right)\right]^{1/2} + 1.65\left[\log\left(\frac{E^*}{Y}\right)\right]^{-3/2}\left(\log\bar{\delta}\right)^2 \tag{2.13}$$

Figure 2.7 shows the variation of the dimensionless contact area $\bar{a}$ with indentation depth $\bar{\delta}$ in the LEP, NLEP, and TFP deformation regimes ($1.78/(E^*/Y) \le \bar{\delta} \le [0.82 + 0.553(E^*/Y)]^{-1}$) for E^*/Y in the range of 11–2200. From curve fitting the finite element data shown in Figure 7, the following expression of the real contact area in the LEP, NLEP, and TFP deformation regimes was obtained:

$$\bar{a} = \frac{1}{2}\left[1 - \left(\frac{E^*}{Y}\right)^{-1/2}\right] + \left[0.39 + 0.03\left(\frac{E^*}{Y}\right)\right]\bar{\delta} - \left[0.86 - 0.0004\left(\frac{E^*}{Y}\right)^2\right]\bar{\delta}^2 \tag{2.14}$$

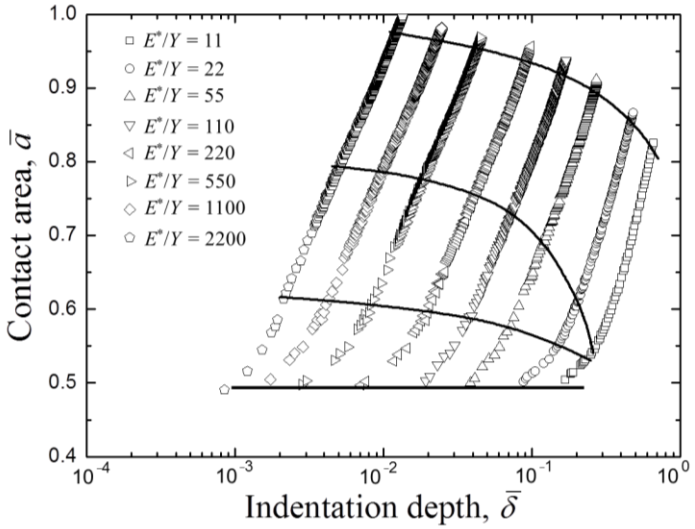

Figure 2.7 Variation of contact area $\bar{a}$ with indentation depth $\bar{\delta}$ for elastic-perfectly plastic half-spaces with E^*/Y = 11–2200. Solid lines represent boundaries between deformation regimes.

For most engineering materials with relatively high E^*/Y values (e.g., E^*/Y > 200) and elastic deformation (i.e., $\bar{\delta} < 0.001$), Eq. (2.14) yields $\bar{a} \approx 0.5$, consistent with the solution obtained from Hertz theory. In the SSFP deformation regime (too narrow to be seen in the scale of Figure 2.7), the contact area $\bar{a}$ is independent of $\bar{\delta}$ and varies only with E^*/Y. Indeed, from curve fitting it was found that:

$$\bar{a} = 1 - 0.51\left(\frac{E^*}{Y}\right)^{-0.4} \tag{2.15}$$

It is noted that as E^*/Y increases (i.e., elastic deformation decreases), Eq. (2.15) approaches the solution of a rigid-perfectly plastic half-space obtained from slip-line theory ($\bar{a} = 1$).

Hence, constitutive equations for the different deformation regimes of elastic-perfectly plastic materials are given by Eq. (2.1) (E), Eq. (2.12) (LEP), Eq. (2.13) (NLEP and TFP), and Eq. (2.6) (SSFP) for the mean contact pressure and Eq. (2.2) (E), Eq. (2.14) (LEP, NLEP, and TFP), and Eq. (2.15) (SSFP) for the contact area.

2.3.3. Evolution of plasticity

As discussed in section 2.3.1, a transition from elastic- to plastic-dominant deformation behavior is encountered with the evolution of plasticity, including the initiation and growth of the plastic zone and the shrinking and disappearance of the elastic core. Figure 2.8 shows representative results revealing two modes of plastic zone development. For material behavior dominated by plasticity (high E^*/Y), Figure 2.8(a) shows that the increase of the indentation depth causes the plastic zone to expand initially toward the contact edge, resulting in the formation of an elastic core below the contact interface ($\bar{\delta}$ = 0.0018). As the indentation depth (load) increases, the elastic core shrinks ($\bar{\delta}$ = 0.0034) and eventually disappears ($\bar{\delta}$ = 0.0058). Alternatively, for elastic-dominant material behavior (low E^*/Y), the occurrence of significant elastic deformation before the inception of yielding produces a grossly convex contact interface (Figure 2.8(b)). An elastic strip of uniform thickness inhibits the expansion of the plastic zone toward the surface, even for relatively large indentation depths ($\bar{\delta}$ = 0.204). In this case, increasing the indentation depth leads first to uniform thinning ($\bar{\delta}$ = 0.254) and eventual disappearance ($\bar{\delta}$ = 0.311) of the elastic strip.

Figure 2.9 provides further insight into the first mode of plastic zone development (high E^*/Y) in terms of the dimensionless radius $\bar{r} = r/r_i$ and maximum height (thickness) $\bar{h} = h/h_i$ of the elastic core (Figure 2.8(b)), where h_i and r_i are the height and radius of the elastic core at the inception of NLEP deformation. While the height of the elastic core exhibits a monotonic decrease with increasing indentation depth, the elastic core radius demonstrates a two-stage behavior: relatively shallow indentations ($\bar{\delta} < 0.005$) produce elastic cores of similar radius, whereas the radius of elastic cores produced from deep indentations ($\bar{\delta} > 0.005$) decreases with increasing indentation depth. This trend is attributed to two competing mechanisms: (a) yielding in the elastic core that decreases the core radius and (b) compression of the elastic core (Poisson's effect) that increases the core radius. For shallow indentations, the two competing mechanisms are comparable and the core radius remains constant, while for deep indentations, yielding in the elastic core is dominant and the core radius decreases. For the simulation results shown in Figure 2.9, the critical indentation depth for the disappearance of the elastic core (i.e., transition from NLEP to TFP deformation) is $\bar{\delta} \approx 0.006$.

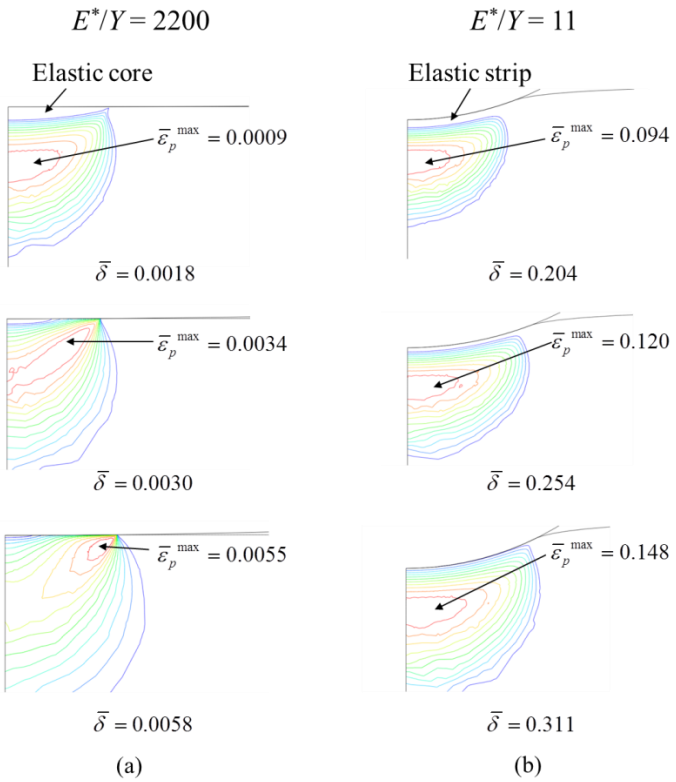

Figure 2.8 Evolution of plastic zone in the nonlinear elastic-plastic (NLEP) deformation regime of an elastic perfectly plastic half-space with (a) E^*/Y = 2200 and (b) E^*/Y = 11.

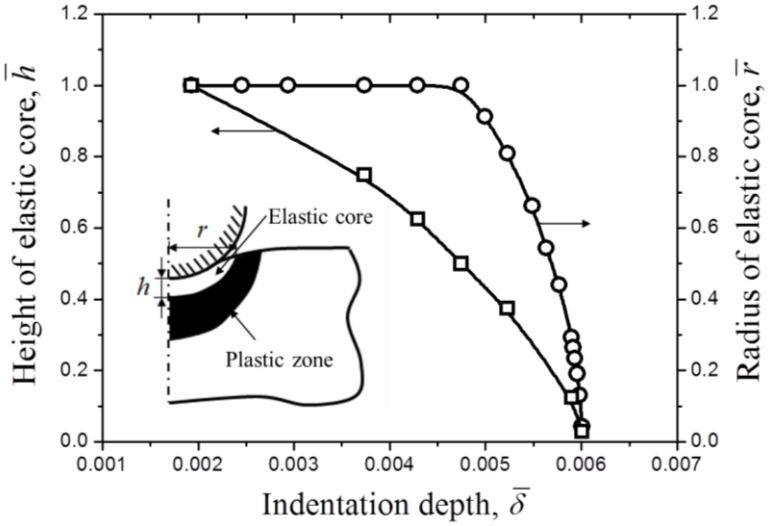

Figure 2.9 Variation of elastic core height $\bar{h}$ and radius $\bar{r}$ with indentation depth $\bar{\delta}$ in the nonlinear elastic-plastic (NLEP) deformation regime of an elastic-perfectly plastic half-space with E^*/Y = 2200.

2.3.4. Hardening effect

Although the results presented above provide insight into the deformation characteristics of indented elastic-perfectly plastic materials, most engineering metals and alloys exhibit strain hardening that increases the capacity of the material to accumulate plastic deformation above the initial yield strength Y. Finite element results are presented in this section for elastic-plastic half-spaces demonstrating isotropic strain hardening that follows Eq. (2.3b). Figures 2.10(a) and 2.10(b) show the mean contact pressure $\bar{p}_m = p_m/Y$ and contact area $\bar{a} = a/a'$ as functions of indentation depth $\bar{\delta}$ for E^*/Y =11 and n between 0 and 0.5. Different deformation regimes are distinguished by dashed vertical lines. The effect of strain hardening in the LEP deformation regime is shown to be negligible, in agreement with the results of a previous study (Park and Pharr, 2004) showing a secondary hardening effect on the indentation response for elastic-dominant deformation ($\bar{p}_m$< 2.1). This finding can be explained by considering the evolution of plasticity. Under conditions of LEP deformation ($\bar{\delta} < 0.3$), the plastic zone is fully confined into the subsurface because of the formation of an elastic core (strip) below the contact interface, as observed for $n = 0$ (Figure 2.8). Thus, the elastic-plastic half-space can be approximated by a layered medium consisting of an elastic layer and an elastic-plastic substrate exhibiting strain hardening. For relatively shallow indentations (LEP deformation), the substrate effect is secondary because the indentation depth is small relative to the thickness of the elastic core (strip); therefore, the overall contact response is not sensitive to the strain hardening behavior of the substrate. As the indentation depth (load) increases, the thickness (and radius) of the elastic core (strip) decreases and the substrate effect becomes dominant. This explains the increase in contact stiffness with strain hardening exponent for $\bar{\delta} > 0.3$.

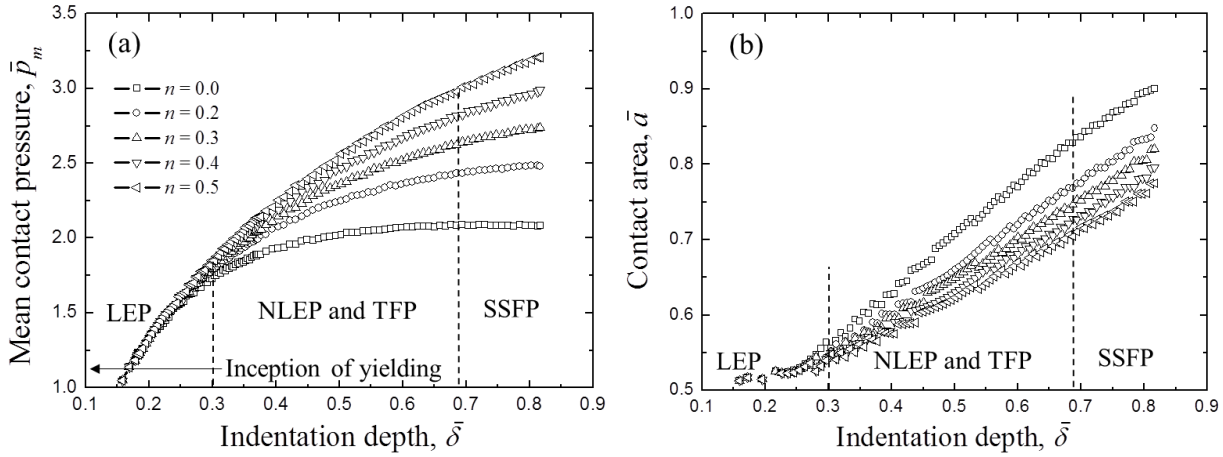

Figure 2.10 Variation of (a) mean contact pressure $\bar{p}_m$ and (b) contact area $\bar{a}$ with indentation depth $\bar{\delta}$ for elastic-plastic half-spaces with E^*/Y = 11 and n = 0–0.5.

To obtain a general constitutive contact model accounting for strain hardening, the mean contact pressure was normalized by the effective yield strength Y^*, which depends on the *current* indentation depth, strain hardening exponent, and initial yield strength. Using Eqs. (2.3a) and (2.3b) and the idea of the effective material strength Y^*, it follows that

$$Y^* = Y \ \ (\varepsilon^* \le \varepsilon_Y) \tag{2.16a}$$

$$Y^* = Y(\varepsilon^*/\varepsilon_Y)^n \ \ (\varepsilon^* > \varepsilon_Y) \tag{2.16b}$$

where ε^* is the effective strain. Y^* was obtained in terms of E^*/Y and n by equating finite element results of $\bar{p}_m^* = p_m/Y^*$ ($n \neq 0$) with results of $\bar{p}_m = p_m/Y$ ($n = 0$) for the same indentation depth. The calculated value of Y^* was then substituted into Eq. (2.16b) to obtain ε^* in terms of E^*/Y, n, and $\bar{\delta}$. Figure 2.11(a) shows the variation of ε^* with $\bar{\delta}$ and n for $E^*/Y = 11$. The close agreement between results corresponding to different n values validates the concept of effective strain. The data shown in Figure 2.11 indicate a fairly linear variation of ε^* with $\bar{\delta}$. Thus, from a linear curve fit, it is found that $\varepsilon^* \approx 0.3\bar{\delta}$. Figure 2.11(b) shows the variation of the mean contact pressure $\bar{p}_m^*$ normalized by the effective yield strength with indentation depth $\bar{\delta}$ for n = 0–0.5. It can be seen that the mean contact pressure data of all hardening cases are fairly close with those of the elastic-perfectly plastic case. This is important because it indicates no hardening effect on the boundaries of the various deformation regimes for n = 0 and given E^*/Y (e.g., dashed lines in Figures 2.4 and 2.10).

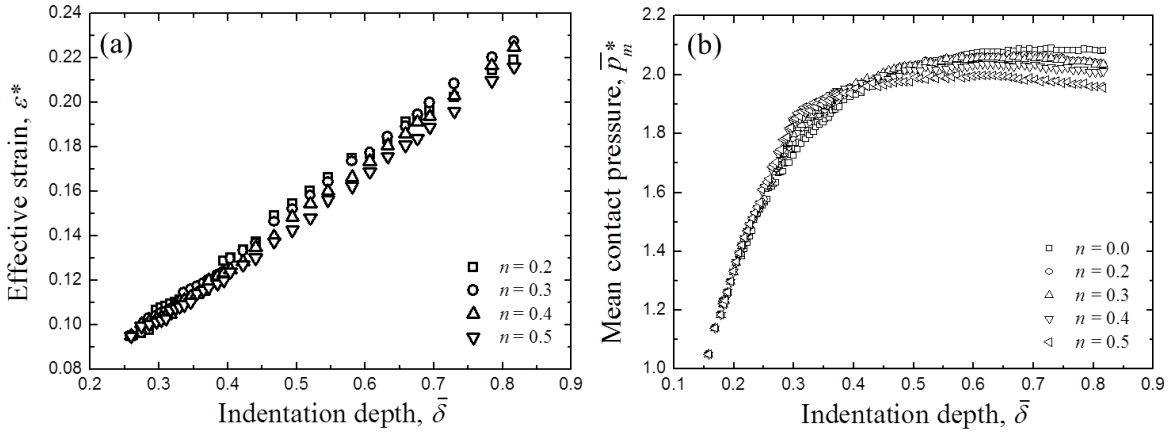

Figure 2.11 (a) Effective strain ε^* versus indentation depth $\bar{\delta}$ for elastic-plastic half-spaces with E^*/Y = 11 and n = 0.2–0.5 and (b) mean contact pressure $\bar{p}_m^*$ (normalized by the effective yield strength Y^*) versus indentation depth $\bar{\delta}$ for elastic-plastic half-spaces with E^*/Y = 11 and n = 0–0.5.

Substituting the later relation and Eq. (2.16b) into Eq. (2.13), the following general constitutive contact relation is obtained for both NLEP and TFP deformation regimes $[0.54 + 0.25(E^*/Y)]^{-1} \le \bar{\delta} \le [0.82 + 0.553(E^*/Y)]^{-1}$):

$$\bar{p}_m = \left[0.3\bar{\delta}\left(\frac{E^*}{Y}\right)\right]^n \left[2.13\left[\log\left(\frac{E^*}{Y}\right)\right]^{1/2} + 1.65\left[\log\left(\frac{E^*}{Y}\right)\right]^{-3/2}\left(\log\bar{\delta}\right)^2\right] \tag{2.17}$$

From similar curve fitting of finite element results, the contact area in the NLEP and TFP deformation regimes can be expressed as

$$\bar{a} = \frac{1}{2}\left\{1 - \left[\frac{E^*}{\left(0.3\bar{\delta}E^*\right)^n Y^{(1-n)}}\right]^{-1/2}\right\} + \left\{0.39 + 0.03\left[\frac{E^*}{\left(0.3\bar{\delta}E^*\right)^n Y^{(1-n)}}\right]\right\}\bar{\delta} - \left\{0.86 - 0.0004\left[\frac{E^*}{\left(0.3\bar{\delta}E^*\right)^n Y^{(1-n)}}\right]^2\right\}\bar{\delta}^2 \quad (2.18)$$

It is noted that the SSFP deformation regime cannot be distinguished in the mean contact pressure versus indentation depth response of hardening materials, which, contrary to elastic-perfectly plastic materials, do not show a pressure plateau at large indentation depths. This problem can be overcome by substituting Eq. (2.16b) into Eq. (2.6). Hence, in the SSFP deformation regime

$$H = 2.96\left[0.3\bar{\delta}\left(\frac{E^*}{Y}\right)\right]^n\left[1 - \left(\frac{E^*}{Y}\right)^{-1/2}\right] \quad (2.19)$$

Similar to other deformation regimes, curve fitting of finite element results yields the following equation of the contact area in the SSFP deformation regime:

$$\bar{a} = 1 - 0.51\left[\frac{E^*}{\left(0.3\bar{\delta}E^*\right)^n Y^{(1-n)}}\right]^{-0.4} \quad (2.20)$$

Thus, constitutive equations for different deformation regimes of hardening materials are given by Eq. (2.1) (E), Eq. (2.12) (LEP), Eq. (2.17) (NLEP and TFP), and Eq. (2.19) (SSFP) for the mean contact pressure and Eq. (2.2) (E), Eq. (2.14) (LEP), Eq. (2.18) (NLEP and TFP), and Eq. (2.20) (SSFP) for the contact area.

In addition to providing insight into the indentation behavior of elastic-plastic materials and the true material hardness, the present study has direct implications in contact mechanics analysis of rough surfaces. In particular, the mean contact pressure and contact area at each asperity contact can be determined from Eq. (2.1), (2.6), (2.12), (2.13), (2.17), or (2.19) and Eq. (2.2), (2.14), (2.15), (2.18), or (2.20), respectively, depending on the deformation regime of each asperity contact. This will allow for distributing the contact load among asperity contacts according to the deformation regime that they belong and accurate determination of the fraction of the real contact area corresponding to each of the deformation regimes.

2.4. Conclusions

A finite element analysis of the post-yield deformation behavior of homogeneous half-spaces indented by a rigid spherical indenter was performed for a wide range of elastic-plastic material properties. The indentation response was analyzed in terms of dimensionless parameters, allowing for interpretation of the deformation behavior and the development of generalized constitutive equations. Based on the presented results and discussion the following main conclusions can be drawn from the present analysis.

(1) The post-yield deformation behavior consists of four deformation regimes: linear elastic-plastic (LEP), nonlinear elastic-plastic (NLEP), transient fully plastic (TFP), and steady-state fully plastic (SSFP). Equations for the boundaries between these deformation regimes were extracted from finite element results and interpreted in the context of results showing the evolution of the plastic zone with increasing indentation depth.

(2) The mean contact pressure does not reach a maximum (hardness) at the inception of fully-plastic deformation but increases continuously with the indentation depth (TFP regime), eventually reaching a plateau corresponding to the true material hardness (SSFP regime).

(3) General post-yield constitutive equations of the mean contact pressure and contact area were obtained in terms of indentation depth and elastic-plastic materials properties by curve fitting finite element results. For half-spaces exhibiting predominantly plastic deformation, the derived constitutive equations are in close agreement with slip-line plasticity solutions (rigid-perfectly plastic materials).

(4) For elastic-perfectly plastic materials, subsurface plasticity is characterized by two deformation modes, depending on the effective elastic modulus-to-yield strength ratio E^*/Y. For high E^*/Y, the elastic core between the plastic zone and the indenter surface disappears at small indentation depths, and the deformation behavior is controlled by the unconstrained plastic zone. Alternatively, for low E^*/Y, the elastic strip separating the plastic zone from the surface is maintained even for large indentation depths, resulting in elastic- and plastic-dominant deformation behavior at small and large indentation depths, respectively.

(5) Strain hardening affects the indentation behavior only in the NLEP, TFP, and SSFP deformation regimes. This effect is attributed to the growth pattern of the plastic zone toward the surface.

(6) General constitutive equations of the mean contact pressure and contact area were also obtained for hardening materials over the entire elastic-plastic deformation regime in terms of the effective yield strength, indentation depth, and elastic-plastic material properties.

Chapter 3

Unloading of an elastic-plastic half-space indented by a rigid sphere and the evolution of plasticity due to repetitive normal load

3.1 Introduction

In chapter 2, the constitutive equations of the indentation process have been derived for a rigid sphere and an elastic-plastic half-space and in this chapter, we focus on the constitutive modeling of the unloading process, which provides the theoretical foundation to interpret the mechanical properties of bulk and thin film detected by probe-based technique across scales: from macroscopic Vickers hardness test to micro/nanoindentation (Fischer-Cripps, 2011). Furthermore, the repetitive normal contact is analyzed to study the evolution of plasticity, motivated by the desire of in-depth understanding of product fatigue performance and improvement of component mechanical reliability, in the presence of cyclic normal contact, such as micro-switches (Majumder et al., 2001) and head-disk interface in magnetic storage devices (Komvopoulos, 2000). It can also simulate single asperity contact in multi-scale model of contacting rough surfaces (Yan and Komvopoulos, 1998, Jackson and Streator, 2006, Kadin et al., 2006), which enables the prediction of contact behavior of real, rough surfaces.

While extensive studies on contact behavior of elastic-plastic half-space during indentation (loading) process have been documented by numerous publications in theoretical (Johnson, 1985, Hill et al., 1989, Biwa and Storåkers, 1995) and numerical aspects (Bhattacharya and Nix, 1988, Komvopoulos and Ye, 2001, Kogut and Etsion, 2002, Song and Komvopoulos, 2012), the mechanical response of an indented elastic-plastic half-space during unloading process is relatively unclear and has recently attracted more research interests. The first analytical model for unloading process of elastic-plastic indentation was attributed to Johnson (1985). Assuming the unloading process is purely elastic, the deflection at the center of contact area was derived as a function of contact force, mean contact pressure and effective elastic modulus, and the model shows close agreement with the observations of Tabor (1948) on permanent indentations made by a hard steel ball in the flat surface of a softer metal. Under the same assumption, Mesarovic and Johnson (2000) analyzed the evolution of contact area and contact pressure distribution during unloading process, following a fully-plastic loading process. Using rigid punch decomposition method, a closed-form solution of pressure distribution was derived, which approaches Hertzian pressure distribution asymptotically as contact area diminishes. Li and Gu (2009) considered the unloading of two contacting bodies, whose profiles are of the form $A_n r^{2n}$ (i.e. spherical surface under small deformation assumption) and obtained analytical solutions for the contact force, contact displacement and contact pressure distribution using the superposition of Steuermann solutions. Kogut and Komvopoulos (2003) analyzed the unloading behavior of an elastic-perfectly plastic half-space indented by a rigid sphere using finite element method. Simulation covers a wide range of E^*/Y values and good correlation was observed between the percentage of vertical displacement recovery at the center of contact and the ratio of elastic energy released upon complete unloading to the total work done by indenter during loading process. Etsion et al. (2005) studied the unloading process of an elastic-plastic

loaded sphere, in frictionless contact with a rigid plate by finite element analysis. Constitutive equations of contact force and contact during unloading were obtained by curve fitting simulation data. An elastic-plastic loading index (EPL index) was suggested as a measure of plastic deformation accumulated during loading half-cycle. The unloading analysis was extended to full-stick contact condition by Zait et al., (2010) and a larger contact area is observed in comparison with the frictionless contact since the radial elastic recovery is prevented by friction. Kral et al. (1993) examined the elastic-plastic deformation due to repetitive normal contact of an elastic-plastic half-space by a rigid sphere with load up to 300 times of the critical load to initiate subsurface plastic deformation. Surface and subsurface stresses were analyzed and a spherical band of tensile hoop stress was found to be developed from the axis of symmetry to the surface and prevents the expansion of the plastically deformed material, thus increases the likelihood of surface radial cracking. Re-yielding is found in the surface region just outside the contact area on the completion of the first unloading, while the subsequent cycles were found to produce continued yielding within the plastic zone built in the first cycle and the increment of average plastic strain decays rapidly with number of cycles, implying a shakedown behavior. Yan and Li (2003) studied contact behavior between a rigid sphere and an elastic-perfectly plastic half-space by finite element analysis and contact pressure distribution was found not to recover to the Hertzian pressure distribution during subsequent loading cycles. Kadin et al. (2006) analyzed the multiple loading-unloading of an elastic-plastic spherical contact for materials of a wide range of elastic modulus, yield strength and plastic modulus. Re-yielding was found to occur in a circumferential region close to the edge of the contact area during the first unloading. Furthermore, it was observed that secondary plastic flow occurs in this circumferential region when the maximum normal displacement exceeds a threshold value that increases with Poisson's ratio v and strain hardening ratio E_T/E.

Despite of the significant progress in the theoretical and numerical studies of the unloading behavior, a general constitutive model that governs the unloading mechanics of an elastic-plastic half-space indented by a rigid sphere is still lacking and the influence of strain hardening characteristics on the unloading behavior has not been quantified yet. Accumulation of plasticity in elastic-plastic half-space during repetitive normal contact has not been fully understood and the effect of strain hardening, particularly kinematic strain hardening is not clear yet. Therefore, the main objectives of present study are to derive constitutive equations that include the strain hardening effect for the unloading of indented elastic-plastic half-space, and to understand the accumulation of plasticity by tracing the evolution of plastic zone and dissipated plastic energy over number of cycles.

3.2 Contact model of loading-unloading cycle

Figure 3.1(a) and 3.1(b) show the schematics of a rigid sphere indented into and retracted from a deformable half-space, respectively, which together comprise a complete loading-unloading cycle. Contact force, indentation depth and contact radius are denoted as P, δ and r, respectively. In the loading half-cycle, the rigid sphere is incrementally pressed into the half-space until the maximum contact force P_{max} is obtained, with the maximum indentation depth δ_{max} and contact area $A_{max} = \pi {r_{max}}^2$ reached simultaneously; during the unloading half-cycle, the rigid sphere is gradually retracted from the deformed half-space until the contact force

decreases to zero. Due to the plasticity accumulated in the half-space, a residual impression is present, characterized by residual indentation depth δ_{res}.

The elastic-plastic half-space was modeled by a power-law, isotropic strain hardening model, which allows the yield strength of material to increase with the accumulation of plastic strain, as indicated by Eqs. (3.1a) and (3.1b).

$$\sigma = E^*\varepsilon \qquad (\sigma < Y) \tag{3.1a}$$

$$\sigma = Y(\varepsilon/\varepsilon_Y)^n \qquad (\sigma \geq Y) \tag{3.1b}$$

where $E^* = E/(1-\nu^2)$ is the effective elastic modulus, Y is the initial yield strength, $\varepsilon_Y = Y/E^*$ is the yield strain and n is strain hardening exponent. All simulations were performed by commercial, multi-purpose finite element code ABAQUS/STANDARD (Implicit) (version 6.9 EF) and the detail of the finite element mesh was described elsewhere (Song and Komvopoulos, 2012).

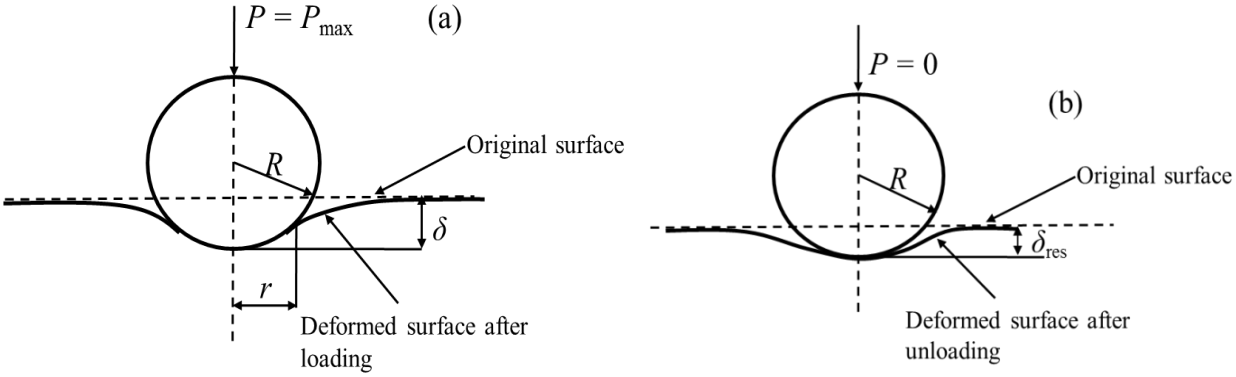

Figure 3.1 Schematic of a deformable half-space indented by a rigid sphere.

3.3 Results and discussions

3.3.1 Universal loading-unloading behavior

Figure 3.2(a) and 3.2(b) show the dimensionless contact force $\bar{P} = P/P_Y$ and contact area $\bar{A} = A/A_Y$ verse dimensionless indentation depth $\bar{\delta} = \delta/\delta_Y$ through a complete loading-unloading cycle, for an elastic-perfectly plastic half-space of effective elastic modulus-to-yield strength ratio E^*/Y values from 11 to 1100. P_Y, A_Y and δ_Y denote the critical contact force, contact area and indentation depth at the onset of subsurface plastic deformation, as given by Eqs. (3.2), (3.3) and (3.4) (Johnson, 1985).

$$P_Y = 21.14R^2Y^3/E^{*2} \tag{3.2}$$

$$A_Y = 19.81R^2Y^2/E^{*2} \tag{3.3}$$

$$\delta_Y = 6.32RY^2/E^{*2} \tag{3.4}$$

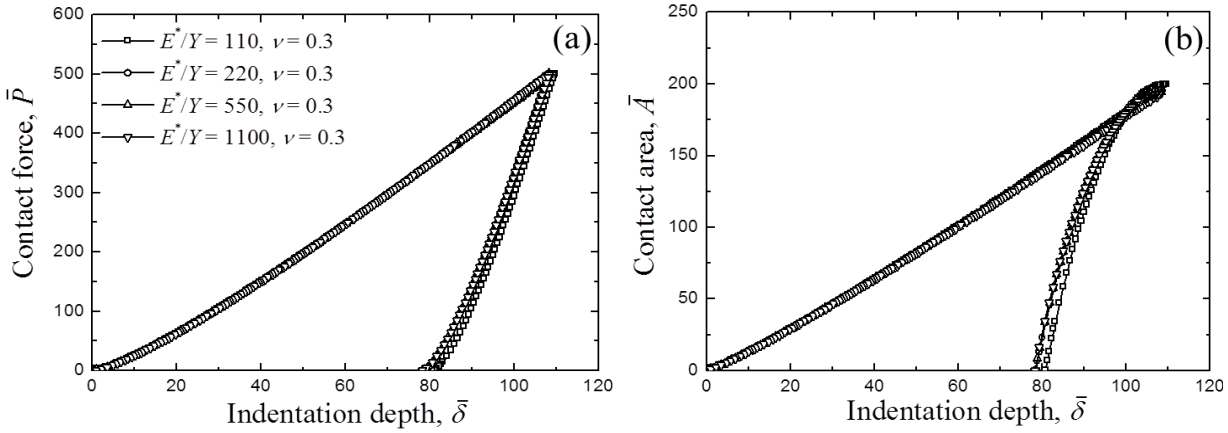

Figure 3.2(a) Dimensionless normal force $\bar{P}$ and (b) contact area $\bar{A}$ verse dimensionless indentation depth $\bar{\delta}$, for elastic-perfectly plastic half-space of E^*/Y =110, 220, 550 and 1100

As implied by the overlapping curves shown in Figure 3.2(a) and 3.2(b), the constitutive behavior is independent of E^*/Y value in dimensionless form; thus, in present paper, the constitutive equations are derived from the finite element simulation results for elastic-plastic half-space of E^*/Y = 550.

3.3.2 Residual indentation depth and dissipated plastic energy

Residual indentation depth is defined as the depth of the permanent impression at the center of contact area after complete unloading and a dimensionless residual indentation depth $\tilde{\delta}_{res} = \delta_{res}/\delta_{max}$ characterizes the significance of plastic deformation in the total deformation during loading half-cycle. Figure 3.3 shows $\tilde{\delta}_{res}$ as a function maximum indentation depth $\bar{\delta}_{max}$ and a curve fitting of the simulation data yields Eq. (3.5).

$$\tilde{\delta}_{res} = \left(1 - \bar{\delta}_{max}{}^{-1/3}\right) \cdot \left(1 - \bar{\delta}_{max}{}^{-2/3}\right) \tag{3.5}$$

The significance of plastic deformation increases with the maximum indentation depth: when $\bar{\delta}_{max} \to 1^+$, contact behavior is dominated by elastic deformation, thus completely recoverable ($\tilde{\delta}_{res} \to 0$); when $\bar{\delta}_{max} \to \infty$, elastic deformation is negligible and the impression is almost permanent. ($\tilde{\delta}_{res} \to 1$)

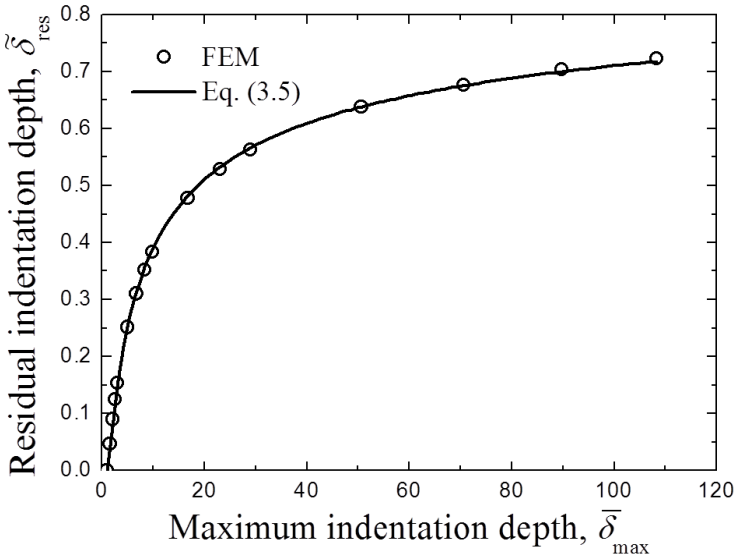

Figure 3.3 Dimensionless residual indentation depth $\tilde{\delta}_{res}$ verse dimensionless maximum indentation depth $\bar{\delta}_{max}$

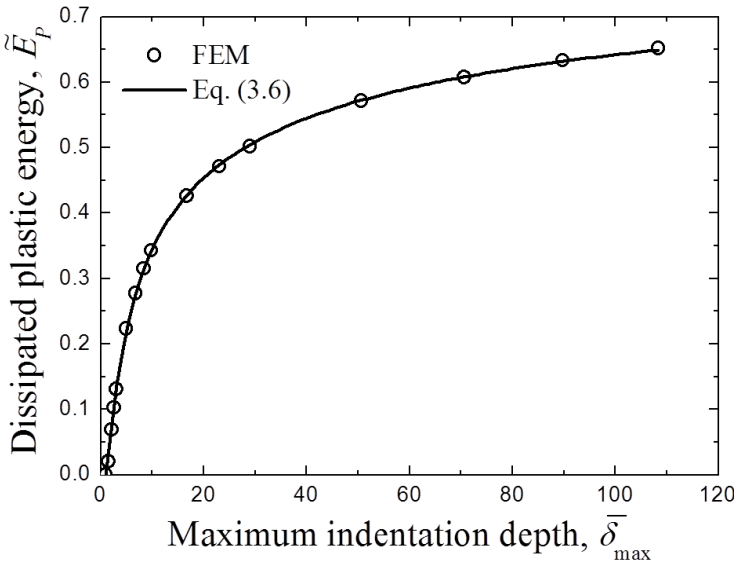

Figure 3.4 Dimensionless dissipated plastic energy $\tilde{E}_P$ verse dimensionless maximum indentation depth $\bar{\delta}_{max}$

Another important measure of the contribution of plastic deformation is dimensionless dissipated plastic energy, defined as the ratio of dissipated plastic energy to the total work done by the rigid sphere during loading half-cycle. Figure 3.4 shows $\tilde{E}_P = E_P/W$ verse $\bar{\delta}_{max}$ and Eq. (3.6) is obtained following the same curve fitting method as Eq. (3.5).

$$\tilde{E}_P = \left(1 - {\bar{\delta}_{max}}^{-1/4}\right) \cdot \left(1 - {\bar{\delta}_{max}}^{-3/4}\right) \tag{3.6}$$

Similar to $\tilde{\delta}_{res}$, Eq. (3.6) indicates that $\tilde{E}_P$ is a monotonic increasing function of $\bar{\delta}_{max}$, with asymptotes of purely elastic and perfectly plastic behavior at very small ($\bar{\delta}_{max} \to 1^+$) and large ($\bar{\delta}_{max} \to \infty$) maximum indentation depth.

3.3.3 Unloading constitutive equations

As shown in Figure 3.2(a) and 3.2(b), the unloading path completely deviates from the loading curve, as a result of excessive plastic deformation accumulated during loading half-cycle. Following a similar curve fitting method proposed by Etsion et al., (2005), Eq. (3.7) is derived to correlate the normalized contact force $\tilde{P} = P/P_{max}$ and the unloading depth $\tilde{\delta} = (\delta - \delta_{res})/(\delta_{max} - \delta_{res})$

$$\tilde{P} = \tilde{\delta}^{\alpha} \tag{3.7}$$

where the exponent α is obtained in Eq. (3.8) by curve fitting the simulation data

$$\alpha = 1.5\bar{\delta}_{max}{}^{-0.036} \tag{3.8}$$

When the indentation behavior is predominantly elastic ($\bar{\delta}_{max} \to 1^+$), Eq. (3.5) and (3.8) yields $\delta_{res} = 0$ and $\alpha = 1.5$, respectively, which in together recover the unloading constitutive equation (Eq. (3.7)) to that of classical Hertz contact ($\tilde{P} = \tilde{\delta}^{1.5}$).

In contrast to the normalized contact force $\tilde{P}$, the normalized contact area $\tilde{A} = A/A_{max}$ exhibits a different dependence on the unloading depth $\tilde{\delta}$, as suggested by Figure 3.2(b). At the initial stage of unloading, indented half-space undergoes elastic recovery that conforms the profile of rigid sphere, thus the contact area is almost unchanged; with further unloading, elastic recovery is prevented by residual stresses in half-space and the contact area decreases to zero rapidly. Therefore, instead of the power law fitting used in Eq. (3.7), an asymptotic equation was employed to fit the simulation data of contact area, yielding Eq. (3.9).

$$\tilde{A} = \frac{1}{\beta}\left[1 - (1-\beta)^{\tilde{\delta}}\right] \tag{3.9}$$

where the exponent β is obtained in Eq. (3.10) by curve fitting the simulation data

$$\beta = 0.9\left(1 - \bar{\delta}_{max}{}^{-0.937}\right) \tag{3.10}$$

Although Eq. (3.9) looks more complicated than Eq. (3.7), it has to be emphasized that it is also a single-parameter equation, which yields much better linear regression than fitting the simulation data with a power-law equation. When the indentation behavior is predominantly elastic ($\bar{\delta}_{max} \to 1^+$), Eq. (3.5) and (3.10) yields $\delta_{res} = 0$ and $\beta = 0$, thus Eq. (3.9) recovers to the unloading equation of classical Hertz contact ($\tilde{A} = \tilde{\delta}$), by applying the l'Hôpital's rule.

3.3.4 Effect of strain hardening

The constitutive equations derived above have established quantitative relationships among the contact force, contact area and indentation depth for indented elastic-perfectly plastic half-space during the unloading half-cycle; however, most of the engineering metals and alloys exhibit strain hardening behavior, allowing material yield strength increases as the plastic strain accumulates, characterized by strong hardening exponent n, as illustrated by Eq. (3.1b). Therefore, a complete loading-unloading cycle is simulated for elastic-plastic half-space of strain hardening exponent in the range of 0.1 to 0.5.

Figure 3.5(a) and 3.5(b) show the contact force $\tilde{P}$ and contact area $\tilde{A}$ vs. the unloading depth $\tilde{\delta}$ from a maximum indentation depth of $\bar{\delta}_{max}$ =110, for elastic-plastic half-space exhibiting of strain hardening exponent n, from 0 to 0.5. Overlapped curves indicate that Eqs. (3.7) and (3.9), developed for elastic-perfectly plastic half-space, are applicable for strain hardening half-space. However, in order to apply Eqs. (3.7) and (3.9) for strain hardening half-space, the residual indentation depth $\tilde{\delta}_{res}$, which is a variable of $\tilde{\delta}$, has to be determined beforehand. Figure 6 shows that $\tilde{\delta}_{res}$ decreases from 0.71 to 0.51, as n increases from 0 to 0.5. In order to find out the dependence of $\tilde{\delta}_{res}$ on n, the concept of effective strain ($\varepsilon^* = 0.3\delta/r'$) proposed by Song and Komvopoulos (2012) is adopted and the effective yield strength Y^* at $\bar{\delta}_{max}$ due to strain hardening is calculated in Eq. (3.11a); consequently, the effective critical indentation depth to failure δ_{Y^*} and effective dimensionless maximum indentation depth $\bar{\delta}^*_{max}$ were obtained by Eqs. (3.11b) and (3.11c), respectively.

$$Y^* = Y\left(\frac{\varepsilon^*_{max}}{\varepsilon_Y}\right)^n = Y\left(\frac{0.3E}{Y}\sqrt{\frac{\delta_{max}}{2R}}\right)^n \tag{3.11a}$$

$$\delta_{Y^*} = \delta_Y\left(\frac{Y^*}{Y}\right)^2 = \delta_Y\left(\frac{0.045E^2\delta_{max}}{Y^2R}\right)^n \tag{3.11b}$$

$$\bar{\delta}^*_{max} = \frac{\delta_{max}}{\delta_{Y^*}} = \bar{\delta}_{max}\left(\frac{Y^2R}{0.045E^2\delta_{max}}\right)^n \tag{3.11c}$$

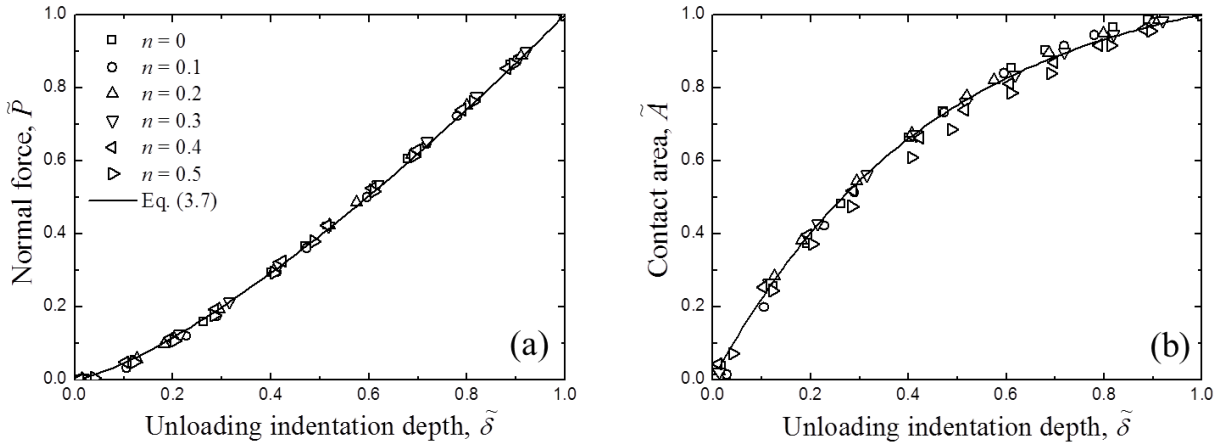

Figure 3.5 (a) Dimensionless normal force $\tilde{P}$ and (b) contact area $\tilde{A}$ verse dimensionless unloading indentation depth $\tilde{\delta}$ (comparison of simulation results and curve fitted equations)

By replacing $\bar{\delta}_{max}$ with $\bar{\delta}^*_{max}$ in Eq. (3.5), Eq. (3.12) is obtained. As validated by Figure. 3.6, $\tilde{\delta}_{res}$ predicted by Eq. (3.12) exhibits close agreement with finite element simulation result for a range of n = 0 – 0.5.

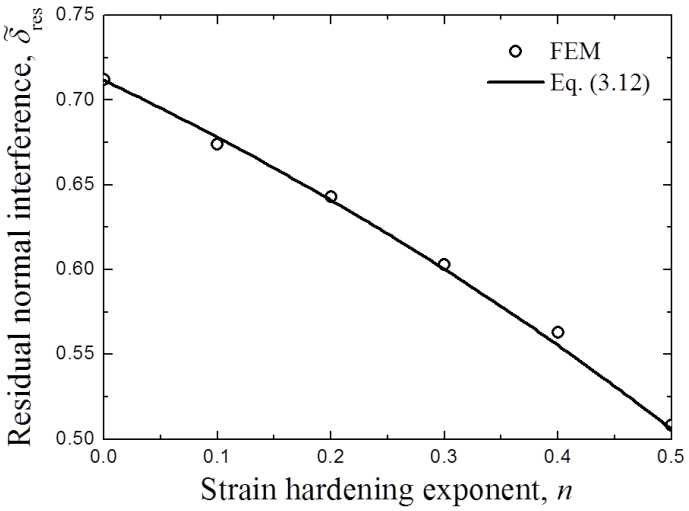

Figure 3.6 Dimensionless residual indentation depth $\tilde{\delta}_{res}$ vs. strain hardening exponent n (unloading from $\bar{\delta}_{max}$= 110)

$$\tilde{\delta}_{res} = \left\{1 - \left[\bar{\delta}_{max}\left(\frac{Y^2R}{0.045E^2\delta_{max}}\right)^n\right]^{-0.3}\right\}\left\{1 - \left[\bar{\delta}_{max}\left(\frac{Y^2R}{0.045E^2\delta_{max}}\right)^n\right]^{-0.65}\right\} \quad (3.12)$$

3.3.5 Evolution of plastic zone in multiple loading-unloading cycles

Accumulation of plasticity in elastic-plastic half-space due to repetitive, normal contact is of particular interest for its direct implication in the reliability of micro-electronic-mechanical system (MEMS) devices operating in contact mode, such as microswitches and head-disk interface (HDI) in magnetic storage system. In order for a better understanding of plasticity accumulation, four consecutive loading-unloading cycles were simulated for an elastic-plastic half-space of E^*/Y = 550 in normal contact with a rigid sphere, with the maximum contact force $\bar{P}_{max}$ = 500. Figure 3.7(a) and 3.7(b) show the contours of equivalent plastic strain $\bar{\varepsilon}_P$ in half-space after 1st loading and unloading half-cycle are almost identical. Figure 3.8(a) and 3.8(b) show the contour of $\bar{\varepsilon}_P$ after 2nd loading and unloading half-cycle and it is noticed that the maximum $\bar{\varepsilon}_P$ increases slightly in comparison with that after the 1st cycle, despite of the same contour shape. Figure 3.9 plots normalized dissipated plastic energy $\bar{E}_P = E_P/(P_{max} \cdot \delta_{max})$ at the end of each loading and unloading half cycle. Although no visible accumulation of plastic strain is observed in the contour of $\bar{\varepsilon}_P$ shown in Figure 3.8, the 1st unloading half-cycle is found to be inelastic, evidenced by the increasing dissipated plastic energy. Subsequent unloading half-cycles are shown to be purely elastic and the accumulation of dissipated plastic energy in

subsequent loading half-cycles also decays as the number of cycles increases, leading to elastic shakedown.

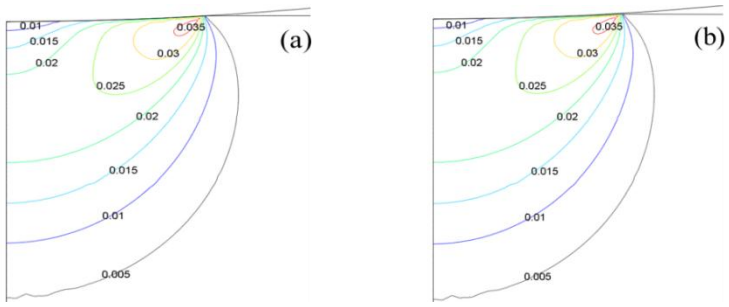

Figure 3.7 Distribution of equivalent plastic strain $\bar{\varepsilon}_P$ in elastic-plastic half-space of E^*/Y = 550, subjected to repetitive normal load $\bar{P}_{max}$ = 500, after 1st (a) loading and (b) unloading half-cycle

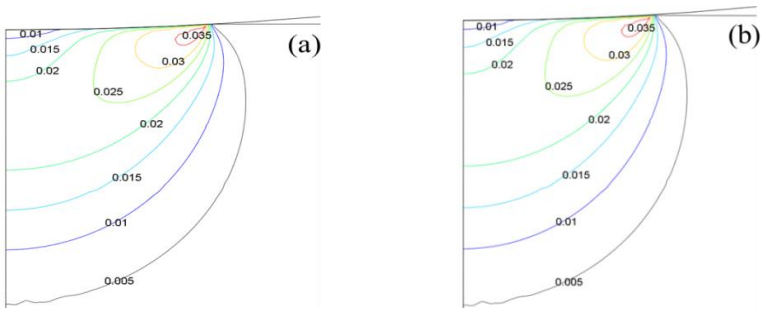

Figure 3.8 Distribution of equivalent plastic strain $\bar{\varepsilon}_P$ in elastic-plastic half-space of E^*/Y = 550, subjected to repetitive normal load $\bar{P}_{max}$ = 500, after 2nd (a) loading and (b) unloading half-cycle

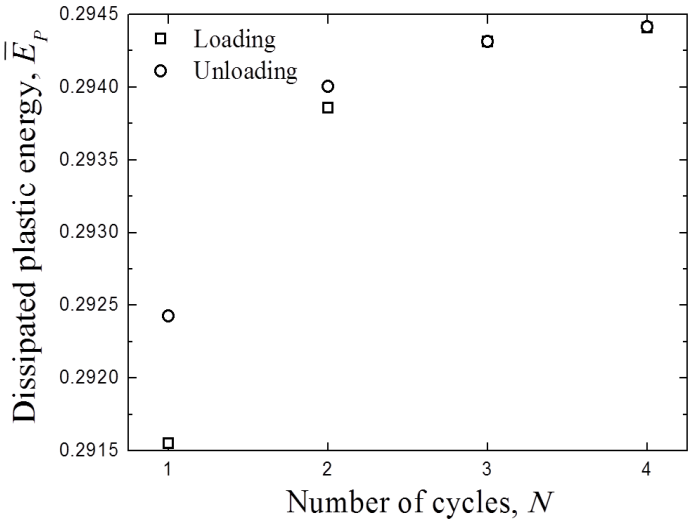

Figure 3.9 Dimensionless dissipated plastic energy $\bar{E}_P$ verse the number of cycles N after each loading and unloading half-cycle for elastic-plastic half-space of E^*/Y = 550, subjected to repetitive normal load $\bar{P}_{max}$ = 500

Figure 3.10(a) and 3.10(b) show the contour of $\bar{\varepsilon}_P$ in elastic-plastic half-space of E^*/Y = 55, after 1st loading and unloading half-cycle, respectively. Although the maximum $\bar{\varepsilon}_P$ stays unchanged, the accumulation of plastic strain during unloading is captured by the propagation of the high equivalent plastic strain contour ($\bar{\varepsilon}_P = 0.55$) toward the center of contact. Figure 3.11(a) and 3.11(b) show the contour of $\bar{\varepsilon}_P$ in elastic-plastic half-space after 2nd loading and unloading half-cycle, respectively. A comparison of figure 3.10(b) and 3.11(a) reveals that both the maximum $\bar{\varepsilon}_P$ increases slightly and the high equivalent plastic strain contour ($\bar{\varepsilon}_P = 0.55$) continues to propagate to the center during the 2nd loading process. In contrast to the case of $E^*/Y = 550$, Figure 3.12 indicates $\bar{E}_P$ increases linearly with the number of cycles; therefore a plastic shakedown or ratcheting is resembled, implying a potential low cycle fatigue.

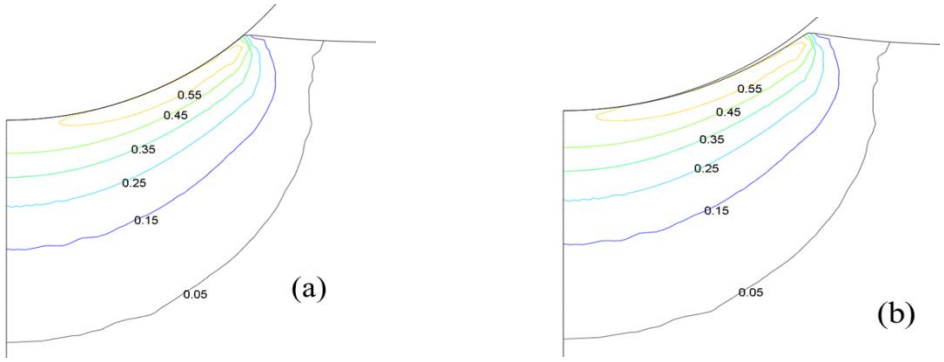

Figure 3.10 Distribution of equivalent plastic strain $\bar{\varepsilon}_P$ in elastic-plastic half-space of E^*/Y = 55, subjected to repetitive normal load $\bar{P}_{max}$ = 500, after 1st (a) loading and (b) unloading half-cycle

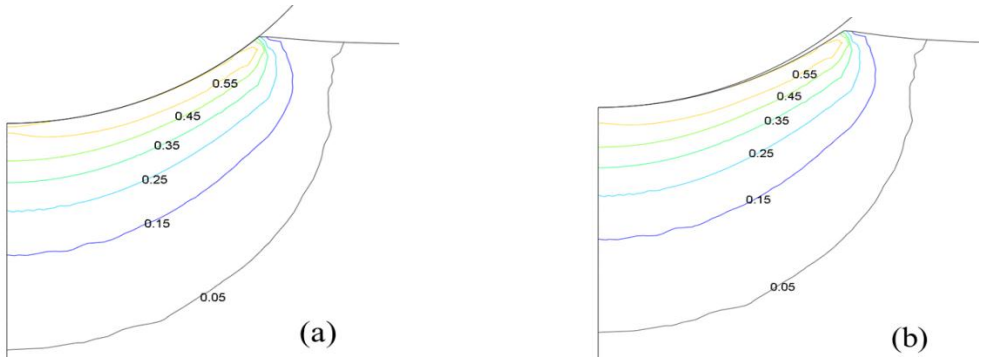

Figure 3.11 Distribution of equivalent plastic strain $\bar{\varepsilon}_P$ in elastic-plastic half-space of E^*/Y = 55, subjected to repetitive normal load $\bar{P}_{max}$ = 500, after 2nd (a) loading and (b) unloading half-cycle

Figure 3.13(a) and 3.13(b) show the evolution of equivalent plastic strain $\bar{\varepsilon}_P$ along the axis of symmetry (*z*-axis) and the contact surface (*r*-axis), respectively, for elastic-plastic half-space of E^*/Y = 55 with the number of cycles. Three different regions were obeserved: (1) an elastic region that is sufficiently apart from contact area with effective stress lower than the yield

strength, thus the deformation is purely elastic through cycles. (2) a shakedown region that is closer to the contact, in comparison with elastic region. Plastic deformation occurs during 1st cycle, but further accumulation of plastic strain in subsequent cycles is prevented by residual stresses. (3) a ratcheting region that is right underneath the contact area, with relatively small distance (i. e. $0 \le r \le 0.5a$; $0 \le z \le 0.5a$). Equivalent plastic strain $\bar{\varepsilon}_P$ increases consistently with number of cycles, which may account for material removal in the form of delamination and/or adhesive wear.

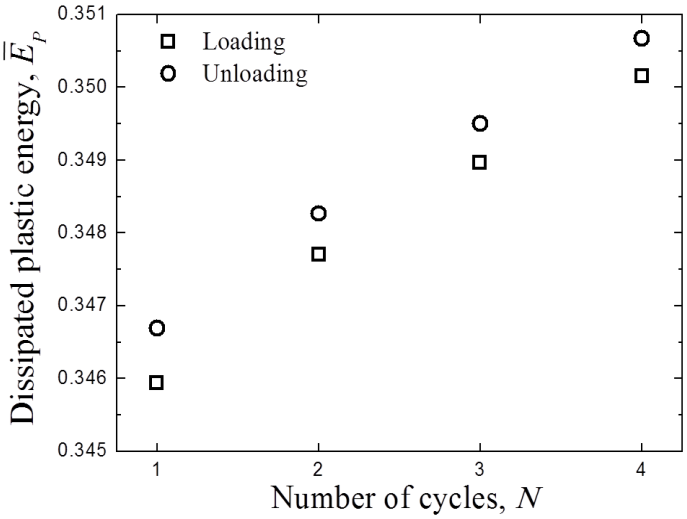

Figure 3.12 Dimensionless dissipated plastic energy $\bar{E}_P$ verse the number of cycles N after each loading and unloading half-cycle for elastic-plastic half-space of E^*/Y = 55, subjected to repetitive normal load $\bar{P}_{max}$ = 500

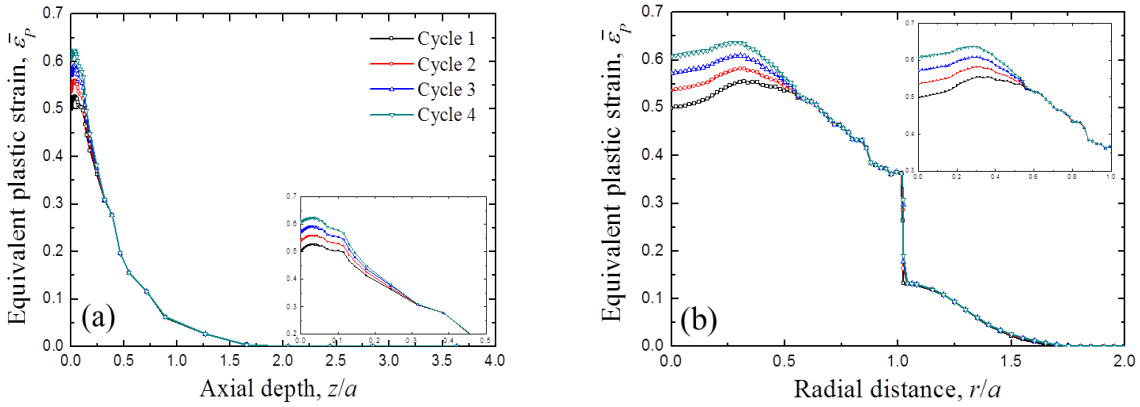

Figure 3.13 Evolution of equivalent plastic strain $\bar{\varepsilon}_P$ along (a) the axis of symmetry in depth direction (z-axis) and (b) contact surface in radial direction (r-axis) with the number of cycles

While isotropic strain hardening is expected to suppress the plastic strain accumulation and plastic energy dissipation in repetitive normal contacts, the effect of kinematic strain hardening, which involves both the expansion of yield surface and shift of center of yield surface, can be more complicated and interesting. The repetitive normal contact was considered for a

rigid sphere and an elastic-plastic half-space exhibiting a combined isotropic/kinematic strain hardening behavior (Lemaitre and Chaboche, 1994), with an effective elastic modulus $E^* =$ 55GPa.

The plastic hardening behavior is described by Eqs. (3.13) and (3.14). Eq. (3.13) describes the expansion the yield surface with the accumulation of plastic strain, where the original yield strength, maximum expansion of yield surface and expansion rate of yield surface were specified given by Y_0 = 100MPa; Q = 1Gpa and b = -0.26, respectively; Eq. (3.14) represents the evolution of the center of yield surface, where C = 25.5GPa and γ = 81 are material constants that characterize the initial hardening modulus and the rate at which hardening modulus decreases with plastic strain. Back stress α is the center of yield surface with initial value α_0= 0. Ziegler's rule of linear kinematic hardening is recovered by setting γ = 0

$$Y = Y_0 + Q \cdot (1 - e^{-b\bar{\varepsilon}_P}) \tag{3.13}$$

$$\dot{\alpha} = C\dot{\bar{\varepsilon}}_P \cdot \frac{\sigma - \alpha}{Y} - \gamma\alpha\dot{\bar{\varepsilon}}_P + \frac{\alpha\dot{C}}{C} \tag{3.14}$$

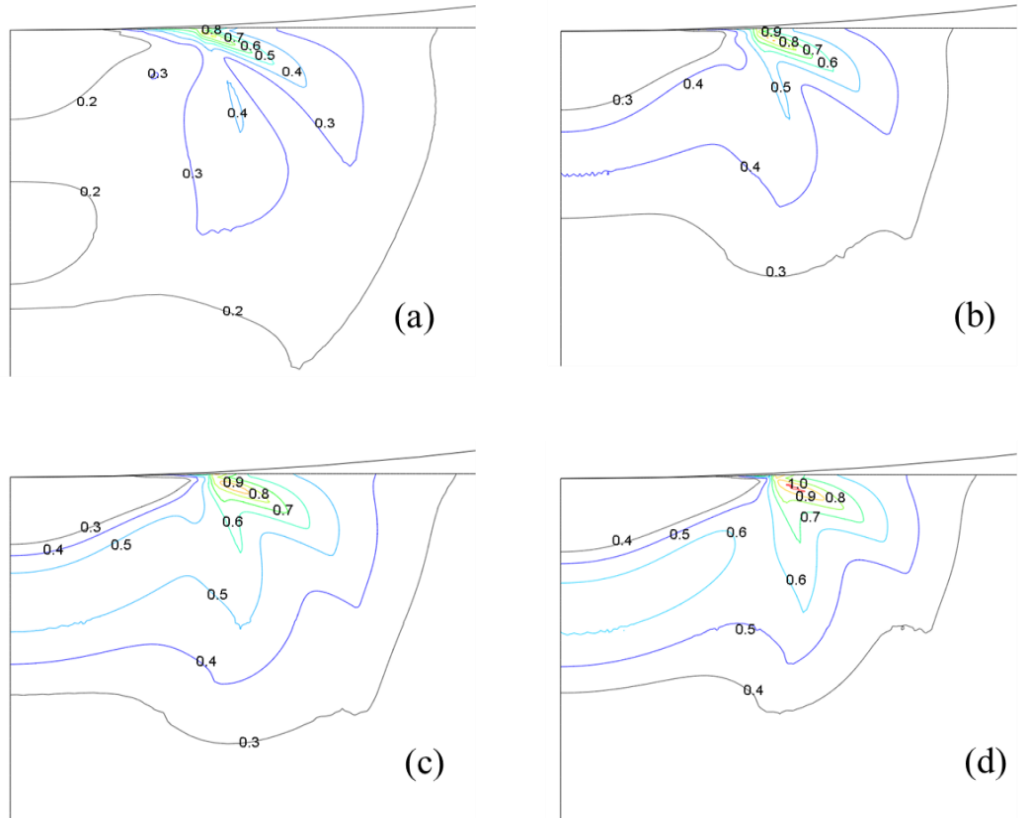

Figure 3.14 Distribution of effective stress σ_V for elastic-plastic half-space, described by a combined isotropic/kinematic strain hardening behavior half-space, subjected to repetitive normal load of $\bar{P}_{max}$ = 500, after (a) 1st, (b) 2nd , (c) 3rd and (d) 4th unloading half-cycle

Figure 3.14(a) to 3.14(d) show the contour of dimensionless effective stress σ_V/Y_0 in elastic-plastic half-space after 1st, 2nd, 3rd and 4th unloading half-cycle. It is noticed that σ_V/Y_0 in the vicinity of the circumference of contact region increases with the number of cycle, from 0.8 (elastic deformation) to 1.02 (plastic deformation), which indicates that yielding occurs in subsequent cycles.

3.4. Conclusions

Finite element analysis was performed to study the unloading behavior of an elastic-plastic half-space indented by a rigid sphere and the accumulation of plasticity due to repetitive loading-unloading cycles. The major findings from present study are listed as following:

(1) The dimensionless constitutive model of unloading process is independent of the E^*/Y value of elastic-plastic half-space.

(2) Dimensionless residual indentation depth and the dissipated plastic energy are obtained as functions of maximum indentation depth for elastic-perfectly plastic medium by curve fitting the simulation data.

(3) Unloading constitutive equations were derived for elastic-perfectly plastic medium in a dimensionless form and shown also applicable for elastic-plastic medium exhibiting isotropic strain hardening behavior.

(4) By adopting the concept of effective strain (Song and Komvopoulos, 2012), a general expression of residual indentation depth that includes strain hardening exponent as a variable was derived for elastic-plastic medium exhibiting isotropic strain hardening behavior.

(5) Mechanical behavior of elastic-plastic medium subjected to repetitive loading-unloading cycles was investigated: for high E^*/Y value, only 1st unloading is inelastic, while the subsequent unloading is purely elastic; thus, elastic shakedown is expected; for low E^*/Y value, plastic energy is dissipated incrementally in subsequent loading-unloading, implying plastic shakedown or ratcheting.

(6) For elastic-plastic half-space of low E^*/Y value subjected to repetitive normal load, three different deformation regions were identified in the medium: 1. Ratcheting region: a small region adjunct to the center of contact area, inside which the plastic strain accumulates incrementally with the number of cycles. 2. Shakedown region: the plastically deformed material surrounding the ratcheting region, inside which the material undergoes plastic deformation in 1st cycle, but does not accumulate plastic strain in subsequent cycles. 3. Elastic region: remaining area outside the shakedown region where is sufficiently apart from the contact and no plastic deformation occurs through the cycles.

(7) For elastic-plastic medium exhibiting combined isotropic/kinematic hardening behavior, effective stress in the vicinity of the circumference of contact area increases incrementally and yielding occurs in subsequent cycles.

Chapter 4

A fretting contact analysis of fractal surfaces

4.1. Introduction

Fretting contact refers to small-amplitude, oscillatory, tangential motion of preloaded contact surfaces. The amplitude of relative surface motion is usually on the order from micrometers to millimeters, but may also down to several nanometers, depending on morphology of contact surfaces. Contact surfaces may undergo full slip and form wear debris (fretting wear) when fretting amplitude is relatively large; while induce crack in the vicinity of partial slip zone (fretting fatigue) for small amplitude fretting contact. Fretting contact is mostly caused by vibration, for example, fretting contact at blade-shroud interface due to aerodynamic load induced vibration is known as the primary failure mechanism of gas turbine blade.

The pioneering work on the contact analysis under combined normal and tangential load dates back to Cattaneo (1938) and Mindlin (1949), who independently worked out the tangential force-displacement relationship of preloaded spherical contacts. It was revealed that with a fixed normal load $\boldsymbol{P}$, tangential load $\boldsymbol{Q}$ increases nonlinearly with tangential displacement $\boldsymbol{\delta}$ and the circular contact region consists of a center stick zone and a surrounding annulus slip zone, known as partial slip. The stick zone shrinks concentrically with the increase of $\boldsymbol{Q}$ and eventually vanishes when full slip occurs $\boldsymbol{Q = \mu P}$, and $\boldsymbol{\mu}$ is friction coefficient and assumed to be a constant that correlates the tangential and normal tractions on contact surfaces upon full slip. This stick-slip model was later confirmed by Johnson experimentally (1955), in which stick and slip zones were clearly demonstrated when tangential force was not sufficient to induce full slip. Mindlin et al., (1952) further extended the stick-slip model and analyzed the cyclic tangential loading behavior. The unloading the reloading curves were derived analytically and a hysteresis loop was presented, with the enclosed area representing the dissipated fretting energy per cycle.

However, Mindlin's model is not directly applicable for most of the real contact surfaces for mainly two reasons: first, most of the real contact surfaces, if not all of them, exhibit multi-scale roughness; thus, even the contact of two macroscopically flat surfaces is not continuous, but compromises discrete micro contact spots (asperities); second, as a result of surface roughness, even very small contact load may induce plastic deformation at asperity contacts. Berthoud and Bauberger (1998) implemented Mindlin's model of single asperity tangential contact into a statistical rough surface model proposed by Greenwood and Williamson (1966), hereafter referred as GW model. The tangential stiffness of two macroscopically flat rough surfaces was calculated and a linear elastic response was predicted before the inception of full slip, which was in good agreement with experiment. Bjorklund (1997) used similar modeling approach, but an asperity height distribution different from that of GW model, to analyze the fretting contact of nominally flat rough surface and showed that the fretting (hysteresis) loop and energy dissipation per cycle are essentially independent of asperity height distribution, given the same root-mean-square surface roughness. In order to account for the plastic deformation at asperity contact, Eriten et al., (2011) utilized the elastic-plastic constitutive equations developed by Kogut and Etsion (2002) for the normal contact of asperity contact and modeled the fretting

contact of two nominally flat rough surfaces; in addition, a preload dependent friction coefficient (Brizmer et al., 2007) was employed, which associates the inception of sliding to plastic deformation. Plasticity index was found to be the most influential parameter on fretting loop and energy dissipation and predicted fretting loop showed fairly good agreement with experiment. Eriten et al. (2011) further analyzed the effect of surface roughness and revealed that more energy is dissipated per cycle for rougher contact surface.

Despite of the significance of aforementioned work on fretting contact modeling of rough surfaces, it is noticed that the widely accepted GW model does not account for scale-independence of topography parameters, an intrinsic feature of multi-scale roughness of engineering surfaces. In order to overcome the shortcoming of scale-dependence in GW model, fractal geometry has been extensively used to describe rough surfaces in contemporary contact mechanics (Majumdar and Bhushan,1990, 1991; Wang and Komvopoulos, 1994a,b, 1995; Sahoo and Roy Chowdhury, 1996; Komvopoulos and Yan, 1998; Borri-Brunetto et al., 1999; Ciavarella et al., 2000; Persson et al., 2002; Yang and Komvopoulos, 2005; Komvopoulos and Gong, 2007; Yin and Komvopoulos, 2010), because the fractal geometry is known for the its continuity, non-differentiability, self-invariance and self-affinity (Mandelbrot, 1973). Furthermore, The preload-dependent friction model (Brizmer et al., 2007) used assumes implicitly that the interfacial adhesion is sufficiently high to yield the surface or subsurface material. It is a very reasonable assumption for sticky interface, but could be questionable for slippery interface, such as very clean and smooth interface with anti-sticking coating. The contact interface could be order of magnitude weaker than the material strength of contact bodies and full slip can easily occur at very low tangential force and without any plastic deformation induced.

The main objective of present analysis is to present a fretting contact model for rough surfaces exhibiting fractal geometry, and study the effects of surface roughness, nominal contact pressure, fretting amplitude, elastic modulus-to-yield strength ratio and interfacial adhesion parameter on maximum tangential force, fretting energy dissipation and slip index. A friction model accounts for both adhesion and plowing effect is used and the interfacial shear stress is in the range is determined by the shear strength of elastic-plastic half-space and interfacial adhesion characterized by an interfacial adhesion parameter in the range of 0 to 1. This chapter is organized as following: in section 4.2, the friction model used for asperity contact is discussed and the fractal surface is formulated mathematically in section 4.3. Contact mechanics analysis is then performed on both normal and tangential directions in section 4.4; section 4.5 presents the effects of different parameters in the light of numerical results.

4.2. Friction model

In present study, the friction coefficient consists of two components: adhesion friction coefficient μ_a and plowing friction coefficient μ_p. Adhesion friction force is assumed to be is uniquely determined by the contact area a and interfacial shear stress $\tau = m\tau_0$, where τ_0 is the shear strength of material and m is interfacial adhesion parameter, floating in the range of 0 to 1. Since plowing effect is associated with plastic deformation, for asperities in elastic contact, the friction coefficient is obtained by

$$\mu = \mu_a = \frac{3\pi^{3/2} msR}{2\sqrt{2}Ea'^{1/2}} \tag{4.1}$$

For asperities in plastic contact, the plowing friction coefficient is non-zero and the friction coefficient was obtained in a close-form through integration (Komvopoulos, 1986)

$$\mu = \frac{2R^2}{a}\left\{sin^{-1}\left(\sqrt{\frac{a}{\pi R^2}}\right) - \sqrt{\frac{a}{\pi R^2}}\sqrt{1-\frac{a}{\pi R^2}} + 2\frac{\tau}{H}\left(1-\sqrt{1-\frac{a}{\pi R^2}}\right)\right\} \tag{4.2}$$

4.3. Surface description

Figure 4.1 shows a typical isotropic and self-affine fractal rough surface and its three-dimensional surface profile $z(x, y)$ is given by (Yan and Komvopoulos, 1998)

$$z(x,y) = L\left(\frac{G}{L}\right)^{(D-2)}\left(\frac{ln\gamma}{M}\right)^{1/2}\sum_{m=1}^{M}\sum_{q=0}^{q_{max}}\gamma^{(D-3)q}\times\left\{cos\phi_{m,q} - cos\left[\frac{2\pi\gamma^q\sqrt{x^2+y^2}}{L}\times cos\left(tan^{-1}\left(\frac{y}{x}\right)-\frac{\pi m}{M}\right)+\phi_{m,q}\right]\right\} \tag{4.3}$$

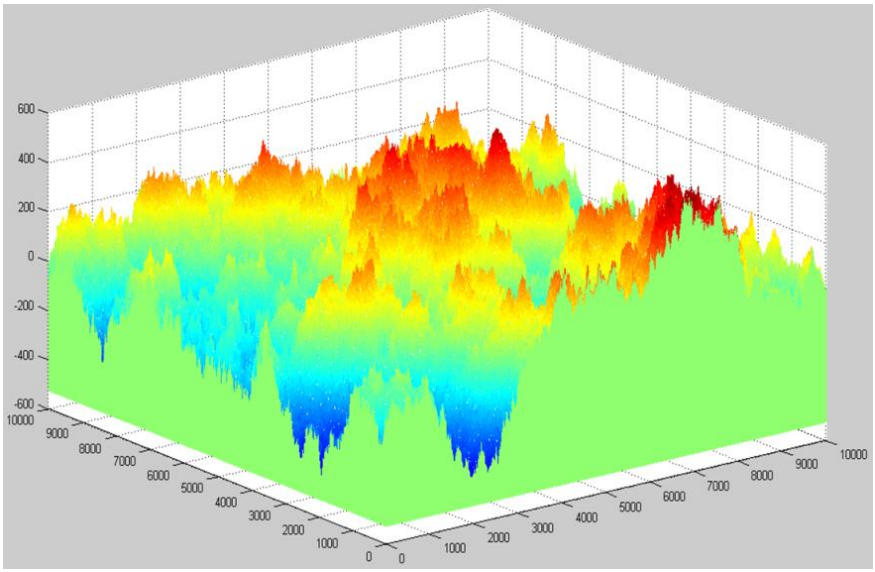

Fig. 4.1 Typical three dimensional fractal rough surface generated from Eq. (3) with M= 20, γ = 1.5, L = 10 mm, L_s = 5nm, G = 50 nm and D = 2.5.

where D ($2 < D < 3$) and G are the fractal dimension and fractal roughness, respectively. L is the sample length; In Figure 1, L = 10 mm, G = 50 nm and D = 2.5. γ ($\gamma > 1$) is a parameter that determines the density of frequency in the surface profile, which is typically chosen to be 1.5 for frequency distribution density consideration (Komvopoulos and Yan, 1997) M denotes the number of superposed ridges; $\phi_{m,q}$ is a random phase uniformly distributed in the range of [0, 2π] by a random number generator to prevent the coincidence of different frequencies at any point of the surface profile; q is a spatial frequency index.

The fractal dimension D is the governing parameter of the extent of space occupied by the rough surface and the amplitudes of high-frequency components become comparable to those of low-frequency components as D increases.

4.4 Contact mechanics analysis

4.4.1 Normal contact of a rigid rough (fractal) surface and a deformable half-space

The advancement of rigid fractal surface toward the half-space results in truncated segments and each truncated segment is approximated by an spherical asperity of based radius r' equal to one-fourth of asperity's base wavelength and height equal to the local interference δ given by eq. (4.4)

$$\delta = 2G^{(D-2)}(ln\gamma)^{1/2}(2r')^{(3-D)} \tag{4.4}$$

and the radius of spherical asperity is then determined as

$$R = \frac{(a')^{(D-1)/2}}{2^{(5-D)}\pi^{(D-1)/2}G^{(D-2)}(ln\gamma)^{1/2}} + \frac{G^{(D-2)}(ln\gamma)^{1/2}2^{(3-D)}(a')^{(3-D)/2}}{\pi^{(3-D)/2}} \tag{4.5}$$

where $a' = \pi r'^2$ is the truncated area of the asperity contact. It is noticed that in previous studies (Komvopoulos and Yan, 1998; Yin and Komvopoulos, 2010), the second term in Eq. (4.5) is ignored, by assuming local interference $\delta \ll R$; however, this assumption could be inaccurate for the small asperities in plastic deformation, and consequently leads to inaccuracy in friction force calculation.

The discrete truncated areas of asperity contact has been found to follow island-like distribution in geophysics, which obeys a power-law relationship (Menderbrot, 1983)

$$N(a') = \left(\frac{a'_L}{a'}\right)^{(D-1)/2} \tag{4.6}$$

where $N(a')$ is the number of asperities with truncated area greater than a' and a'_L is the largest truncated area; the distribution function of truncated areas of asperity contacts is therefore derived (Yan and Komvopoulos, 1998)

$$n(a') = -\frac{dN(a')}{da'} = \frac{(D-1)}{2a'_L}\left(\frac{a'_L}{a'}\right)^{(D+1)/2} \tag{4.7}$$

and the number of asperities with truncated area in the interval of $[a', a' + da']$ equals $n(a')da'$. Consequently, the total truncated area of asperity contact S' is obtained (Komvopoulos and Ye, 2001)

$$S' = \int_{a'_S}^{a'_L} a' \; n(a')da' = \left(\frac{D-1}{3-D}\right) a'_L \left[1 - \left(\frac{a'_S}{a'_L}\right)^{(3-D)/2}\right] \tag{4.8}$$

where a_S' is the smallest truncated area of asperity contact. It represents the cut-off dimension, below which continuum mechanics theory is not applicable, and the in present study, it is set to be 5 nm.

The total truncated area S' is calculated numerically by counting the number of pixels, which reconstructs the rigid fractal surface, with z-height greater than that of truncation plane; then a_L' and $n(a')$ are obtained by eqs. (4.7) and (4.8); therefore, with a given global interference, the spatial distribution of truncated areas of asperity contacts is completely determined.

Depending on local interference δ and asperity radius R, asperity contacts can be either elastic or plastic, which may substantially affect the distribution of normal load among asperities. Following the simplified elastic-perfectly plastic model (Yin and Komvopoulos, 2010), elastic deformation occurs when truncated area of asperity contact $a' > a_c'$, while the asperity contact undergoes fully-plastic deformation when $a' < a_c'$, where a_c' is known as critical truncated area of contact, obtained by

$$\Delta F_e(a_c') = \Delta F_p(a_c') \tag{4.9}$$

where ΔF_e and ΔF_p denote the normal contact load of elastic and fully-plastic deformation, given by eqs. (4.10) and (4.11), respectively.

$$\Delta F_e = \frac{4E^* r^3}{3R} = \frac{\sqrt{2}E^* {a'}^{3/2}}{3R\pi^{3/2}} \tag{4.10}$$

$$\Delta F_p = H^* a' \tag{4.11}$$

The critical truncated area of contact is then determined

$$a_c' = \frac{9\pi^3 R^2 {H^*}^2}{2{E^*}^2} \tag{4.12}$$

The total normal load F can be obtained as the sum of total normal load of elastic and fully-plastic asperity contacts, F_e and F_p, respectively, as given by eqs. (4.13) and (4.14).

$$F_e = \int_{a_c'}^{a_l'} \Delta F_e n(a') da' \tag{4.13}$$

$$F_p = \int_{a_s'}^{a_c'} \Delta F_p n(a') da' \tag{4.14}$$

4.4.2 Tangential contact of a rigid rough (fractal) surface and a deformable half-space

Figure 4.2(a) and 4.2(b) show the schematic of tangential force-displacement relationship of a preloaded rigid sphere in contact with an elastic half space (Mindlin et al., 1952), for partial slip and full slip state, respectively. Curve OAB represents the initial loading procedure, which is completely partial slip (OA) (Fig. 4.2(a)), or consists of a partial slip stage (OA) and a full slip

stage (AB) (Fig. 4.2(b)). Curves $BCDE$ and $EFAB$ represent the steady-state backward and forward fretting half-cycles, respectively, which are symmetric with each other, with respect to the origin O and in together form an enclosed hysteresis (fretting) loop. A sudden drop of tangential force ΔQ occurs when the direction of fretting displacement is reversed, as a result of the loss of plowing friction and slip index $\theta = \Delta s/2S_{max}$ is defined to quantify the relative slip.

It has to be noticed depending on material properties and loading conditions, it may takes from tens to thousands cycles for hysteresis loop to be stabilized; however, these unstable cycles were ignored in present study for two reasons: first, the energy dissipation during unstable cycles is not significantly different from the steady-state cycles; second, most fretting fatigue undergoes millions of cycles, thus the initial stabilization process is secondary.

During the initial forward fretting (OAB), given a tangential displacement s, asperity contacts may be in partial slip (OA), or a full slip stage (AB), depending on the truncated area: asperities of small truncated area ($a' < a'_T$) undergoes full slip, while large truncated area ($a' > a'_T$) leads to partial slip. The transition truncated area a'_T for elastically and plastically deformed asperities is given by eq. (4.15) and (4.16) respectively.

$$a'_T = a'_{Te} = \pi \left[\frac{G^* s}{2^{(2-D)} G^{(D-2)} (log\gamma)^{1/2} \mu E^*}\right]^{\left(\frac{2}{3-D}\right)} \tag{4.15}$$

$$a'_T = a'_{Tp} = \frac{1}{\pi}\left(\frac{16G^* s}{3\mu H}\right)^2 \tag{4.16}$$

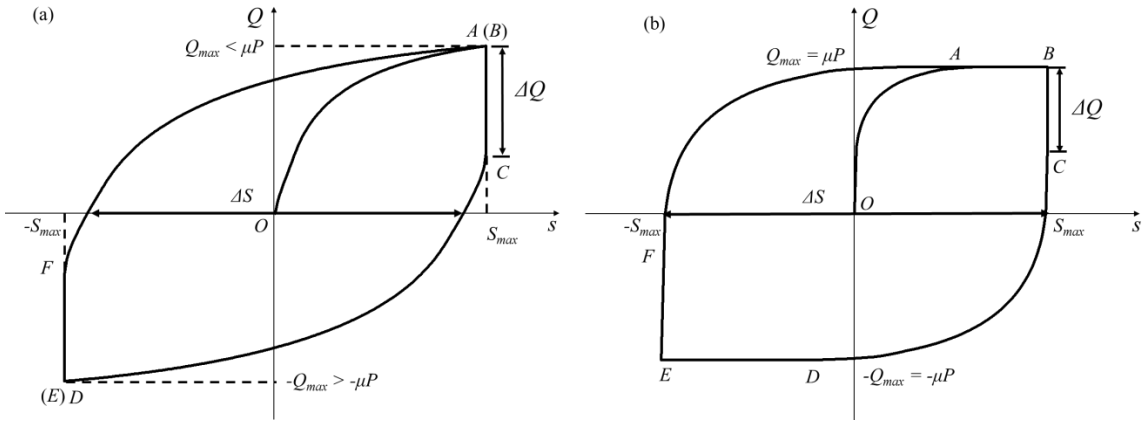

Fig. 4.2 Schematic of fretting loop for (a) partial slip and (b) full slip at at maximum fretting amplitude

where $G^* = [(2-\nu_1)/G_1 + (2-\nu_2)/G_2]^{-1}$ is equivalent shear modulus. For asperity contacts under full slip condition ($a' < a'_T$), the tangential load is constant and independent of s, as given by eq. (4.17)

$$\Delta Q_i = \mu P \tag{4.17}$$

while for asperity contacts in partial slip stage ($a' > a'_T$), Mindlin's solution (Eq. (4.18)) is used to characterize the relationship between tangential force and displacement (1952).

$$\Delta Q_i = \mu P \left[1 - \left(1 - \frac{16G^* rs}{3\mu P}\right)^{3/2}\right] \tag{4.18}$$

The total tangential force during initial forward fretting is then obtained by eq. (4.19)

$$Q_i = \int_{a'_s}^{a'_{Tp}} \mu \Delta F_p n(a') da' + \int_{a'_{Tp}}^{a'_L} \mu \Delta F_e \left[1 - \left(1 - \frac{16G^* r\delta}{3\mu \Delta F_p}\right)^{3/2}\right] n(a') da' + \int_{a'_c}^{a'_{Te}} \mu \Delta F_e n(a') da' + \int_{a'_{Te}}^{a'_L} \mu \Delta F_e \left[1 - \left(1 - \frac{16G^* r\delta}{3\mu \Delta F_e}\right)^{3/2}\right] n(a') da' \tag{4.19}$$

As illustrated by Eqs. (4.17) and (4.18), depending on normal and tangential load, material properties and interfacial adhesion, asperity contacts may be in partial slip or full slip, at the beginning of the backward fretting half-cycle (point B in Fig. 4.2). The asperity contacts in partial slip at point B (Fig. 4.2(a)) will remain in partial slip through the backward fretting half-cycle; while for asperity contacts in full slip at point B (Fig. 4.2(b)), the initial backward fretting will be in partial slip, followed by full slip.

Given a tangential displacement s ($-s_{max} < s < s_{max}$), the transition truncated area of partial slip and full slip states during backward fretting half-cycle is determined for asperities in elastic and plastic contact, respectively, by eq. (4.20) and (4.21).

$$a'_{TB} = a'_{TBe} = \pi \left[\frac{G^*(s_{max} - s)}{2^{(3-D)} G^{(D-2)} (log\gamma)^{1/2} \mu E^*}\right]^{\left(\frac{2}{3-D}\right)} \tag{4.20}$$

$$a'_{TB} = a'_{TBp} = \frac{1}{\pi}\left[\frac{8G^*(s_{max} - s)}{3\mu H}\right]^2 \tag{4.21}$$

For asperity contacts under full slip condition ($a' < a'_{TB}$), the tangential load is constant and independent of s, as given by eq. (4.22)

$$Q_{un} = -\mu P \tag{4.22}$$

while for asperity contacts in partial slip stage ($a' > a'_{TB}$), Mindlin's solution (Eq. (4.23)) is used to characterize the relationship between tangential force and displacement (1952).

$$\Delta Q_B = \Delta Q_{max} - 2\mu P \left\{1 - \left[1 + \frac{8G^* r}{3\mu P}(\delta - \delta_{max})\right]^{3/2}\right\} \tag{4.23}$$

Therefore, the total tangential force during unloading is obtained by eq. (4.24)

$$Q_B = \int_{a_s'}^{a_{Tup}'} \mu \Delta F_p n(a') da' + \int_{a_{Tup}'}^{a_c'} \mu \left[\Delta Q_{max} - 2\mu \Delta F_p \left\{ 1 - \left[1 + \frac{8G^* r}{3\mu P} (s - s_{max}) \right]^{3/2} \right\} \right] n(a') da' + \int_{a_c'}^{a_{Tue}'} \mu \Delta F_e n(a') da' + \int_{a_{Tue}'}^{a_L'} \mu \left[\Delta Q_{max} - 2\mu \Delta F_e \left\{ 1 - \left[1 + \frac{8G^* r}{3\mu P} (s - s_{max}) \right]^{3/2} \right\} \right] n(a') da' \quad (4.24)$$

Considering the fact that forward fretting half-cycle is symmetric with the backward fretting half-cycle, with respect to the origin (Figure 4.2), the tangential force-displacement relationship during the forward fretting half-cycle (curve DEB) is obtained by Eq. (4.25) (Eriten et al., 2011)

$$Q_F(s) = -Q_B(-s) \quad (4.25)$$

Consequently, the energy dissipation is obtained by calculating the area enclosed by the fretting loop (Eq. (4.26)).

$$W = \int_{-s_{max}}^{s_{max}} [Q_F(s) - Q_B(s)] \, ds \quad (4.26)$$

4.5. Numerical results and discussion

In present study, sample length L is10 mm and the cut-off length L_s is selected to be 5 nm. The fractal dimension D is set to be 2.5 and the yield strength Y of elastic-plastic half-space is 500 MPa. The numerical results are interpreted in terms of dimensionless parameters, such as dimensionless fractal roughness $\bar{G} = G/L$, dimensionless tangential displacement $\bar{s} = s/s_{max}$, dimensionless fretting amplitude $\bar{s}_{max} = s_{max}/L$, dimensionless nominal contact pressure $\bar{p} = p/Y$, dimensionless tangential force $\bar{Q} = Q/pL^2$ and dimensionless fretting energy dissipation $\bar{W} = W/pL^2 s_{max}$.

4.5.1 Effect of surface roughness

Figure 4.3(a) shows the tangential force $\bar{Q}$ vs. tangential displacement $\bar{s}$ (fretting loops) for rough surfaces of fractal roughness $\bar{G} = 10^{-7}$ (RMS roughness $\sigma/L = 6.9 \times 10^{-6}$), 5×10^{-7} ($\sigma/L = 1.6 \times 10^{-5}$), 2×10^{-6} ($\sigma/L = 3.1 \times 10^{-5}$), and 10^{-5} ($\sigma/L = 7.2 \times 10^{-5}$), in fretting contact with an elastic-plastic half-space of E^*/Y = 440, subjected to nominal contact pressure $\bar{p}$ = 0.3, fretting amplitude $\bar{s}_{max} = 5 \times 10^{-4}$ and interfacial adhesion parameter m = 0.5. A spontaneous drop of tangential force is observed for all cases at the maximum and minimum fretting displacement, as a result of the loss of plowing friction when the direction of fretting displacement is reversed. Figure 4.3(b) shows the drop of tangential force $\overline{\Delta Q}$ =$\Delta Q/Q_{max}$ as a function of $\bar{G}$. The increase of $\Delta\bar{Q}$ with $\bar{G}$ implies that more asperities are in plastic contact for rougher surfaces under the same nominal contact pressure. Figure 4.4(a) shows the maximum tangential force $\bar{Q}_{max}$and fretting energy dissipation $\bar{W}$ as a function of $\bar{G}$. Both $\bar{Q}_{max}$ and $\bar{W}$ initially decrease, then increase as fractal roughness $\bar{G}$ increases. This non-monotonic trend can be interpreted by considering the evolution of truncated area of asperities in elastic and plastic contact, respectively, as shown in Figure 4.4(b). With the increase of $\bar{G}$, elastic contact area S_e decreases and plastic contact area S_p increases. At small surface roughness range ($\bar{G} < 10^{-6}$), the decrease of S_e is significantly faster than the increase of S_p, consequently leads

to lower tangential force and less fretting energy dissipation. With further increase of surface roughness range ($\bar{G} > 10^{-6}$), the decrease of S_e slows down and becomes comparable with the increase of S_p; therefore, with roughly constant total contact area, the increase of S_p results in higher plowing friction force and consequently raises up the tangential force and fretting energy dissipation.

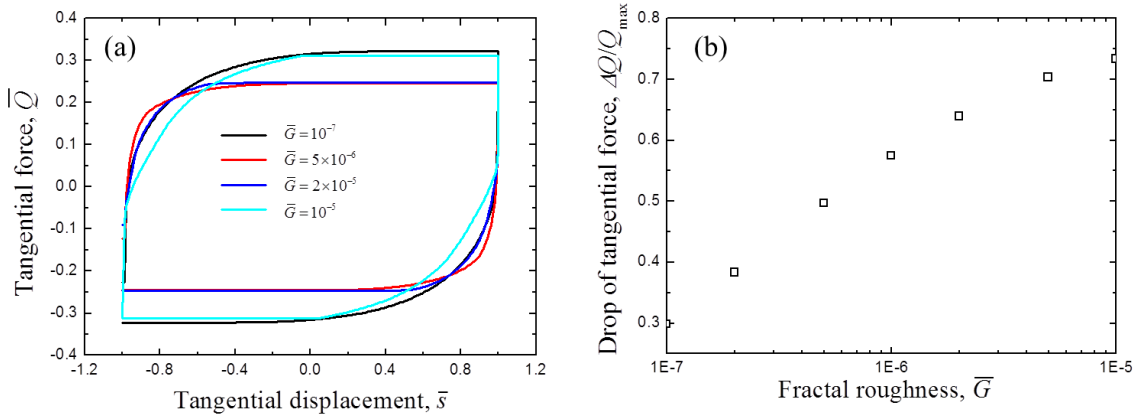

Fig. 4.3 (a) Dimensionless tangential force $\bar{Q}$ vs. dimensionless tangential displacement $\bar{s}$ for rough surfaces of fractal roughness $\bar{G} = 10^{-7}$ (RMS roughness $\sigma/L = 6.9 \times 10^{-6}$), 5×10^{-7} ($\sigma/L = 1.6 \times 10^{-5}$), 2×10^{-6} ($\sigma/L = 3.1 \times 10^{-5}$), and 10^{-5} ($\sigma/L = 7.2 \times 10^{-5}$), in fretting contact with an elastic-plastic half-space of E^*/Y = 440, subjected to nominal contact pressure $\bar{p}$ = 0.3, fretting amplitude $\bar{s}_{max} = 5 \times 10^{-4}$ and interfacial adhesion parameter m = 0.5. (b) The drop of tangential force $\Delta\bar{Q}$ =$\Delta Q/Q_{max}$ vs. fractal roughness $\bar{G}$.

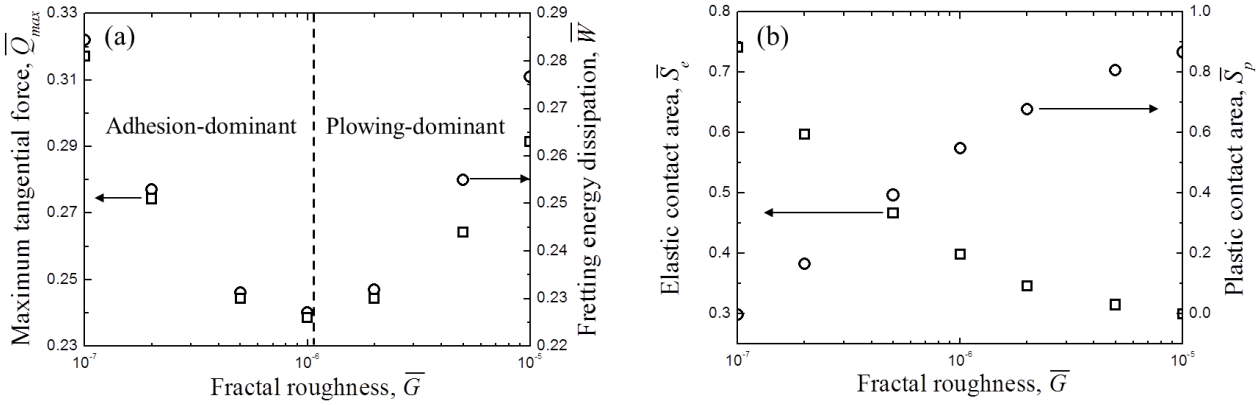

Fig. 4.4 (a) maximum tangential force $\bar{Q}_{max}$ and fretting energy dissipation $\Delta\bar{W}$ vs. fractal roughness $\bar{G}$ (b) Elastic contact area $\bar{S}_e$ and plastic contact area $\bar{S}_p$ vs. fractal roughness $\bar{G}$ for rough surfaces in fretting contact with an elastic-plastic half-space of E^*/Y = 440, subjected to nominal contact pressure $\bar{p}$ = 0.3, fretting amplitude $\bar{s}_{max} = 5 \times 10^{-4}$ and interfacial adhesion parameter m = 0.5.

4.5.2 Effect of nominal contact pressure

Figure 4.5(a) shows the tangential force $\bar{Q}$ vs. tangential displacement $\bar{s}$ (fretting loops) for fractal rough surfaces $\bar{G} = 2 \times 10^{-6}$ in fretting contact with an elastic-plastic half-space of

E^*/Y = 440, subjected to nominal contact pressure $\bar{p}$ = 0.1, 0.6 and 1.5, fretting amplitude $\bar{s}_{max} = 5 \times 10^{-4}$ and interfacial adhesion parameter m = 0.5. The fretting loop indicates higher $\bar{p}$ yields lower maximum tangential force $\bar{Q}_{max}$ and fretting energy dissipation $\Delta\bar{W}$. This counter-intuitive trend is further explored in Figure 4.6(a), which shows that both maximum tangential force $\bar{Q}_{max}$and dissipated fretting energy $\Delta\bar{W}$ decrease with nominal contact pressure $\bar{p}$. Similar phenomenon (less fretting energy is dissipated at higher nominal contact pressure) is also captured in fretting contact analysis using GW model (Eriten and Polycarbou, 2011), but the interpretation is different: in GW model, all asperities are assumed of the identical radius of curvature; therefore, at higher $\bar{p}$, more asperities are plastically deformed and tend to stay in partial slip state, thus result in less fretting energy; whereas in fractal surface model, the asperities in plastic contact are of smaller contact area than those in elastic contact. Therefore, at low nominal contact pressure, area of discrete contact regions are small, thus majority of the asperities are in plastic contact; with the accumulation of normal load, the fraction of contact area for asperities in elastic contact increases, as indicated by Figure 4.6(b), which leads to smaller tangential force and lower fretting energy dissipation. The argument above is also consistent with the observation that higher tangential stiffness when nominal contact pressure is lower: since the area of discrete contact region is smaller, the tangential displacement required to drive an asperity from partial slip to full slip is also smaller, and consequently, the tangential stiffness is higher.

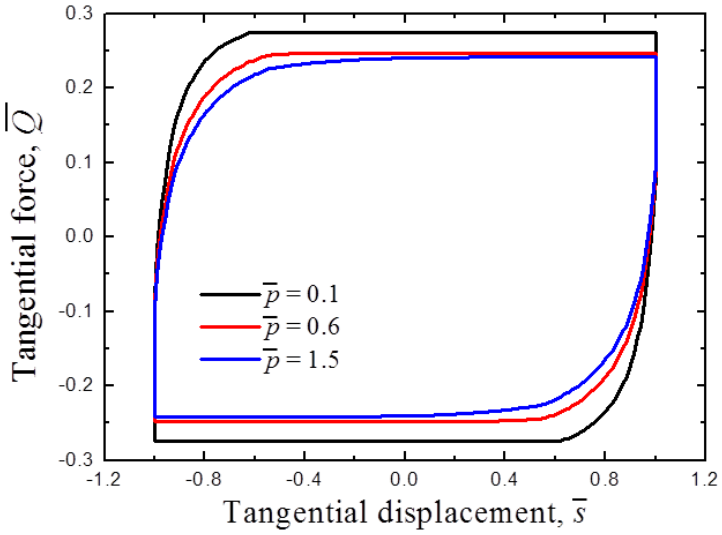

Fig. 4.5 Tangential force $\bar{Q}$ vs. tangential displacement $\bar{s}$ for fractal rough surfaces $\bar{G} = 2 \times 10^{-6}$ in fretting contact with an elastic-plastic half-space of E^*/Y = 440, subjected to nominal contact pressure $\bar{p}$ = 0.1, 0.6 and 1.5, fretting amplitude $\bar{s}_{max} = 5 \times 10^{-4}$ μm and interfacial adhesion parameter m = 0.5.

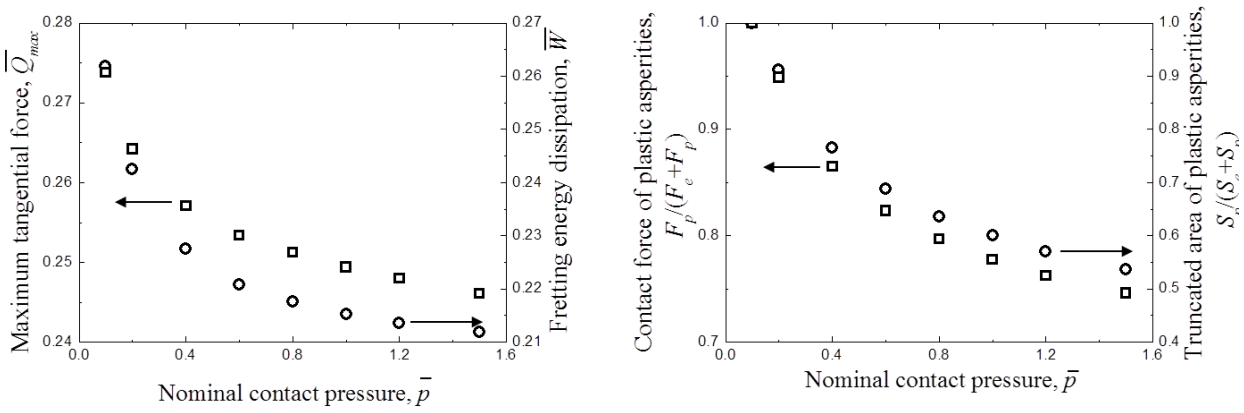

Fig. 4.6 (a) maximum friction force $\bar{Q}_{max}$ and fretting energy dissipation $\Delta\bar{W}$ vs. nominal contact pressure $\bar{p}$ and (b) fraction of plastic contact force $F_p/(F_e+F_p)$ and plastic contact area $S_p/(S_e+S_p)$ vs. nominal contact pressure $\bar{p}$ for fractal rough surfaces $\bar{G}=2\times10^{-6}$ in fretting contact with an elastic-plastic half-space of E^*/Y = 440, subjected to fretting amplitude $\bar{s}_{max}=5\times10^{-4}$ μm and interfacial adhesion parameter m = 0.5.

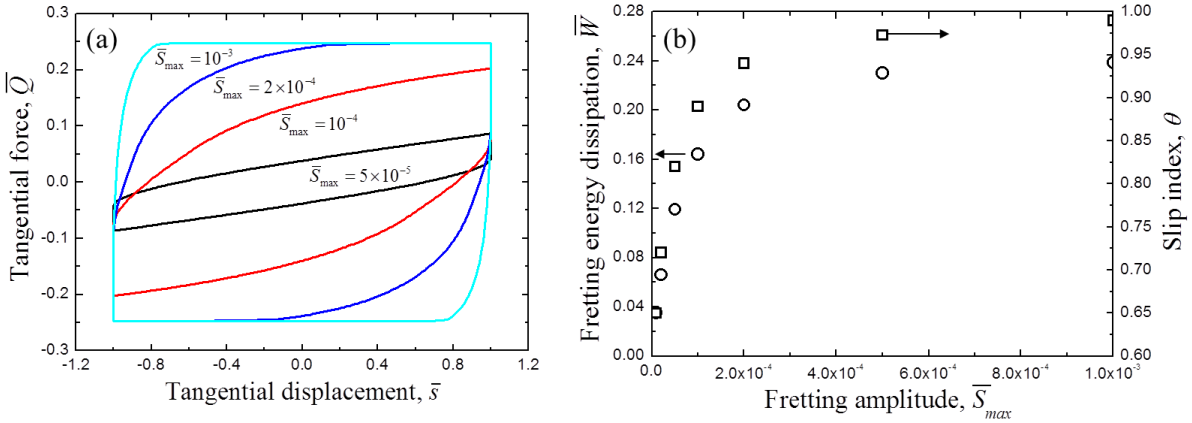

Fig. 4.7 (a) Tangential force $\bar{Q}$ vs. tangential displacement $\bar{s}$ for fractal rough surfaces $\bar{G}=2\times10^{-6}$ in fretting contact with an elastic-plastic half-space of E^*/Y = 440, subjected to nominal contact pressure $\bar{p}$ = 0.3, fretting amplitude $\bar{Q}_{max}=5\times10^{-5}$, 10^{-4}, 2×10^{-4} and 10^{-3} and interfacial adhesion parameter m = 0.5. (b) Fretting energy dissipation $\Delta\bar{W}$ vs. fretting amplitude s_{max}.

4.5.3 Effect of fretting amplitude

Figure 4.7(a) shows the tangential force $\bar{Q}$ vs. tangential displacement $\bar{s}$ (fretting loops) for rigid rough surface of fractal roughness $\bar{G}=2\times10^{-6}$ in fretting contact with an elastic-plastic half-space of E^*/Y = 440, subjected to nominal contact pressure $\bar{p}$ = 0.3, fretting amplitude $\bar{s}_{max}=5\times10^{-5}$, 10^{-4}, 2×10^{-4} and 10^{-3} and interfacial adhesion parameter m = 0.5. At small fretting amplitude (e.g. $\bar{s}_{max}=10^{-5}$), most asperities are under partial slip state, thus dissipated fretting energy is low. As fretting amplitude increases, more asperities are in full slip state, resulting in higher tangential force and more fretting energy dissipation. When fretting amplitude $\bar{s}_{max}$ is sufficiently large (e.g. $\bar{s}_{max}=2\times10^{-4}$ and 10^{-3}), all asperity contacts have been in full slip state before $\bar{s}_{max}$ is reached, thus a plateau is encountered for tangential force. As $\bar{s}_{max}$ increases, the contribution of partial slip range becomes less significant, evidenced by

the fact that slip index θ increases to 1 asymptotically (Figure 4.7(b)); thus the fretting loop can be approximated as a rectangle of length $2\bar{s}_{max}$and width $2\bar{Q}_{max}$, and fretting energy dissipation $\Delta\bar{W}$ also approaches the value of maximum tangential force $\bar{Q}_{max}$ asymptotically. It is noticed that in most energy-based fretting wear analysis, this approximation is generally used, in order to simplify the calculation of fretting energy dissipation; however, when fretting amplitude is not sufficiently large to ignore the partial slip range, it may noticeably overestimate the fretting energy dissipation, thus wear rate.

4.5.4 Effect of elastic modulus-to-yield strength ratio

Figure 4.8(a) shows the tangential force $\bar{Q}$ vs. tangential displacement $\bar{s}$ (fretting loop) for rigid rough surface of fractal roughness $\bar{G} = 2 \times 10^{-6}$ in fretting contact with an elastic-plastic half-space of E^*/Y = 110, 220, 440 and 660, subjected to nominal contact pressure $\bar{p}$ = 0.3, fretting amplitude $\bar{s}_{max} = 5 \times 10^{-4}$ and interfacial adhesion parameter m = 0.5. For small E^*/Y value, the fretting loop is under partial slip and the plateau of maximum tangential force is not achieved at s_{max}; for high E^*/Y value, the tangential force $\bar{Q}$ approaches its maximum asymptotically before s_{max} is reached, implying all asperities are in full slip state. The dependence of stick-slip state on E^*/Y value can be interpreted by considering the contact area: because the yield strength of elastic-plastic half-space is fixed in present study, lower E^*/Y value indicates lower elastic modulus; therefore, larger contact area has to be established to achieve the same nominal contact pressure, and larger fretting displacement is required for asperities transit from partial slip to full slip state. This interpretation is consistent with the trend that slip index θ increases with E^*/Y value, as plotted in Figure 4.8(b). Meanwhile, larger elastic contact area caused by lower E^*/Y value induces higher friction force; therefore, the maximum tangential force $\bar{Q}_{max}$ increases as E^*/Y value decreases, as shown in Figure 4.9(a). Due to the two competing factors (decrease of $\bar{Q}_{max}$and increase of slip index θ with the increase of E^*/Y value), a non-monotonic trend is captured in Figure 4.9(b), that fretting energy dissipation $\Delta\bar{W}$ first increases, then decreases with E^*/Y value. However, it has to be noticed that, there exists some critical value of E^*/Y value, beyond which the critical truncated area a_c' is sufficiently large such that all asperities are in plastic contact and the influence of elastic material properties is negligible.

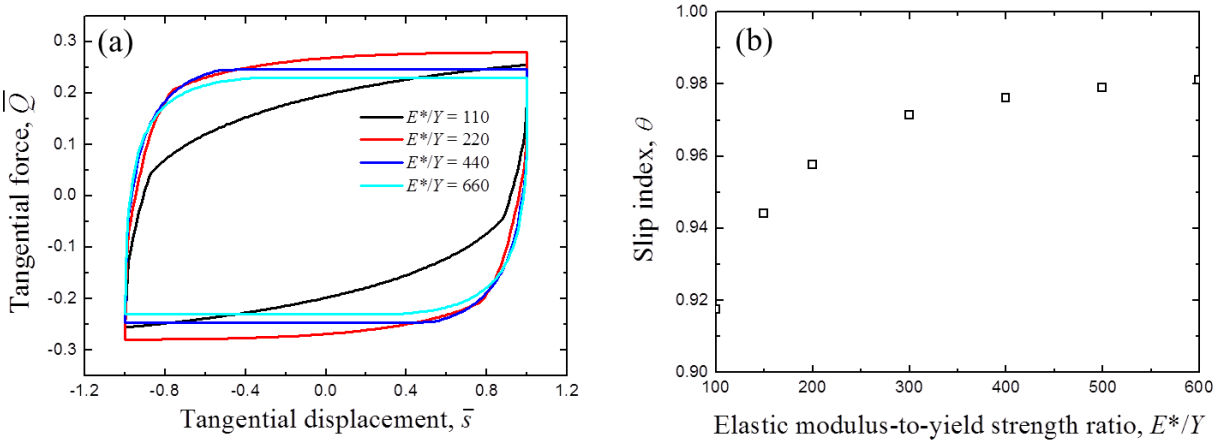

Fig. 4.8(a) Tangential force $\bar{Q}$ vs. tangential displacement $\bar{s}$ for fractal rough surfaces $\bar{G} = 2 \times 10^{-6}$ in fretting contact with an elastic-plastic half-space of E^*/Y = 110, 220, 440 and 660, subjected to nominal contact pressure $\bar{p}$ = 0.3, fretting amplitude $\bar{s}_{max} = 5 \times 10^{-4}$ and interfacial adhesion parameter m = 0.5. (b) Slip index θ vs. elastic modulus-to-yield strength ratio E^*/Y.

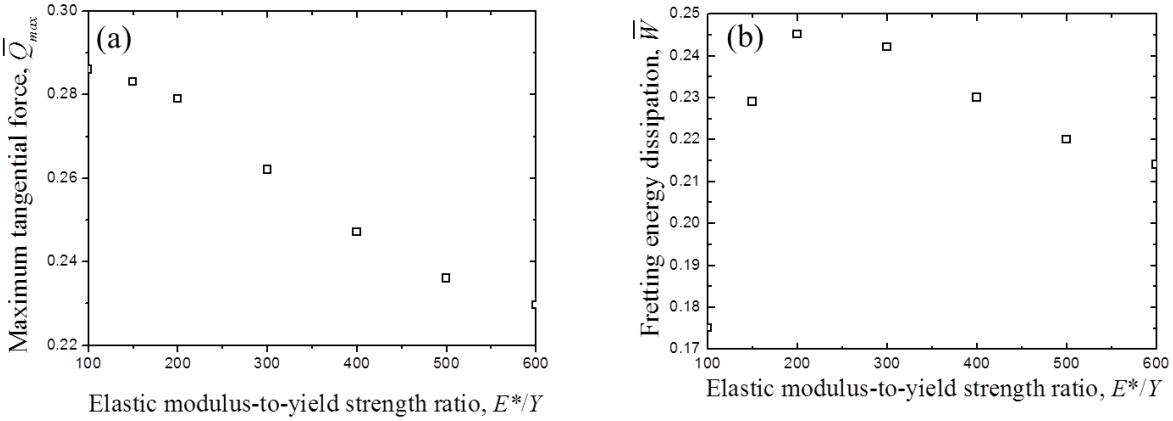

Fig. 4.9(a) maximum friction force $\bar{Q}_{max}$ vs. elastic modulus-to-yield strength ratio E^*/Y. (b) fretting energy dissipation $\Delta\overline{W}$ vs. elastic modulus-to-yield strength ratio E^*/Y for fractal rough surfaces $\bar{G} = 2 \times 10^{-6}$ in fretting contact with an elastic-plastic half-space, subjected to nominal contact pressure $\bar{p}$ = 0.3, fretting amplitude $\bar{s}_{max} = 5 \times 10^{-4}$ and interfacial adhesion parameter m = 0.5.

4.5.5 Effect of interfacial condition

As discussed in section 4.2, interfacial shear stress is bounded between 0 and the shear strength of the elastic-plastic half-space τ_0, characterized by interfacial adhesion parameter m, floating in the range of 0 to 1, representing the strength of interfacial adhesion: small m value represents low interfacial adhesion and when m = 0, interface is known as frictionless; on the other hand, large m value is applicable for sticky surfaces and when m = 1, the adhesion at interface junction is sufficiently strong such that plastic deformation occurs at surface and/or subsurface and full slip starts, before junction breaks, which is essentially equivalent to the friction model of Brizmer et al. (2007). The value of m is primarily determined by the material compatibility of two contact surfaces, but is also significantly influenced by environmental conditions (e.g. temperature, humidity, cleanness) and can be alternated intentionally by surface modification (e.g. anti-sticking coating). Therefore, it is of interest to see the influence of m on fretting contact.

Figure 4.10(a) shows the maximum tangential force $\bar{Q}_{max}$ vs. interfacial adhesion parameter m for rigid rough surfaces of fractal roughness $\bar{G} = 2 \times 10^{-6}$, 10^{-5}, 5×10^{-5} in fretting contact with an elastic-plastic half-space of E^*/Y = 220, subjected to nominal contact pressure $\bar{p}$ = 0.3 and fretting amplitude $\bar{s}_{max} = 5 \times 10^{-4}$. Smoother surface ($\bar{G} = 2 \times 10^{-6}$) exhibits the highest increasing rate of $\bar{Q}_{max}$with respect to m, comparing with rougher surfaces ($\bar{G} = 5 \times 10^{-5}$), indicating that interfacial friction is more sensitive to interfacial adhesion for smooth surface. The explanation can be made by considering the fraction of elastic and plastic contact area for different surface roughness. From Eqs (4.1) and (4.2), it is realized that friction coefficient of asperities in elastic contact is proportional to m; while for asperities in plastic

contact, only adhesion friction coefficient increases with m linearly and plowing friction force is independent of m, thus exhibit less significant dependence on m. As analyzed in section 4.5.1, with the increase of surface roughness $\bar{G}$, more asperities are in plastic contact; therefore, the influence of m is less pronounced for rougher surfaces. Figure 4.10(b) shows the fretting energy dissipation $\Delta\bar{W}$ as a function of m for $\bar{G} = 2\times10^{-6}, 10^{-5}, 5\times10^{-5}$, respectively. Similar to $\bar{Q}_{max}$, $\Delta\bar{W}$ also increases faster with m for smoother surfaces; furthermore, it is noticed when $\bar{G} = 5\times10^{-5}$, $\Delta\bar{W}$ even decreases slightly as m increases. This counter-intuitive trend is interpreted by considering the variation of slip index θ, as demonstrated in Figure 4.11. For $\bar{G} = 2\times10^{-6}$ and 10^{-5}, the decrease of θ with m is negligible in comparison with the increase of $\bar{Q}_{max}$, thus $\Delta\bar{W}$ increases; however, when $\bar{G} = 5\times10^{-5}$, $\bar{Q}_{max}$ increases very slightly with m, as shown in Figure 4.10(a) and decrease of θ is more pronounced, since more asperities will be in partial slip condition due to stronger interfacial adhesion, therefore $\Delta\bar{W}$ decreases with m.

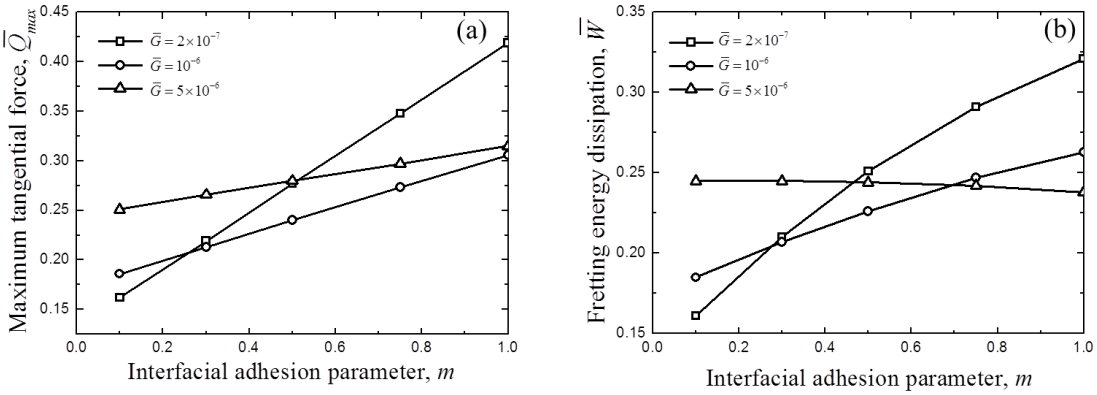

Fig. 4.10(a) maximum friction force $\bar{Q}_{max}$ vs. interfacial adhesion parameter m for fractal rough surfaces $\bar{G} = 2\times10^{-6}, 10^{-5}, 5\times10^{-5}$ in fretting contact with an elastic-plastic half-space of $E^*/Y = 220$, subjected to nominal contact pressure $\bar{p} = 0.3$ and fretting amplitude $\bar{s}_{max} = 5\times10^{-4}$. (b) fretting energy dissipation $\Delta\bar{W}$ vs. interfacial adhesion parameter m for $G = 2$, 10 and 50nm.

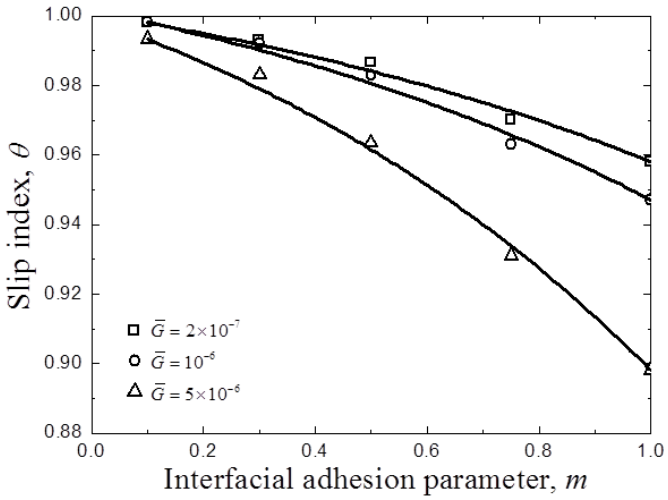

Fig. 4.11 Slip index θ vs. interfacial adhesion parameter m.

4.6. Conclusions

A fretting contact model was proposed for a rigid surface exhibiting multi-scale roughness (fractal) and an elastic-plastic half-space. Mindlin's theory of partial slip was employed as asperity scale and the status (partial slip or full slip) of each asperity contact was identified. In contrast to the Coulomb friction model used in the original work of Mindlin, as well as the preload dependent friction model (Brizmer et al., 2007) which implicitly assumes the interface adhesion is sufficiently strong, thus inception of sliding is associated with plastic deformation, present study breaks down the friction force into two components: adhesion and plowing. Adhesion friction force is applicable for all asperity contacts, regardless of the nature of contact (elastic or plastic) and tangential motion (partial slip or full slip). It depends on real contact area, shear strength of elastic-plastic half-space and interfacial condition, which is characterized by an interfacial adhesion parameter, floating between 0 and 1; but is independent of contact pressure. On the other hand, plowing friction force is only applicable for asperities in plastic contact and full slip regime and determined by the plastic deformation of asperity contact.

The effects of surface roughness, nominal contact pressure, fretting amplitude, elastic modulus-to-yield strength ratio and interfacial adhesion parameter were elucidated in the context of fretting energy dissipation, maximum tangential force and slip index obtained by numerical method. Both maximum tangential force and fretting energy dissipation demonstrate a non-monotonic dependence on surface roughness. The initial decrease of the maximum tangential force and fretting energy dissipation is attributed to rapid decrease of elastic contact area, while with continued increase of surface roughness, the increase of plastic contact area is dominant and the maximum tangential force and fretting energy dissipation increase.

Both maximum tangential force and fretting energy dissipation were found decreasing with nominal contact pressure. This counter-intuitive result can be understood by considering that asperities of large truncated area in elastic contact, while small truncated area represents plastic contact in contact of fractal surfaces. Therefore, the fraction of elastic contact area increases with nominal contact pressure, which reduces both the friction coefficient, thus fretting energy dissipation.

Transition from partial slip to full slip was reproduced at macroscopic scale with the increase of fretting amplitude, accompanied by accumulation of fretting energy dissipation. While a rectangle with length of two times of fretting amplitude and width of two times of maximum tangential force is a good approximation of the fretting loop when fretting amplitude is sufficiently large, this simple multiplication may significantly overestimate the fretting energy dissipation at small fretting amplitude, and consequent wear prediction.

The influence of elastic modulus-to-yield strength ratio (E^*/Y) on fretting contact behavior is driven by two competing mechanisms: the maximum tangential force is higher for smaller E^*/Y value because of larger contact area; meanwhile, slip index shows the opposite dependence because larger contact area implies that more asperities are in partial slip with given fretting amplitude. At small E^*/Y value, the increase of slip index with E^*/Y value is the dominant factor, thus fretting energy dissipation increases; with further increase of E^*/Y, slip

index approaches 1 asymptotically and the second first mechanism becomes more important; as a result, fretting energy dissipation decreases.

The effect of interfacial adhesion parameter was examined at three different surface roughness values. For smooth surface, the maximum tangential force increases significantly with the interfacial adhesion parameter; but for rough surface, maximum tangential force is relatively insensitive to interfacial adhesion parameter. In order to understand the difference of interfacial adhesion effect on maximum friction force for different surface roughness value, we have to revisit the roughness effect discussed above. As surface roughness decreases, elastic contact area where friction is proportional with interfacial adhesion parameter increases and plastic contact area where friction is relatively less dependent on interfacial adhesion parameter decreases. The observation above implies that to reduce friction efficiently, it is necessary to smooth the surface before depositing any anti-sticking layer. Interestingly, it is noticed that fretting energy dissipation may even decrease slightly with interfacial adhesion parameter, as a result of more asperities in partial slip due to strong interface adhesion.

CHAPTER 5

Adhesion-induced instabilities in elastic and elastic-plastic contacts during single and repetitive normal loading

5.1. Introduction

In chapter 2-4, we have systematically investigated the adhesionless contact behavior at both asperity scale (chapter 2 and 3) and for rough surfaces (chapter 4). It is generally acceptable to neglect surface adhesion in contact analysis at macroscopic scale, however, as contact surfaces scale down and surface forces exceed bulk forces, surface adhesion is of great importance and plays a dominant role in many engineering systems, such as microelectromechanical systems, hard-disk drives, and surface force microscopes (Du et al., 2007) to name just a few. One of the first studies of adhesive contact is attributed to Bradley (1932), who examined the effect of adhesion on the contact force between two rigid spheres and reported that the pull-off force P_{off} (defined as the maximum adhesive (attractive) force at the instant of surface separation) is given by $P_{off} = -2\pi R\Delta\gamma$, where R is reduced radius of curvature ($R = (1/R_1 + 1/R_2)^{-1}$, where R_1 and R_2 are the radii of curvature of the two spheres) and $\Delta\gamma$ is the work of adhesion ($\Delta\gamma \equiv \gamma_1 + \gamma_2 - \gamma_{12}$, where γ_1 and γ_2 are the surface energies of the two spheres, respectively, and γ_{12} is the interfacial energy). Pioneering studies of adhesive contact between elastic spherical bodies have been performed by Johnson, Kendall, and Roberts (JKR) (1971) and Derjaguin, Muller, and Toporov (DMT) (1975). In the JKR model, the adhesion force is assumed to arise within the contact region in conjunction with the Hertzian contact pressure, resulting in the formation of a neck that increases the contact area. The contact stress predicted by the JKR model increases asymptotically to infinity at the contact edge and the resulting pull-off force is given by $P_{off} = -1.5\pi R\Delta\gamma$. According to the DMT model, the adhesion force is produced over an annulus surrounding the contact region without affecting the surface profiles of the elastically deformed spheres and $P_{off} = -2\pi R\Delta\gamma$. Elastic behavior of adhesive contacts can be described by so-called Tabor parameter μ given by (Tabor, 1977)

$$\mu = \left(\frac{R\Delta\gamma^2}{E^{*2}\varepsilon^3}\right)^{1/3} \tag{5.1}$$

where $E^* = [(1-\nu_1^2)/E_1 + (1-\nu_2^2)/E_2]^{-1}$ is the effective elastic modulus (E_1, ν_1 and E_2, ν_2 denote elastic modulus and Poisson's ratio of the two contacting elastic spheres, respectively) and ε is the atomic equilibrium distance. The JKR model holds for large and compliant spheres (high μ), whereas the DMT model is applicable in cases of small and stiff spheres (low μ). The parameter μ can be viewed as the ratio of the elastic surface displacement at the instant of separation to the effective range of surface force characterized by the equilibrium distance (Johnson and Greenwood, 1997). Zhao et al. (2003) considered the nature of physical contacts in the context of the Tabor parameter and reported μ values for different material systems, e.g., Si tip in contact with a $NbSe_2$ surface under vacuum (μ = 0.2–0.3), contact between 1-μm-diameter carbon particles (μ = 0.5–1.5) and between 8-μm-diameter polymer monofilaments ($\mu \approx 12$), and

polyurethane sphere in contact with a glass substrate ($\mu \approx 1000$). Johnson and Greenwood (1997) have reported similarly wide range of μ values, e.g., $\mu < 1$ for stiff materials in contact with a sharp (~100 nm in radius) Si tip of an atomic force microscope (AFM) and $\mu \approx 50$ for crossed cylinders of mica sheet glued to glass cylinders used in the surface force apparatus (Israelachvili, 1992). In view of the wide range of Tabor parameter, understanding its significance in adhesive contact behavior is of particular importance.

Muller, Yushenko, and Derjaguin (MYD) (1980) used the Lennard-Jones (L-J) potential to determine the surface traction and deformation of an elastic sphere in adhesive contact with a rigid plane, and observed a smooth transition of the pull-off force between values predicted by the DMT ($\mu < 0.1$) and JKR ($\mu > 5$) models. Greenwood (1997) confirmed the results of the MYD model and showed that jump-in and jump-out due to adhesion in spherical contacts commence only when $\mu > 1$. Maguis (1992) used the Dugdale approximation (MD model) to represent the surface traction and derived a closed-form solution of the pull-off force that yields a smooth transition between the DMT and JKR solutions in the intermediate range of Tabor parameter $0.1 < \mu < 5$. Johnson and Greenwood (1997) constructed an adhesion map that shows the ranges of dimensionless normal load and Tabor parameter where different contact models (e.g., JKR, DMT, and MD) are appropriate.

Neglecting short-range repulsive forces, Attard and Parker (1992) derived a contact instability condition for surface deformation larger than the perturbations of the surface profile given by

$$(x_o/\varepsilon)^{7/2} = 3\sqrt{2}\pi\mu^{3/2} \tag{5.2}$$

where x_o is the central gap. Pethica and Sutton (1988) argued that surface instabilities occur when the surface force gradient exceeds that of the restoring force due to elastic deformation of the interacting bodies and obtained an instability condition given by

$$(x_o/\varepsilon)^{7/2} = 16\pi\mu^{3/2}/3 \tag{5.3}$$

In all of the analytical and numerical studies mentioned above, contact deformation was assumed to be purely elastic. However, Maugis and Pollock (1984) showed that a high adhesion force may induce plastic deformation, even in the absence of an externally applied load. Therefore, for comprehensive analysis of adhesive contact, it is essential to consider elastic-plastic material behavior. Mesarovic and Johnson (2000) studied separation of two adhering elastic-plastic spheres under the assumption of predominantly elastic deformation during unloading. Kogut and Etsion (2003) extended the classical DMT analysis of elastic adhesive contacts to fully plastic adhesive contacts and used a finite element model to calculate surface separation outside the contact region. Kadin et al. (2008a) used the finite element method and the L-J potential to model adhesive contact between a rigid flat and an elastic-plastic sphere that exhibited kinematic hardening and observed a dependence of the load-unload behavior on the Tabor parameter, plasticity parameter, maximum surface approach, and evolution of plasticity during the loading and unloading phases. Kadin et al. (2008b) also modeled cyclic loading of an elastic-plastic sphere in adhesive contact with a rigid flat and studied the effect of isotropic and kinematic strain hardening of the sphere on the shakedown behavior.

Wu and Adams (2009) used the JKR, DMT, and GJ (Greenwood and Johnson, 1998) stress fields to determine the critical load at the onset of yielding in the subsurface and confirmed that, for sufficiently high μ and low yield strength Y, yielding may occur even in the absence of an external load. Kadin et al. (2008c) used a semi-analytical model of adhesive contact and reported that jump-in may induce plastic deformation, depending on the combined effect of E^* and R [Eq. (5.1)]. Song and Srolovitz (2006) performed molecular dynamics simulations of adhesive contact between a rigid flat and an elastic-plastic sphere and observed material transfer to the rigid flat due to excessive plastic deformation during unloading.

A common feature in the surface instability criteria of the above studies is that jump-in and jump-out do not occur when $\mu < 1$; however, this criterion appears to be limited to infinitely stiff systems. The main objective of this chapter was to examine adhesion-induced contact instabilities in elastic and elastic-plastic contacts of systems with a finite stiffness. Solutions of the critical central gap at the instant of jump-in and jump-out and interpretation of these phenomena in the context of force-displacement responses are presented first, followed by finite element results of elastic and elastic-plastic adhesive contacts illustrating the effect of plastic deformation on adhesive contact behavior during single and multiple approach-retraction cycles.

5.2. Analytical model of adhesive contact

Figure 5.1 shows the equivalent system of two elastic spheres in close proximity, i.e., a rigid sphere of reduced radius R and an elastic half-space of effective modulus E^*. The separation of the two surfaces is given by $x = x_o + r^2/2R$, where r is the radial distance from the axis of symmetry. For surface interaction controlled by the L-J potential (Israelachvili, 1992), the local traction distribution $p(r)$ can be expressed as

$$p(r) = \frac{8\Delta\gamma}{3\varepsilon}\left\{\left[\frac{\varepsilon}{x(r)}\right]^3 - \left[\frac{\varepsilon}{x(r)}\right]^9\right\} \tag{5.4}$$

The above equation was first introduced by Johnson and Greenwood (1997) without proof and has since been used in several adhesion studies (e.g., Kogut and Etsion, 2003; Du et al., 2007; Kadin et al., 2008a-c). A detailed derivation of Eq. (5.4) is given in Appendix A (Eq. (A9)).

Although the geometrical relationship $x = x_o + r^2/2R$ gives the true surface separation only in the case of undeformed half-space, it may also yield fair estimates of the surface gap when deformation is small, as before the commencement of jump-in. This assumption is validated by finite element results presented in a following section. The surface displacement of an axisymmetric elastic solid due to distributed surface traction can be obtained by integrating the Boussinesq solution of the surface displacement u of a half-space due to a concentrated normal force P given by (Timoshenko and Goodier, 1970)

$$u = \frac{(1-\nu^2)}{\pi E}\left(\frac{P}{r}\right) \tag{5.5}$$

Since adhesive surface interaction also exists outside the contact region, the surface displacement at $r = 0$ can be obtained as

$$h_o = \int_0^\infty \frac{p(r)}{\pi E^* r} 2\pi r dr \tag{5.6}$$

Substitution of Eq. (5.4) into Eq. (5.6) followed by integration yields

$$h_o = \frac{16\Delta\gamma\sqrt{R}}{3\sqrt{2}E^*\varepsilon}\left(\frac{3\pi\varepsilon^3}{8x_o^{5/2}} - \frac{6435\pi\varepsilon^9}{32768x_o^{17/2}}\right) \tag{5.7}$$

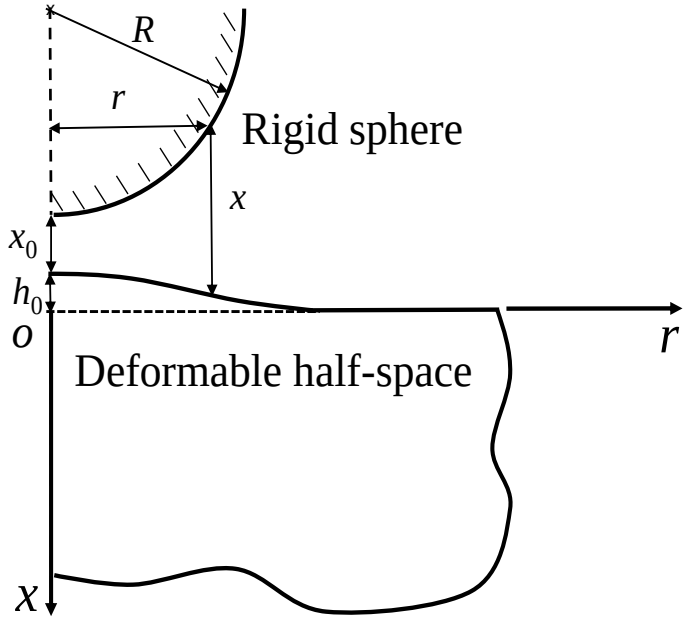

Figure 5.1 Equivalent model of a rigid sphere in close proximity with an elastic half-space. The pile-up at the half-space surface is due to the effect of adhesion.

Figure 5.2 shows a schematic of the jump-in phenomenon. At a critical central gap x_o (Figure 5.2(b)), an infinitesimally small relative displacement $d\delta$ causes the upwardly displaced surface to jump into contact with the sphere and the central gap vanishes (Figure 5.2(c)). Therefore, the jump-in condition can be mathematically expressed as

$$dx_o/d\delta \to \infty \text{ or } d\delta/dx_o \to 0 \tag{5.8}$$

In the present analysis, contact does not imply "hard" contact as defined in classical contact mechanics because the repulsive term in the L-J potential prevents intimate surface contact. Therefore, the sphere is assumed to be in contact with the elastic half-space when surface separation reaches an infinitesimally small value, on the order of the atomic equilibrium distance. Using the geometric relationship

$$x_o = -(\delta + h_o) \tag{5.9}$$

in conjunction with Eq. (5.8), the instability criterion can be expressed as

$$\partial h_o / \partial x_o = -1 \tag{5.10}$$

After subtituting Eq. (5.7) into Eq. (5.10), the dimensionless critical central gap at the instant of jump-in or jump-out $\bar{x}_{o,c} = x_{o,c}/\varepsilon$ can be obtained as the solution of equation

$$11.1\bar{x}_o^{-7/2} - 19.8\bar{x}_o^{-19/2} = \mu^{-3/2} \tag{5.11}$$

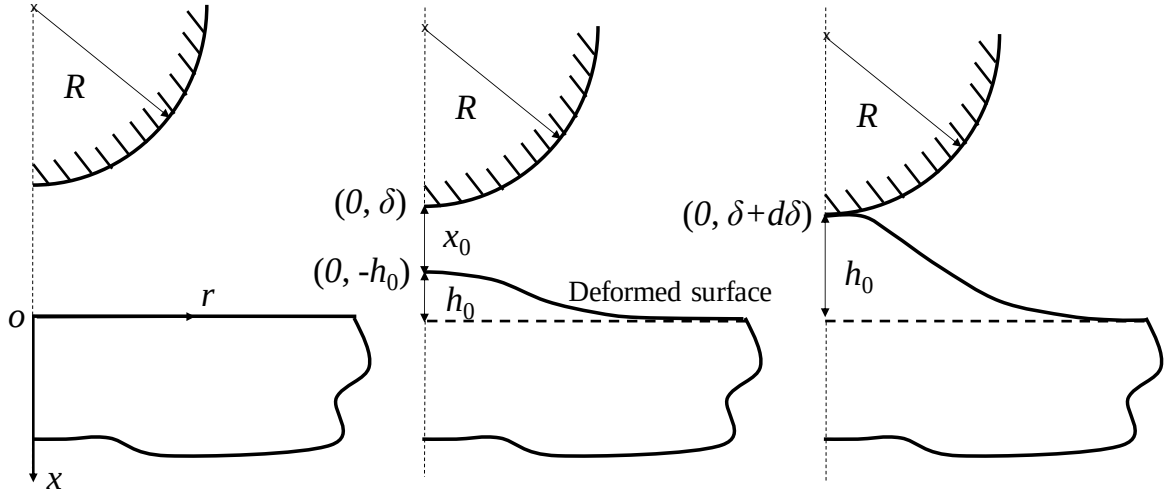

Figure 5.2. Schematics of a rigid sphere in proximal distance with an elastic half-space: (a) relatively large gap (no surface deformation), (b) pile-up formation due to adhesive interaction, and (c) sudden surface contact (jump-in).

Figure 5.3 shows the critical central gap $\bar{x}_{o,c}$ as a function of Tabor number μ. Below a critical (threshold) value $\mu^* = 0.5$, neither instability is encountered and both approach and retraction paths of the force-displacement response are smooth.

The critical Tabor parameter determined from the present analysis ($\mu^* = 0.5$) is less than that reported previously ($\mu^* = 1$) (Greenwood, 1997) and validated by finite element results (Kadin et al., 2008a). This discrepancy is attributed to the apparatus stiffness effect. As pointed out by Greenwood (1997), $\mu^* = 1$ holds only for an infinitely stiff apparatus, whereas for an apparatus of finite stiffness, jump events can occur when $\mu^* = 0.5$ or even less. In all previous studies that reported $\mu^* = 1$, adhesive contact was modeled between two elastic spheres (Greenwood, 1997) or an elastic sphere and a rigid plate (Kadin et al., 2008a-c), implying infinite stiffness apparatus, whereas contact of a rigid sphere with an elastic half-space investigated in this study is typical of a finite stiffness apparatus, i.e., deformation of the elastic half-space is not constrained by physical boundaries, which explains the lower critical Tabor parameter in the present analysis. For $\mu^* > 0.5$, Eq. (5.11) yields two solutions $\bar{x}_{o,c}$; the large root corresponds to jump-in and the small root to jump-out. As μ decreases, the two solutions

approach each other, converging to a single value $\bar{x}_{o,c}$ = 1.3 for μ = 0.5. In the case of jump-in, $\bar{x}_{o,c}$ shows a strong dependence on μ, as opposed to jump-out where $\bar{x}_{o,c}$ varies slightly in the range of 1.1–1.3.

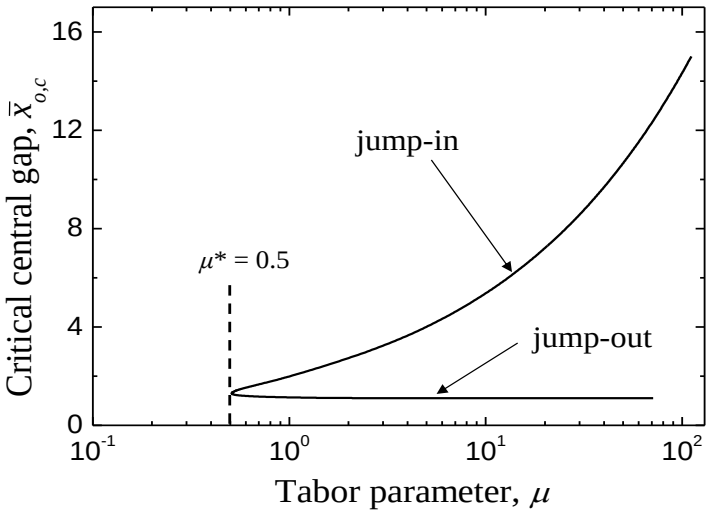

Figure 5.3. Critical central gap at the instant of jump instabilities versus Tabor parameter.

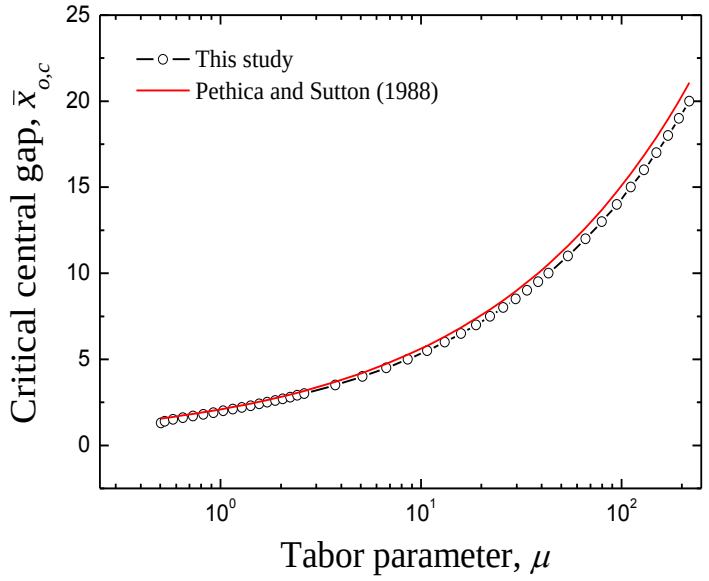

Figure 5.4. Critical central gap at the instant of the jump-in instability versus Tabor parameter.

Figure 5.4 shows the critical central gap at the instant of jump-in $\bar{x}_{o,c}$ as a function of Tabor parameter μ. Good agreement is shown between results of the present analysis and that of Pethica and Sutton (1988), which is for the same contact geometry (Figure 5.1). The slightly higher values of $\bar{x}_{o,c}$ predicted from the analysis of Pethica and Sutton are attributed to the absence of a repulsive term in the interatomic potential used in their study. In the absence of a

repulsive force, jump instabilities can occur regardless of Tabor parameter because the contact stiffness remains negative. Therefore, a critical Tabor parameter cannot be obtained from the analysis of Pethica and Sutton.

5.3. Finite element model of adhesive contact

Figure 5.5 shows the finite element model used to analyze elastic and elastic-plastic adhesive contact. The purpose of the elastic finite element analysis was to validate the analytical model. Finite element simulations were performed with the multi-purpose finite element code ABAQUS (version 6.7). The ABAQUS/STANDARD solver was used in all simulations of this study. The half-space was modeled with 69,736 axisymmetric, four-node, linear, isoparametric elements consisting of 70,528 nodes. The nodes at the bottom and left boundaries of the mesh were constrained against displacement in the vertical and horizontal direction, respectively. The distance between two adjacent surface nodes of the refined mesh is equal to ~$0.003R$. The rigid surface option was used to model the sphere. Similar to a previous study (Kadin et al., 2008a), nonlinear spring elements (SPRINGA) with a prescribed force-displacement relationship governed by the L-J potential were used to model interfacial adhesion. The (adhesion) force dP generated by a spring assigned to a surface node at a distance r from $x = 0$ is given by

$$dP(r) = p(r)2\pi r dr = \frac{16\pi r\Delta\gamma}{3\varepsilon}\left\{\left[\frac{\varepsilon}{x(r)}\right]^3 - \left[\frac{\varepsilon}{x(r)}\right]^9\right\} dr \tag{5.12}$$

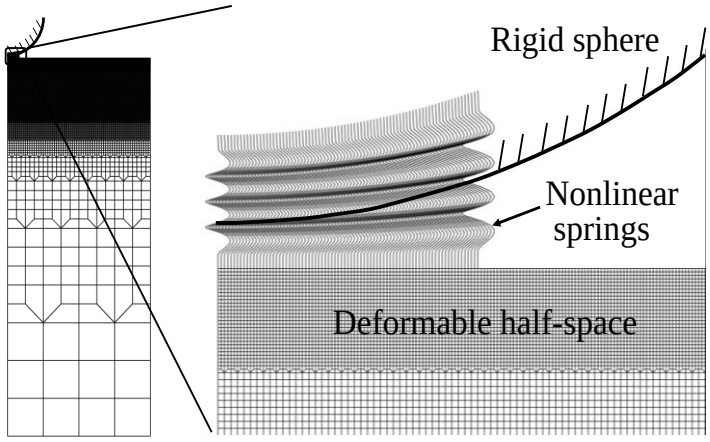

Figure 5.5. Finite element model of a rigid sphere in close proximity with a deformable half-space. Surface adhesion is modeled by nonlinear springs (shown by serrated lines) with a force-distance relationship governed by the L-J potential.

The half-space was modeled as an elastic-perfectly plastic material. The transition from elastic to plastic deformation obeyed the von Mises yield criterion. Plastic deformation was based on the associated flow rule. To examine the accuracy of the finite element model, simulations were performed with a linear-elastic half-space using different μ values. Figure 5.6 shows a smooth transition of the dimensionless pull-off force $\bar{P}_{off} = P_{off}/(-2\pi R\Delta\gamma)$ from the

DMT solution ($\bar{P}_{off}$ = 1) to the JKR solution ($\bar{P}_{off}$ = 0.75), which in good agreement with previous studies (Greenwood, 1997; Maguis, 1992).

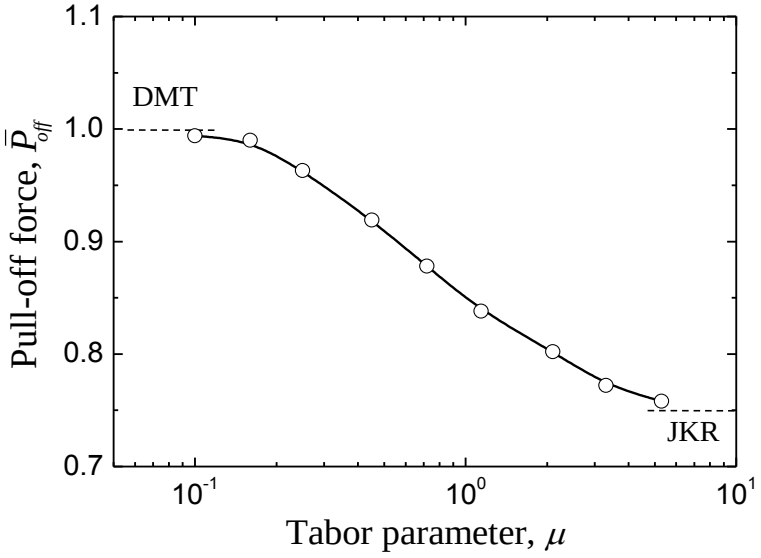

Figure 5.6. Pull-off force versus Tabor parameter.

5.4. Results and discussion

5.4.1. Elastic adhesive contact

Finite element simulations of elastic adhesive contact were performed to validate the elastic model and the predicted instabilities. In theory, the normal force-displacement response should exhibit an infinite slope at the instant of jump instability. However, an infinite slope in the force response cannot be captured in the finite element analysis because only one output (i.e., either normal force or surface gap) is known at any given time step. Therefore, a jump instability in the finite element simulations appears as abrupt increase or decrease in normal force accompanied by a large finite slope in the force-distance response.

As mentioned above, the geometrical relationship $x = x_o + r^2/2R$ can be used to estimate the surface gap when surface deformation is small, as prior to the commencement of jump-in. The validity of this assumption can be examined by considering the surface gap error x_{err} defined as

$$x_{err} = \frac{x_{FEM} - (x_o + r^2/2R)}{x_{FEM}} \tag{5.13}$$

where x_{FEM} is the surface gap obtained from the finite element analysis, which accounts for the effect of surface deformation.

Figure 5.7 shows x_{err} as a function of dimensionless radial distance $\bar{r} = r/\varepsilon$ for μ = 2.1. Because the maximum error is less than 6%, using the geometrical relationship $x = x_o + r^2/2R$ to calculate the surface gap before the occurrence of jump-in is an acceptable approximation. In addition to jump-in, Eq. (5.11) was also proven to hold in the case of jump-out instability, as evidenced by the good agreement between analytical predictions (small root of Eq. (5.11)) and finite element results.

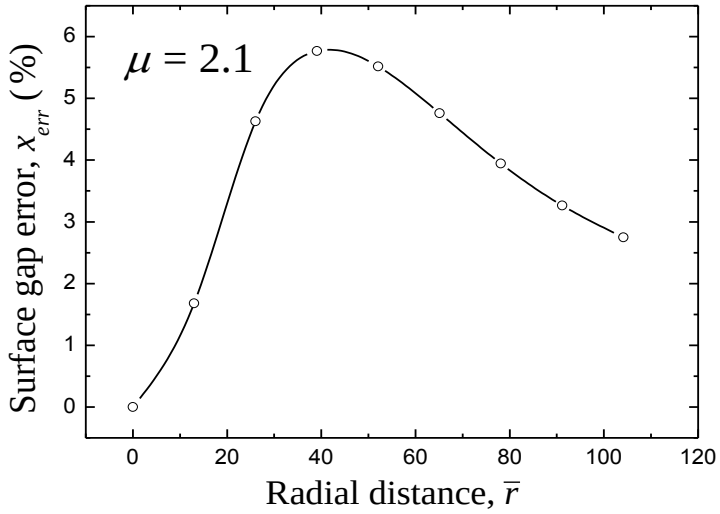

Figure 5.7. Surface gap error versus radial distance for μ = 2.1.

Figure 5.8 shows the variation of the central gap $\bar{x}_o$ with the dimensionless normal approach $\bar{\delta} = \delta/\varepsilon$ during the approach and retraction of the rigid sphere for different values of μ. A comparison of Figures. 5.8(a)–5.8(c) shows that the approach and retraction paths converge as μ decreases, in agreement with the elastic analysis. Figure 5.8(d) confirms the analytical prediction that neither jump-in nor jump-out occur when $\mu < \mu^*$ = 0.5 (Figure 5.3). In addition, the finding that the jump-in displacement is always larger than the jump-out displacement is in good agreement with experimental observations and can be explained by the analytical model. Jump-in is characterized by the sudden decrease in central gap, from the large root of Eq. (5. 11) to a value of ~1.0 ε corresponding to the maximum adhesive (attractive) force, whereas jump-out commences abruptly as soon as the smoothly increasing central gap reaches a value in the range of 1.1 ε –1.3 ε. Thus, jump-out always occurs at a smaller $\bar{\delta}$ than jump-in. Table 5.1 shows a comparison between analytical and finite element results of the critical central gap at the instant of jump-in versus the Tabor parameter. The close agreement between the predictions of the two methods confirms the validity of the elastic analysis presented in Sect. 5.2.

Tabor parameter (μ)	Dimensionless critical central gap ($\bar{x}_{o,c}$)	
	Analytical	FEM
0.16	–	–
0.72	1.7	1.6
1.14	2.1	2.1
2.10	2.7	2.8

Table 5.1. Comparison of analytical and finite element method (FEM) results of dimensionless critical central gap at the instant of jump-in for different values of Tabor parameter.

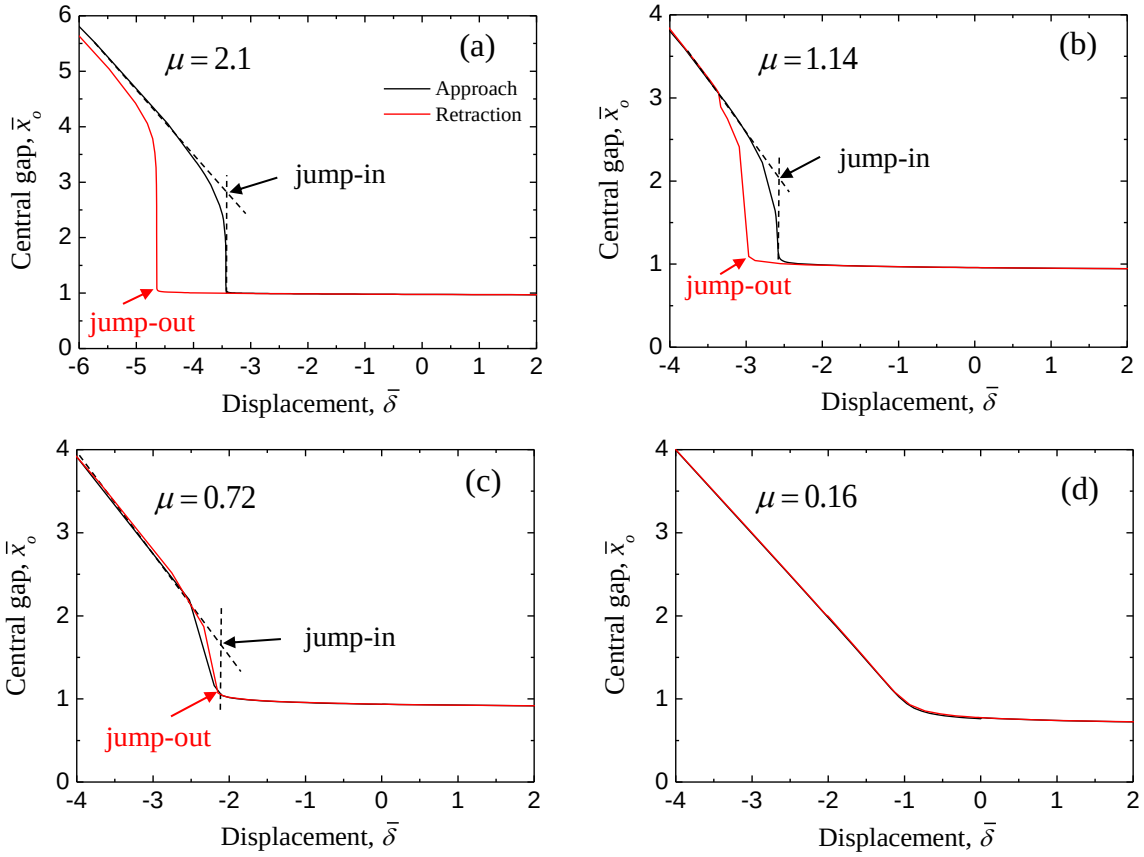

Figure 5.8. Central gap versus displacement for (a) μ = 2.1, (b) μ = 1.14, (c) μ = 0.72, and (d) μ = 0.16.

5.4.2. Elastic-plastic adhesive contact

Finite element results of elastic-plastic adhesive contact are presented in this section. In addition to the Tabor parameter μ that governs elastic adhesive contact, a plasticity parameter $\beta = \Delta\gamma/\varepsilon Y$ (Kadin et al., 2008a) and the dimensionless normal displacement $\bar{\delta}$ are used to analyze elastic-plastic adhesive contact.

Figure 5.9 shows the dimensionless normal force $\bar{P} = P/2\pi R\Delta\gamma$ and central gap $\bar{x}_o$ as functions of $\bar{\delta}$ for μ = 1.14, β = 1.67, and $\bar{\delta}_{max}$ = 6.67. As shown in Figure 5.9(a), the retraction path deviates from the approach path even at the onset of retraction and the pull-off force is about –2.5 $\pi R\Delta\gamma$, which is well above the pull-off force predicted by the JKR and DMT models. This is attributed to the partial recovery of the deformed surface after retraction because of plastic deformation in the half-space. Figure 5.9(b) shows that both jump-in and jump-out occurred in this simulation case, in agreement with the analytical prediction that both type of instability occur when $\mu > \mu^*$ = 0.5.

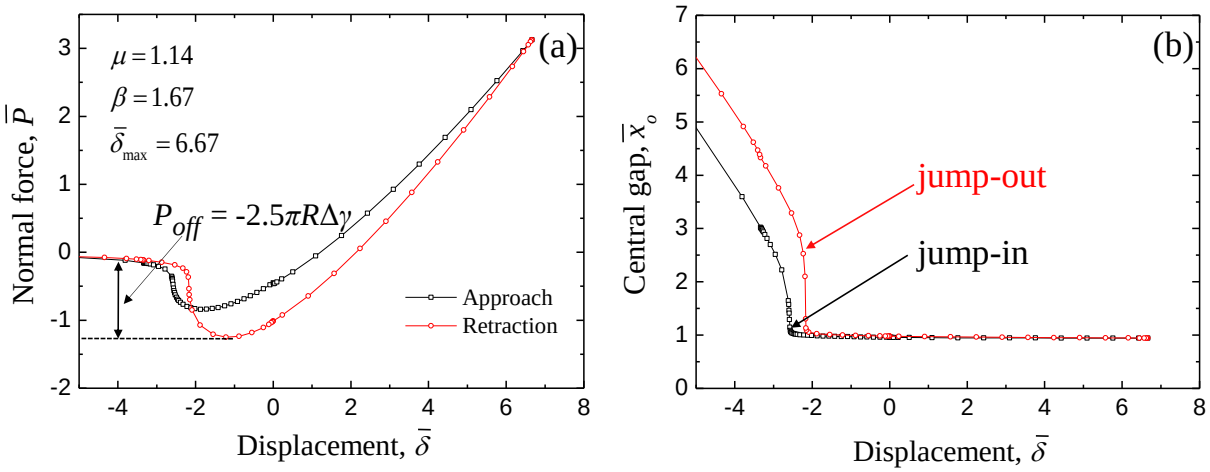

Figure 5.9. (a) Normal load and (b) central gap versus displacement for μ = 1.14, β = 1.67, and $\bar{\delta}_{max}$ = 6.67.

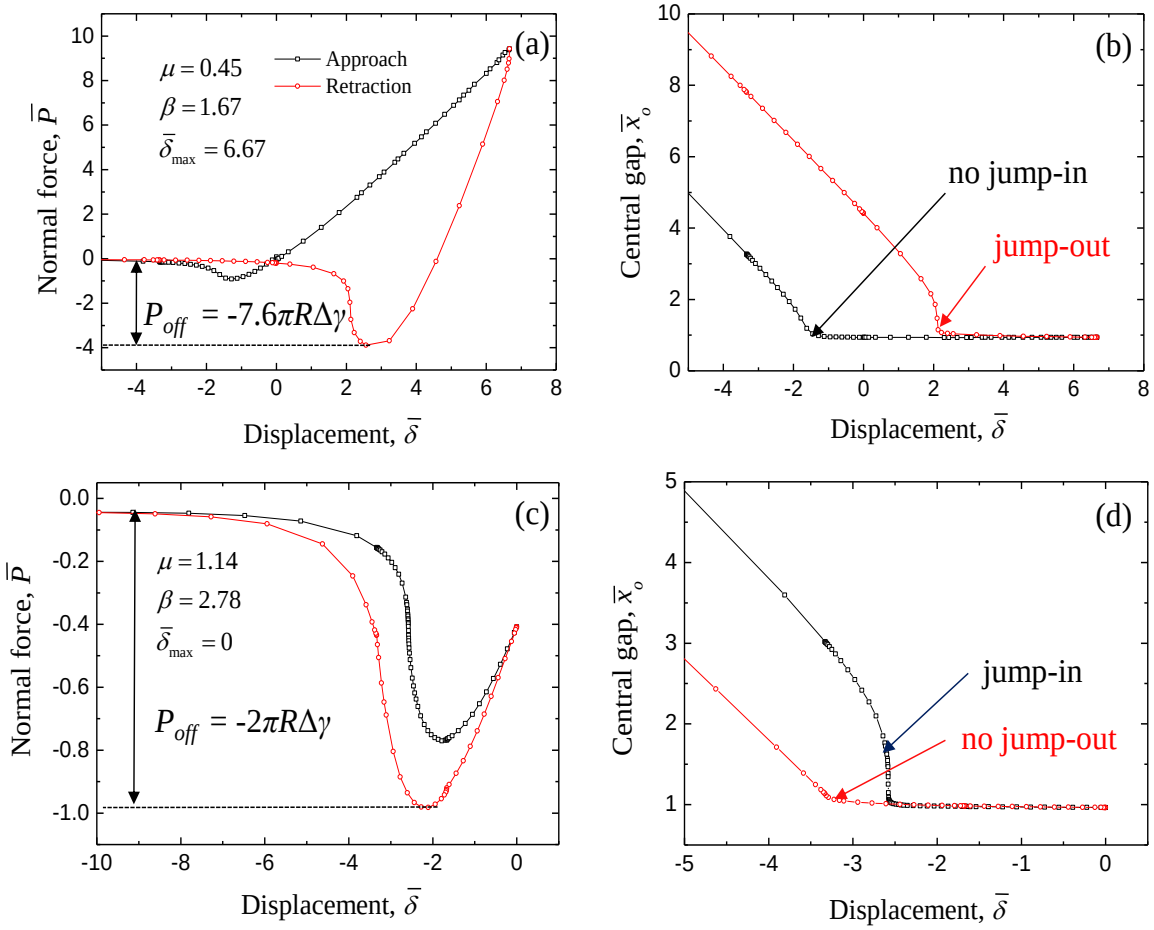

Figure 5.10. Normal load and central gap versus displacement for (a, b) μ = 0.45, β = 1.67, $\bar{\delta}_{max}$ = 6.67 and (c, d) μ = 1.14, β = 2.78, $\bar{\delta}_{max}$ = 0.

Figure 5.10 shows $\bar{P}$ and $\bar{x}_o$ as functions of $\bar{\delta}$ for the cases of μ = 0.45, β = 1.67, $\bar{\delta}_{max}$ = 6.67 and μ = 1.14, β = 2.78, $\bar{\delta}_{max}$ = 0. Figures. 5.10(a) and 5.10(c) show a pull-off force P_{off}= –7.6 $\pi R\Delta\gamma$ and –2 $\pi R\Delta\gamma$, respectively, i.e., larger than the pull-off force predicted by the elastic models of adhesive contact. The fact that the pull-off force in the second simulation case is not significantly higher than that predicted by elastic models is attributed to the dominance of elastic deformation because of the very small surface approach ($\bar{\delta}_{max}$ = 0) as compared to the first simulation case where deformation was predominantly plastic due to the much larger surface displacement ($\bar{\delta}_{max}$ = 6.67). Figure 5.10(b) shows that jump-in did not occur in the case of μ = 0.45, β = 1.67, and $\bar{\delta}_{max}$ = 6.67, which is consistent with the elastic prediction that jump instabilities cannot occur when $\mu < \mu^*$ = 0.5. However, the occurrence of jump-out is in disagreement with the elastic analysis. This discrepancy between elastic and elastic-plastic analysis is attributed to a decrease in the effective radius of curvature due to plastic deformation during surface approach, which increased the Tabor parameter above the threshold value (μ^* = 0.5).

As shown schematically in Figure 5.11(a), the formation of a residual impression during surface approach increases the radius of curvature from R to R_{eff} (Figure 5.11(a)), resulting in a higher Tabor parameter. Figure 5.10(d) shows an opposite trend for μ = 1.14, β = 2.78, and $\bar{\delta}_{max}$ = 0. In this case, only jump-in commenced because plastic deformation mostly occurred during retraction due to the relatively high plasticity parameter. The decrease in the radius of curvature from R to R_{eff} due to the development of a pile-up during retraction (Figure 5.11(b)) resulted in μ < 0.5. Thus, to interpret surface instabilities in elastic-plastic adhesive contacts, the Tabor parameter (Eq. (5.1)) must be modified to account for the effect of plastic deformation on the effective radius of curvature R_{eff} (Kadin et al., 2008b). For the two possible scenarios shown schematically in Figure 5.11, the corresponding effective Tabor parameter μ_{eff} is given by

$$\mu_{eff} \equiv \left(\frac{R_{eff}\Delta\gamma^2}{E^{*2}\varepsilon^3}\right)^{1/3} = \left[\frac{RR^*\Delta\gamma^2}{(R^*-R)E^{*2}\varepsilon^3}\right]^{1/3} \tag{5.14a}$$

$$\mu_{eff} \equiv \left(\frac{R_{eff}\Delta\gamma^2}{E^{*2}\varepsilon^3}\right)^{1/3} = \left[\frac{RR^*\Delta\gamma^2}{(R^*+R)E^{*2}\varepsilon^3}\right]^{1/3} \tag{5.14b}$$

where R^* is the radius of the plastically deformed surface. Significant differences in normal displacement at the instant of surface contact and separation (either smooth or abrupt) δ_c and δ_s, respectively, were observed in the previous two cases. In the case of μ = 0.45, β = 1.67, and $\bar{\delta}_{max}$ = 6.67, the formation of a residual impression (Figure 5.11(a)) resulted in $\delta_c < \delta_s$, whereas in the case of μ = 1.14, β = 2.78, and $\bar{\delta}_{max}$ = 0, pile-up formation (Figure 5.11(b)) resulted in $\delta_c > \delta_s$. These different behaviors are attributed to the evolution of plasticity during surface approach and retraction in the first and second simulation case, respectively. These trends cannot be observed in elastic adhesive contacts where $\delta_c \geq \delta_s$ always holds.

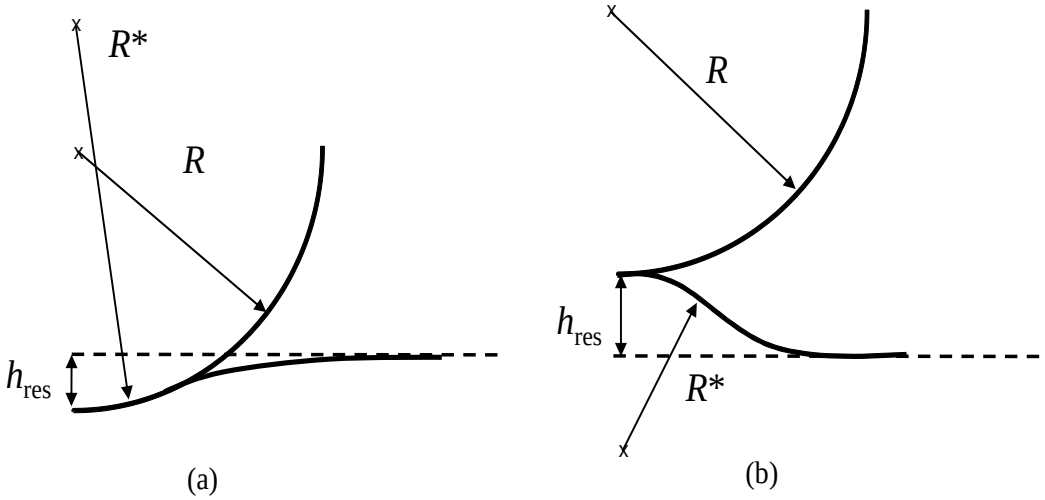

Figure 5.11 Schematics of (a) residual impression and (b) necking produced during surface approach and surface retraction, respectively.

The effect of the maximum normal displacement $\bar{\delta}_{max}$ can be interpreted in light of the approach-retraction curves shown in Figure 5.12 for μ = 1.14, β = 1.67, and different values of $\bar{\delta}_{max}$. Although all of the approach paths overlap, showing the occurrence of jump-in at a displacement $\delta_c \approx -2.5\varepsilon$ corresponding to a dimensionless maximum attractive force at the instant of contact $\bar{P}_c \approx 1.85$, the retraction paths demonstrate significant dependence on $\bar{\delta}_{max}$. For $\bar{\delta}_{max}$ = 0, 6.67, and 13.33, the dimensionless pull-off force is $\bar{P}_{off}$ = 1.85, 2.7, and 4.0, respectively. The trend for $\bar{P}_{off}$ and δ_s to increase with $\bar{\delta}_{max}$ is associated with plasticity intensification, resulting in higher R_{eff} due to the increase in residual depth h_{res} (Figure 5.11).

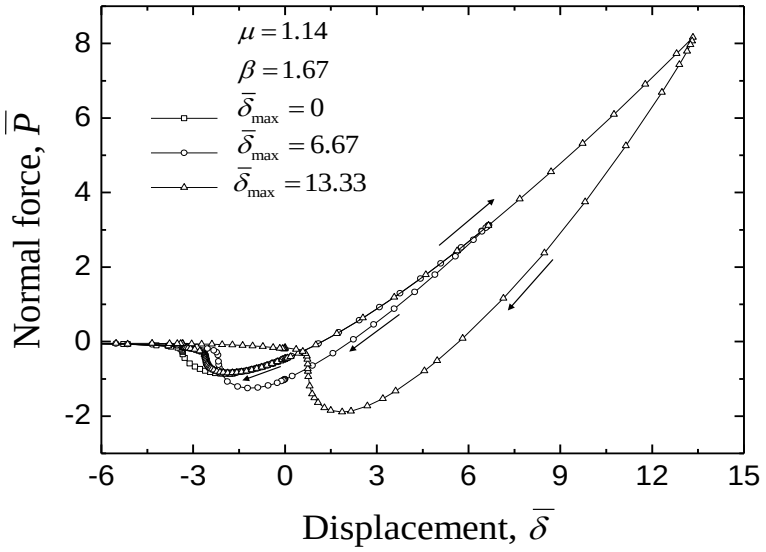

Figure 5.12. Normal load versus displacement for μ = 1.14, β = 1.67, and $\bar{\delta}_{max}$ = 0, 6.67, and 13.33.

Figure 5.13 shows the variation of the pull-off force $\tilde{P}_{off} = log\left(P_{off}^{ep}/P_{off}^{e}\right)$ with the maximum normal displacement $\tilde{\delta}_{max} = (\delta_{max}/\delta_Y) - 1$, where P_{off}^{ep} and P_{off}^{e} are the pull-of forces of elastic-plastic and elastic adhesive contacts, respectively, and δ_Y is the normal displacement at the inception of yielding, for μ = 1.14 and β = 1.67. The numerical data shown in Figure 5.13 reveal a linear dependence of $\tilde{P}_{off}$ on $\tilde{\delta}_{max}$. Thus, curve fitting the data shown of Figure 5.13 yields the following exponential relationship of the pull-off force of elastic-plastic adhesive contacts:

$$P_{off}^{ep} = P_{off}^{e} e^{0.041\tilde{\delta}_{max}} \tag{5.15}$$

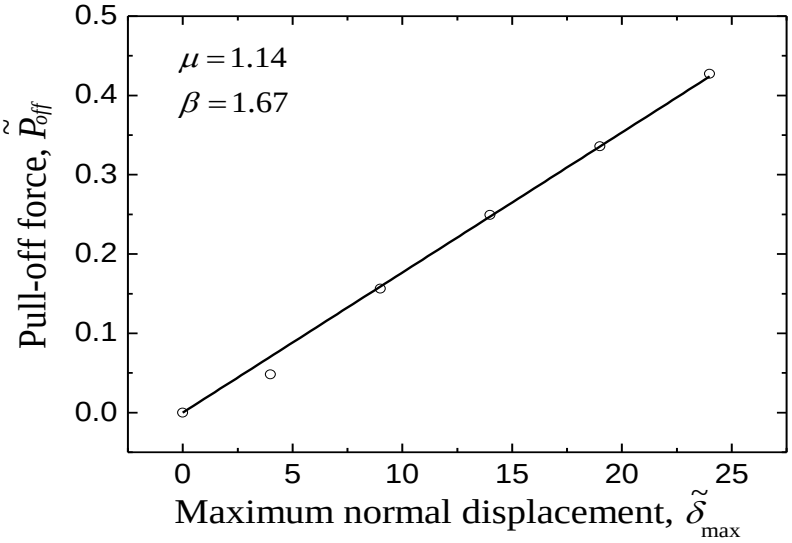

Figure 5.13. Pull-off force versus maximum normal displacement for μ = 1.14 and β = 1.67.

Figure 5.14 shows the variation of the dimensionless normal force $\bar{P}$ with the dimensionless normal displacement $\bar{\delta}$ in four consecutive approach-retraction cycles of three representative cases. (A cycle consists of an approach and a retraction half-cycle.) For μ = 1.14, β = 1.67, and $\tilde{\delta}_{max}$= 6.67, plastic deformation occurred only in the first half-cycle, as indicated by the overlap of all subsequent responses (Figure 5.14(a)), implying elastic shakedown at steady-state. This elastic shakedown differs from classical elastic shakedown, where the coincidence of the loading and unloading paths signifies the absence of energy dissipation. In the present case, the force hysteresis due to the jump instabilities indicates the occurrence of energy dissipation. In the finite element simulations, the dissipated energy was removed from the system by a stabilizing algorithm that uses artificial damping to compensate for local instabilities. However, because the force hysteresis due to such surface instabilities is intrinsically different from that due to excessive plastic deformation and the force hysteresis loops retrace each other after the first half-cycle, the cyclic behavior shown in Figure 5.14(a) may be classified as elastic shakedown in adhesive contacts. A different behavior was found in the second simulation case of μ = 0.45, β = 1.67, and $\tilde{\delta}_{max}$ = 6.67 (Figure 5.14(b)). Although jump-in did not occur in the first half-cycle (expected since μ < 0.5), both jump-in and jump-out instabilities occurred in

subsequent half-cycles because the residual impression generated in the first half-cycle increased the effective Tabor parameter above the threshold (i.e., $\mu_{eff} > 0.5$, Eq. 5.14(a)). The stable and non-overlapping approach and retraction paths in following half-cycles reveal a steady-state behavior that resembles plastic shakedown. The development of a force hysteresis with increasing number of cycles is also evident in Figure 5.14(c) for the case of $\mu = 1.14$, $\beta = 2.78$, and $\bar{\delta}_{max} = 0$. However, in contrast to the results shown in Figure 5.14(b), jump-in occurred in the first half-cycle, whereas neither jump-in nor jump-out were encountered in subsequent half-cycles. The effect of plasticity parameter on shakedown behavior can be understood by comparing the results shown in Figures. 14(a) and 14(c), which are for $\mu = 1.14$. For relatively low plasticity parameter ($\beta = 1.67$), elastic shakedown occurred even for a relatively large maximum normal displacement ($\bar{\delta}_{max} = 6.67$), while for high plasticity parameter ($\beta = 2.78$), plastic shakedown occurred even for a very small maximum normal displacement ($\bar{\delta}_{max} = 0$) because of the low yield strength of the material. In contrast to an earlier study (Kadin et al., 2008b) where elastic and plastic shakedown was predicted only for isotropic and kinematic strain hardening, respectively, the present study shows that both elastic and plastic shakedown may occur even with elastic-perfectly plastic materials, depending on the plasticity parameter.

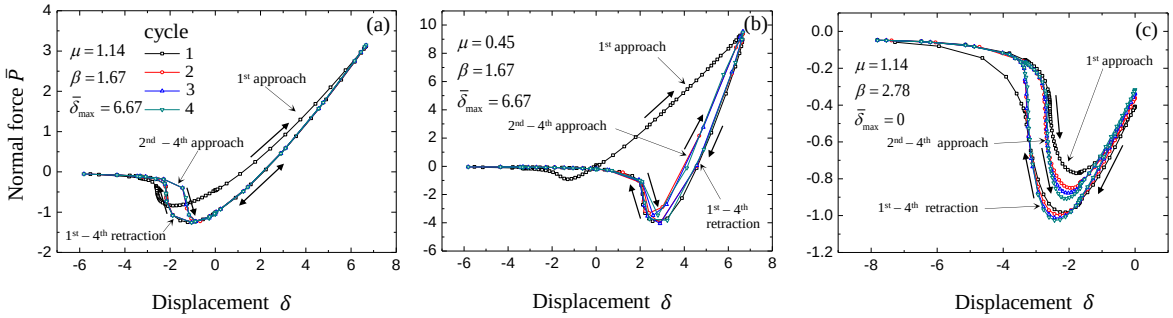

Figure 5.14 Normal load versus displacement for four complete approach-retraction cycles: (a) $\mu = 1.14$, $\beta = 1.67$, $\bar{\delta}_{max} = 6.67$, (b) $\mu = 0.45$, $\beta = 1.67$, $\bar{\delta}_{max} = 6.67$, and (c) $\mu = 1.14$, $\beta = 2.78$, $\bar{\delta}_{max} = 0$.

Figure 5.15 shows contours of equivalent plastic strain $\bar{\varepsilon}_p$ in the half-space subsurface for $\mu = 1.14$, $\bar{\delta}_{max} = 0$, and different β values. For relatively low plasticity parameter ($\beta = 1.67$), only elastic deformation occurred and the flatness of the half-space surface was fully recovered upon surface separation (Figure 5.15(a)). For intermediate plasticity parameter ($\beta = 2.78$), plastic deformation evolved during both approach and retraction half-cycles, resulting in neck formation during surface retraction (Figure 5.15(b)). For high plasticity parameter ($\beta = 4.17$), necking intensified significantly, causing sharp displacement gradients at the neck edge that induced severe localized deformation, e.g., $\bar{\varepsilon}_p = 1.6$ near the neck edge (Figure 5.15(c)). Complete separation of the rigid sphere from the half-space was not simulated in this case due convergence problems associated with excessive element distortion due to strong adhesion of the neck to the sphere. Material transfer to indenter surfaces due to high adhesive forces is often observed and has also been captured in molecular dynamics studies (Song and Sorolovitz, 2006). The excessive plastic deformation shown in Figure 5.15(c) suggests that subsurface microcracking parallel to the surface and/or perpendicular to the surface at the neck edge are possible failure

processes. Propagation of these cracks in adhesive contacts due to cyclic loading may eventually result in the transfer of detached material to the rigid sphere after complete surface separation.

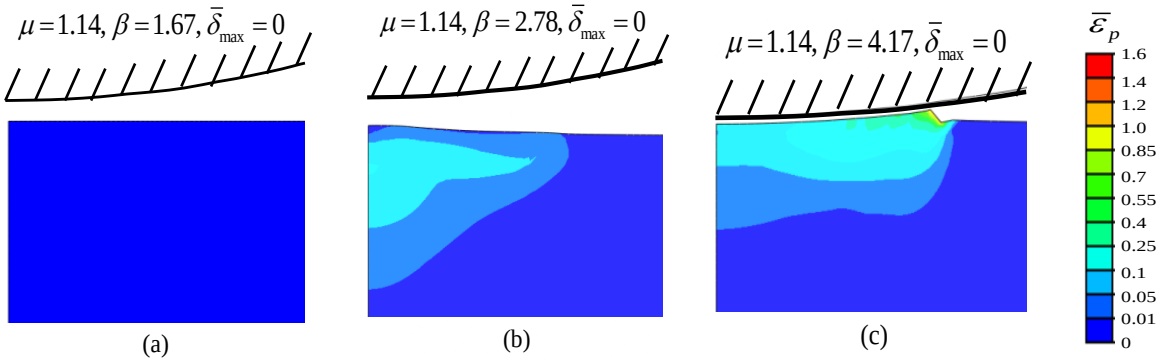

Figure 5.15. Contours of equivalent plastic strain in the subsurface of an elastic-plastic half-space for μ = 1.14 and $\bar{\delta}_{max}$ = 0: (a) β = 1.67, (b) β = 2.78, and (c) β = 4.17. Contours in (a) and (b) are at the instant of surface separation (jump-out), whereas contours in (c) are due to stretching of a neck strongly adhered to the retracting rigid sphere.

5.5 Conclusions

A continuum mechanics model of adhesive surface interaction which accounts for contact instabilities during surface approach (jump-in) and surface retraction (jump-out) was developed in this study. Interfacial adhesion was represented by the L-J potential. A criterion of jump-in and jump-out in elastic adhesive contacts was derived from geometry considerations using the surface displacements of the elastically deformed half-space. For elastic deformation, the critical central gap at the instant of jump instabilities was obtained implicitly in terms of the Tabor parameter, using an elastic solution of the surface displacements. The critical central gap at the instant of jump-in increased with the Tabor parameter, whereas the critical central gap at the instant of jump-out decreased slightly in the range of 1.1ε–1.3ε. According to the elastic analysis, neither type of instability should occur below a threshold value of the Tabor parameter $\mu^* = 0.5$, which is less than the threshold $\mu^* = 1$ predicted in earlier studies. This discrepancy is attributed to differences in the apparatus stiffness, i.e., $\mu^* = 1$ for infinitely stiff apparatus (earlier studies) and $\mu^* = 0.5$ (or even less) for finite stiffness apparatus (present study).

A finite element model of a rigid sphere and an elastic or elastic-plastic half-space was used to analyze elastic and elastic-plastic adhesive contact behavior. Surface interaction was modeled by nonlinear springs that obeyed a force-displacement relationship governed by the L-J potential. The finite element model was validated by the JKR and DMT models. Simulation results yielded a smooth transition of the pull-off force between JKR and DMT estimates. The good agreement between analytical and finite element predictions for the jump instabilities and results of the critical central gap at the instant of these instabilities validated the analysis of elastic adhesive contact.

Finite element simulations of elastic-plastic adhesive contact performed for different values of Tabor parameter, maximum normal displacement, and plasticity parameter showed

higher pull-off forces for elastic-plastic adhesive contacts than those predicted by JKR and DMT elastic contact models because plastic deformation inhibited full recovery of the half-space after surface retraction. Curve fitting of finite element results showed that the pull-off force of elastic-plastic adhesive contacts is an exponential function of the maximum normal displacement. Two interesting behaviors were observed with elastic-plastic adhesive contacts. For relatively low Tabor parameter and intermediate plasticity parameter, surface approach was characterized by a smooth path, while the surface retraction path was disrupted by a jump-out instability caused by the decrease in effective radius of curvature due to a residual impression formed during surface approach. Alternatively, for intermediate Tabor parameter and large plasticity parameter, jump-in occurred during surface approach, while surface retraction followed a smooth path because necking prevented jump-out.

Repetitive adhesive contact was studied by simulating four complete approach-retraction cycles for different values of Tabor parameter, maximum normal displacement, and plasticity parameter. High Tabor parameter and low plasticity parameter resulted in elastic shakedown, as opposed to low Tabor parameter and high plasticity parameter that led to plastic shakedown. Surface separation demonstrated a strong dependence on plasticity parameter. High plasticity parameter enhanced necking, which, in turn, caused a transition from abrupt to smooth surface separation.

Chapter 6

Adhesive Contact of Elastic-Plastic Layered Media: Effective Tabor Parameter and Mode of Surface Separation

6.1. Introduction

In chapter 5, we have successfully implemented spring elements of prescribed force-displacement relationship derived from Lennard-Jones (LJ) potential into finite element model and analyzed the contact instabilities for homogeneous elastic-plastic half-space; however, in most of the MEMS devices, if not all, the surfaces exposed to mechanical contact are protected by an intentionally deposited hard layer, in order to improve the tribological performance and mechanical robustness of the device. Precise stress analysis of layered media is critical to the longevity of contact-mode mechanical systems. Both theoretical and numerical analyses have been carried out for various elastic-plastic contact systems (Komvopoulos et al., 1987; O'Sullivan and King, 1988; Komvopoulos, 1988; Kral et al., 1995a; Kral et al., 1995b; Li and Chou, 1997). However, because real contact interfaces demonstrate multi-scale roughness, the overall contact behavior may be strongly affected by adhesion forces arising at asperity microcontacts. Therefore, accurate analysis of contact deformation and failure mechanisms of layered media requires mechanistic models that take into account adhesion effects encountered at the asperity microcontact level.

Pioneering studies of adhesive contact between elastic solids have been performed by Johnson et al. (1971) and Derjaguin et al. (1975), who are credited for the development of two widely used adhesive contact models of elastic spheres, known as the JKR and DMT models, respectively. These models give that the force at the instant of separation of two adhering spheres of radius R_1 and R_2 (referred to as the pull-off force P_{off}) is equal to $-1.5\pi R\Delta\gamma$ (JKR) and $-2\pi R\Delta\gamma$ (DMT), where $R = R_1R_2/(R_1 + R_2)$ is the reduced radius of curvature and $\Delta\gamma = \gamma_1 + \gamma_2 - \gamma_{12}$ is the work of adhesion (γ_1 and γ_2 are the surface energies of the two spheres and γ_{12} is the interfacial energy). Hereafter, an attractive surface force between interacting solids is designated as a negative force. Tabor (1977) interpreted the JKR and DMT models in terms of a dimensionless parameter μ, known as the Tabor parameter, given by

$$\mu = \left(\frac{R\Delta\gamma^2}{E^{*2}\varepsilon^3}\right)^{1/3} \tag{6.1}$$

where $E^* = [(1 - \nu_1{}^2)/E_1 + (1 - \nu_2{}^2)/E_2]^{-1}$ is the effective elastic modulus (symbols E and ν represent elastic modulus and Poisson's ratio, respectively) and ε is the interatomic equilibrium distance, typically on the order of a few angstroms. Tabor argued that the JKR model is suitable for compliant surfaces and relatively large radius of curvature (i.e., $\mu > 5$), whereas the DMT model is more appropriate for stiff surfaces and small radius of curvature (i.e., $\mu < 0.1$).

Maguis (1992) used the Dugdale approximation to model surface adhesion and obtained a solution of P_{off} in the transition range $0.1 < \mu < 5$, bounded by the DMT and JKR solutions.

Using the solution obtained by Maugis and a curve fitting method, Carpick et al. (1999) expressed P_{off} in terms of λ ($\lambda = 1.16\,\mu$). Wu (2008) used the same curve fitting method and a traction-separation law based on the Lennard-Jones (LJ) potential (1992), similar to that derived by Muller et al. (1980), Greenwood (1997), and Feng (2001), and obtained a numerical solution of P_{off} similar to that reported by Carpick et al.

In contemporary contact mechanics studies, surface adhesion has been represented by nonlinear spring elements with a force-displacement constitutive relation obeying traction-separation laws derived from the LJ potential (Du et al., 2007; Song and Komvopoulos, 2011) Incorporating these spring elements into finite element method (FEM) models has allowed for elastic-plastic adhesive contacts, observed under different experimental settings (Maugis and Pollock, 1984; Wang et al., 2010), to be analyzed numerically. For example, it was shown (Song and Komvopoulos, 2011; Kadin et al., 2008) that in the presence of plasticity, P_{off} can be significantly higher than that predicted by the JKR and DMT models.

Contact instabilities caused by surface adhesion are common phenomena in microprobe-based measurements and dynamic micromachines. Approach and retraction of two elastic spheres may occur smoothly ($\mu \leq 1$) or abruptly ($\mu > 1$) (Greenwood, 1997), depending on surface and bulk material properties and contact geometry. According to the study of Greenwood (1997), the critical Tabor parameter for the transition from continuous (stable) to discontinuous (unstable) elastic contact behavior (such as instantaneous surface contact (jump-in) and detachment (jump-out) during surface approach and retraction, respectively) is $\mu_c = 1.0$. This is also supported by studies of adhesive spherical contacts of Feng (2001) and Kadin et al. (2008). However, analytical results of Song and Komvopoulos (2011) show that for a rigid sphere interacting with a semi-infinite elastic medium $\mu_c = 0.5$ and, in addition to the Tabor parameter, contact instabilities (especially jump-out) can be affected by the accumulation of plasticity. For example, excessive plastic deformation in an elastic-plastic half-space due to normal contact with a rigid sphere results in smooth surface detachment (i.e., no jump-out) even for $\mu > \mu_c$.

Sridhar et al. (1997) obtained FEM solutions of the adhesion force for a wide range of contact radius, layer thickness, and elastic material properties and observed a strong dependence of P_{off} on dimensionless adhesion parameter $\alpha = 2R^2\Delta\gamma/E^*t^3$, where E^* is the effective elastic modulus of the layered medium and t is the layer thickness. Based on the former study, Johnson and Sridhar (2001) examined adhesion effects at the scale of atomic force microscope measurements, while Sridhar and Sivashanker (2004) analyzed adhesive indentation of a multi-layered medium. Sergici et al. (2006) used the Dugdale approximation to study the effects of layer thickness, layer-to-substrate elastic modulus ratio, and Maugis parameter on the constitutive relation of a layered medium in frictionless contact with a spherical indenter. Perriot and Barthel (2004) developed a quasi-analytical method for studying adhesionless contact of a layered medium, and later extended this method to study adhesive contact of elastic layered media and the dependence of various contact parameters on substrate inhomogeneity (2007). Based on the FEM model of Du et al. (2007), Eid et al. (2011) analyzed elastic-plastic adhesive contact of a rigid plate with a gold hemisphere coated with a thin ruthenium layer and reported a dependence of the adhesion force and contact radius on the layer thickness and maximum contact displacement (maximum compressive force).

The present study uses an FEM model to analyze adhesive contact of a rigid sphere with an elastic layer attached to an elastic-perfectly plastic substrate. Contact instabilities during surface approach (loading) and retraction (unloading) are interpreted in terms of the effective Tabor parameter, which depends on the layer thickness (substrate effect) and elastic properties of the layer and substrate materials. The effects of surface and bulk material properties (e.g., work of adhesion, elastic modulus, and yield strength), layer thickness, and maximum surface separation on the contact behavior of layered media with an elastic layer stiffer than the substrate are analyzed in the context of numerical results. Brittle- and ductile-like modes of surface separation (detachment) are discussed for a wide range of plasticity parameter and maximum surface separation. Simulations of cyclic adhesive contact provide insight into the accumulation of plasticity and propensity for delamination at the layer/substrate interface or in the bulk of the substrate due to repeated adhesive contact loading and unloading.

6.2 Finite element model

Figure 6.1(a) shows a rigid sphere of radius R in close proximity with a layered medium consisting of an elastic layer of thickness t and a semi-infinite elastic-plastic substrate. The layered medium is shown displaced in the z-direction due to the effect of adhesion. Because of symmetry, the maximum deflection of the layered medium h_o occurs at $r = 0$. Figure 6.1(b) shows the axisymmetric FEM model used in this study. The layer and the substrate are modeled by 4096 and 26656 axisymmetric, four-node, linear, isoparametric elements consisting of 4618 and 27170 nodes, respectively. The nodes at the bottom boundary of the mesh and the axis of symmetry ($r = 0$) are constrained against displacement in the z- and r-direction, respectively. The distance between two adjacent nodes in the layer mesh is equal to ~$0.003R$. Surface adhesion is modeled by nonlinear spring elements obeying a traction-separation law derived from the LJ potential. More details about the nonlinear spring elements used in the present FEM model can be found elsewhere (Song and Komvopoulos, 2011). At any simulation stage, the layer/substrate interface is modeled as a continuous interface, i.e., no separation or relative slip due to normal and shear stresses arising at the interface. All quasi-static simulations were performed with the multi-purpose FEM code ABAQUS/Standard (version 6.9EF), using an implicit solver.

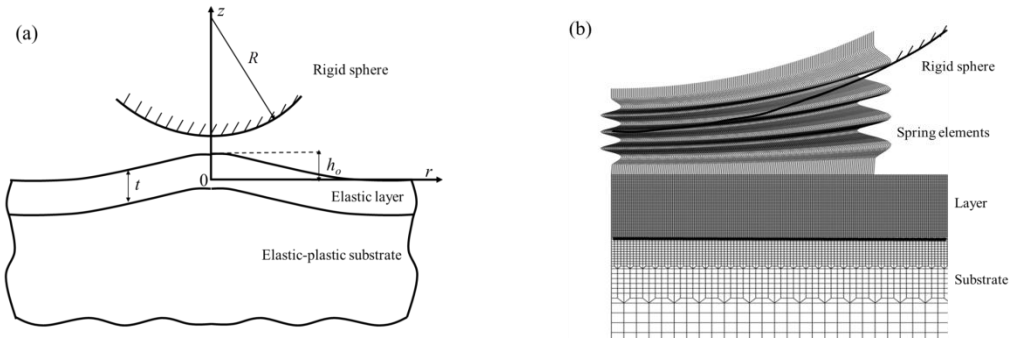

Figure 6.1 (a) Schematic showing a rigid sphere of radius R in close proximity with a layered medium consisting of an elastic layer of thickness t and an elastic-plastic substrate (center deflection h_o is due to an adhesion (attractive)

surface force) and (b) finite element mesh of the layered medium, showing the nonlinear spring elements used to model interfacial adhesion.

To confirm the validity of the FEM mesh and modeling assumptions, adhesive contact between a rigid sphere and a layered medium consisting of a rigid substrate and an elastic layer of fixed elastic modulus (E_l = 20 GPa) and dimensionless thickness $\bar{t} = t/\varepsilon$ varied in the range of 4–152 was examined first. Figure 6.2 shows a continuous variation of the dimensionless pull-off force $\bar{P}_{off} = P_{off}/2\pi R\Delta\gamma$ with the layer thickness $\bar{t}$. For $\bar{t}\rightarrow 1$, the problem reduces to that of a rigid sphere in adhesive contact with a rigid half-space, for which the FEM solution approaches asymptotically to –1.0 (DMT solution). Alternatively, for $\bar{t} > 10^2$, the problem can be approximated by that of a rigid sphere in adhesive contact with an elastic half-space, and the FEM solution approaches asymptotically to –0.79, which is the solution for an elastic half-space with elastic modulus equal to that of the layer. The results shown in Figure 6.2 indicate that the present FEM model is suitable for analyzing adhesive contact of layered media.

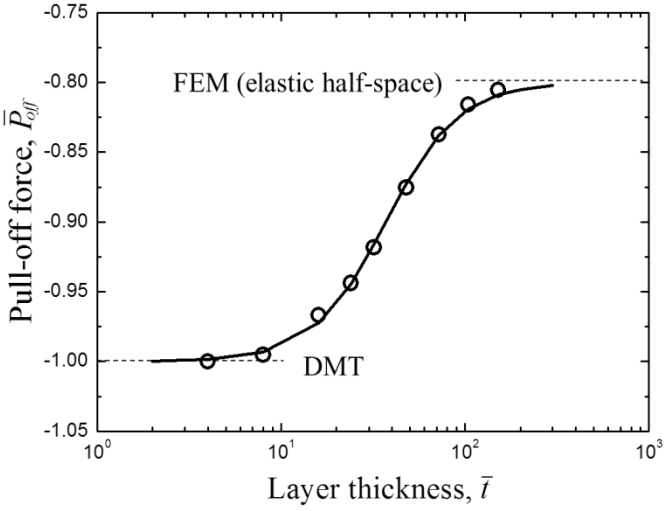

Figure 6.2 Pull-off force $\bar{P}_{off}$ versus layer thickness $\bar{t}$ for a layered medium consisting of an elastic layer of E_l = 20 GPa and a rigid substrate.

6.3 Results and discussion

Numerical results from displacement-controlled quasi-static simulations are interpreted in this section in terms of dimensionless parameters, such as layer-to-substrate elastic modulus ratio $\boldsymbol{E_l/E_s}$, plasticity parameter $\boldsymbol{\beta = \Delta\gamma/\varepsilon Y_s}$ (where $\boldsymbol{Y_s}$ is the substrate yield strength), effective Tabor parameter $\boldsymbol{\mu_{eff}}$ (introduced in section 6.3.1), layer thickness $\boldsymbol{\bar{t}}$, and maximum surface separation (interaction distance) $\boldsymbol{\delta_{max} = \delta/\varepsilon}$. In addition, to obtain general solutions, surface forces were normalized by $\boldsymbol{2\pi R\Delta\gamma}$, while all dimensions were normalized by $\boldsymbol{\varepsilon}$, except the residual center height $\boldsymbol{h_{o,r}}$ which was normalized by $\boldsymbol{t}$.

6.3.1. Substrate Effect and Effective Tabor Parameter

The Tabor parameter is a dimensionless quantity representing the height of the elastic pile-up (neck) produced by an adhesion force during surface retraction (unloading) divided by a characteristic length of adhesion, such as the interatomic equilibrium distance. Therefore, the Tabor parameter is a governing parameter of adhesive elastic contact. Figure 6.3 shows FEM results of the center deflection $\bar{h}_o = h_o/\varepsilon$ before surface separation (detachment) as a function of μ for a rigid sphere interacting with a homogeneous elastic half-space. From a linear fit through the FEM data, it follows that

$$\bar{h}_o = 1.63\mu \tag{6.2}$$

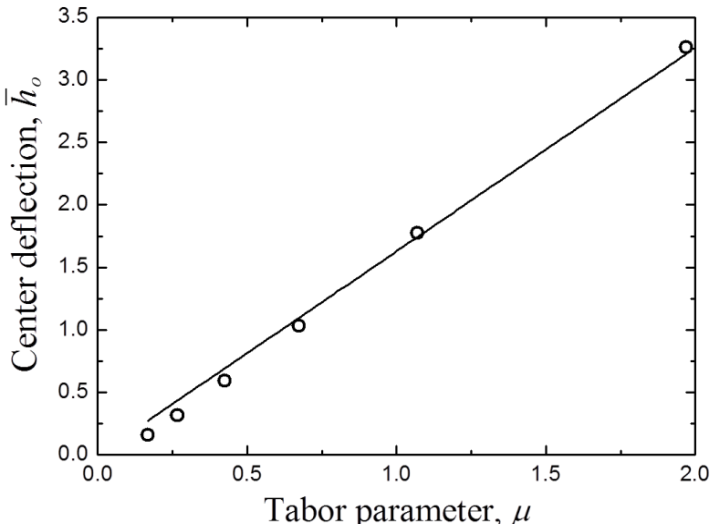

Figure 6.3 Center deflection before surface separation $\bar{h}_o$ versus Tabor parameter μ for homogeneous elastic half-space.

Equation (6.2) cannot be used for layered media because it does not account for the effect of the layer thickness and mechanical properties. To obtain an effective Tabor parameter μ_{eff} for layered media, a series of adhesive contact simulations were performed for a rigid sphere and a layered medium with layer-to-substrate elastic modulus ratio E_l/E_s in the range of 2.5–40, layer thickness $\bar{t}$ between 4 and 152, and fixed substrate elastic modulus (E_s= 20 GPa). An effective Tabor parameter was calculated for each simulation case by substituting the obtained value of $\bar{h}_o$ into Eq. (6.2). The effective Tabor parameter should be bounded by the Tabor parameters corresponding to a half-space with elastic modulus equal to E_l and E_s, denoted by μ_l and μ_s, respectively. The effect of the substrate on μ_{eff} is represented by the dimensionless parameter θ, defined as

$$\theta = \frac{\mu_{eff}-\mu_l}{\mu_s-\mu_l} \qquad (0 \leq \theta \leq 1) \tag{6.3}$$

Equation (6.3) indicates that the higher the value of θ the stronger the substrate effect. Extreme values of θ represent trivial cases of homogeneous half-spaces with layer (θ = 0) and substrate (θ = 1) material properties. Figure 6.4 shows the dependence of the substrate effect

(indicated by θ) on the layer thickness $\bar{t}$ for E_l/E_s in the range of 2.5–40. As expected, the substrate effect decreases nonlinearly with increasing layer thickness, and this trend becomes more pronounced with increasing E_l/E_s. The more rapid transition from substrate- to layer-controlled contact behavior observed with higher E_l/E_s values is attributed to the layer stiffness effect. For fixed E_s and $\bar{t}$, the overall contact stiffness increases with E_l/E_s, resulting in less upward deflection of the layered medium due to the adhesion force exerted by the rigid sphere. Smaller surface vertical displacement implies smaller substrate effect. Similar to normalizing the contact radius with the layer thickness to obtain a general relation for the effective elastic modulus of layered media (King, 1987), the dimensionless maximum layer deflection at $r = 0$, hereafter referred to as the center layer deflection ξ, defined as

$$\xi = \frac{\varepsilon\, \mu_{eff}}{t} = \frac{\mu_{eff}}{\bar{t}} \tag{6.4}$$

can be introduced to study the substrate effect on the overall contact behavior of layered media.

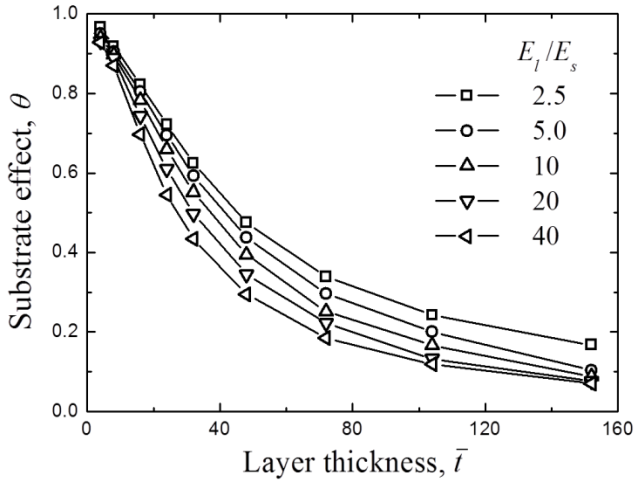

Figure 6.4 Substrate effect θ versus layer thickness $\bar{t}$ for elastic layered medium with E_l/E_s in the range of 2.5–40.

Figure 6.5 shows the variation of θ with ξ for a wide range of E_l/E_s. Curve fitting of the numerical data shown in Figure 6.5 yields,

$$\theta = \frac{30\xi}{1+30\xi} \tag{6.5}$$

Equations (6.3)–(6.5) lead to the following relation of the effective Tabor parameter of layered media with a layer stiffer than the substrate:

$$\mu_{eff} = \frac{1}{2}\left(\mu_s - \frac{\bar{t}}{30}\right) + \left[\frac{1}{4}\left(\mu_s - \frac{\bar{t}}{30}\right)^2 + \mu_l\left(\frac{\bar{t}}{30}\right)\right]^{1/2} \tag{6.6}$$

For a homogeneous elastic half-space ($\mu_l = \mu_s$), Eq. (6.6) reduces to $\mu_{eff} = \mu_l = \mu_s$, while for a layered medium with very thin or thick layer, Eq. (6.6) shows that $\mu_{eff}|_{\bar{t}\to 0} \to \mu_s$ and $\mu_{eff}|_{\bar{t}\to\infty} \to \mu_l$, respectively.

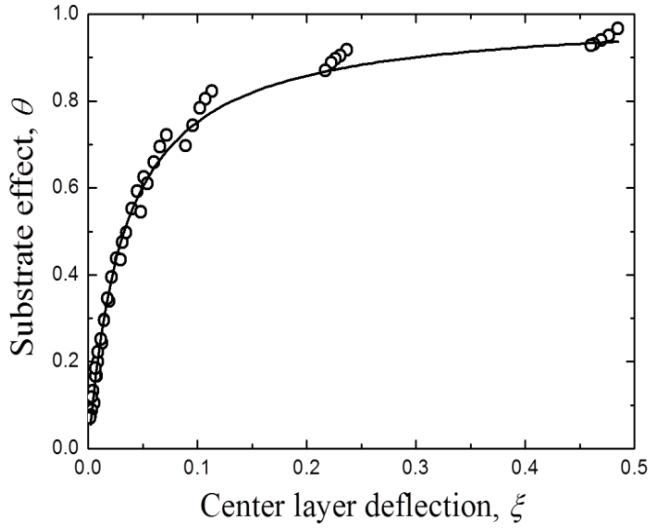

Figure 6.5 Substrate effect θ versus center layer deflection ξ for elastic layered medium having a wide range of E_l/E_s.

6.3.2. Effect of Plasticity Parameter

To elucidate adhesive contact of layered media, FEM simulations were performed for relatively wide ranges of E_l/E_s, β, $\bar{t}$, and $\bar{\delta}_{\max}$. Figure 6.6(a) shows the surface force $\bar{P} = P/2\pi R\Delta\gamma$ as a function of surface separation $\bar{\delta} = \delta/\varepsilon$ during a full loading cycle for E_l/E_s = 10, β = 33.3, $\bar{t}$ = 8, and $\bar{\delta}_{\max}$ = 3.33, 10, and 16.67, while Figure 6.6(b) shows corresponding residual surface height distributions that provide information about the shape and size of the residual protrusion (neck) obtained after surface detachment. The increase of $\bar{P}_{off}$ with $\bar{\delta}_{\max}$ is attributed to the increase in substrate plasticity that enhanced the surface conformity at the sphere/layer interface. Under the displacement-control conditions of this study, the rigid sphere did not detach from the elastic layer at the instant of $\bar{P}_{off}$. Instead, the adhesion surface force continued to decrease smoothly with the incremental retraction of the rigid sphere up to a critical surface separation when it abruptly reduced to zero, indicating the commencement of surface detachment (jump-out). It can be seen that the surface force at the instant of jump-out, termed the separation force $\bar{P}_{sep}$, is independent of $\bar{\delta}_{\max}$. This can be attributed to the similar radius of curvature (i.e., similar R_{eff}) of the summits of corresponding residual surface profiles (Figure 6.6(b)). The increase in residual surface height $\bar{h}_r = h_r/\varepsilon$ with $\bar{\delta}_{\max}$ seen in Figure 6.6(b) indicates more necking during unloading, suggesting that surface detachment exhibited an increasingly more ductile-like behavior with the increase of $\bar{\delta}_{\max}$.

To examine the plasticity parameter effect on contact deformation, FEM simulations were performed with a layered medium of lower plasticity parameter (β = 6.67) than that in Figure 6.6 and identical all other parameters. Compared to the case of β = 33.3, significantly different

plastic deformation behavior occurred during unloading for β = 6.67. Surface separation at the instant of jump-out increased (Figure 6.7(a)) and the residual surface profile changed from concave to convex (Figure 6.7(b)) with the decrease in $\bar{\delta}_{\max}$. In addition, it is difficult to identify $\bar{P}_{sep}$ in the unloading responses shown in Figure 6.7(a). Instead of necking during unloading leading to the formation of a tall pile-up (neck) (Figure 6.6(b)), a residual impression was produced for $\bar{\delta}_{\max}$ = 10 and 16.67 and a very shallow pile-up for $\bar{\delta}_{\max}$ = 3.33 (Figure 6.7(b)). Because lack of necking during tensile stretching is considered to be indicative of brittle behavior, the residual surface profiles shown in Figure 6.7(b) reveal increasingly more brittle-like behavior of surface detachment with increasing $\bar{\delta}_{\max}$. Furthermore, the concavity of the residual impressions for $\bar{\delta}_{\max}$ = 10 and 16.67 and the merely flat summit surface of the shallow pile-up produced for $\bar{\delta}_{\max}$ = 3.33 indicate a higher effective radius of curvature in the simulation case of β = 33.3, which also provides an explanation for the increase of $\bar{P}_{sep}$ with decreasing β.

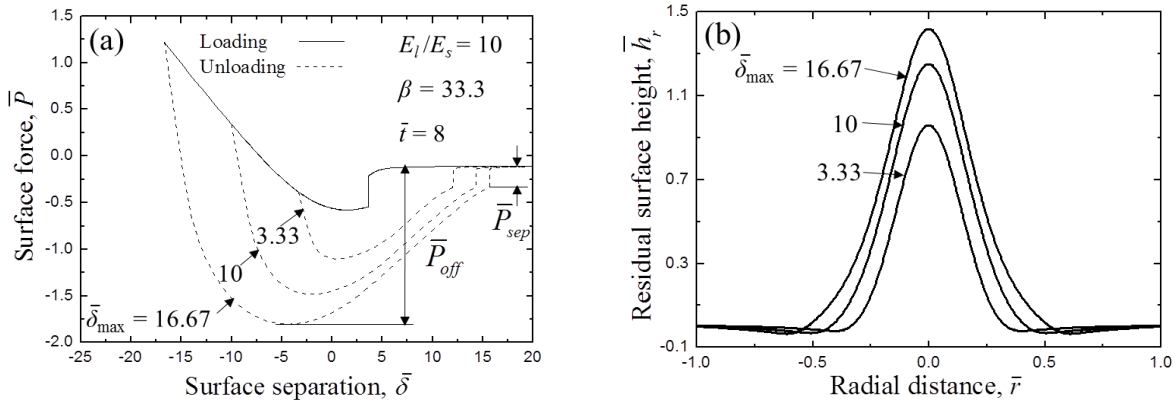

Figure 6.6 (a) Surface force $\bar{P}$ versus surface separation $\bar{\delta}$ during loading (solid lines) and unloading (dashed lines) and (b) residual surface height $\bar{h}_r$ versus radial distance $\bar{r}$ for elastic-plastic layered medium, E_l/E_s = 10, β = 33.3, $\bar{t}$ = 8, and $\bar{\delta}_{\max}$= 3.33, 10, and 16.7. (Pull-off force $\bar{P}_{off}$ and separation force $\bar{P}_{sep}$ are defined in (a).)

The opposite dependence of the separation mode and accumulation of plasticity during unloading on $\bar{\delta}_{\max}$ for high and low β values can be explained by considering the competing effects of the adhesion surface force and the residual stress in the substrate adjacent to the interface. Both contact area and surface conformity of the layered medium with the rigid sphere increase with $\bar{\delta}_{\max}$ during loading, resulting in a higher adhesion surface force conducive to necking. However, the concomitant increase in substrate plasticity with $\bar{\delta}_{\max}$ inhibits elastic recovery during unloading, because the resulting residual impression constrains the elastic deflection of the layer in the upward direction (in response to the adhesion force applied by the retracting sphere), which plays an important role in necking. For high β, the effect of the characteristic surface stress due to adhesion $\Delta\gamma/\varepsilon$ (surface force) dominates the effect of the substrate yield strength Y_s (substrate plasticity). Therefore, the increase of the surface force is the dominant factor and the separation mode demonstrates more ductile-like behavior (necking) with the increase of $\bar{\delta}_{\max}$. Alternatively, for low β, the effect of substrate plasticity (yield strength Y_s) is more prevalent than that of the surface force (adhesive stress $\Delta\gamma/\varepsilon$), and the high tensile residual stress at the layer/substrate interface due to plastic deformation in the substrate opposes necking by the adhesion surface force. Because the net surface force is reduced in the latter case,

less plastic deformation occurs during unloading and surface detachment commences before the formation of a neck, demonstrating more brittle-like behavior with the increase in $\bar{\delta}_{\max}$. A similar dependence of the separation mode on $\bar{\delta}_{\max}$ and Y_s has been reported for a rigid plate in adhesive contact with an elastic-plastic hemisphere (Du et al., 2008).

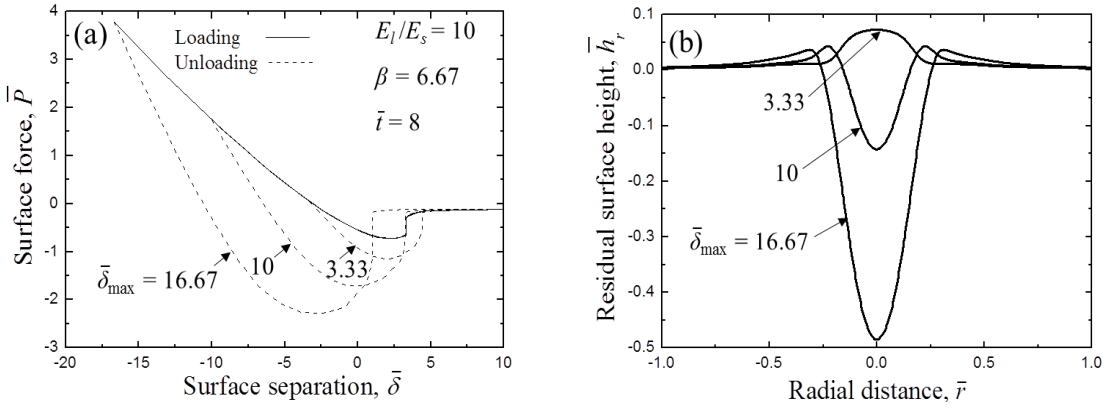

Figure 6.7 (a) Surface force $\bar{P}$ versus surface separation $\bar{\delta}$ during loading (solid lines) and unloading (dashed lines) and (b) residual surface height $\bar{h}_r$ versus radial distance $\bar{r}$ for elastic-plastic layered medium, E_l/E_s = 10, β = 6.67, $\bar{t}$ = 8, and $\bar{\delta}_{\max}$= 3.33, 10, and 16.7.

To obtain additional insight into the dependence of the surface separation mode on β, parametric FEM simulations were performed for a wide range of $\bar{\delta}_{\max}$ and β. Figure 6.8 shows the residual center height $\bar{h}_{o,r} = h_{o,r}/t$ as a function of $\bar{\delta}_{\max}$ for β in the range of 3.33–33.3, E_l/E_s = 10, and $\bar{t}$ = 8. For β = 33.3 and 22.2, $\bar{h}_{o,r}$ increases monotonically with $\bar{\delta}_{\max}$, indicating an increasingly more ductile-like mode of surface separation. For β = 16.7 and 13.3, $\bar{h}_{o,r}$ demonstrates a non-monotonic dependence on $\bar{\delta}_{\max}$. This is attributed to the dominant effect of the increasing surface force and intensifying substrate plasticity (residual stress effect) in the low and high ranges of $\bar{\delta}_{\max}$, respectively, as evidenced by the increase and decrease in $\bar{h}_{o,r}$ with $\bar{\delta}_{\max}$, i.e., ductile- and brittle-like modes of surface separation, respectively. For 11.1 ≥ β ≥ 3.33, $\bar{h}_{o,r}$ decreases monotonically with increasing $\bar{\delta}_{\max}$, indicating more brittle-like mode of surface separation. In view of the results shown in Figure 6.8, it may be inferred that surface detachment exhibits more ductile-like behavior (high β) when $\bar{h}_{o,r}$ > 0 and brittle-like behavior (low β) when $\bar{h}_{o,r}$ < 0. This phenomenological criterion of the surface separation mode is depicted in Figure 6.8 by a horizontal dashed line. Thus, for E_l/E_s = 10 and $\bar{t}$ = 8, ductile- and brittle-like surface separation always occurs for high and low β, i.e., β > 13.3 and β < 6.67, respectively, while for intermediate β values (6.67 < β < 13.3), a transition from ductile- to brittle-like mode of surface separation is encountered with increasing $\bar{\delta}_{\max}$.

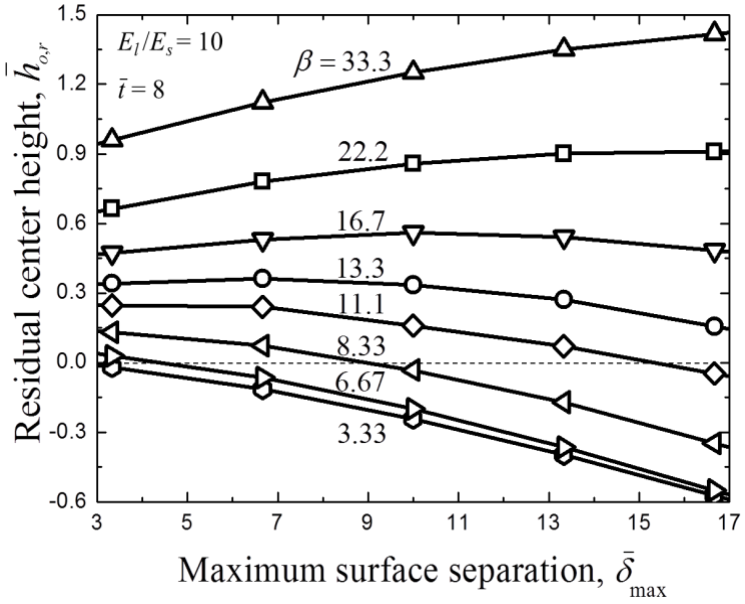

Figure 6.8 Residual center height $\bar{h}_{o,r}$ versus maximum surface separation $\bar{\delta}_{\max}$ for elastic-plastic layered medium, E_l/E_s = 10, β = 3.33–33.3, and $\bar{t}$ = 8.

Further insight into the effect of plasticity on the loading/unloading response of layered media subjected to adhesive contact is provided by simulation results shown in following figures. Figure 6.9 shows the surface force $\bar{P}$ versus surface separation $\bar{\delta}$ and distributions of residual surface height $\bar{h}_r$ for E_l/E_s = 10, β = 1.67, 6.67, and 33.3, $\bar{t}$ = 8, and $\bar{\delta}_{\max}$ = 10. $\bar{P}_{off}$ demonstrates a non-monotonic dependence on β. For a low β value (β = 1.67), deformation is predominantly elastic because the high yield strength of the substrate prevents plastic deformation. As a consequence, $\bar{P}_{off}$ is close to the values predicted by the JKR and DMT models. For an intermediate β value (β = 6.67), the large force hysteresis indicates the accumulation of significant plastic deformation in the substrate. Thus, a much higher $\bar{P}_{off}$ arises due to the residual tensile stress at the layer/substrate interface induced by the adjacent plastic zone in the substrate. For a high β value (β = 33.3), $\bar{P}_{off}$ is less than that obtained with intermediate β values, despite the fact that plastic deformation in the substrate is much more extensive for β = 33.3 than β = 6.67. The dependence of $\bar{P}_{sep}$ on β is similar to that of $\bar{P}_{off}$. This trend of $\bar{P}_{sep}$ can be explained in the context of corresponding residual surface profiles, shown in Figure 6.9(b), Tabor parameter, and effective radius of curvature R_{eff} in adhesive contact (Song and Komvopoulos, 2011). In the low β range, $R_{eff} \approx R$ because deformation in the layered medium is fully reversible (elastic), as evidenced by the overlapping of the loading and unloading curves for β = 1.67 (Figure 6.9(a)), for example. In the intermediate β range, however, the formation of a residual impression due to the evolution of plasticity in the substrate during loading yields a larger R_{eff}, while in the high β range, plastic deformation during unloading leads to the formation of a neck with a small summit radius of curvature, implying a decrease in R_{eff}. Thus, the non-monotonic variation of $\bar{P}_{sep}$ with β observed in Figure 6.9(a) can be attributed to the indirect effects of substrate plasticity and necking on R_{eff}.

6.3.3. Effect of Layer-to-Substrate Elastic Modulus Ratio

In addition to the plasticity parameter, the layer-to-substrate elastic modulus ratio E_l/E_s plays an important role in contact deformation of layered media. Although this effect has been studied extensively for adhesionless contacts (O'Sullivan, and King, 1987; Komvopoulos, 1988; Kral et al., 1995a, 1995b, Li and Chou, 1997; Perriot and Barthel, 1997; King, 1987), relatively less is known about the effect of E_l/E_s on the mechanical response of layered media subjected to adhesive contact loads. Figure 6.10 shows representative results of the surface force $\bar{P}$ and residual surface height $\bar{h}_r$ for E_l/E_s = 2.5, 10, and 40, β = 33.3, $\bar{t}$ = 8, and $\bar{\delta}_{\max}$ = 10. (E_l/E_s was varied by changing E_l while fixing E_s at 20 GPa.) The decrease in $\bar{P}_{off}$ with increasing E_l/E_s is attributed to the decrease in substrate plasticity with increasing layer stiffness, a well-known effect (Komvopoulos et al., 1987, Komvopoulos, 1988; Kral et al., 1995a, 1995b). Low $\bar{P}_{off}$is desirable in microscopic devices demonstrating inherently low spring-back forces and, therefore, prone to fail due to excessive adhesion (stiction). In contrast to $\bar{P}_{off}$, $\bar{P}_{sep}$ increases monotonically with E_l/E_s. This trend can be explained by writing Eq. (6.6) in the following form:

$$\frac{\mu_{eff}}{\mu_s} = \frac{1}{2}\left(1 - \frac{\bar{t}}{30\mu_s}\right) + \left[\frac{1}{4}\left(1 - \frac{\bar{t}}{30\mu_s}\right)^2 + \mu_l\left(\frac{\bar{t}}{30\mu_s}\right)\right]^{1/2} \tag{6.7}$$

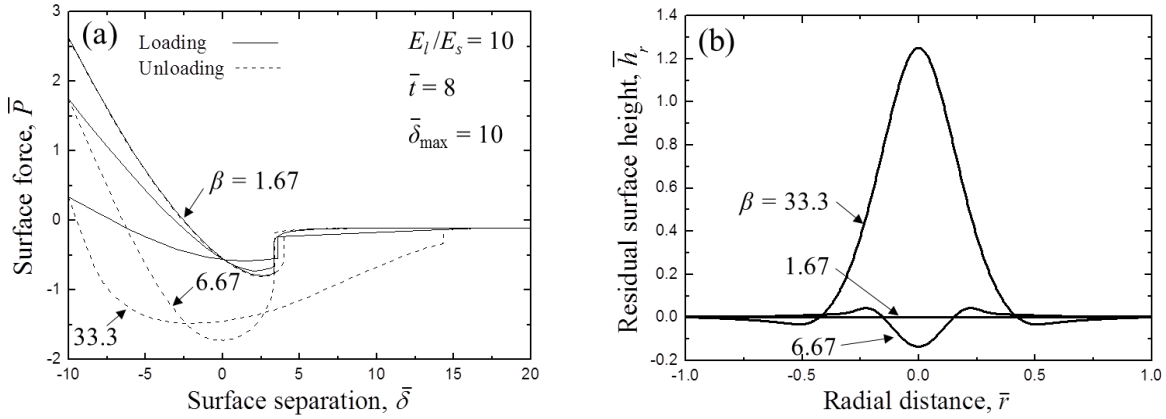

Figure 6.9 (a) Surface force $\bar{P}$ versus surface separation $\bar{\delta}$ during loading (solid lines) and unloading (dashed lines) and (b) residual surface height $\bar{h}_r$ versus radial distance $\bar{r}$ for elastic-plastic layered medium, E_l/E_s = 10, β = 1.67, 6.67, and 33.3, $\bar{t}$ = 8, and $\bar{\delta}_{\max}$= 10.

Because $\bar{t}$ and μ_s were fixed in this simulation case (Figure 6.10), Eq. (6.7) indicates that $\mu_{eff} \propto \mu_l^{1/2}$. Thus, considering that $\mu_l \propto E_l^{-2/3}$ (Eq. (6.1)), it follows that $\mu_{eff} \propto (E_l/E_s)^{-1/3}$, because E_s was fixed, which implies a monotonic decrease in μ_{eff} with increasing E_l/E_s. Hence, considering the dependence of $\bar{P}_{sep}$ on μ_{eff}, it is concluded that $\bar{P}_{sep}$ increases monotonically with E_l/E_s. An alternative interpretation of the effect of E_l/E_s on $\bar{P}_{sep}$ can be obtained by considering the effect of E_l/E_s on the residual surface height. As shown in Figure 6.10(b), necking becomes more pronounced with decreasing E_l/E_s. Considering that the enhancement of necking is accompanied by a decrease in R_{eff} at the instant of surface detachment (discussed above), it follows that $\bar{P}_{sep}$ increases monotonically with E_l/E_s.

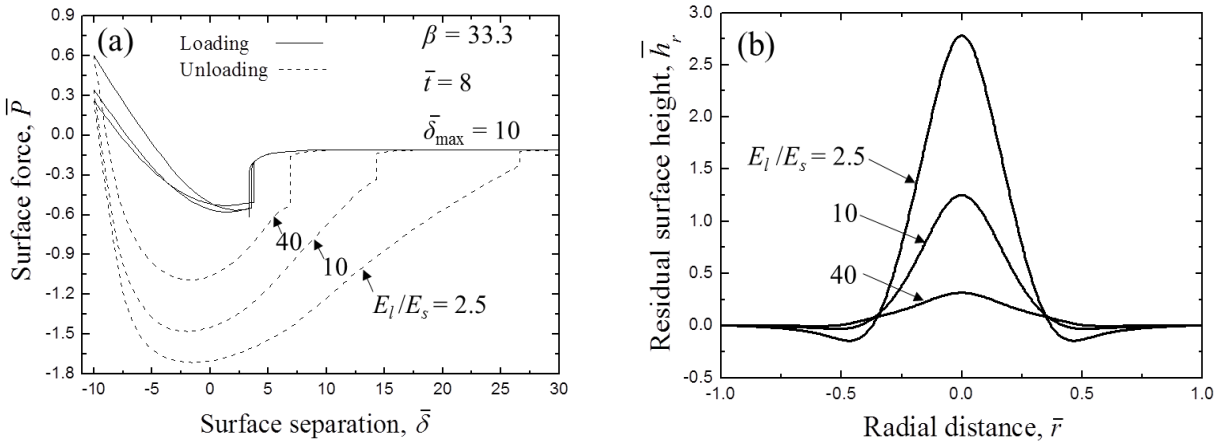

Figure 6.10 (a) Surface force $\bar{P}$ versus surface separation $\bar{\delta}$ during loading (solid lines) and unloading (dashed lines) and (b) residual surface height $\bar{h}_r$ versus radial distance $\bar{r}$ for elastic-plastic layered medium, E_l/E_s = 2.5, 10, and 40, β = 33.3, $\bar{t}$ = 8, and $\bar{\delta}_{max}$= 10.

Figure 6.11 shows contours of equivalent plastic strain $\bar{\varepsilon}_p$ obtained after complete unloading for E_l/E_s = 2.5, 10, and 40, β = 33.3, $\bar{t}$ = 8, and $\bar{\delta}_{max}$= 10. Significant necking in the case of a relatively compliant layer ($E_l/E_s = 2.5$) is indicative of a ductile-like mode of surface detachment, whereas very low substrate plasticity and merely flat surface of the layered medium with a stiff layer ($E_l/E_s = 40$) are evidence of a brittle-like mode of surface detachment. The maximum equivalent plastic strain $\bar{\varepsilon}_p^{max}$ increases from approximately 0.3 to 2.1 with the decrease of E_l/E_s from 40 to 2.5. For a stiff layer (Figure 6.11(c)), $\bar{\varepsilon}_p^{max}$ arises below the layer/substrate interface at r = 0, while for a compliant layer (Figure 6.11(a)), $\bar{\varepsilon}_p^{max}$ occurs at the layer/substrate interface close to the neck edge. Similar (although milder) deformation characteristics with those of the relatively compliant and stiff layers were observed for a layer of intermediate stiffness (Figure 6.11(b)). These results indicate that stiff surface layers suppress substrate plasticity and reduce the likelihood of interfacial delamination, provided that the elastic layer is sufficiently strong to resist brittle fracture and contact fatigue.

The effect of the ratio of the layer to the substrate Poisson's ratio is relatively secondary, because contrary to the significant mismatch of the layer and substrate elastic modulus, the variation of the Poisson's ratio is less pronounced (typically, in the range of 0.2–0.4) and, most importantly, the Poisson's ratio effect during unloading is secondary because excessive plastic deformation in the substrate dominates the unloading behavior.

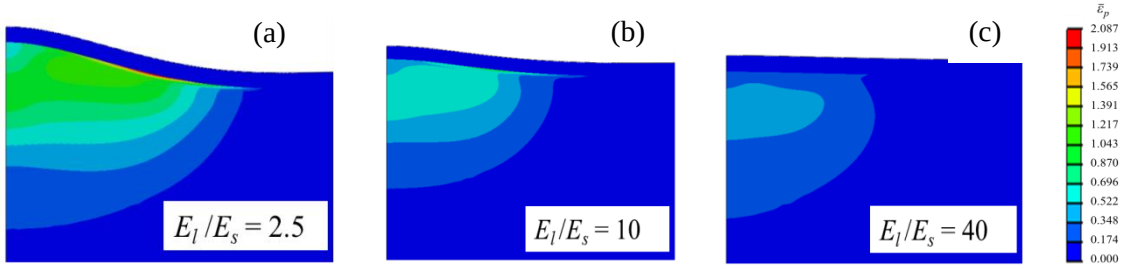

Figure 6.11 Contours of equivalent plastic strain $\bar{\varepsilon}_p$ after complete unloading for elastic-plastic layered medium, E_l/E_s = 2.5, 10, and 40, β = 33.3, $\bar{t}$ = 8, and $\bar{\delta}_{\max}$= 10.

6.3.4. Effect of Layer Thickness

Another important factor affecting contact deformation in layered media is the layer thickness. Simulation results of surface force $\bar{P}$ and residual surface height $\bar{h}_r$ for E_l/E_s = 10, β = 33.3, $\bar{t}$ = 4, 8, and 16, and $\bar{\delta}_{\max}$= 10 are shown in Figure 6.12. $\bar{P}_{off}$ decreases continuously with the increase of $\bar{t}$ (Figure 6.12(a)) due to the decrease in substrate plasticity, while the mode of surface separation exhibits more ductile-like behavior with the decrease in $\bar{t}$ (Figure 6.12(b)). However, an opposite trend is observed for $\bar{P}_{sep}$, which can be explained in terms of the first derivative of μ_{eff} with respect to $\bar{t}$. From Eq. (6.6), it follows that

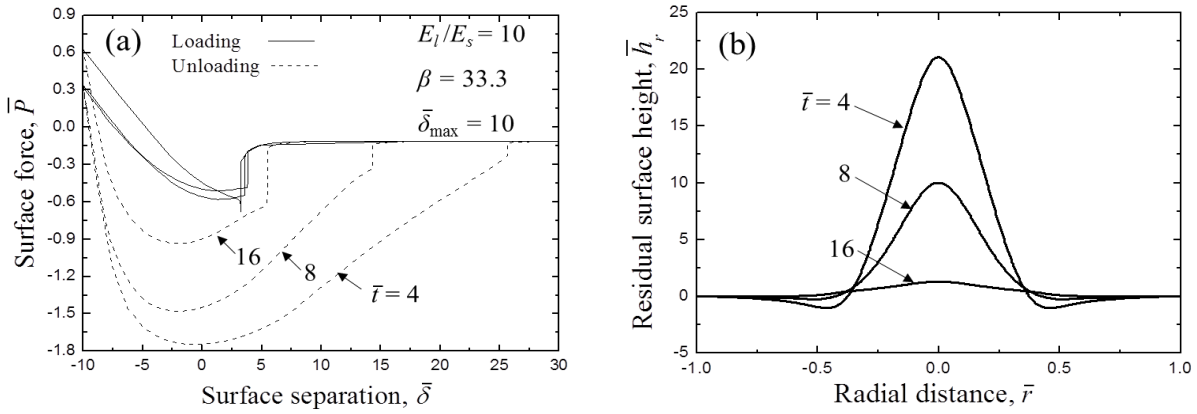

Figure 6.12 (a) Surface force $\bar{P}$ versus surface separation $\bar{\delta}$ during loading (solid lines) and unloading (dashed lines) and (b) residual surface height $\bar{h}_r$ versus radial distance $\bar{r}$ for elastic-plastic layered medium, E_l/E_s = 10, β = 33.3, $\bar{t}$ = 4, 8, and 16, and $\bar{\delta}_{\max}$= 10.

$$\frac{d\mu_{eff}}{d\bar{t}} = \frac{1}{60}\left[\left[1 + \frac{1-\left(\frac{\mu_s}{\mu_l}\right)}{\frac{1}{4}\left(\frac{\mu_s}{\mu_l}\right)^2\left(1-\frac{\bar{t}}{30\mu_s}\right)^2 + \left(\frac{\mu_s}{\mu_l}\right)\left(\frac{\bar{t}}{30\mu_s}\right)}\right]^{1/2} - 1\right] \tag{6.8}$$

Equation (6.1) gives that $\mu_l < \mu_s$ for $E_l > E_s$. Thus, from Eq. (6.8) it follows that $d\mu_{eff}/d\bar{t} < 0$ for $E_l > E_s$, implying that μ_{eff} increases with the decrease in $\bar{t}$, which explains the monotonic increase in $\bar{P}_{sep}$ with $\bar{t}$ shown in Figure 6.12(a). This trend is also consistent with the results of the residual surface height shown in Figure 6.12(b). The neck profiles indicate that the decrease in $\bar{t}$ is conducive to necking (i.e., high $\bar{P}_{sep}$).

6.3.5. Effect of Cyclic Contact Loading

Contact fatigue due to repetitive loading is of particular importance in miniaturized devices, such as microscopic switches, relays, and electrical contacts. To obtain insight into the effect of cyclic loading in adhesive contact of layered media, quasi-static FEM simulations of

four consecutive loading cycles were performed for E_l/E_s = 10, β = 6.67 and 33.3, $\bar{t}$ = 8, and $\bar{\delta}_{\max}$ = 10. Figures 6.13(a) and 6.13(b) shows the surface force $\bar{P}$ versus surface separation $\bar{\delta}$ and loading/unloading cycles for β = 33.3 and 6.67, respectively. The development of a force hysteresis suggests that energy was dissipated irreversibly in each loading cycle. In addition to energy dissipation due to contact instabilities (i.e., jump-in and jump-out), energy is also dissipated in the form of plastic deformation in the substrate. As expected, higher β yielded larger force hysteresis. After the first cycle, loading and unloading paths are essentially identical. For β = 33.3, subsequent loading half-cycles demonstrate smaller adhesion force and larger surface separation at the instant of jump-in compared to the first loading half-cycle (Figure 6.13(a)). This is attributed to pronounced necking in the first unloading half-cycle (Figure 6.9(b)), resulting in a smaller R_{eff} in subsequent loading half-cycles and, in turn, lower adhesion surface force and larger surface separation at the instant of jump-in. For β = 6.67, the residual impression produced in the first loading half-cycle (Figure 6.9(b)) yields a larger R_{eff} in subsequent loading half-cycles, which increases the adhesion surface force and causes jump-in to occur at a smaller surface separation than that observed in the first cycle.

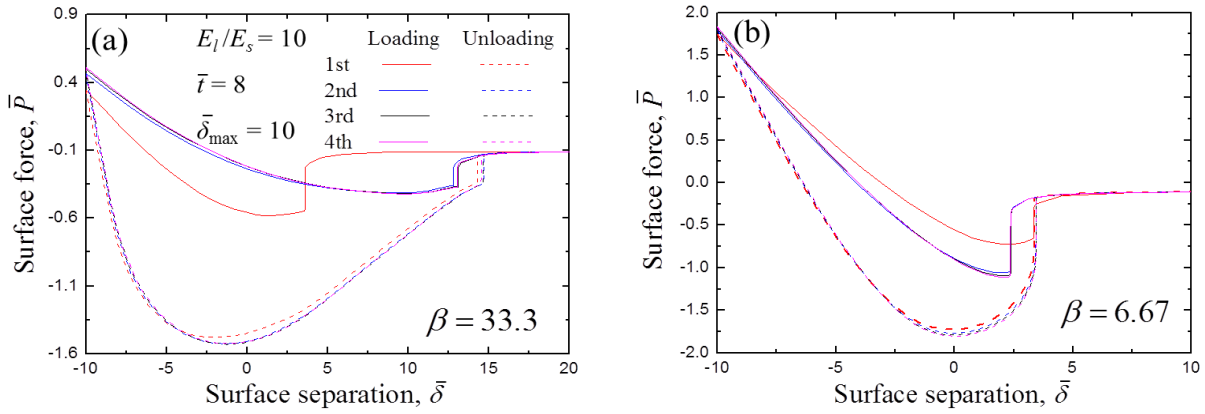

Figure 6.13 Surface force $\bar{P}$ versus surface separation $\bar{\delta}$ during loading (solid lines) and unloading (dashed lines) for four consecutive loading cycles, elastic-plastic layered medium, E_l/E_s = 10, (a) β = 6.67 and (b) 33.3, $\bar{t}$ = 8, and $\bar{\delta}_{\max}$= 10.

The results shown in Figure 6.13 can be further interpreted by considering the variation of ε_p along the axis of symmetry ($\bar{r}$ = 0) and the layer/substrate interface ($\bar{z} = z/\varepsilon$= –8) for β = 33.3 and 6.67, shown in Figures 6.14 and 6.15, respectively. Both simulation cases demonstrate ratcheting, as evidenced by the evolution of $\bar{\varepsilon}_p$ in the substrate with the accumulation of contact cycles. For β = 33.3, $\bar{\varepsilon}_p^{\max}$ arises below the layer/substrate interface (Figure 6.14(a)) and along the interface at a radial distance corresponding to that of the edge of the residual pile-up (neck) (Figure 6.15(a)), whereas for β = 6.67, $\bar{\varepsilon}_p^{\max}$ arises at the layer/substrate interface (Figure 6.14(b)) and within the residual impression (Figure 6.15(b), suggesting that interface and substrate delamination are likely failure modes. The above cyclic contact simulations reveal a higher propensity for delamination in the substrate and the layer/substrate interface due to ratcheting in layered media characterized by low and high plasticity parameters.

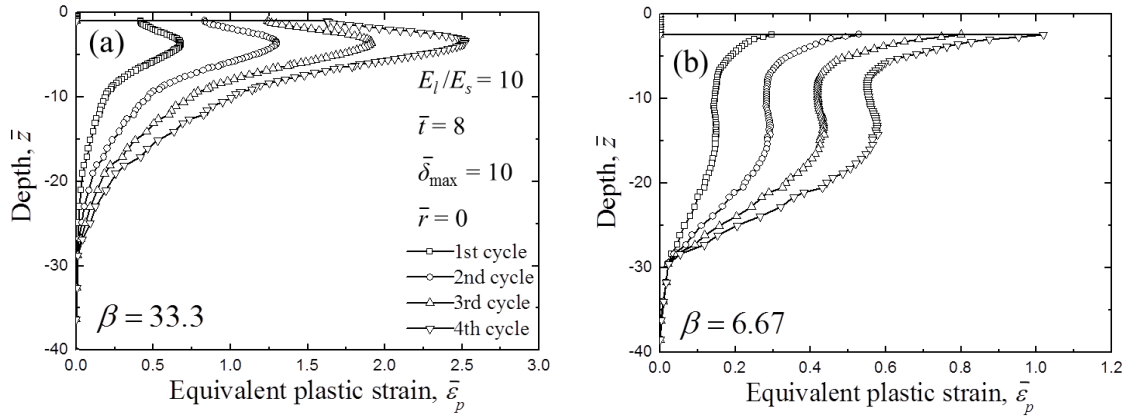

Figure 6.14 Depth distributions of equivalent plastic strain $\bar{\varepsilon}_p$ along the axis of symmetry ($\bar{r}$ = 0) for four consecutive loading/unloading cycles, elastic-plastic layered medium, E_l/E_s = 10, β = 6.67 and 33.3, $\bar{t}$ = 8, and $\bar{\delta}_{max}$= 10.

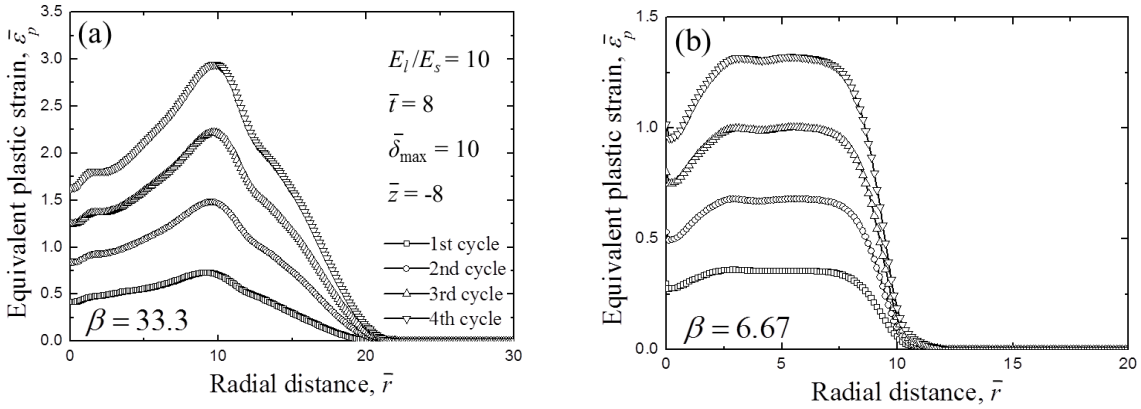

Figure 6.15 Radial distributions of equivalent plastic strain $\bar{\varepsilon}_p$ along the layer/substrate interface ($\bar{z}$ = –8) for four consecutive loading/unloading cycles, elastic-plastic layered medium, E_l/E_s = 10, β = 6.67 and 33.3, $\bar{t}$ = 8, and $\bar{\delta}_{max}$= 10.

6.4. Conclusions

A finite element analysis of adhesive contact between a rigid sphere and a layered medium was performed to elucidate the effect of adhesion on contact deformation. Adhesive surface interaction was modeled by nonlinear springs with a force-displacement constitutive relation derived from the LJ potential. An effective Tabor parameter was introduced for layered media with a layer stiffer than the substrate, which is a function of the layer thickness and Tabor parameters corresponding to half-spaces with the layer and substrate elastic modulus. The effects of plasticity parameter, layer-to-substrate elastic modulus ratio, layer thickness, maximum surface separation (interaction distance), and cyclic contact loading on adhesive contact behavior of layered media were elucidated in the context of simulation results. The pull-off force increased with the maximum surface separation due to the enhancement of necking or substrate

plasticity. Abrupt surface separation (jump-out) was not encountered at the instant of maximum pull-off force but at larger surface separation (smaller surface gap) and smaller surface force, controlled by the radius of curvature of the neck summit or residual impression produced after complete unloading, not the maximum surface separation.

The dependence of the surface separation (detachment) mode on maximum surface separation was affected by the plasticity parameter. Results were interpreted in terms of competing effects between the adhesion (attractive) surface force and the residual stress at the layer/substrate interface induced by the adjacent plastic zone in the substrate. A separation mode map was constructed for different ranges of plasticity parameter and maximum surface separation. For high plasticity parameter, necking during surface retraction intensified with increasing maximum surface separation and surface detachment exhibited more ductile-like behavior, because the unloading response was controlled by the adhesion surface force. For low plasticity parameter, however, surface detachment demonstrated more brittle-like behavior with increasing maximum surface separation, because the unloading response was mostly affected by residual stresses caused by the residual impression formed during loading. A non-monotonic dependence of the surface separation mode on maximum surface separation was observed in the intermediate range of plasticity parameter, which was attributed to the dominant effect of the increasing adhesion surface force (residual stress) on the contact behavior in the low (high) range of maximum surface separation.

The pull-off force decreased with increasing layer-to-substrate elastic modulus ratio, while the separation force demonstrated an opposite trend explained in terms of the effective Tabor parameter. Plastic deformation decreased significantly with the increase in layer stiffness and the maximum equivalent plastic strain shifted from the layer/substrate interface below the edge of the residual pile-up (neck) into the substrate below the center of the contact region, indicating a decreasing propensity for interfacial delamination with increasing layer stiffness. Substrate plasticity intensified and surface separation exhibited more ductile-like behavior with decreasing layer thickness. The dependence of the pull-off and separation forces on the layer thickness was interpreted in terms of the evolution of plasticity in the substrate and the effective Tabor parameter, respectively.

FEM simulations of repetitive adhesive contact on layered media demonstrated the accumulation of incremental plasticity with loading cycles. Irreversible energy dissipation increased with plasticity parameter. Despite overlapping of unloading paths, surface force and surface separation at the instant of jump-in during the loading phase of each subsequent cycle deviated significantly from those in the first loading cycle due to differences in residual deformation produced in the first cycle (i.e., necking and residual impression). Profiles of equivalent plastic strain in the depth direction and along the layer/substrate interface revealed that interfacial and substrate delamination due to incremental plasticity (ratcheting) are likely failure mechanisms in layered media subjected to cyclic adhesive contact loading.

Chapter 7

Delamination of an elastic film from an elastic-plastic substrate during adhesive contact loading and unloading

7.1. Introduction

Thin films are widely used as protective coatings of various devices having contact interfaces to maintain low friction and improve surface wear resistance. For example, thin diamond-like carbon films are used to protect the surfaces of hard disks and magnetic recording heads against mechanical wear caused intermittent contact during operation and to enhance the lifetime and reliability of contact-mode microelectromechanical systems (Komvopoulos, 1996, 2000, 2003; Smallwood et al., 2006). In chapter 6, we have extended the finite element analysis of adhesive contact from homogeneous half-space to layered media, and obtained insight of substrate plasticity effect on contact instabilities and separation mode. However, the film-substrate interface is assumed sufficiently strong, thus excludes the failure mode of interface delamination, which is one of the most widely observed failure modes in thin-film structure. In addition to the formation of ring and median cracks generated by tensile contact stresses, Chai (2003) demonstrated that delamination at the film/substrate interface may occur due to the mismatch of film. Bagchi and Evans (1996) showed that substrate elastic-plastic properties also play an important role in delamination. Marshall and Evans (1984) modeled a delaminating thin film as a rigidly clamped disc and used the indentation method to evaluate the fracture toughness of the film/substrate interface. Drory and Hutchison (1996) analyzed conical indentation of a brittle film on a ductile substrate and proposed a method for determining the interface fracture toughness in terms of applied normal load, delamination radius, film thickness, and mechanical properties of film and substrate materials.

Delamination mechanics is generally complicated by geometry and material nonlinearities. In the presence of plasticity and absence of an initial defect at the film/substrate interface, analytical solutions are cumbersome or impossible and, consequently, numerical methods such as the finite element method (FEM) must be used to obtain a solution. Xia et al. (2007) simulated normal contact between a rigid spherical indenter and an elastic film on an elastic-plastic substrate and, using a cohesive zone model for the film/substrate interface, they observed shear cracking outside the contact area for indentations deeper than a critical depth and tensile cracking at the interface below the center of contact upon unloading. Chen et al. (2009) used a FEM model to examine wedge indentation of a soft film on a hard substrate and determined the critical indentation load for crack initiation as a function of interface toughness and strength, reporting good agreement between experimental and FEM results of interface properties for wedge angles equal to 90° and 120°.

Although the previous studies have provided insight into contact-induced delamination of film/substrate systems, the effect of surface adhesion on contact deformation was not examined. Pioneering studies of the role of surface adhesion in contact mechanics carried out by Johnson et al. (1971) and Derjaguin et al. (1975) have led to the development of analytical models of

adhesive contact between two elastic spheres, known as the JKR and DMT models, respectively. These models yield estimates of the pull-off force P_{off}, defined as the force at the instant of full separation of the adhering elastic spheres during unloading. Tabor (1977) has argued that the JKR and DMT models represent extreme conditions of adhesion systems, yielding accurate predictions of P_{off} for $\mu > 5$ and $\mu < 0.1$, respectively, where μ is referred to as the Tabor parameter. Maguis (1992) used the Dugdale approximation to describe the adhesive contact stress and obtained a solution of P_{off} in the transition range $0.1 < \mu < 5$, which is bounded by the JKR and DMT solutions. Muller et al. (1980), Greenwood (1997), and Feng (2001) used a traction-separation law derived from the Lennard-Jones (LJ) potential to model the adhesive stress between contacting elastic spheres and obtained numerical solutions representing a smooth transition between the JKR and DMT solutions. Although the former solutions based on the LJ potential differ slightly from that reported by Maguis (1992), they reproduce adhesion-induced instability phenomena, such as instantaneous surface contact (jump-in) and separation (jump-out), commonly observed with microprobe instruments and suspended microstructures.

In recent FEM studies, nonlinear spring elements with a force-displacement constitutive relation derived from the LJ potential were used to model adhesive contact of a rigid plate with an elastic-plastic hemisphere (Du et al., 2007; Kadin et al., 2008) or a rigid sphere with an elastic-plastic half-space (Song and Komvopoulos, 2011). These studies have shed light into the effects of various geometrical, loading, and material parameters on the evolution of P_{off} and contact instabilities. Eid et al. (2011) used the FEM model developed by Du et al. (2007) to study adhesive contact between a rigid plate and an elastic-plastic layered hemisphere and observed a dependence of the adhesion force and contact radius on maximum contact displacement (maximum compressive force) and film thickness. Song and Komvopoulos (2012) analyzed single and repetitive normal contact between a rigid sphere and a hard elastic film bonded to an elastic-perfectly plastic substrate and obtained a multi-parameter deformation map of brittle- and ductile-like surface separation of adhesive contacts.

Despite important information about the role of adhesion in contact deformation provided by aforementioned studies, a comprehensive analysis of adhesion-induced delamination at film/substrate interfaces is still lacking. The objective of this study was to investigate the effect of surface adhesion, governed by the LJ potential, on interfacial delamination in elastic-plastic layered media with interfaces modeled by a cohesive zone obeying a bilinear traction-separation constitutive law. Interface damage (crack) initiation and evolution (delamination) during a full load-unload cycle are discussed in light of FEM results. Irreversible bending of the elastic film and crack-tip opening and closure before and after full unloading (jump-out) are interpreted in terms of residual cohesive zone and energy release rate concepts. The effects of minimum surface separation (maximum compressive force), substrate yield strength, interface work of adhesion, cohesive strength, and preexisting crack size are examined in light of numerical solutions.

7.2. Contact model

Figure 7.1 shows the axisymmetric problem under consideration, i.e., a rigid sphere of radius R in proximity with a half-space consisting of an elastic film of thickness t and a semi-

infinite elastic-perfectly plastic substrate. FEM meshes of the substrate and film media comprise 4096 and 26656 axisymmetric, four-node, linear, isoparametric elements with a total of 4618 and 27170 nodes, respectively. The nodes at the bottom boundary and axis of symmetry ($r = 0$) of the entire mesh are constrained against displacement in the z- and r-direction, respectively. The distance between adjacent nodes at the film surface and the film/substrate interface is equal to ~$0.006R$. Adhesion between the sphere and the film is modeled by nonlinear spring elements with a prescribed traction-separation relation governed by the LJ potential. Details of the nonlinear spring constitutive equation can be found elsewhere (Song and Komvopoulos, 2011). All contact simulations were performed with the multi-purpose FEM code ABAQUS (version 6.9EF).

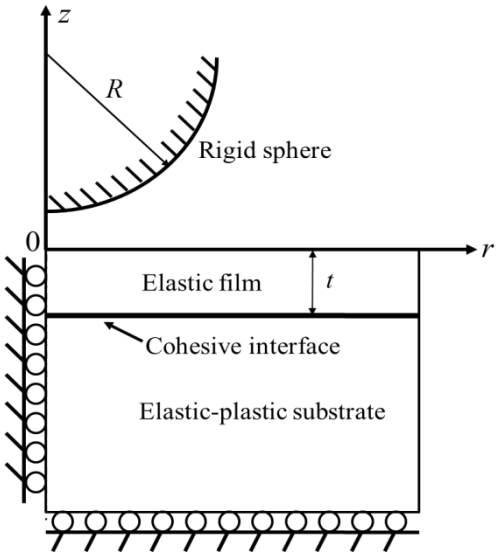

Figure 7.1 Model of a rigid sphere in close proximity with a layered medium consisting of an elastic film and a semi-infinite elastic-plastic substrate.

Coherence at the film/substrate interface is modeled by a cohesive-zone law (Tvergaard and Hutchinson, 1994, 1996) that allows the film to separate from the substrate to simulate crack initiation and growth. Figure 7.2 shows a schematic of the bilinear traction-separation law of the cohesive interface, where σ is the surface traction (normal or parallel to the film/substrate interface), h is the film-substrate separation, σ_c is the cohesive strength, h^* is the film-substrate separation for damage (crack) initiation, h_c is the film-substrate separation for failure (permanent surface separation, i.e., delamination), and Γ is the interface work of adhesion, represented by area (OAB), i.e.,

$$\Gamma = \frac{1}{2}\,\sigma_c h_c \tag{7.1}$$

In the present analysis, h^*, h_c, σ_c, and Γ are assumed to be the same in both normal and in-plane interfacial directions. In all simulations, h^* (on the order of the interatomic distance) is fixed, while h_c (3–10 times h^*) is varied with σ_c and Γ according to Eq. (7.1). Interface damage initiation and failure are respectively controlled by the following criteria:

$$[\sigma_n^2 + \sigma_t^2 + \sigma_s^2]^{1/2} = \sigma_c \tag{7.2}$$

$$\Gamma_n + \Gamma_t + \Gamma_s = \Gamma \tag{7.3}$$

where subscript n denotes the normal direction and subscripts t and s denote the two in-plane directions at the film/substrate interface.

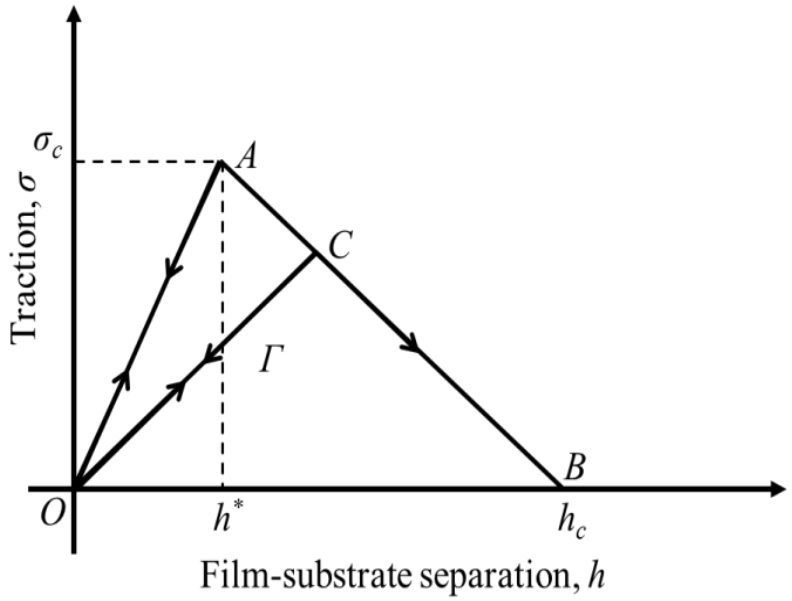

Figure 7.2 Schematic representation of traction versus film-substrate separation constitutive law of a bilinear cohesive zone. Surface separation larger than h^* leads to either partial damage (point C) or full damage (point B), accompanied by a decrease in cohesive strength σ_c.

The traction-separation law at the interface of the layered medium is expressed as

$$\sigma = \begin{cases} \left(\frac{h}{h^*}\right)\sigma_c & (0 < h \leq h^*) \\ \left(\frac{h_c - h}{h_c - h^*}\right)\sigma_c & (h^* < h < h_c) \\ 0 & (h \geq h_c) \end{cases} \tag{7.4}$$

For $h < h^*$, the traction increases linearly with film-substrate separation, implying purely elastic stretching at the interface, while for $h^* \leq h < h_c$, the traction decreases linearly from σ_c toward 0 due to damage accumulation. Damage leads to a different unloading path (CO) than the loading path (OA). Failure (full damage) occurs when $h \geq h_c$, resulting in locally traction-free interface.

7.3. Results and discussion

Figures 7.3(a) and 7.3(b) show schematics of the deformed layered medium before and after full surface separation (jump-out), respectively. In general, three distinct interface regions can be observed before jump-out (Figure 7.3(a)): a fully damaged (white) region of zero strength ($h \geq h_c$), representing an interfacial crack of radius a_c and crack-tip surface separation h_c, a partially damaged cohesive zone (gray) of strength less than σ_c ($h^* < h < h_c$), and an elastically stretched (red) region ahead of the damaged cohesive zone ($0 < h \leq h^*$). The fully damaged region (crack) together with the partially damaged cohesive zone represent a fictitious crack of radius a_{fc} and tip surface separation $h_{fc} = h^*$. After jump-out (Figure 7.3(b)), full unloading yields a crack-tip opening displacement CTOD and a residual fictitious crack of radius a_{fc}^{res} and crack-tip maximum tensile stress $\sigma_{\max}$. Although jump-out does not affect the crack radius, it reduces the radius of the elastically stretched (red) region and the damaged cohesive zone (gray) due to the elastic recovery of the film and nonuniform plastic deformation at the substrate face of the cohesive zone, respectively. This produces a closed region (blue) of cohesive zone between the residual fictitious crack and the elastically stretched region. As a consequence, $a_{fc}^{\text{res}} \leq a_{fc}$ and $h_{fc}^{\text{res}} < h^*$. (Superscript "res" indicates "residual" parameters obtained after full unloading (jump-out).)

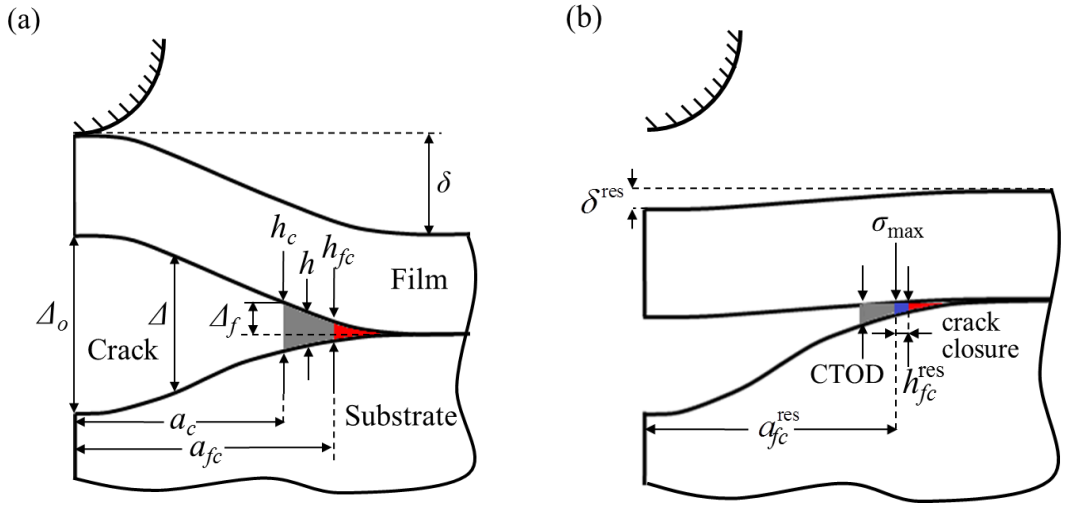

Figure 7.3 Schematics of deformed layered medium (a) before and (b) after complete separation (jump-out) of the elastic film from the rigid sphere. Formation of a crack and a cohesive zone (gray region), partial closure of the cohesive zone (blue region), and high tensile stresses (red region) can be encountered at the film/substrate interface during a full load-unload cycle, depending on the material properties and minimum surface separation (maximum compressive force).

Results from displacement-control simulations are presented and discussed below in terms of dimensionless parameters, such as surface force $\bar{P} = P/2\pi RW$ (where W is the work of adhesion of the sphere/film contact system), surface separation $\bar{\delta} = \delta/t$, minimum surface separation (maximum compressive force) $\bar{\delta}_{\min} = \delta_{\min}/t$, interfacial separation $\bar{\Delta} = \Delta/h_c$, film-substrate separation below the center of contact $\bar{\Delta}_o = \Delta_o/h_c$, residual film deflection at the center of contact $\bar{\delta}^{\text{res}} = \delta^{\text{res}}/h_c$, cohesive strength $\bar{\sigma}_c = \sigma_c\varepsilon/W$ (where ε is the equilibrium interatomic distance), substrate yield strength $\bar{Y} = Y/\sigma_c$, interface work of adhesion $\bar{\Gamma} = \Gamma/W$,

film deflection at the crack-tip location $\bar{\Delta}_f = \Delta_f/h_c$, crack radius $\bar{a}_c = a_c/t$, radius of fictitious crack $\bar{a}_{fc} = a_{fc}/t$, radius of residual fictitious crack $\bar{a}_{fc}^{\text{res}} = a_{fc}^{\text{res}}/t$, closure of residual fictitious crack $c = 1 - \left(a_{fc}^{\text{res}}/a_{fc}\right)^2$, and radius of initial crack $\bar{a}_i = a_i/t$. The film-to-substrate elastic modulus ratio $E_{\text{film}}/E_{\text{sub}}$ and sphere radius-to-film thickness ratio R/t on contact behavior are also important parameters. However, the focus in the present study is on adhesive contact of layered media with films much stiffer than the substrate, typical of hard protective films used in hard-disk drives and dynamic microelectomechanical devices. Thus, all simulation results presented below are for $E_{\text{film}}/E_{\text{sub}}$= 10 and R/t = 10. Hereafter, a positive (negative) surface force will be designated as a compressive (tensile) force.

7.3.1. Effect of minimum surface separation

Figures 7.4(a) and 7.4(b) show the surface force $\bar{P}$ and corresponding film-substrate separation below the center of contact $\bar{\Delta}_o$ as functions of surface separation $\bar{\delta}$, respectively, for $\bar{\Gamma}$ = 0.125, $\bar{Y}$ = 0.4, $\bar{\sigma}_c$ = 0.075, and $\bar{\delta}_{\text{min}}$ = –0.5, –1.0, and –1.5. Because the three simulation cases demonstrate similar characteristics, the case of $\bar{\delta}_{\text{min}}$= –1.5 is used to describe the general loading (solid lines) and unloading (dashed lines) contact behavior. For all three simulation cases, the variation of $\bar{\Delta}_o$ with $\bar{\delta}$ during loading is shown by the barely visible response at the bottom of Figure 7.4(b). At a critical surface separation ($\bar{\delta} \approx 0.25$), abrupt contact (jump-in) occurs due to the effect of long-range surface attraction, resulting in the upward displacement of the layered medium, as evidenced by the development of a negative (tensile) surface force. As surface separation decreases further, a transition from tensile to compressive surface force is encountered in conjunction with the downward displacement of the layered medium. The linear force response from jump-in to minimum surface separation (point A) can be explained by a simple model of plate bending. Owing to the low yield strength of the substrate ($\bar{Y} = 0.125$) and significantly higher elastic modulus of the film, plastic deformation in the substrate below the center of contact leads to a situation approximately analogous to a circumferentially clamped circular plate (film) subjected to elastic bending by a concentrated force applied to its center. Thus, the linear loading path observed in Figure 7.4(a) is dominated by the bending behavior of the elastic film not contact deformation. This attribution is supported by results of a layered medium with a high-yield strength substrate (section 7.3.2) demonstrating a nonlinear increase in $\bar{P}$ with $\bar{\delta}$, characteristic of contact deformation. The appearance of a force hysteresis after full unloading indicates irreversible deformation, i.e., plastic deformation in the substrate and/or film debonding (delamination). Initial unloading is characterized by a purely linear elastic response (AB), with the film remaining fully bonded to the substrate ($\bar{\Delta}_o = 0$). Further retraction of the rigid sphere produces a nonlinear elastic-plastic force response (BC), because plastic deformation in the substrate accumulated during loading inhibits further elastic recovery. As a consequence, large strain gradients develop at the film/substrate interface, resulting in a cohesive tensile stress ($\bar{\Delta}_o > 0$) that causes re-yielding in the substrate adjacent to the interface. Interface damage initiation commences at a critical surface separation ($\bar{\delta} \approx -0.8$), as evidenced by the sharp change in slope of the force response (point C). Additional damage caused by further unloading decreases the cohesive stress and the resulting partial recovery of the upward displacement of the substrate leads to delamination ($\bar{\Delta}_o$ = 1.0) and the decrease of the tensile surface force (CD). The subsequent increase of the tensile surface force (DE) is due to upward bending of the elastic film. Abrupt surface separation (jump-out) (point E) leading to full

unloading (point F) occurs when further elastic deflection of the film cannot be compensated by interfacial adhesion. Equivalent plastic strain contours in the highly deformed regions of the substrate adjacent to the interface (not shown here), corresponding to characteristic points of the unloading response for $\bar{\delta}_{\min} = -1.5$ shown in Figure 7.4, confirmed that accumulation of plasticity in the substrate during unloading occurred only along path BC, indicating that the cause of substrate re-yielding was the increase in cohesive stress with film-substrate separation (OA path in Figure 7.2).

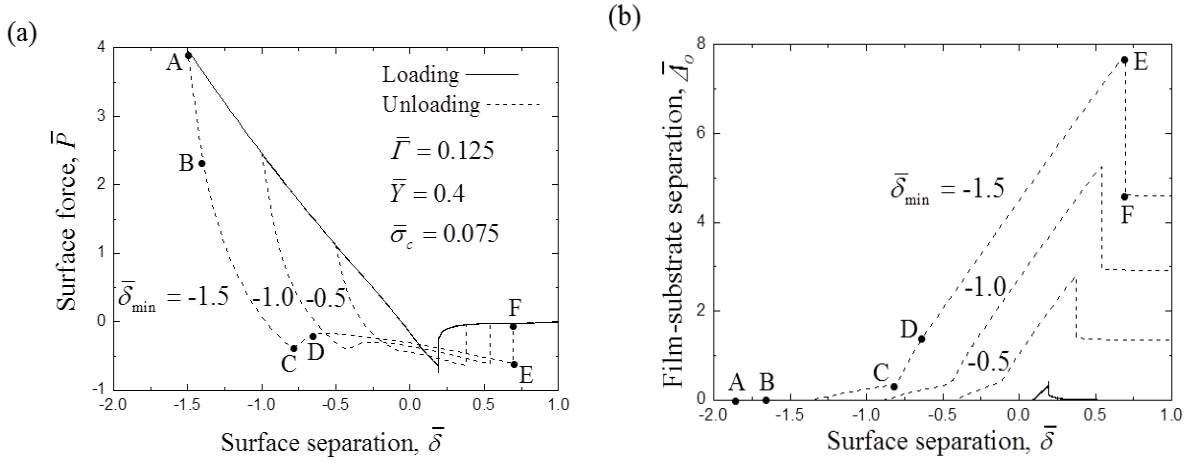

Figure 7.4 (a) Surface force $\bar{P}$ and (b) corresponding film-substrate separation below the center of contact $\bar{\Delta}_o$ versus surface separation $\bar{\delta}$ for $\bar{\Gamma} = 0.125$, $\bar{Y} = 0.4$, $\bar{\sigma}_c = 0.075$, and $\bar{\delta}_{\min} = -0.5$, -1.0, and -1.5 (loading = solid lines; unloading = dashed lines). Characteristic points are shown for $\bar{\delta}_{\min} = -1.5$.

Figure 7.5(a) shows contours of dimensionless residual normal stress $\bar{\sigma}_{zz}^{\text{res}} = \sigma_{zz}/Y$ for $\bar{\Gamma} = 0.125$, $\bar{Y} = 0.4$, $\bar{\sigma}_c = 0.075$, and $\bar{\delta}_{\min} = -1.5$. Tensile stresses arise around the fictitious crack tip, whereas the stress field ahead of the fictitious crack tip is compressive. The presence of these regions of tensile and compressive residual stress can be explained by considering the evolution of plasticity in the substrate. Before jump-out (point E in Figure 7.4), a cohesive zone exists at the crack-tip front because the plastically deformed substrate cannot follow the upward deflection of the elastic film (Figure 7.3(a)). At the instant of jump-out (point F in Figure 7.4), the surface force decreases abruptly to zero, resulting in elastic spring-back of the film. However, plastic deformation in the substrate adjacent to the interface allows only partial crack closure (blue region in Figure 7.3(b)). This produces a residual cohesive zone of smaller radius and lower tensile stress, which accounts for the residual tensile stress at the fictitious crack tip seen in Figure 7.5(a). This residual tensile stress is responsible for the downward bending of the elastic film, quantified by the residual deflection δ^{res} at the center of contact (Figure 7.3(b)). Figure 7.5(b) shows a linear variation of the dimensionless residual film deflection $\bar{\delta}^{\text{res}}$ with $\bar{\delta}_{\min}$ for $\bar{\Gamma} = 0.125$, $\bar{Y} = 0.4$, and $\bar{\sigma}_c = 0.075$.

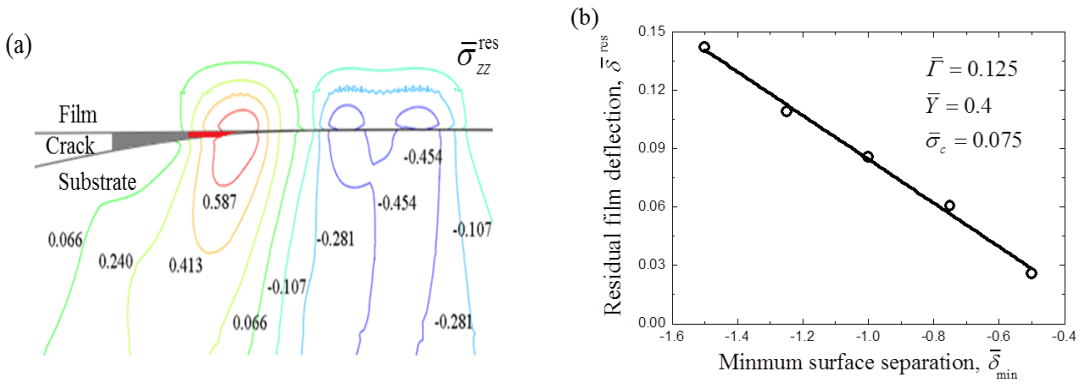

Figure 7.5 (a) Contours of residual $\bar{\sigma}_{zz}^{res}$ stress and (b) variation of residual film deflection at the center of contact $\bar{\delta}^{res}$ with minimum surface separation $\bar{\delta}_{min}$ for $\bar{\Gamma} = 0.125$, $\bar{Y} = 0.4$, and $\bar{\sigma}_c = 0.075$.

The crack-tip opening displacement CTOD is a measure of fracture toughness in classical fracture mechanics, because it is proportional to the energy release rate G and inversely proportional to the cohesive strength σ_c (Anderson, 1995). Figure 7.6 shows the dimensionless crack-tip opening displacement $\beta = \text{CTOD}/h_c$ after jump-out as a function of $\bar{\delta}_{min}$ for $\bar{\Gamma} = 0.125$, $\bar{Y} = 0.4$, and $\bar{\sigma}_c = 0.075$. The increase of β with $\bar{\delta}_{min}$ implies an increase in fracture toughness with minimum surface separation, which can be associated with the increase in crack-tip blunting with substrate plasticity. To interpret the dependence of β on $\bar{\delta}_{min}$, it is instructive to consider the energy release rate before and after jump-out. Just before jump-out (point E in Figure 7.4), $\beta = 1.0$ and the energy release rate G_E consists of the elastic strain energy in the film E_f, the plastic strain energy in the substrate E_s, and the interface work of adhesion Γ, i.e., $G_E = E_f + E_s + \Gamma$. After jump-out (point F in Figure 7.4), E_f is almost fully recovered (the film remains slightly deflected because of the tensile stress in the residual cohesive zone) and Γ is almost unchanged because the fictitious crack exhibits only partial closure, i.e., $G_F \approx E_s + \Gamma$. Thus, considering that CTOD $\propto G$, the dimensionless crack-tip opening displacement after surface separation can be expressed as

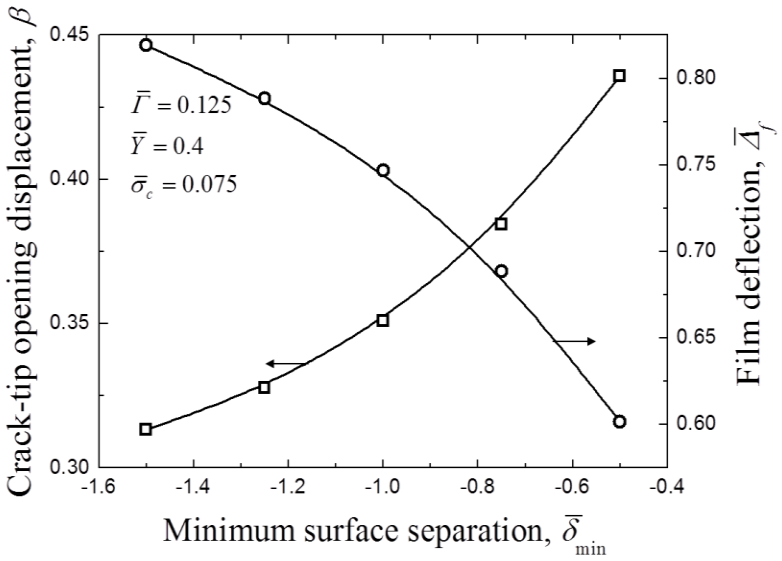

Fig. 7.6 Crack-tip opening displacement β and film deflection at the crack-tip location $\bar{\Delta}_f$ versus minimum surface separation $\bar{\delta}_{\min}$ for $\bar{\Gamma}$= 0.125, $\bar{Y}$= 0.4, and $\bar{\sigma}_c$= 0.075.

$$\beta \approx \left[1 + \frac{E_f/E_s}{1+\Gamma/E_s}\right]^{-1} \tag{7.5}$$

As shown in Figure 7.6, the film upward deflection at the crack-tip location $\bar{\Delta}_f$ (Figure 7.3(a)) decreases with increasing $\bar{\delta}_{\min}$. This can be attributed to the accumulation of more plasticity in the substrate during loading with increasing $\bar{\delta}_{\min}$, resulting in more residual deformation upon unloading and, in turn, less upward deflection of the film. Thus, considering that E_f decreases with $\bar{\Delta}_f$ and that E_s increases with $\bar{\delta}_{\min}$, the tendency for β to increase with $\bar{\delta}_{\min}$ can be explained in light of Eq. (7.5).

7.3.2. Effect of substrate yield strength

Figures 7.7(a) and 7.7(b) show the effect of the substrate yield strength $\bar{Y}$ on the variation of the surface force $\bar{P}$ and corresponding film-substrate separation below the center of contact $\bar{\Delta}_o$ with surface separation $\bar{\delta}$, respectively, for $\bar{\Gamma}$ = 0.125, $\bar{\sigma}_c$ = 0.075, and $\bar{\delta}_{\min}$ = –1.0. As expected, the contact stiffness increases with substrate yield strength. For $\bar{Y} = 10$, the loading curve almost overlaps with the unloading curve, indicating negligible substrate plasticity or film delamination. The higher values of $\bar{\Delta}_o$ and $\bar{\delta}$ at the instant of jump-out for $\bar{Y}$ = 1.0 than 0.1 and 10 (Figure 7.7(b)) suggest the existence of an intermediate yield strength range that is conducive to film delamination. This effect of the substrate yield strength can be better understood by considering the variation of the interfacial separation $\bar{\Delta}$ before (solid lines) and after (dashed lines) jump-out for $\bar{\Gamma}$ = 0.125, $\bar{Y}$ = 0.1, 1.0, and 10, $\bar{\sigma}_c$ = 0.075, and $\bar{\delta}_{\min}$ = –1.0, shown in Figure 7.8. For $\bar{Y}$ = 0.1, the relatively high cohesive strength leads to significant plastic deformation in the substrate during unloading that enhances the conformity of the deflected elastic film with the substrate (i.e., small $\bar{\Delta}$). For $\bar{Y}$ = 1.0, strain incompatibility at the interface due to the mismatch of film and substrate material properties leads to film delamination. For $\bar{Y}$ = 10, plastic deformation is negligible due to the high strength of the substrate and delamination is encountered before jump-out because the elastic deflection of the film caused by surface adhesion can be compensated by the cohesive stress. However, because residual deformation in the substrate is negligible, film debonding from the substrate is less than that for $\bar{Y}$ = 1.0. Consequently, elastic deflection of the film is fully recovered upon jump-out, resulting in full crack closure. The condition of maximum interface delamination cannot be determined from only three simulation cases and because of the effect of other important parameters, particularly E_s and $\bar{\delta}_{\min}$. Nevertheless, considering the results shown in Figure 7.8 and opposite effects of excessive plasticity during unloading for low $\bar{Y}$ and negligible plasticity during loading for high $\bar{Y}$, it may be inferred that maximum interface delamination is expected to occur in an intermediate $\bar{Y}$ range.

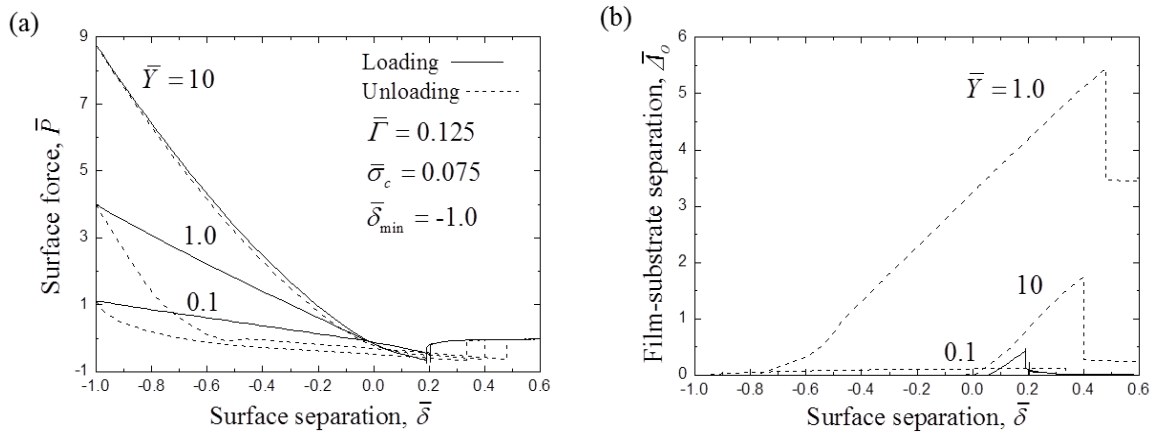

Fig. 7.7 (a) Surface force $\bar{P}$ and (b) corresponding film-substrate separation below the center of contact $\bar{\Delta}_o$ versus surface separation $\bar{\delta}$ for $\bar{\Gamma}$= 0.125, $\bar{Y}$ = 0.1, 1.0, and 10, $\bar{\sigma}_c$ = 0.075, and $\bar{\delta}_{\min}$ = –1.0 (loading = solid lines; unloading = dashed lines).

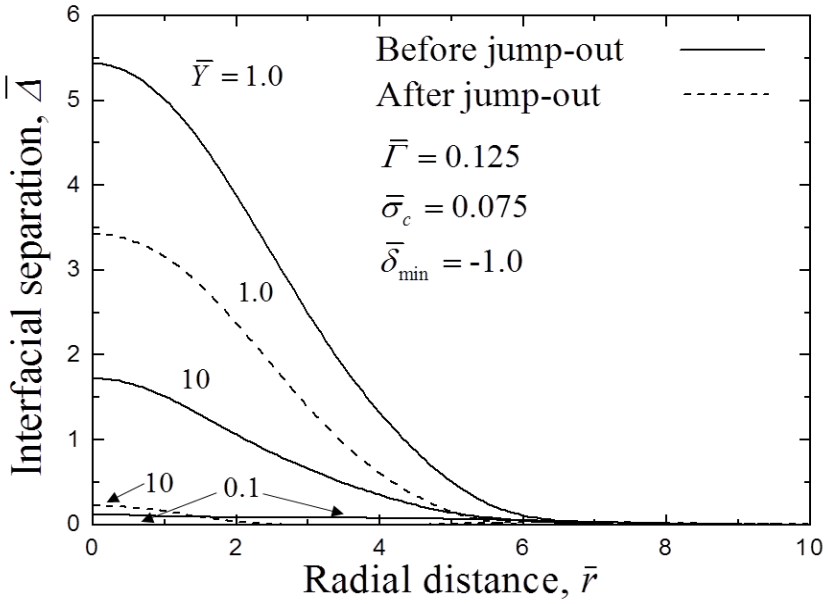

Fig. 7.8 Interfacial surface separation $\bar{\Delta}$ before (dashed lines) and after (solid lines) jump-out versus radial distance $\bar{r}$ for $\bar{\Gamma}$ = 0.125, $\bar{Y}$= 0.1, 1.0, and 10, $\bar{\sigma}_c$= 0.075, and $\bar{\delta}_{\min}$ = –1.0.

7.3.3. Effect of interface work of adhesion

Figures 7.9(a) and 7.9(b) show the surface force $\bar{P}$ and corresponding film-substrate separation below the center of contact $\bar{\Delta}_o$ as functions of surface separation $\bar{\delta}$, respectively, for $\bar{\Gamma}$ = 0.125, 0.25, and 0.5, $\bar{Y}$ = 0.4, $\bar{\sigma}_c$ = 0.075, and $\bar{\delta}_{\min}$ = –1.0. In all three simulation cases, the variation of $\bar{\Delta}_o$ with $\bar{\delta}$ during loading (solid lines) is shown by the barely visible response at the bottom of Figure 7.9(b). Characteristic points (similar to those shown in Figure 7.4) are shown for $\bar{\Gamma}$ = 0.125. The loading response does not show a dependence on interface work of adhesion

because the dominance of compressive deformation during loading prevents delamination even for low interface work of adhesion ($\bar{\Gamma}$ = 0.125). This is also evidenced by the very small $\bar{\Delta}_o$ values produced during loading (Figure 7.9(b)). Similar to loading, unloading (dashed lines) does not show a dependence on interface work of adhesion initially (AB). In this stage of unloading, a cohesive zone does not form ($\bar{\Delta}_o = 0$) because the interface is still under compression. However, further unloading induces localized film debonding characterized by a nonlinear force response (BC). Unloading up to the point of damage initiation ($\Delta_o \approx h^*$) is independent of $\bar{\Gamma}$ because h^* and $\bar{\sigma}_c$ are fixed in these simulation cases. However, upon the formation of a cohesive zone (point C), the unloading behavior shows a strong dependence on interface work of adhesion. For $\bar{\Gamma}$ = 0.125, the surface force first decreases slightly (CD) and then increases gradually with further unloading up to the instant of jump-out (point E) when it decreases abruptly to zero (point F). Point D is not distinguishable in the simulation cases of $\bar{\Gamma} = 0.25$ and 0.5 because the decrease in cohesive stress as a result of interfacial damage is limited by the relatively high $\bar{\Gamma}$ and h_c values (Eq. (7.1)). Slightly lower $\bar{P}$ and significantly higher $\bar{\Delta}_o$ values were obtained at jump-out with higher $\bar{\Gamma}$, implying smaller surface separation at jump-out for higher interface strength.

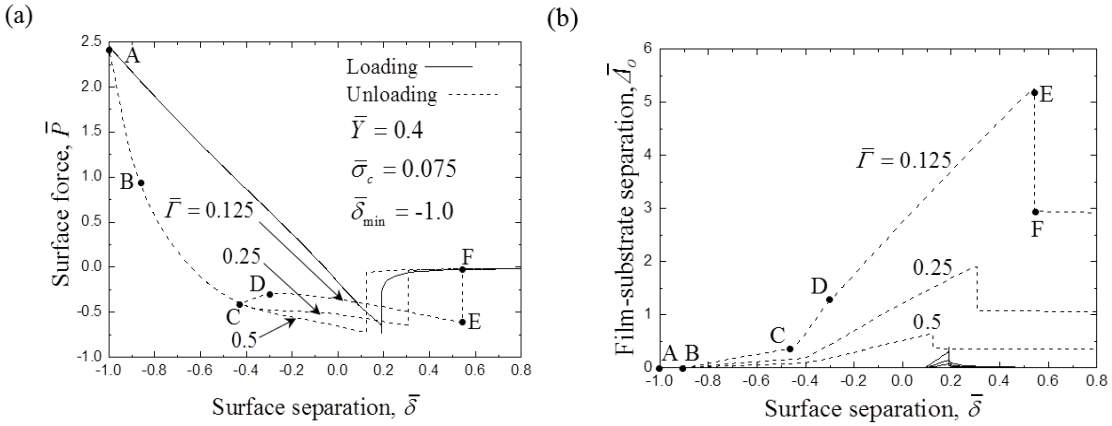

Fig. 7.9 (a) Surface force $\bar{P}$ and (b) corresponding film-substrate separation at the center of contact $\bar{\Delta}_o$ versus surface separation $\bar{\delta}$ for $\bar{\Gamma}$= 0.125, 0.25, and 0.5, $\bar{Y}$= 0.4, $\bar{\sigma}_c$ = 0.075, and $\bar{\delta}_{\min}$ = –1.0 (loading = solid lines; unloading = dashed lines). Characteristic points are shown for $\bar{\Gamma}$ = 0.125.

Figures 7.10(a) and 7.10(b) show the radius of the fictitious crack $\bar{a}_{fc}$ and residual fictitious crack $\bar{a}_{fc}^{\text{res}}$ (points E and F, respectively, in Figures 7.4 and 7.9) and fictitious crack closure upon jump-out c as functions of interface work of adhesion $\bar{\Gamma}$ for $\bar{Y}$ = 0.4, $\bar{\sigma}_c$ = 0.075, $\bar{\delta}_{\min}$= –1.0, and similar $\bar{P}_{off}$, as evidenced from Figure 7.9. The monotonic decrease of $\bar{a}_{fc}$ and $\bar{a}_{fc}^{\text{res}}$ with increasing $\bar{\Gamma}$ reveals an increase in interface resistance against interfacial damage initiation ($h > h^*$) and delamination ($h > h_c$) for fixed $\bar{P}_{off}$. Figure 7.10(b) shows that crack closure increases with interface work of adhesion, approaching asymptotically full closure (c = 1) for $\bar{\Gamma}$ > 1.4. This implies that layered media characterized by high interface work of adhesion not only exhibit a higher resistance against interface delamination but also greater affinity for crack closure.

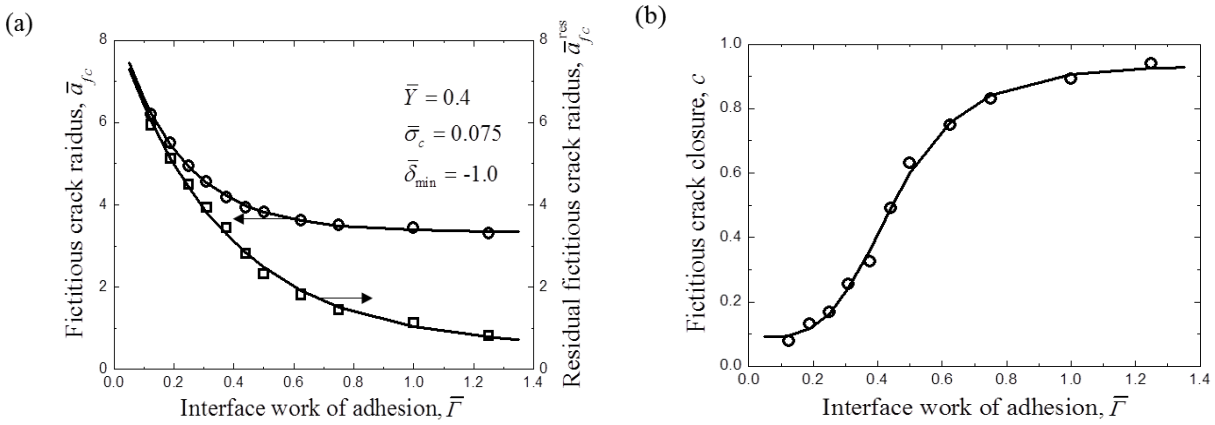

Fig. 7.10 (a) Radius of fictitious crack $\bar{a}_{fc}$ and residual fictitious crack $\bar{a}_{fc}^{\text{res}}$ and (b) closure of residual fictitious crack c versus interface work of adhesion $\bar{\Gamma}$ for $\bar{Y}$= 0.4, $\bar{\sigma}_c$ = 0.075, and $\bar{\delta}_{\min}$ = –1.0.

Figure 7.11 shows that the crack-tip opening displacement after jump-out β increases monotonically with interface work of adhesion $\bar{\Gamma}$ for $\bar{Y}$ = 0.4, $\bar{\sigma}_c$ = 0.075, and $\bar{\delta}_{\min}$ = –1.0. This trend can be attributed to the decrease of film deflection before jump-out with increasing interface work of adhesion. Indeed, as shown in Figure 7.11, the film deflection at the crack-tip location $\bar{\Delta}_f$ before jump-out decreases with the increase of $\bar{\Gamma}$. Because this implies a decrease in E_f/E_s (for fixed E_s) with increasing $\bar{\Gamma}$, the increasing trend of β seen in Figure 7.11 can be explained in light of Eq. (7.5).

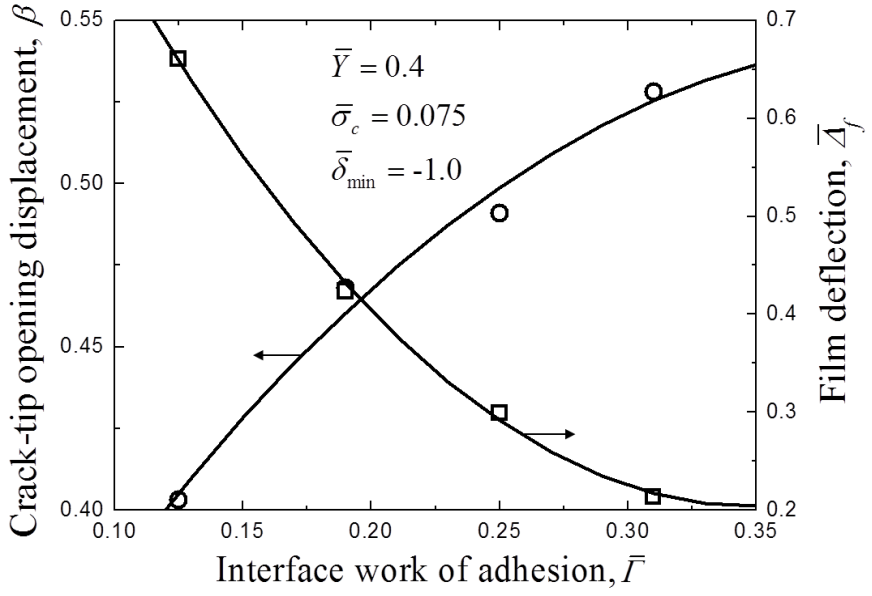

Fig. 7.11 Crack-tip opening displacement β and film deflection at the crack-tip location $\bar{\Delta}_f$ versus interface work of adhesion $\bar{\Gamma}$ for $\bar{Y}$ = 0.4, $\bar{\sigma}_c$ = 0.075, and $\bar{\delta}_{\min}$ = –1.0.

7.3.4. Effect of cohesive strength

Figures 7.12(a) and 7.12(b) show the surface force $\bar{P}$ and corresponding film-substrate separation below the center of contact $\bar{\Delta}_o$ as functions of surface separation $\bar{\delta}$, respectively, for $\bar{\Gamma}$= 0.125, $\bar{Y}$= 0.4, $\bar{\sigma}_c$= 0.015, 0.075, and 0.2, and $\bar{\delta}_{\min}$= –1.0. As expected, the stiffness increases with the cohesive strength. For a relatively low cohesive strength ($\bar{\sigma}_c$= 0.015), the unloading response does not show any distinguishable discontinuity until the commencement of jump-out, implying a secondary effect of interface damage to the overall contact stiffness. For an intermediate cohesive strength ($\bar{\sigma}_c$= 0.075), however, the unloading behavior shows that the contact stiffness during damage (crack) initiation (BC) differs significantly from that obtained during damage evolution (delamination) (CD). Discontinuities in the surface force and film-substrate separation (CD in Figures 7.12(a) and 7.12(b), respectively) responses were encountered only for a relatively high cohesive strength ($\bar{\sigma}_c = 0.2$), indicating unstable crack initiation at the interface. This behavior can be interpreted in terms of dimensionless parameter $\Lambda = E^* h_c / a\sigma_c$, where $E^*$is the effective elastic modulus of the layered medium and a is the contact radius at minimum surface separation (Gao and Bower, 2004), representing the layered medium-to-interface stiffness ratio. Analytical and numerical results of the former study show that unstable crack initiation is characterized by low Λ values. This is in good agreement with the finding of the present study that high $\bar{\sigma}_c$ yields unstable crack initiation. Because low $\bar{\sigma}_c$ produces a high Λ value (i.e., layered medium stiffness higher than the interface stiffness), the effect of the cohesive interface on the overall unloading response is secondary compared to that of the film's elastic deflection. This suggests that damage (cracking) at a low cohesive strength interface does not affect the continuity of the unloading response up to the instant of jump-out, in agreement with the results for $\bar{\sigma}_c$ = 0.015 and 0.075 shown in Figure 7.12(a).

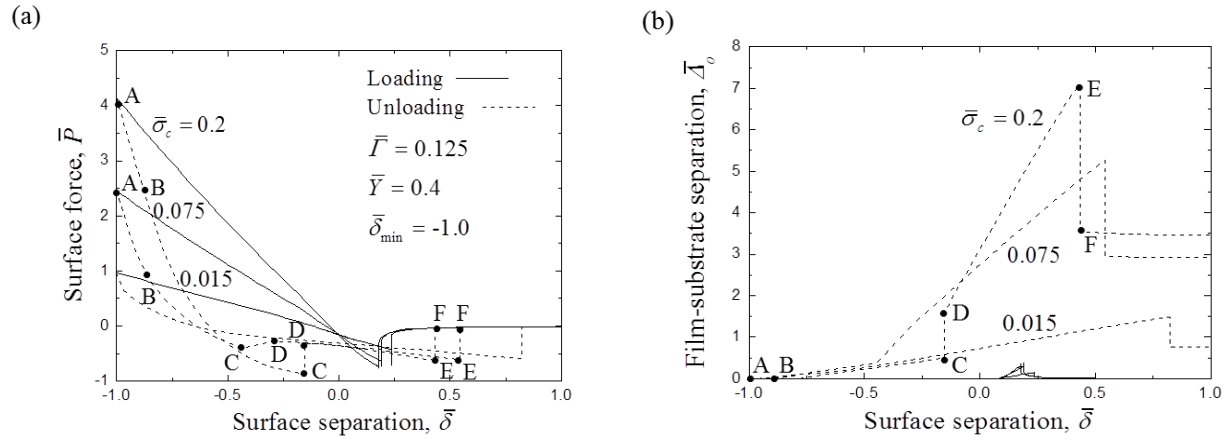

Fig. 7.12 (a) Surface force $\bar{P}$ and (b) corresponding film-substrate separation at the center of contact $\bar{\Delta}_o$ versus surface separation $\bar{\delta}$ for $\bar{\Gamma}$ = 0.125, $\bar{Y}$ = 0.4, $\bar{\sigma}_c$ = 0.015, 0.075, and 0.2, and $\bar{\delta}_{\min}$ = –1.0 (loading = solid lines; unloading = dashed lines). Characteristic points are shown for $\bar{\sigma}_c$ = 0.075 and 0.2.

Figure 7.13(a) shows the radius of the fictitious crack $\bar{a}_{fc}$ and residual fictitious crack $\bar{a}_{fc}^{\text{res}}$ as functions of cohesive strength $\bar{\sigma}_c$ for $\bar{\Gamma}$ = 0.125, $\bar{Y}$ = 0.4, and $\bar{\delta}_{\min}$ = –1.0. It is noted that $\bar{a}_{fc}$ decreases monotonically with increasing $\bar{\sigma}_c$ because the critical stress for damage initiation increases with $\bar{\sigma}_c$. However, $\bar{a}_{fc}^{\text{res}}$ exhibits a non-monotonic dependence on $\bar{\sigma}_c$ because of partial closure of the fictitious crack and approaches asymptotically to $\bar{a}_{fc}$ with increasing $\bar{\sigma}_c$. Figure

7.13(b) shows that closure of the fictitious crack c after full unloading (jump-out) decreases sharply with the increase of $\bar{\sigma}_c$, approaching asymptotically to zero. This trend can be explained by considering that $h_c \propto \sigma_c^{-1}$ for fixed $\bar{\Gamma}$ (Eq. (7.1)). Thus, the decrease of crack closure with increasing cohesive strength can be attributed to the simultaneous decrease of h_c, which is conducive to failure (cracking). Figure 7.14 shows the crack-tip opening displacement after jump-out β and the film deflection at the crack-tip location before jump-out $\bar{\Delta}_f$ as functions of cohesive strength $\bar{\sigma}_c$ for $\bar{\Gamma}$ = 0.125, $\bar{Y}$ = 0.4, and $\bar{\delta}_{\min}$ = –1.0. The decrease in β with the increase of $\bar{\sigma}_c$ can be interpreted as a decrease in interfacial fracture resistance with increasing cohesive strength. This counterintuitive result can be explained by considering that $\bar{\Delta}_f$ increases with $\bar{\sigma}_c$, implying a simultaneous increase in E_f/E_s, which, in view of Eq. (7.5), explains the decrease of β with increasing $\bar{\sigma}_c$.

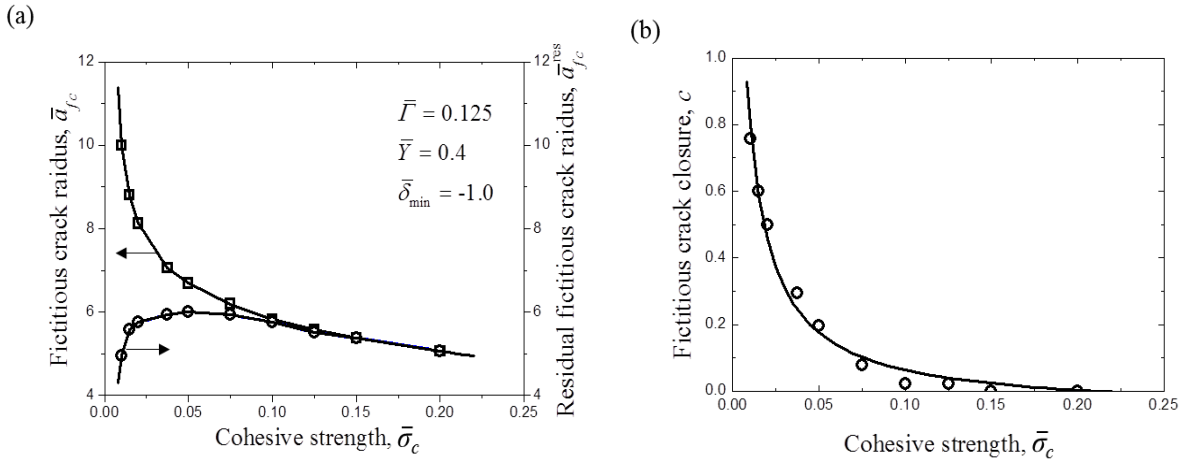

Fig. 7.13 (a) Radius of fictitious crack $\bar{a}_{fc}$ and residual fictitious crack $\bar{a}_{fc}^{\text{res}}$ and (b) closure of residual fictitious crack c versus cohesive strength $\bar{\sigma}_c$ for $\bar{\Gamma}$ = 0.125, $\bar{Y}$ = 0.4, and $\bar{\delta}_{\min}$ = –1.0.

7.3.5. Effect of preexisting crack

In all simulation cases discussed above, the film/substrate interface was assumed to be flawless, i.e., no preexisting defect. The effect of a penny-shaped crack of radius $\bar{a}_i$ located at the interface below the center of contact on the resulting surface force and contact behavior is examined in this section. Figures 7.15(a) and 7.15(b) show the surface force $\bar{P}$ and corresponding film-substrate separation below the center of contact $\bar{\Delta}_o$ as functions of surface separation $\bar{\delta}$, respectively, for $\bar{\Gamma}$ = 0.125, $\bar{Y}$= 0.4, $\bar{\sigma}_c$ = 0.015, $\bar{\delta}_{\min}$ = – 1.0, and $\bar{a}_i$ = 1, 4, and 8. The increase of surface separation at jump-in and jump-out with crack radius is attributed to the decrease of the layered medium stiffness with increasing crack radius. The loading paths (solid lines) for different $\bar{a}_i$ values begin to gradually overlap after jump-in as the interface is increasingly compressed. The initial unloading response (dashed lines) is not affected by variations in $\bar{a}_i$ because the interface is under compression ($\bar{\Delta}_o$ = 0). However, beyond a critical surface separation ($\bar{\delta} >$ –0.75) the unloading behavior shows a dependence on $\bar{a}_i$ (Figure 7.15(a)), and the film-substrate separation at jump-out increases significantly with crack radius (Figure 7.15(b)).

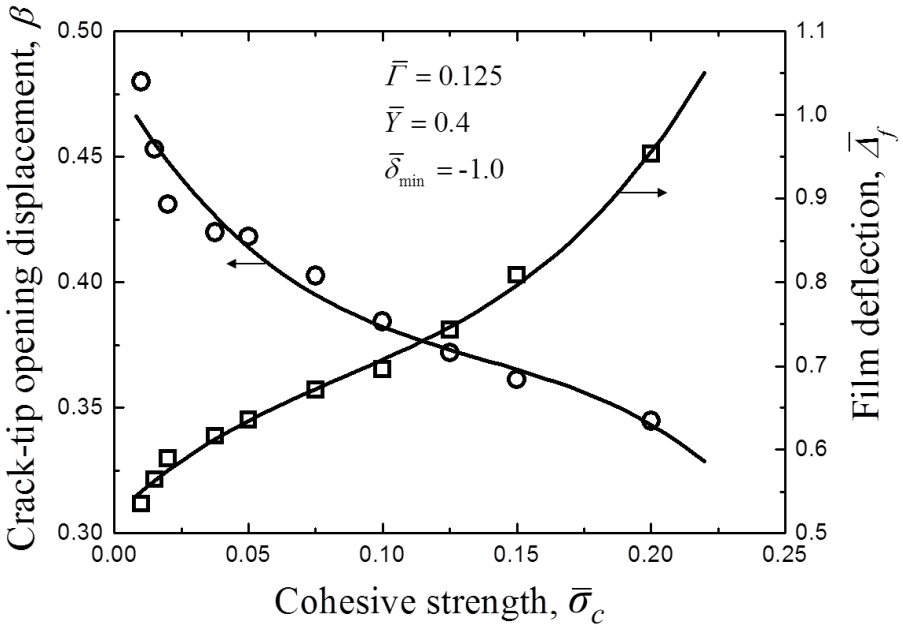

Fig. 7.14 Crack-tip opening displacement β and film deflection at the crack-tip location $\bar{\Delta}_f$ versus cohesive strength $\bar{\sigma}_c$ for $\bar{\Gamma} = 0.125$, $\bar{Y} = 0.4$, and $\bar{\delta}_{\min} = -1.0$.

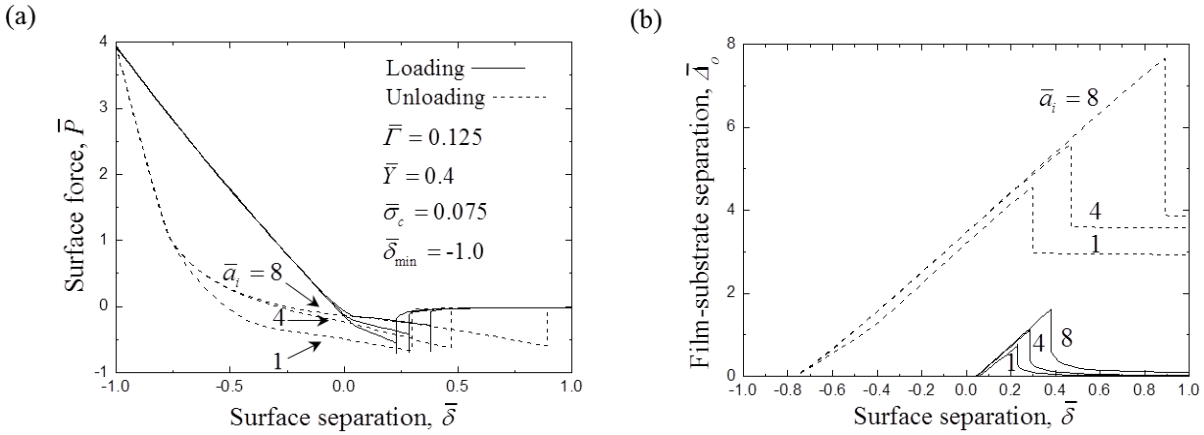

Fig. 7.15 (a) Surface force $\bar{P}$ and (b) corresponding film-substrate separation at the center of contact $\bar{\Delta}_o$ versus surface separation $\bar{\delta}$ for $\bar{\Gamma} = 0.125$, $\bar{Y} = 0.4$, $\bar{\sigma}_c = 0.075$, $\bar{\delta}_{\min} = -1.0$, and $\bar{a}_i = 1$, 4, and 8 (loading = solid lines; unloading = dashed lines).

Figure 7.16 shows the critical surface separation at jump-in $\bar{\delta}_{\text{in}} = \delta_{\text{in}}/t$ and jump-out $\bar{\delta}_{\text{out}} = \delta_{\text{out}}/t$ versus initial crack radius $\bar{a}_i$ for $\bar{\Gamma} = 0.125$, $\bar{Y} = 0.4$, $\bar{\sigma}_c = 0.075$, and $\bar{\delta}_{\min} = -1.0$. For a very small initial crack (i.e., $\bar{a}_i < 2$), $\bar{\delta}_{\text{in}}$ and $\bar{\delta}_{\text{out}}$ are almost constant, implying that adhesion-induced contact instabilities are not affected by a relatively small interfacial defect. However, above a critical defect size (e.g., $\bar{a}_i > 2.5$), $\bar{\delta}_{\text{in}}$ and $\bar{\delta}_{\text{out}}$ demonstrate a linear dependence on $\bar{a}_i$. This suggests that the size of a preexisting interfacial defect can be correlated to the surface separation at jump-in or jump-out, particularly jump-out that shows a higher

sensitivity to defect size, as indicated by the larger slope of the $\bar{\delta}_{\text{out}}$ versus $\bar{a}_i$ linear fit shown in Figure 7.16.

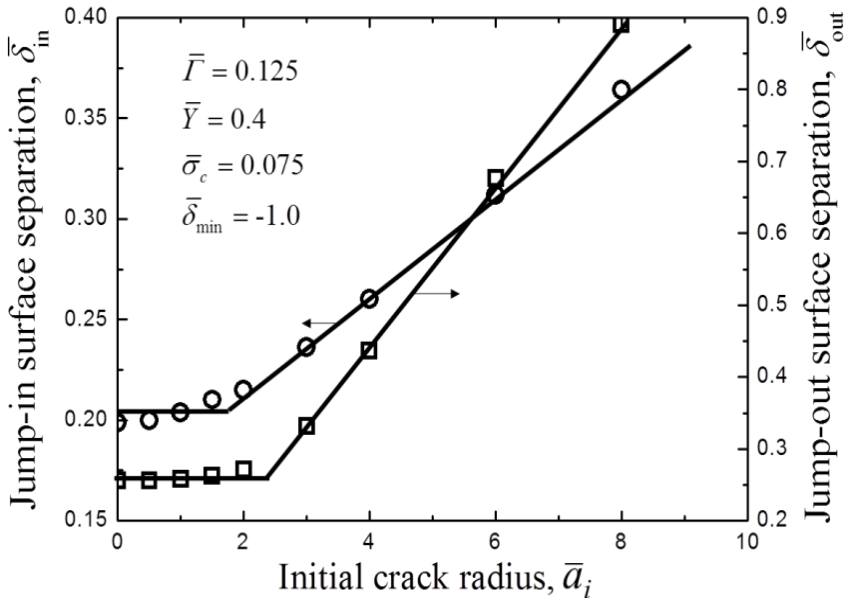

Fig. 7.16 Surface separation at jump-in $\bar{\delta}_{\text{in}}$ and jump-out $\bar{\delta}_{\text{out}}$ versus initial crack radius $\bar{a}_i$ for $\bar{\Gamma} = 0.125$, $\bar{Y} = 0.4$, $\bar{\sigma}_c = 0.075$, and $\bar{\delta}_{\text{min}} = -1.0$.

7.4. Conclusions

A finite element analysis of a rigid sphere in adhesive contact with a half-space consisting of an elastic film and an elastic-plastic semi-infinite substrate was performed to elucidate damage (crack) initiation and evolution (delamination) at the film/substrate interface. Surface adhesion was simulated by nonlinear springs obeying a force-displacement constitutive relation derived from the LJ potential. The film/substrate interface was modeled as an irreversible cohesive zone of fixed cohesive strength and work of adhesion. The overall contact behavior was analyzed by tracking the evolution of the surface force and surface separation at the interface during a full load-unload cycle.

Differences in deformation response were most pronounced during unloading. Variations in the surface force and contact stiffness during unloading correlated with the initiation and development of interfacial damage (cracking). Re-yielding in the elastic-plastic substrate occurred only in the course of damage initiation during unloading, resulting in the formation of a cohesive zone at the interface. Substrate plasticity resulted in irreversible downward deflection of the partially delaminated elastic film and the formation of a residual cohesive zone at the interface that produced tensile stresses at the tip of the interfacial crack after full unloading (jump-out). The dependence of crack-tip opening displacement on minimum surface separation (maximum compressive force) was interpreted in the context of energy release rate considerations before and after jump-out. Crack-tip opening displacement increased whereas

residual deflection (bending) of the elastic film decreased with increasing minimum surface separation.

Different unloading mechanisms were observed, depending on the yield strength of the elastic-plastic substrate. For a low-strength substrate, interface delamination was not observed during unloading, while for a substrate of intermediate strength, damage (crack) initiation and failure (delamination) at the interface occurred during unloading, leading to the formation of a residual crack upon jump-out. For a high-strength substrate, deformation during loading was essentially elastic and the interface crack formed during unloading exhibited almost complete closure upon jump-out.

The interface work of adhesion affected the contact behavior only during unloading. In particular, both surface force and contact stiffness were influenced by the evolution of interfacial damage during unloading only in the case of relatively low interface work of adhesion. Crack closure and crack-tip opening displacement after jump-out increased with interface work of adhesion.

The cohesive strength exhibited a significant effect on both loading and unloading behavior. Unstable crack initiation was found only in the case of high cohesive strength. This trend was interpreted in terms of a dimensionless parameter representing the layered medium-to-interface stiffness ratio. Crack closure and crack-tip opening displacement after jump-out increased with the decrease of the cohesive strength due to the enhancement of cohesive zone closure and the increase of the critical surface separation for interfacial failure, respectively.

The effect of an initial crack at the layer/substrate interface on the contact behavior was found to be significant only during unloading. Although the effect of the initial crack on the initial unloading response was insignificant, the surface force demonstrated a dependence on initial crack radius (size) at a later stage of unloading. Above a critical crack radius, surface separation at jump-in and jump-out increased linearly with crack radius.

Chapter 8

Contact mechanics of elastic rough surfaces in the presence of adhesion: contact instabilities and strength of adhesion

8.1. Introduction

In chapter 5-7, we have thoroughly analyzed the contact mechanics of smooth surfaces in the presence of adhesion. Great insight has been obtained on the adhesion-induced contact instabilities, plasticity accumulation and interface delamination. However, most of the real engineering surfaces are not smooth, but exhibit multi-scale roughness. To the best of author's knowledge, most of previous contact mechanics and tribology study of rough surfaces does not account for surface adhesion, which exhibits first-order effects on the reliability and endurance of miniaturized devices and accuracy of measurements obtained with microprobe-based techniques, by affecting the contact and fatigue behavior at microscopic length scales. Moreover, owing to the wide range of surface features and microprobe tip sizes (from a few tens of nanometers to several micrometers), it is imperative that contact mechanics analyses account for the multi-scale surface roughness of the probed sample. Therefore, contact models based on simple geometrical configurations, such as a sphere in contact with a flat half-space, do not yield accurate solutions of the contact force and real contact area.

Among the first contact analyses to consider adhesion effects on solid contact deformation are those of Johnson et al. (1971) and Derjaguin et al. (1975), who introduced elastic contact models for two adhering spheres, known as the JKR and the DMT model, respectively. These models yield that the pull-off force P_{off} at the instant of surface detachment is equal to $-(3/2)\pi R\Delta\gamma$ (JKR model) and $-2\pi R\Delta\gamma$ (DMT model), where R is the reduced radius of curvature ($R = [1/R_1 + 1/R_2]^{-1}$, where R_1 and R_2 are the radii of curvature of the two contacting spheres, respectively) and $\Delta\gamma$ is the work of adhesion ($\Delta\gamma = \gamma_1 + \gamma_2 - \gamma_{12}$, where γ_1 and γ_2 are the surface energies of the two spheres, respectively, and γ_{12} is the interfacial energy).

Adhesive elastic contacts can be characterized by a dimensionless parameter μ, known as the Tabor parameter (Tabor, 1977), which is defined as

$$\mu = \left[\frac{R\Delta\gamma^2}{E^{*2}\varepsilon^3}\right]^{1/3} \tag{8.1}$$

where $E^* = [(1-\nu_1^2)/E_1 + (1-\nu_2^2)/E_2]^{-1}$ is the effective elastic modulus (E and ν represent the elastic modulus and Poisson's ratio, respectively) and ε is the equilibrium interatomic distance. Tabor (1977) has argued that the JKR model is suitable for compliant spherical bodies with a large radius of curvature ($\mu > 5$), whereas the DMT model is more appropriate for stiff spherical bodies with a small radius of curvature ($\mu < 0.1$). Maugis (1992) used the Dugdale approximation to represent the adhesive stress at the contact interface and obtained P_{off} as a function of a dimensionless parameter λ ($\lambda = 1.16\mu$) in the transition range of the Tabor parameter bounded by the DMT and the JKR solutions. Carpick et al. (1999) derived a semi-

empirical equation of P_{off} in terms of λ by using a curve-fitting method and numerical results obtained by Maugis (1992). Muller et al. (1980), Greenwood (1997), and Feng (2001) used the Lennard-Jones (LJ) potential to model interfacial adhesion in elastic contacts and a self-consistent integration method to numerically analyze adhesive contact. The solution obtained from the latter approach represents a smooth transition between the DMT and the JKR solutions, but differs from that obtained by Maguis (1992) in the same range of the Tabor parameter. Using a curve-fitting method identical to that of Carpick et al. (1999), Wu (2008) obtained an equation of the dimensionless pull-off force $\bar{P}_{off} = P_{off}/2\pi R\Delta\gamma$ in terms of the Tabor parameter, given by

$$\bar{P}_{off} = -\frac{1}{8}\left(7 + \frac{1-1.98\mu^{3/2}}{1+1.98\mu^{3/2}}\right) \tag{8.2}$$

where the negative sign in Eq. (8.2) indicates an attractive force. The aforementioned self-consistent integration method has been used in finite element analyses that model interfacial adhesion by nonlinear spring elements obeying a force-displacement constitutive relation derived from the LJ potential (Du et al., 2007; Kadin et al., 2008; Song and Komvopoulos, 2011).

Although the previous studies have elucidated the role of adhesion in contact deformation of smooth solid bodies and single contacts, their applicability is limited because real surfaces exhibit multi-scale roughness. To overcome this limitation, different surface topography descriptions were used in contemporary adhesion studies of interacting rough surfaces. One of the first fundamental studies of adhesive contact between elastic rough surfaces is attributed to Fuller and Tabor (1975). Using the statistical rough-surface model of Greenwood and Williamson (1966), known as the GW model, and the JKR approximation at the asperity level, Fuller and Tabor showed that the strength of adhesion of contacting rough surfaces decreases with the dimensionless adhesion parameter θ, given by

$$\theta = \frac{E^*\sigma^{3/2}}{R^{1/2}\Delta\gamma} = \left[\frac{\sigma}{R^{1/3}\Delta\gamma^{2/3}/E^{*2/3}}\right]^{3/2} \tag{8.3}$$

where σ is the root-mean-square (rms) surface roughness. The physical meaning of θ can be understood by considering that it represents the ratio of the surface roughness to the elastic deformation caused by adhesion at the instant of surface separation, as shown by the second form of Eq. (8.3). The strength of adhesion between a smooth rubber sphere and a hard rough surface, evaluated in terms of θ (Eq. (8.2)), has been found to be in good agreement with experimental results (Fuller and Tabor, 1975). Maugis (1996) used a similar approach and the DMT model to study the contact behavior of adhering asperities and observed a contribution of the adhesion force outside the contact region of interacting asperities to the total normal force. The existence of an adhesion force in most contact systems explains the finite friction force obtained with a zero or negative (adhesive) normal force and the higher friction of clean surfaces. Morrow et al. (2003) incorporated an improved Maugis (1992) solution, originally derived by Kim et al. (1998) for the transition range bounded by the DMT and the JKR solutions, into the model of Fuller and Tabor (1975) and determined the adhesion force produced from non-contact and contact asperity regions in the entire range of λ.

To examine the effect of multi-scale roughness on the elastic-plastic deformation of adhesive contacts, Sahoo and Chowdhury (1996) described the surface topography by fractal geometry. This model was later improved by Mukherjee et al. (2004), who analyzed elastic-plastic deformation of adhering asperities by the finite element method. Li and Kim (2009) used a homogenized projection method to study the behavior of the effective cohesive zone in adhesive contact of rough surfaces and observed oscillations in the traction-separation response due to contact instabilities caused by adhesion and decohesion events between the adhering asperities. Experimental and analytical studies of Kesari et al. (2010) have shown that the force hysteresis observed in atomic force microscopy and nanoindentation measurements can be correlated to a series of asperity-contact instabilities attributable to adhesion and roughness effects. Kesari and Lew (2011) analyzed the compression of an elastic half-space by an axisymmetric rigid punch with random periodic undulations in the radial direction and observed multiple equilibrium contact regions during the loading and unloading phases by minimizing the potential energy of the system.

Although the previous studies have yielded important insight into the contact behavior of adhesive rough surfaces, the majority of these studies are either restricted to "hard" contact at the asperity scale (i.e., negligible adhesion forces between noncontacting asperities) or rely on a solution derived by Maguis (1992) that does not reproduce important physical phenomena, such as contact instabilities due to instantaneous surface contact (jump-in) encountered with contact microprobes and suspended microstructures. The objective of this study was to develop an adhesive contact analysis of elastic rough surfaces, which models surface adhesion with nonlinear springs obeying a force-displacement law derived from the LJ potential. Jump-in contact instabilities are identified by the sharp increase of the interfacial force or the instantaneous establishment of surface contact. The motivation of this study is the different dependence of macrocontact instabilities on the Tabor parameter than single-asperity contacts, reported in a previous study (Song and Komvopoulos, 2011). The effects of surface roughness and Tabor parameter on the strength of adhesion and the evolution of the interfacial force and the contact area are discussed in the context of numerical solutions. It is shown that the classical adhesion parameter of Fuller and Tabor (1975) only governs the strength of adhesion of compliant rough surfaces (high μ range). Thus, a new adhesion parameter is introduced for relatively stiff contact systems (low μ range). The applicable ranges of the aforementioned adhesion parameters are determined for three different characteristic length scales at the single-asperity and rough-surface levels and a generalized adhesion parameter is proposed for the entire range of the Tabor parameter.

8.2. Analysis of single adhesive contacts

Because contact between real (rough) surfaces comprises numerous microscopic asperity contacts, it is necessary to derive constitutive deformation relations that are applicable at the asperity level. The problem of two elastic spherical asperities in close proximity is equivalent to that of a rigid sphere of reduced radius of curvature R and an elastic half-space of effective elastic modulus E^*. In the presence of interfacial adhesive (attractive) pressure, the surface of the half-space deforms in the upward direction, as shown schematically in Fig. 8.1.

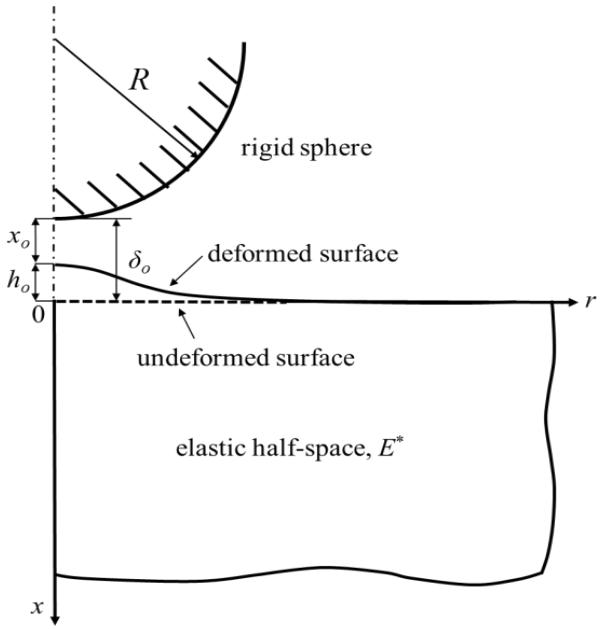

Fig. 8.1 Equivalent model of a rigid sphere of reduced radius of curvature R and an elastic half-space of effective elastic modulus E^*.

For small deformation, $x(r) = x_o + r^2/2R$, where x is the surface gap between the rigid sphere and the deformed surface of the elastic half-space, r is the horizontal (radial) coordinate, and x_o is the minimum surface gap, which is always encountered at $r = 0$. The former equation of $x(r)$ has been proven to fold for elastically deformed contacts (Song and Komvopoulos, 2011). Thus, the dimensionless elastic deflection at the center of the proximity region $\bar{h}_0 = h_0/\varepsilon$ can be obtained by integrating the solution of a point surface force acting on an elastic half-space (Boussinesq, 1885), i.e.,

$$\bar{h}_0 = \int_0^\infty \frac{p(r)}{\pi E^* r} 2\pi r dr = \sqrt{2}\pi\mu^{3/2}\left[\bar{x}_0^{-5/2} - \frac{2145}{4096}\bar{x}_0^{-17/2}\right] \tag{8.4}$$

where $\bar{x}_o = x_o/\varepsilon$ is the dimensionless minimum surface gap and $p(r)$ is the adhesive pressure, derived from the LJ potential (Song and Komvopoulos, 2011). Consequently, the dimensionless minimum surface separation at $r = 0$, defined as $\bar{\delta}_o = \delta_o/\varepsilon$, can be expressed as

$$\bar{\delta}_o = \bar{x}_o + \bar{h}_o \tag{8.5}$$

Analytical and finite element results (Song and Komvopoulos, 2011) show that jump-in is not observed for $\mu < 0.5$ and the interfacial force P and contact area A vary continuously as the two asperities approach each other (Fig. 8.2(a)) and 8.2(c), respectively), while for $\mu > 0.5$ jump-in commences, as evidenced by the abrupt increase of the interfacial force (tensile) (Fig. 8.2(b)) and the instantaneous establishment of surface contact (Fig. 8.2(d)). For elastic adhesive contacts, the maximum adhesion force $P_{\max}$ during the approach of the surfaces is equal to the maximum tensile force at the instant of surface detachment during unloading, referred to as the pull-off force P_{off}. The critical (minimum) surface separation corresponding to $P_{\max}$ and the instant of initial contact (i.e., transition from zero to nonzero contact area) are denoted by δ_{oc}

and δ_o^*, respectively (Fig. 8.2). The definition of the contact area may appear to be controversial because "hard" contact, such as that considered in classical contact mechanics, is not possible in the present analysis because of the repulsive term of the LJ potential (Greenwood, 1997; Feng, 2000, 2001). Thus, for consistency with classical contact mechanics, the contact area is defined as the area of compressive normal traction. For $\mu < 0.5$, the contact area at the instant of $P_{\max}$ can be either zero or nonzero. In particular, for very low μ values, $P_{\max}$ is encountered before contact (i.e., $\delta_{oc} > \delta_o^*$), for moderate μ values less than 0.5, contact commences before the occurrence of $P_{\max}$ (i.e., $\delta_{oc} < \delta_o^*$) (Figs. 8.2(a) and 8.2(c)), and for $\mu > 0.5$, both $P_{\max}$ and initial contact are encountered at the instant of jump-in (i.e., $\delta_{oc} = \delta_o^*$) (Figs. 8.2(b) and 8.2(d)).

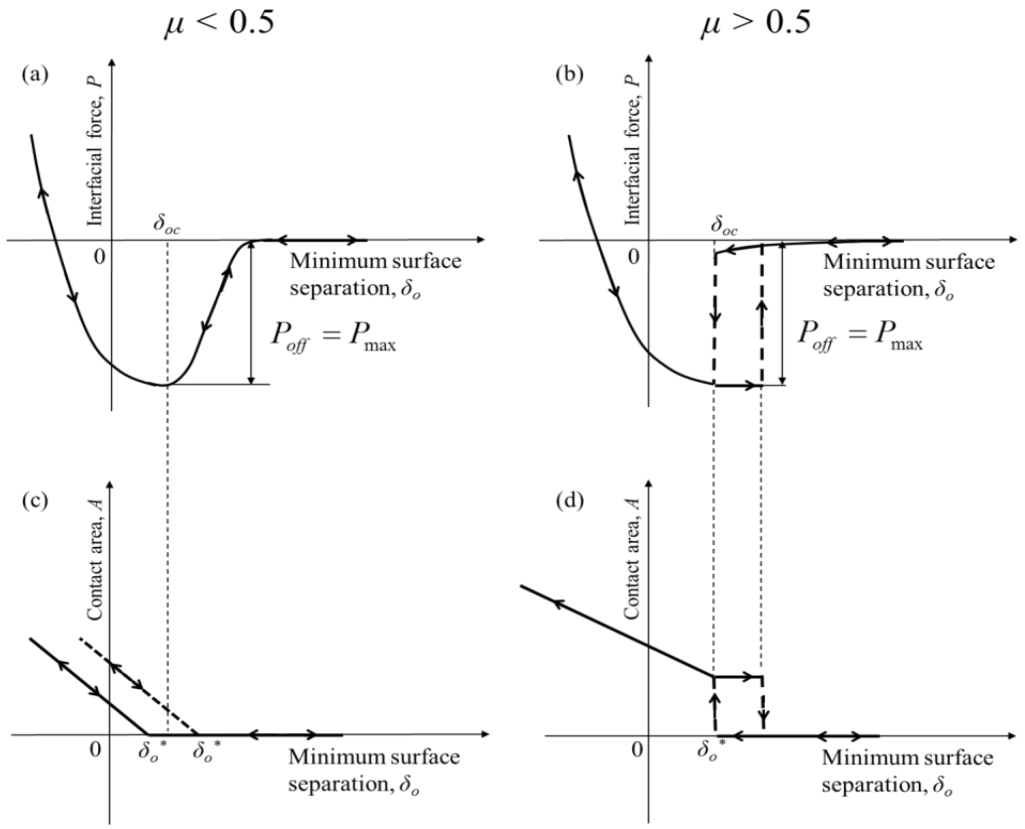

Fig. 8.2 Schematics of interfacial force and contact area versus minimum surface separation for smooth ($\mu < 0.5$) and discontinuous ($\mu > 0.5$) surface approach and retraction.

Fig. 8.3 shows the dimensionless contact radius $\bar{a}_c = a_c/(\varepsilon R)^{1/2}$ corresponding to the critical minimum surface separation δ_{oc} as a function of the Tabor parameter. Discrete data points represent numerical results obtained with a previous finite element model of adhesive contact (Song and Komvopoulos, 2011). Curve fitting of the numerical data yields

$$\bar{a}_c = 0 \qquad (\mu < 0.19) \tag{8.6a}$$

$$\bar{a}_c = 0.83\,(\mu - 0.19)^{1/2} \qquad (\mu \geq 0.19) \tag{8.6b}$$

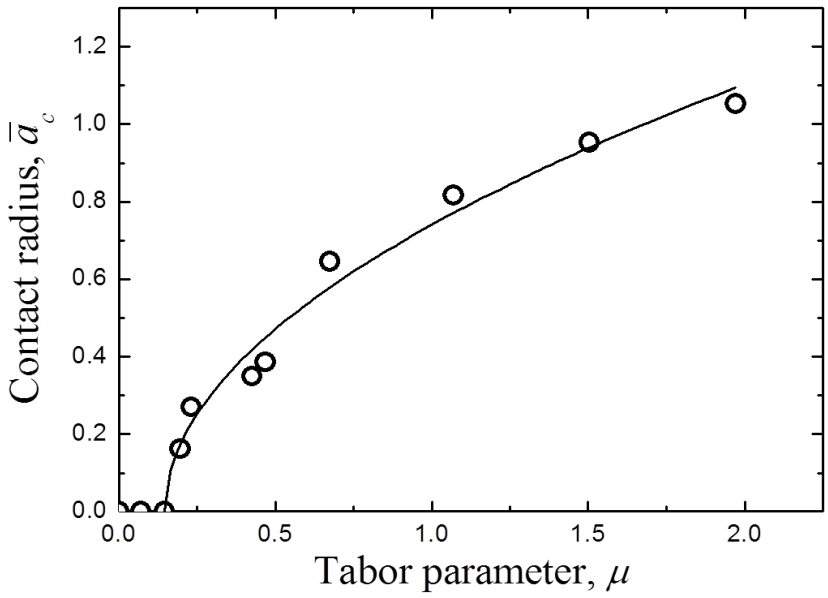

Fig. 8.3 Critical contact radius $\bar{a}_c$ at the instant of maximum adhesive force versus Tabor parameter μ. Discrete data points represent numerical data obtained with a previous finite element model of adhesive contact (Song and Komvopoulos, 2011). The solid curve is a best fit through the numerical data.

Eqs. (8.6a) and (8.6b) indicate that, for $\mu < 0.19$, $P_{\max}$ occurs before the establishment of surface contact (i.e., $\delta_{oc} > \delta_o^*$), while for $\mu \geq 0.19$, contact is established either before or upon the occurrence of $P_{\max}$ (i.e., $\delta_{oc} < \delta_o^*$), with the contact radius given by Eq. (8.6b). It is noted that it is impossible to obtain a closed-form solution of the contact area (defined as the surface region of compressive normal stress) at the instant of $P_{\max}$, particularly the contact area instantaneously established upon jump-in ($\mu \geq 0.5$). Eq. (8.6b) is the first relation to yield the contact area at the instant of $P_{\max}$ in terms of the Tabor parameter. The validity of Eq. (8.6b) is confirmed by favorable comparisons with analytical solutions obtained for large μ values. For example, for $\mu > 5$, Eq. (8.6b) yields $\bar{a}_c \approx 0.83\mu^{1/2}$, which is in excellent agreement with the solution derived from JKR theory, $\bar{a}_c \approx 0.88\mu^{1/2}$ (Eq. (B9) in Appendix B).

Considering the significant effect of the jump-in instability on the evolution of the interfacial force and the contact area, two different sets of constitutive relations of adhesive asperity contacts must be derived – one set for continuous elastic contact and another set for discontinuous elastic contact due to the occurrence of the jump-in instability. Moreover, because of the transition from attractive- to repulsive-dominant contact behavior encountered with the decrease of the surface separation, different constitutive relations must be derived for the surface separation ranges of attractive and repulsive dominant force, i.e., $\delta_o \geq (\delta_{oc}, \delta_o^*)$ and $\delta_o < (\delta_{oc}, \delta_o^*)$, respectively.

8.2.1. Constitutive relations for surface separation range of dominant attractive force

8.2.1.1. Elastic adhesive contacts without jump-in instability

In the absence of the jump-in instability ($\mu < 0.5$), the interfacial force P increases continuously from zero (large δ_o) to a maximum adhesion force $P_{\max}$ with the decrease of δ_o to a critical value δ_{oc} (Fig. 8.2(a)). Fig. 8.4 shows the dimensionless critical minimum surface separation $\bar{\delta}_{oc}$ $(= \delta_{oc}/\varepsilon)$ corresponding to $P_{\max}$ as a function of μ for adhesive elastic contacts that do not exhibit jump-in. From a linear fit through the numerical results (discrete data points), obtained with a previous finite element model (Song and Komvopoulos, 2011), it is found that

$$\bar{\delta}_{oc} = 1 + 0.922\mu \tag{8.7}$$

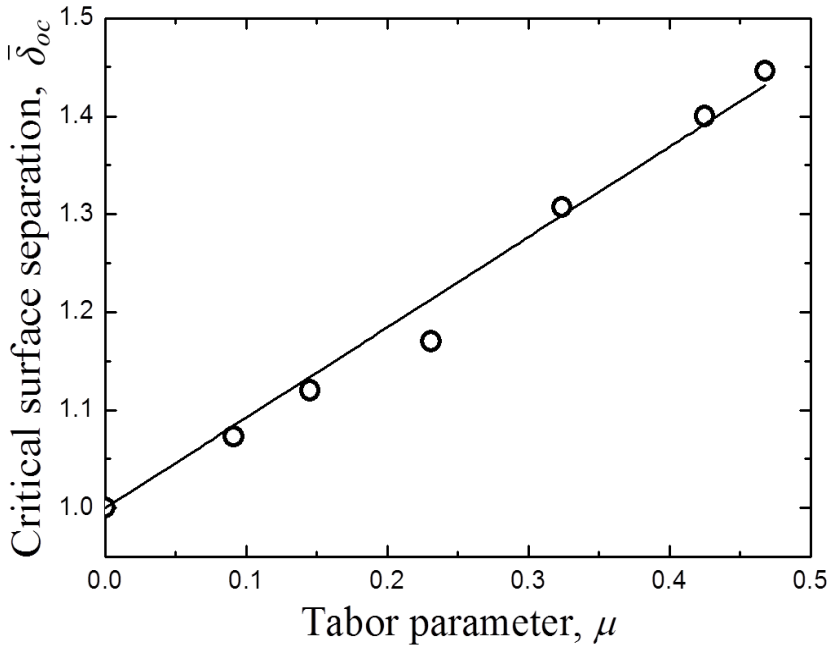

Fig. 8.4 Critical surface separation $\bar{\delta}_{oc}$ versus Tabor parameter μ for single contacts that do not exhibit jump-in instability ($\mu < 0.5$). Discrete data points represent numerical data obtained with a previous finite element model of adhesive contact (Song and Komvopoulos, 2011). The solid line is a best fit through the numerical data.

The validity of Eq. (8.7) is verified by qualitative comparisons. For instance, in the case of a rigid sphere in adhesive contact with a rigid half-space ($\mu = 0$), $P_{\max}$ occurs for $\bar{\delta}_{oc} = 1$, i.e., for a central surface separation equal to the equilibrium interatomic distance, which is the solution obtained by Bradley (1932). The increasing trend of δ_{oc} with μ, indicated by Eq. (8.7), is expected because δ_{oc} at the instant of $P_{\max}$ increases with the half-space compliance (i.e., increase of μ) due to the enhancement of the upward elastic deflection of the half-space surface with the increase of its compliance.

Assuming small deformation in the elastic half-space for $\bar{\delta}_o > \bar{\delta}_{oc}$, the dimensionless interfacial force $\bar{P} = P/2\pi R\Delta\gamma$, obtained by integrating the surface traction applied to the undeformed surface of the half-space (Boussinesq, 1885), is given by

$$\bar{P} = \frac{1}{-2\pi R\varepsilon\Delta\gamma}\int_0^\infty p(r)2\pi r dr = \frac{1}{-2\pi R\varepsilon\Delta\gamma}\int_0^\infty \left[\frac{8\Delta\gamma}{3\varepsilon}\left(\frac{\varepsilon}{\delta_o + r^2/2R}\right)^{-3} - \left(\frac{\varepsilon}{\delta_o + r^2/2R}\right)^{-9}\right] 2\pi r dr = \frac{1}{3}\left(\bar{\delta}_o^{-8} - 4\bar{\delta}_o^{-2}\right) \qquad \left(\bar{\delta}_o \geq \bar{\delta}_{oc}\right) \tag{8.8}$$

Applying the boundary condition $\bar{P}\left(\bar{\delta}_o = \bar{\delta}_{oc}\right) = \bar{P}_{\max} = P_{\max}/2\pi R\Delta\gamma$, where $P_{\max}$ is given by Eq. (8.2), because for elastic adhesive contact $P_{\max} = P_{off}$, while retaining the force-distance proportionality that is intrinsic of the LJ potential (i.e., $\bar{P} \propto \bar{\delta}_o^{-8} - 4\bar{\delta}_o^{-2}$), Eq. (8.8) can be modified as

$$\bar{P} = \left[\frac{\bar{\delta}_o^{-8} - 4\bar{\delta}_o^{-2}}{\bar{\delta}_{oc}^{-8} - 4\bar{\delta}_{oc}^{-2}}\right]\bar{P}_{\max} \qquad \left(\bar{\delta}_o \geq \bar{\delta}_{oc}\right) \tag{8.9}$$

Fig. 8.5 shows analytical solutions (Eq. (8.9)) and finite element method (FEM) results (Song and Komvopoulos, 2011) of the dimensionless interfacial force $\bar{P}$ versus the dimensionless minimum surface separation $\bar{\delta}_o$ at $r = 0$ for μ in the range of 0.091–0.425. The good agreement between analytical and FEM results validates Eq. (8.9).

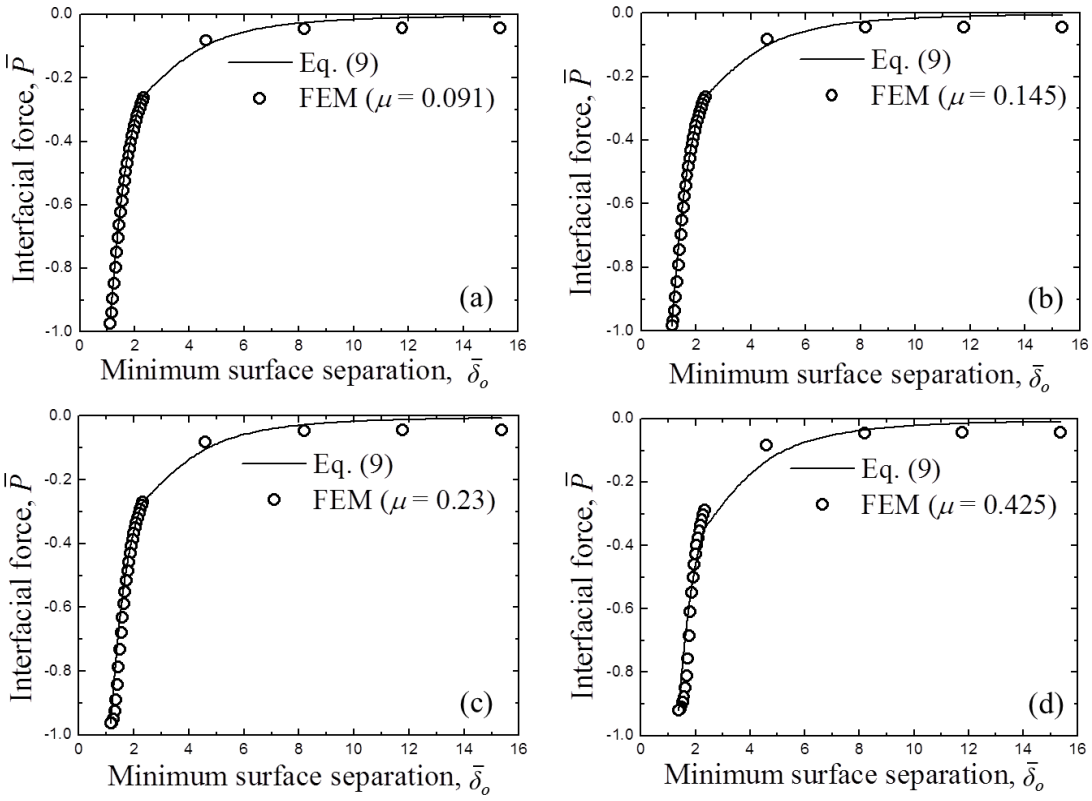

Fig. 8.5 Comparison of analytical solutions (Eq. (9)) and numerical results obtained with the model of a previous FEM study (Song and Komvopoulos, 2011) of interfacial force $\bar{P}$ versus minimum surface separation $\bar{\delta}_o$ for Tabor parameter μ equal to (a) 0.091, (b) 0.145, (c) 0.23, and (d) 0.425.

Because the minimum surface separation occurs at $r = 0$, δ_o^* is obtained for $\bar{x}_0 = 1$. Thus, the following equation of the dimensionless critical minimum surface separation $\bar{\delta}_o^*$ at the instant of initial contact is obtained by substituting $\bar{x}_0 = 1$ into Eqs. (8.4) and (8.5):

$$\bar{\delta}_o^* = 1 + 2.116\,\mu^{3/2} \tag{8.10}$$

For the dimensionless contact area, defined as $\bar{A} = A/\varepsilon R$, it follows that

$$\bar{A} = 0 \quad (\bar{\delta}_o \geq \bar{\delta}_o^*) \tag{8.11}$$

A transition value of the Tabor parameter equal to 0.19 is obtained by equating Eq. (8.7) with Eq. (8.10). For $\mu < 0.19$, $\bar{\delta}_o^* < \bar{\delta}_{oc}$, implying that $\bar{A} = 0$ at the instant of $\bar{P}_{\max}$, whereas for $0.19 < \mu < 0.5$, a finite contact area is established before the occurrence of $\bar{P}_{\max}$, which is in excellent agreement with the predictions of Eqs. (8.6a) and (8.6b).

8.2.1.2. Elastic adhesive contacts with jump-in instability

As mentioned earlier, when $\mu > 0.5$, initial contact and $P_{\max}$ occur simultaneously at the instant of jump-in (i.e., $\delta_{oc} = \delta_o^*$). The dimensionless critical surface gap $\bar{x}_{oc} = x_{oc}/\varepsilon$ at the instant of jump-in is the solution of the following equation (Song and Komvopoulos, 2011):

$$11.1\bar{x}_{oc}{}^{-7/2} - 19.8\bar{x}_{oc}{}^{-19/2} = \mu^{-3/2} \tag{8.12}$$

For $\mu > 0.5$, Eq. (12) yields two solutions of $\bar{x}_{oc}$, with the larger root corresponding to the jump-in instability given by

$$\bar{x}_{oc} = -0.3 + 2.2\mu^{2/5} \tag{8.13}$$

Substitution of Eq. (8.13) into Eqs. (8.4) and (8.5) yields

$$\bar{\delta}_o^* = \bar{\delta}_{oc} = -0.3 + 2.2\mu^{2/5} + \sqrt{2}\pi\mu^{3/2}\left[\left(-0.3 + 2.2\mu^{2/5}\right)^{-5/2} - \frac{2145}{4096}\left(-0.3 + 2.2\mu^{2/5}\right)^{-17/2}\right] \tag{8.14}$$

For the critical Tabor parameter for jump-in ($\mu = 0.5$), Eq. (8.14) gives $\bar{\delta}_{oc} = 4$, which is significantly higher than $\bar{\delta}_{oc} = 1.46$, obtained from Eq. (8.7) for adhesive contacts not exhibiting jump-in. For $\bar{\delta}_o \geq \bar{\delta}_{oc} = \bar{\delta}_o^*$, elastic deformation can be ignored as negligibly small in comparison to the relatively large surface separation. Thus, an approximate expression of the interfacial force can be derived by integrating the surface traction for the undeformed configuration of the half-space, i.e.,

$$\bar{P} = \frac{1}{-2\pi R\varepsilon\Delta\gamma}\int_0^\infty p(r)\,2\pi r dr = = \frac{1}{-2\pi R\varepsilon\Delta\gamma}\int_0^\infty \left[\frac{8\Delta\gamma}{3\varepsilon}\left(\frac{\varepsilon}{\delta_o + r^2/2R}\right)^{-3} - \left(\frac{\varepsilon}{\delta_o + r^2/2R}\right)^{-9}\right] 2\pi r dr = \frac{1}{3}\left(\bar{\delta}_o{}^{-8} - 4\bar{\delta}_o{}^{-2}\right) \tag{8.15}$$

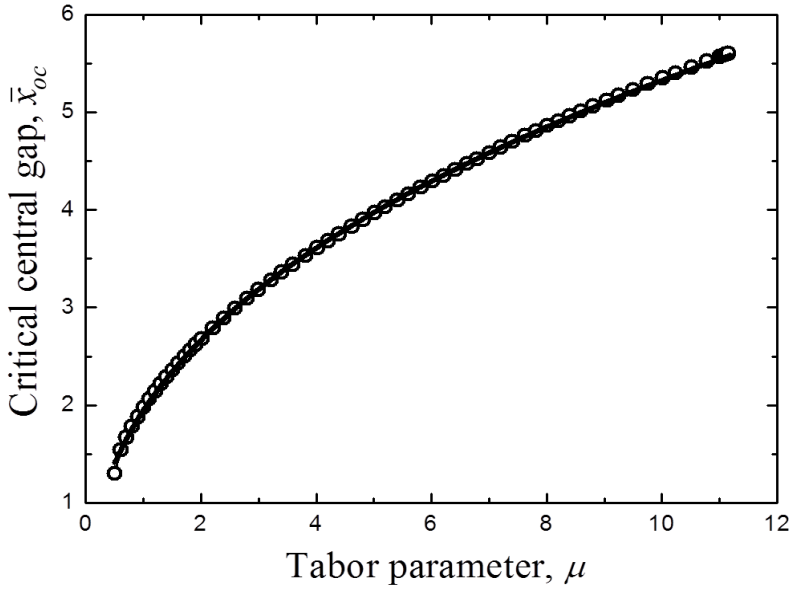

Fig. 8.6 Critical central gap $\bar{x}_{oc}$ for jump-in instability versus Tabor parameter μ. Discrete data points represent numerical data obtained with a previous finite element model of adhesive contact (Song and Komvopoulos, 2011). The solid curve is a best fit through the numerical data.

As evidenced from Fig. 8.6 and Eq. (8.13), before the occurrence of jump-in, $\bar{x}_{oc} > 1$. Thus from Eq. (8.5), it follows that $\bar{\delta}_o > 1$ is always true for $\mu > 0.5$, and because $\bar{\delta}_o$ is the minimum surface separation, it is concluded that the surface traction is attractive everywhere and the contact area is zero, i.e.,

$$\bar{A} = 0 \quad (\bar{\delta}_o \geq \bar{\delta}_o^*) \tag{8.16}$$

At the instant of jump-in ($\bar{\delta}_o = \bar{\delta}_{oc} = \bar{\delta}_o^*$), the interfacial force increases instantaneously from a value given by Eq. (8.15) to a value given by Eq. (8.2), with the simultaneous abrupt formation of a contact area of dimensionless radius $\bar{a}_c$ (Eq. (8.6b)).

8.2.2. Constitutive relations for surface separation range of dominant repulsive force

The decrease of the minimum surface separation δ_o below δ_{oc} and δ_o^* leads to the dominance of the repulsive term in the LJ potential and the dependence of the deformation behavior on the elastic material properties. The evolution of the interfacial force and the contact area was analyzed with a previous FEM model of adhesive contact (Song and Komvopoulos, 2011), using μ in the range of 0.091 (no jump-in) to 1.971 (jump-in). Figs. 8.7(a) and 8.7(b) show the dimensionless interfacial force $(P - P_{\max})/(4E^*R^2/3)$ and the contact area $(A - \pi a_c^2)/\pi R^2$ as functions of the dimensionless minimum surface separation $(\delta_{oc} - \delta_o)/R$ and $(\delta_o^* - \delta_o)/R$, respectively. The good agreement between FEM results and analytical (Hertz) solutions suggests that the jump-in instability does not affect the constitutive relations in the

surface separation range dominated by the repulsive force. Hence, the following constitutive relations hold after the occurrence of $P_{\max}$ and the establishment of initial contact:

(a) For adhesive elastic contacts not exhibiting jump-in ($\mu < 0.5$):

$$\bar{P} = \bar{P}_{\max} + \bar{P}_H = \bar{P}_{\max} + \frac{1}{2\pi R\Delta\gamma}\left(\frac{4}{3}E^* R^{1/2}\right)(\delta_{oc} - \delta_o)^{3/2} = \bar{P}_{\max} + \frac{2}{3\pi}\left(\frac{\bar{\delta}_{oc} - \bar{\delta}_o}{\mu}\right)^{3/2} \quad (\bar{\delta}_o < \bar{\delta}_{oc}) \tag{8.17}$$

$$\bar{A} = \bar{A}_H = \frac{A}{\varepsilon R} = \frac{\pi R(\delta_o^* - \delta_o)}{\varepsilon R} = \pi\left(\bar{\delta}_o^* - \bar{\delta}_o\right) \qquad (\bar{\delta}_o < \bar{\delta}_o^*) \tag{8.18}$$

(b) For adhesive elastic contacts exhibiting jump-in ($\mu > 0.5$):

$$\bar{P} = \bar{P}_{\max} + \bar{P}_H = \bar{P}_{\max} + \frac{1}{2\pi R\Delta\gamma}\left(\frac{4}{3}E^* R^{1/2}\right)(\delta_{oc} - \delta_o)^{3/2} = \bar{P}_{\max} + \frac{2}{3\pi}\left(\frac{\bar{\delta}_{oc} - \bar{\delta}_o}{\mu}\right)^{3/2} \quad (\bar{\delta}_o < \bar{\delta}_{oc}) \tag{8.19}$$

$$\bar{A} = \pi\bar{a}_c^2 + \bar{A}_H = \pi\bar{a}_c{}^2 + \frac{\pi R(\delta_o^* - \delta_o)}{\varepsilon R} = \pi\left[0.69(\mu - 0.19) + \bar{\delta}_o^* - \bar{\delta}_o\right] \qquad \left(\bar{\delta}_o < \bar{\delta}_o^*\right) \tag{8.20}$$

where subscript *H* denotes Hertz analysis.

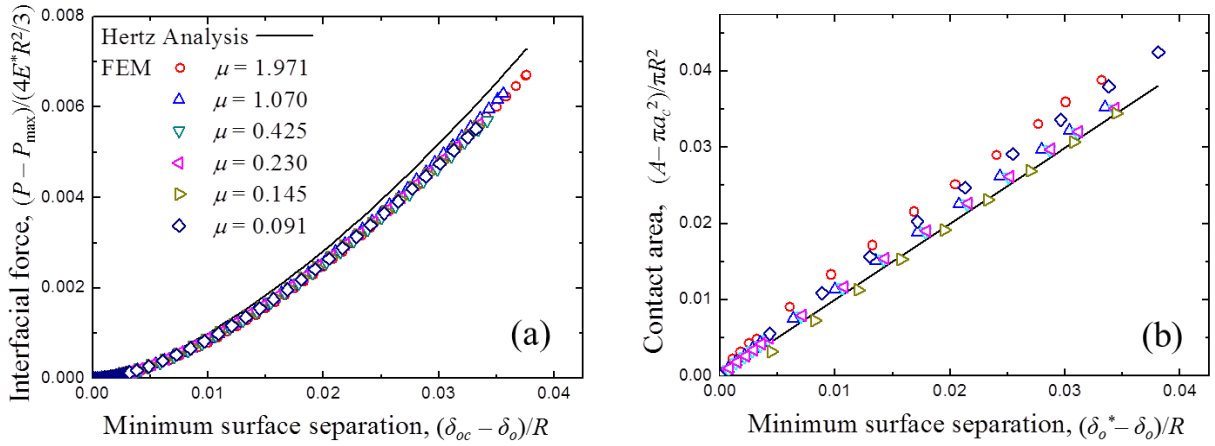

Fig. 8.7 Comparison of analytical solutions (Hertz analysis) and FEM results obtained with a previous finite element model of adhesive contact (Song and Komvopoulos, 2011): (a) interfacial force $(P - P_{\max})/(4E^* R^2/3)$ versus minimum surface separation $(\delta_{oc} - \delta_o)/R$ after the occurrence of maximum adhesive force and (b) contact area $(A - \pi a_c^2)/\pi R^2$ versus minimum surface separation $(\delta_o^* - \delta_o)/R$ after the establishment of contact for Tabor parameter μ = 0.091–1.971.

8.3. Contact analysis of elastic rough surfaces

8.3.1. Rough surface model

Fig. 8.8 shows a cross-sectional schematic of the equivalent system of two rough surfaces consisting of a rigid rough surface and a flat elastic half-space at a mean surface separation d from the rough surface. The rough surface is represented by the GW model, consisting of uniformly distributed spherical asperities of fixed radius of curvature R, area density η, and randomly varying height z. The topography of an isotropic rough surface can be uniquely defined by R, η, and the standard deviation of the surface heights, referred to as the rms surface roughness σ. The ratio of the standard deviation of the asperity heights σ_s to the surface roughness σ, denoted by ω, can be expressed as (McCool, 1986)

$$\omega = \frac{\sigma_s}{\sigma} = \left[1 - \frac{3.717\times10^{-4}}{(\sigma R\eta)^2}\right]^{1/2} \tag{8.21}$$

The probability of an asperity height to be between z and z + dz is equal to $\phi(z)$dz, where $\phi(z)$ is the asperity height distribution function, described by a normal probability density function, which in dimensionless form can be written as

$$\tilde{\phi}(\tilde{z}) = \frac{\omega}{\sqrt{2\pi}}\exp\left(-\frac{\omega^2\tilde{z}^2}{2}\right) \tag{8.22}$$

where $\tilde{z} = z/\sigma$. (Hereafter, symbol ~ over a parameter denotes normalization by σ.) For a rigid rough surface of asperity area density η and apparent contact area A_o, the total number of potentially contacting asperities is $N = A_o\eta$. Because all the asperities possess the same radius of curvature, they are characterized by the same Tabor parameter.

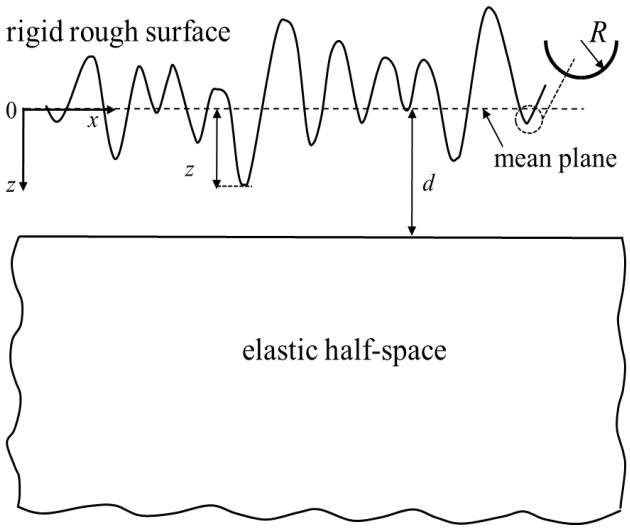

Fig. 8.8 Schematic of equivalent rough-surface contact model comprising a rigid rough surface and an elastic half-space.

8.3.2. Constitutive contact relations for rough elastic surfaces without jump-in instabilities

For rough elastic surfaces comprising asperity contacts that do not exhibit jump-in contact instabilities (i.e., $\mu < 0.5$), the numbers of asperity contacts in the surface separation

range dominated by attraction ($\tilde{d} - \tilde{z} \geq \tilde{\delta}_{oc}$) and repulsion ($\tilde{d} - \tilde{z} < \tilde{\delta}_{oc}$) N_1 and N_2, respectively, where $\tilde{d} = d/\sigma$ is the dimensionless mean surface separation (Fig. 8) and $\tilde{\delta}_{oc} = \delta_{oc}/\sigma$, are given by

$$N_1 = N \int_{-\infty}^{\tilde{d}-\tilde{\delta}_{oc}} \tilde{\phi}(\tilde{z}) d\tilde{z} \tag{8.23a}$$

and

$$N_2 = N \int_{\tilde{d}-\tilde{\delta}_{oc}}^{\infty} \tilde{\phi}(\tilde{z}) d\tilde{z} \tag{8.23b}$$

where $\tilde{\delta}_{oc} = \delta_{oc}/\sigma$ and δ_{oc} is given by Eq. (7).

Using Eqs. (8.2), (8.9), (8.17), (8.23a), and (8.23b), the dimensionless total interfacial force $\bar{F}$ can be expressed as

$$\bar{F} = \frac{F}{2\pi R A_0 \Delta\gamma\eta} = \int_{-\infty}^{\tilde{d}-\tilde{\delta}_{oc}} -\frac{1}{8}\left(7 + \frac{1-1.98\mu^{3/2}}{1+1.98\mu^{3/2}}\right) \frac{4\left[\frac{(\tilde{d}-\tilde{z})\sigma}{\varepsilon}\right]^{-2} - \left[\frac{(\tilde{d}-\tilde{z})\sigma}{\varepsilon}\right]^{-8}}{4\bar{\delta}_{oc}^{-2} - \bar{\delta}_{oc}^{-8}} \tilde{\phi}(\tilde{z}) d\tilde{z}$$
$$+ \int_{\tilde{d}-\tilde{\delta}_{oc}}^{+\infty} \left[-\frac{1}{8}\left(7 + \frac{1-1.98\mu^{3/2}}{1+1.98\mu^{3/2}}\right) + \frac{2E^*R}{3\pi\Delta\gamma}\left[\frac{\left(\tilde{z}-(\tilde{d}-\tilde{\delta}_{oc})\right)\sigma}{R}\right]^{3/2} \right] \tilde{\phi}(\tilde{z}) d\tilde{z} \tag{8.24}$$

The numbers of noncontacting and contacting asperities N_3 and N_4, respectively, are given by

$$N_3 = N \int_{-\infty}^{\tilde{d}-\tilde{\delta}_o^*} \tilde{\phi}(\tilde{z}) d\tilde{z} \tag{8.25a}$$

and

$$N_4 = N \int_{\tilde{d}-\tilde{\delta}_o^*}^{\infty} \tilde{\phi}(\tilde{z}) d\tilde{z} \tag{8.25b}$$

where $\tilde{\delta}_o^* = \delta_o^*/\sigma$ and δ_o^* is given by Eq. (8.10).

Using Eqs. (8.10), (8.18), (8.25a), and (8.25b), the dimensionless total contact area $\bar{S}$ can be expressed as

$$\bar{S} = \frac{S}{RA_0\eta\varepsilon} = \int_{\tilde{d}-\tilde{\delta}_o^*}^{+\infty} \frac{\pi\sigma}{\varepsilon}\left[\tilde{z} - \left(\tilde{d} - \tilde{\delta}_o^*\right)\right] \tilde{\phi}(\tilde{z}) d\tilde{z} \tag{8.26}$$

8.3.3. Constitutive contact relations for rough elastic surfaces exhibiting jump-in instabilities

For asperity contacts demonstrating jump-in contact instabilities ($\mu > 0.5$), all asperities in the surface separation range dominated by attraction are not in contact, whereas all asperities

in the surface separation range dominated by repulsion are in contact because $\delta_{oc} = \delta_o^*$. Thus, the corresponding asperity numbers are given by

$$N_5 = N \int_{-\infty}^{\tilde{d}-\tilde{\delta}_{oc}} \tilde{\phi}(\tilde{z}) d\tilde{z} \tag{8.27a}$$

and

$$N_6 = N \int_{\tilde{d}-\tilde{\delta}_{oc}}^{\infty} \tilde{\phi}(\tilde{z}) d\tilde{z} \tag{8.27b}$$

where $\tilde{\delta}_{oc}$ is obtained from Eq. (8.16).

Using Eqs. (8.2), (8.15), (8.19), (8.27a), and (8.27b), the dimensionless total interfacial force $\bar{F}$ can be written as

$$\bar{F} = \frac{F}{2\pi R A_0 \Delta\gamma\eta} = \int_{-\infty}^{\tilde{d}-\tilde{\delta}_{oc}} \frac{1}{3}\left[-4\left[\frac{(\tilde{d}-\tilde{z})\sigma}{\varepsilon}\right]^{-2} + \left[\frac{(\tilde{d}-\tilde{z})\sigma}{\varepsilon}\right]^{-8}\right]\tilde{\phi}(\tilde{z})d\tilde{z}$$
$$+ \int_{\tilde{d}-\tilde{\delta}_{oc}}^{+\infty}\left[-\frac{1}{8}\left(7 + \frac{1-1.98\mu^{3/2}}{1+1.98\mu^{3/2}}\right) + \frac{2E^*R}{3\pi\Delta\gamma}\left[\frac{\left(\tilde{z}-(\tilde{d}-\tilde{\delta}_{oc})\right)\sigma}{R}\right]^{3/2}\right]\tilde{\phi}(\tilde{z})d\tilde{z} \tag{8.28}$$

From Eqs. (8.16), (8.20), (8.27a), and (8.27b), the dimensionless total contact area $\bar{S}$ can be obtained as

$$\bar{S} = \frac{S}{RA_0\eta\varepsilon} = \int_{\tilde{d}-\tilde{\delta}_o^*}^{+\infty} \pi\left[0.69(\mu - 0.19) + \left[\tilde{z} - \left(\tilde{d} - \tilde{\delta}_o^*\right)\right]\frac{\sigma}{\varepsilon}\right]\tilde{\phi}(\tilde{z})d\tilde{z} \tag{8.29}$$

8.4. Results and discussion

8.4.1. Effect of adhesion-induced instabilities at the asperity level on the contact behavior of rough surfaces

Figs. 8.9(a) and 8.9(b) show the dimensionless total interfacial force $\bar{F}$ and the total contact area $\bar{S}$ of different rough surfaces as functions of the dimensionless mean surface separation $\tilde{d}$, respectively, for fixed surface roughness (σ = 2 nm) and μ in the range of 0.5–46.9. As expected, lower values of the Tabor parameter characterize stiffer contact systems. Differences in the adhesive contact behavior between a single asperity and a rough surface can be examined by considering the variation of the interfacial force for μ = 10. (The inset of Fig. 8.9(a) shows a magnified plot of the interfacial force versus the mean surface separation for μ = 10.) It can be seen that the dimensionless maximum adhesive force $\bar{F}_{\max}$ obtained for μ = 10 is significantly less than 0.75, which is the value predicted by the JKR model (single-asperity contact), and jump-in is not encountered despite that $\mu > 0.5$, which is the critical Tabor parameter for jump-in to occur in single-asperity adhesive contacts (Song and Komvopoulos, 2011). Fig. 8.9(b) shows three distinct surface separation ranges of the evolution of the contact area. In the high range of mean surface separation, contact does not occur (range of zero contact

area) and the interfacial force is very low and attractive because the surfaces are sufficiently apart. The critical surface separation for initial contact increases with the Tabor parameter due to the enhancement of jump-in contact at the asperity level (Eq. (8.14)). In the intermediate range of mean surface separation, the contact area increases nonlinearly as the surfaces approach closer, especially for higher μ values. In this range, asperities on the rough surface jump into contact with the elastic half-space, causing abrupt surface contact and the rapid growth of the contact area. The evolution of the contact area in the intermediate distance range is more pronounced for contact systems characterized by high μ values, implying an enhancement of the jump-in instabilities with increasing Tabor parameter. In addition, the rate of increase of the contact area (slope of $\bar{S}$ curves) also increases with the Tabor parameter (Eq. (8.6b)). In the low range of mean surface separation, the contact area increases linearly with the decrease of the mean surface separation at a rate independent of μ. In this range, the contact behavior is dominated by the repulsive term of the LJ potential and the linear response of the contact area is independent of μ and is accurately described by Hertz theory (Eq. (8.20)). The observed evolution of the contact area, particularly in the intermediate distance range, suggests that even though jump-in instabilities at the asperity level are not reflected in the interfacial force response (Fig. 8.9(a)), they affect the contact behavior. Therefore, it is necessary for constitutive contact models of adhesive rough surfaces to account for such contact instabilities.

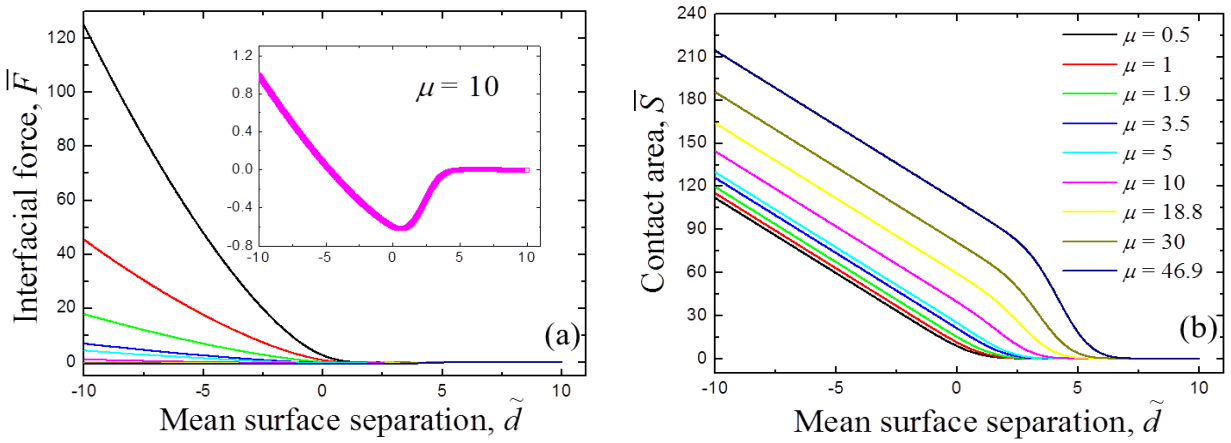

Fig. 8.9 (a) Interfacial force $\bar{F}$ and (b) contact area $\bar{S}$ versus mean surface separation $\bar{d}$ for fixed surface roughness (σ = 2 nm) and Tabor parameter μ = 0.5–46.9. The inset in (a) is a magnified plot of the interfacial force for $\mu = 10$.

8.4.2. Effect of surface roughness on strength of adhesion

Fig. 8.10 shows the dimensionless maximum attractive force between rough surfaces $\bar{F}_{\max}$, hereafter referred to as the strength of adhesion, as a function of the surface roughness σ for μ = 0.1, 1.0, and 10. All three curves show the same general trend, i.e., an enhancement of the strength of adhesion with decreasing surface roughness. For a given surface roughness, the strength of adhesion increases with the Tabor parameter. The critical surface roughness for zero strength of adhesion also increases with the Tabor parameter, implying more pronounced adhesion effects with compliant surfaces. This is in agreement with the adhesion parameter θ of

Fuller and Tabor (1975), which predicts a higher strength of adhesion for smoother and more compliant surfaces (Eq. (8.2)).

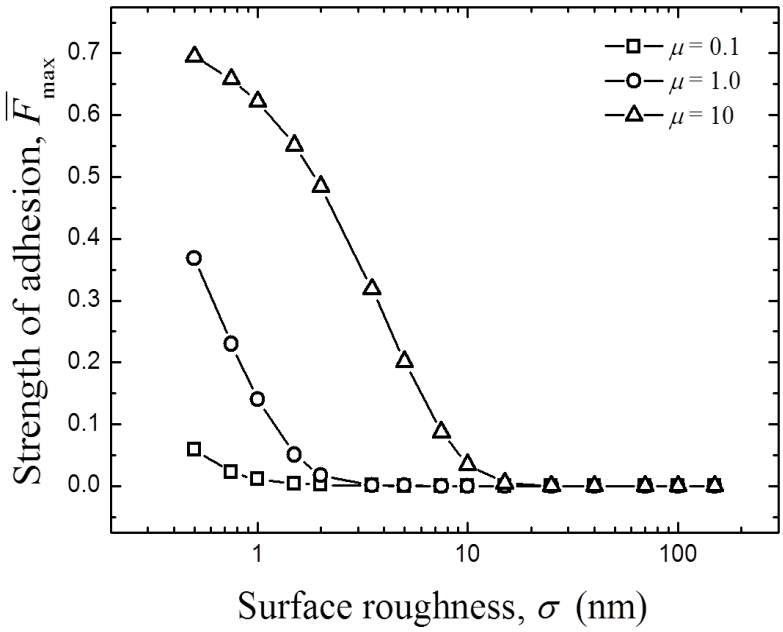

Fig. 8.10 Strength of adhesion $\bar{F}_{\max}$ versus surface roughness σ for Tabor parameter $\mu = 0.1, 1.0$, and 10.

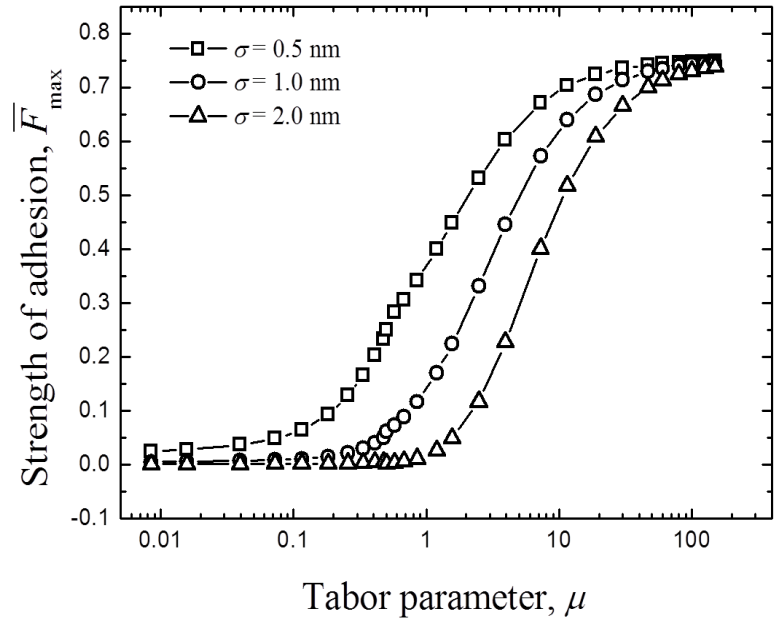

Fig. 8.11 Strength of adhesion $\bar{F}_{\max}$ versus Tabor parameter μ for surface roughness $\sigma = 0.5$, 1.0, and 2.0 nm.

8.4.3. Effect of Tabor parameter on strength of adhesion

Figure 8.11 shows the variation of the strength of adhesion $\bar{F}_{\max}$ with Tabor parameter μ for σ = 0.5, 1.0, and 2.0 nm. Despite quantitative differences among the three curves, $\bar{F}_{\max}$ increases asymptotically with the Tabor parameter to 0.75, which is the value of $\bar{P}_{off}$ obtained from JKR theory. This implies that the adhesive contact behavior of rough surfaces characterized by a sufficiently high value of μ (e.g., $\mu > 10$) can be accurately represented by that of a single-asperity contact. This finding is consistent with the decreasing effect of surface roughness on the strength of adhesion, observed earlier with the increase in Tabor parameter (Figure 8.10). It is also noted that for a given roughness, $\bar{F}_{\max}$ decreases sharply in the 0.1–10 range of μ, approaching asymptotically a small value that decreases with surface roughness.

8.4.4. New adhesion parameter and effective surface separation

Numerical results of the strength of adhesion $\bar{F}_{\max}$ and the relative strength of adhesion, defined as $\chi = \bar{F}_{\max}|_{(\theta,\sigma)}/\bar{F}_{\max}|_{(\theta,\sigma=150\text{ nm})}$, for θ = 0.2, 1.0, and 5.0 and σ in the range of 0–150 nm are shown in Figs. 8.12(a) and 8.12(b), respectively. These results indicate that the strength of adhesion is governed by the adhesion parameter θ only for low θ values and/or high σ values. Because $\mu = \sigma/\varepsilon\theta^{2/3}$ (Eqs. (8.1) and (8.3)), the former implies that θ is a governing parameter of the strength of adhesion only in the high range of the Tabor parameter, as evidenced by experiments with a smooth rubber sphere pressed into contact with a rough surface (Fuller and Tabor, 1975). Therefore, a different adhesion parameter must be used to describe the strength of adhesion in the low range of the Tabor parameter.

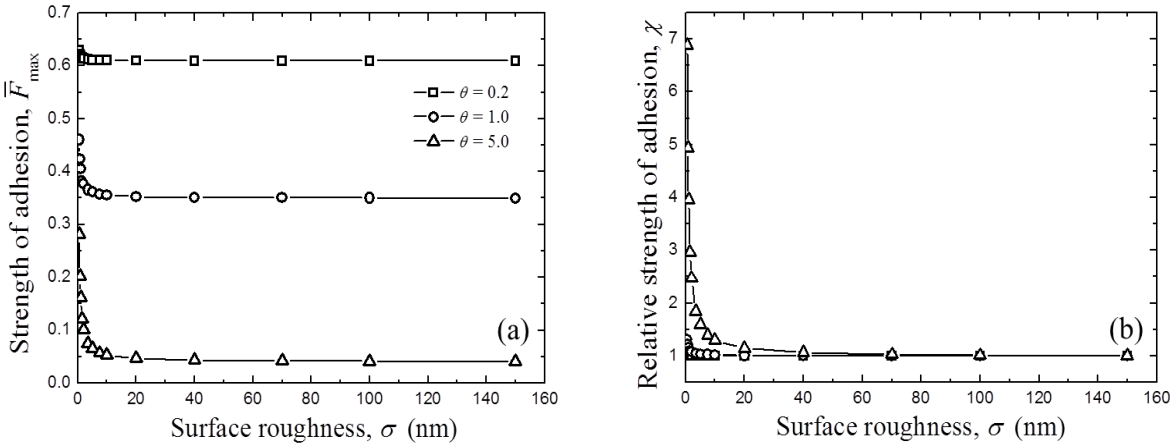

Fig. 8.12 (a) Strength of adhesion $\bar{F}_{\max}$ and (b) relative strength of adhesion χ versus surface roughness σ for adhesion parameter $\theta = 0.2$, 1.0, and 5.0.

The numerical results shown in Fig. 8.13 indicate that $\zeta = \sigma/\varepsilon$ can be used to describe the strength of adhesion in the low range of μ. The relative strength of adhesion χ sharply decreases with the increase of σ in the low-roughness range, approaching asymptotically to 1 (Fig. 8.12(b)). For fixed ζ, ε increases with σ. Considering that $\mu \sim \varepsilon^{-1}$ (Eq. (8.1)), it may be interpreted that μ decreases with the increase of σ. Therefore, ζ is a governing parameter of the strength of adhesion in the low μ range. Consequently, because $\mu\varepsilon = (R\Delta\gamma^2/E^{*2})^{1/3}$ represents the elastic deformation caused by adhesion and ε characterizes the effective range of the

adhesion force, a generalized adhesion parameter for the entire range of the Tabor parameter can be defined as $\xi \sim \sigma/(\mu+1)\varepsilon$. Surface roughness σ characterizes the variation in the separation distance between individual asperities and the undeformed half-space (stress-free state), while asperity elastic deformation induced by adhesion is on the order of $\mu\varepsilon$ and the effective range of the adhesion force is on the order of ε. Therefore, the effective surface separation between individual asperities and the elastically deformed half-space is on the order of $(\mu+1)\varepsilon$, below which the adhesion force significantly affects the contact behavior. The fraction of the asperities in the surface separation range dominated by the attractive force decreases with the surface roughness and increases with the effective surface separation.

The adhesion parameters θ and ζ represent asymptotic values of the general adhesion parameter ξ. For $\mu \gg 1$, the effective surface separation is controlled by adhesion-induced elastic deformation of the asperities and $\xi \to \sigma/\mu\varepsilon = \theta^{2/3}$, in agreement with the finding that θ governs the strength of adhesion of contact systems characterized by a high Tabor parameter (Fig. 8.12). Alternatively, for $\mu \ll 1$, the effective surface separation is controlled by the effective range of the adhesion force and $\xi \to \sigma/\varepsilon = \zeta$, in agreement with the observation that ζ governs the strength of adhesion of contact systems characterized by a low Tabor parameter (Fig. 8.13).

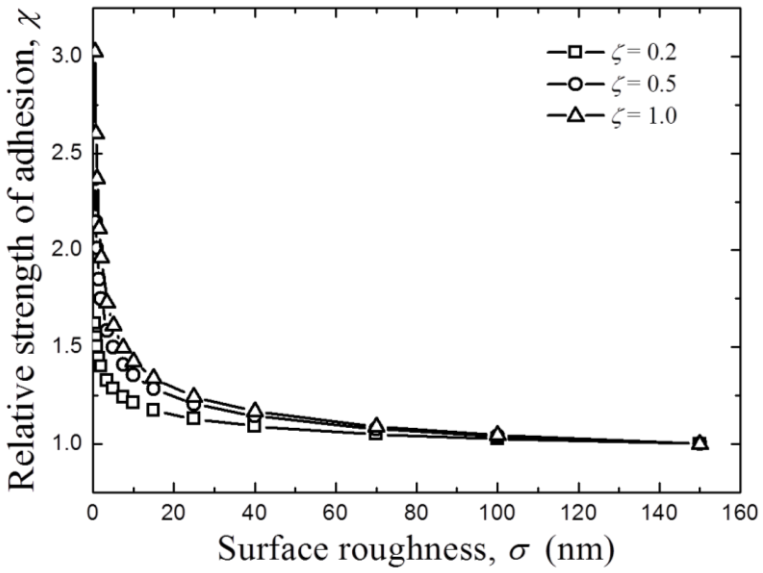

Fig. 8.13 Relative strength of adhesion χ versus surface roughness σ for adhesion parameter $\zeta = 0.2$, 0.5, and 1.0.

8.5. Conclusions

Adhesive contact of elastic rough surfaces was examined within the framework of the GW rough surface model, modified to include contact instabilities (jump-in) at the asperity level. Constitutive relations of the interfacial force and the contact area of single-asperity contacts demonstrating continuous ($\mu < 0.5$) and discontinuous ($\mu > 0.5$) approach paths were obtained in the distance range of attractive- and repulsive-dominant surface force. These relations were

incorporated into the GW rough-surface model, and the interfacial force and contact area were expressed in terms of important parameters, such as surface separation, asperity radius, asperity area density, surface roughness, effective elastic modulus, surface energy, equilibrium interatomic distance, and the Tabor parameter.

Rough surface contact demonstrated a three-stage behavior with decreasing mean surface separation: (1) zero contact area, (2) nonlinear and rapid increase of the contact area caused by jump-in instabilities at the asperity level (particularly for surfaces characterized by high μ values), and (3) linear increase of the contact area (Hertz-like behavior) independent of μ. The strength of adhesion decreased with increasing surface roughness and generally increased with μ, approaching asymptotically to the value predicted by the JKR contact model of elastic spheres, implying a negligible surface roughness effect for $\mu \gg 1$. However, for $\mu \ll 1$, the strength of adhesion approached asymptotically to a very low value, which increased with decreasing surface roughness.

The adhesion parameter θ proposed by Fuller and Tabor (1975) was shown to govern the strength of adhesion of surfaces characterized by high μ values. A new adhesion parameter ζ, defined as the ratio of the surface roughness to the equilibrium interatomic distance, was shown to describe the strength of adhesion of rough surfaces characterized by low μ values. Differences between θ and ζ parameters were interpreted in terms of the effective surface separation, defined as the sum of the effective distance range of the adhesion force and the elastic deformation of asperities caused by adhesion. It was shown that the strength of adhesion can be characterized over the entire range of the Tabor parameter by a generalized adhesion parameter ξ, defined as the ratio of the surface roughness and the effective surface separation, with θ and ζ representing asymptotic values in the high- and low-ranges of the Tabor parameter, respectively.

CHAPTER 9

Conclusions

Analytical and computational mechanics analyses were performed to study the adhesive contact behavior of smooth and rough, homogeneous or layered, elastic-plastic media. The results of this dissertation provide significant insight into contact mechanics behaviors over a wide range of length scales, with special emphasis on indentation and fretting mechanics, adhesion-induced contact instabilities and film delamination, and roughness effects. The main findings of this dissertation are summarized below.

Finite element simulations of a rigid spherical indenter compressing an elastic-plastic half-space showed the existence of four different post-yield deformation regimes, namely linear elastic-plastic (LEP), nonlinear elastic-plastic (NLEP), transient fully-plastic (TFP) and steady-state fully plastic (SSFP). While the residual elastic region disappeared at the inception of TFP, the mean contact pressure continued to increase and the material hardness (i.e., maximum contact pressure) was not achieved until the occurrence of SSFP. Moreover, the hardness-to-yield strength ratio is a function of the elastic modulus-to-yield strength ratio (E^*/Y). The formation of a residual elastic region between the spherical indenter and the plastic zone was observed in LEP regime. For low E^*/Y values, the plastic zone uniformly expanded toward the surface, producing a residual elastic strip adjacent to the spherical indenter, whereas for high E^*/Y values, the plastic zone first propagated to the edge of the contact region, producing a residual elastic core below the spherical indenter. Constitutive equations were derived numerically and the logarithmic dependence of the mean contact pressure on the indentation depth was shown to hold only in the LEP regime. The former constitutive model was extended to include strain hardening effects on the deformation behavior of indented elastic-plastic half-spaces. Based on the concept of an effective yield strength, constitutive relations of the mean contact pressure and contact area that account for the effect of hardening on the material yields strength were derived for elastic-plastic half-spaces with different strain hardening characteristics.

Equations for the residual indentation depth and the energy dissipated due to plastic deformation in indented elastic-perfectly plastic half-spaces after full unloading were extracted form finite element results. Constitutive equations derived for unloaded elastic-perfectly plastic half-space were further modified to include the effect of strain hardening by using the effective yield strength, which accounts for the change of the yield strength due to strain hardening. For high E^*/Y values, only the first unloading was inelastic, i.e., all subsequent unloading resulted in elastic shakedown, whereas for low E^*/Y values, indentation loading-unloading following initial unloading resulted in work dissipation due to plastic deformation, i.e., plastic shakedown or ratcheting. Deformation in a half-space with a low E^*/Y value comprised the formation of a small plastic region adjacent to the indenter and near the center of the contact area were plasticity accumulated continuously (ratcheting), surrounded by a plastic region where plasticity occurred only in the first unloading cycle (elastic shakedown), and stressed region where irreversible deformation did not occur (elastic). For elastic-plastic half-spaces exhibiting isotropic/kinematic

hardening behavior, the effective stress in the vicinity of the circumference of the contact area increased incrementally and yielding occurred in subsequent loading-unloading cycles.

A fretting contact model of a rigid (fractal) rough surface sliding against an elastic-plastic half-space that accounts for asperity-scale stick-slip interactions was developed. Both maximum tangential force and energy dissipation non-monotonically varied with surface roughness, characterized by an adhesion-dominant range and a plowing-dominant range, because of the simultaneous increase of the plastic contact area and the decrease of the elastic contact area, respectively. A higher nominal contact pressure yielded a lower maximum tangential force and less fretting energy dissipation because of the larger elastic contact area and lower slip index. Both maximum tangential force and energy dissipation increased with the oscillation amplitude, asymptotically approaching a plateau value. The maximum friction force increased with the decrease of E^*/Y due to the increase of the contact area, while the slip index showed an opposite trend because larger contact area implies more asperities in partial slip for a given oscillation amplitude. For small E^*/Y values, the slip index effect is more dominant and energy dissipation increases with E^*/Y, whereas for high E^*/Y values, the slip index effect is negligible and energy dissipation decreases. The effect of interfacial adhesion on contact behavior was found be more significant for relatively smooth surfaces, becoming secondary in the case of rough surfaces. This can be attributed to the larger elastic contact area produced with smooth surfaces and the larger plastic contact force produced from rougher surfaces. For a rough surface, energy dissipation due to fretting contact decreased with the increase of the interfacial adhesion parameter due to more asperities exhibiting partial slip.

Contact instabilities, such as abrupt surface contact (jump-in) and detachment (jump-out), were examined by modeling adhesion between the interacting surfaces with the Lennard-Jones (L-J) potential. A condition of contact instability was established as an implicit function of the Tabor parameter. The critical Tabor parameter for contact instability was numerically determined to be μ^* = 0.5, above which surface contact and separation exhibited unstable behavior. The discrepancy between the obtained critical Tabor parameter (μ^* = 0.5) and that determined by Greenwood and later confirmed by others (μ^* = 1.0) was attributed to differences in assumed apparatus stiffness. For finite element analysis, surface adhesion was represented by nonlinear spring elements with a constitutive force-distance law derived from the L-J potential. The pull-off force obtained from finite element simulations was found to be much higher than that predicted by the JKR and the DMT models. A modified Tabor parameter was derived to characterize the influence of necking or residual impression due to excessive plastic deformation on contact instabilities. In repetitive normal contact, a high Tabor parameter and low plasticity parameter resulted in elastic shakedown, whereas a low Tabor parameter and high plasticity parameter led to plastic shakedown. Surface separation demonstrated a strong dependence on plasticity parameter. A high plasticity parameter enhanced necking, causing, in turn, a transition from abrupt to smooth surface separation.

An effective Tabor parameter for layered media was obtained as a function of the layer thickness and the layer and substrate Tabor parameters. Surface separation (detachment) during unloading was not encountered at the instant of maximum adhesion (pull-off) force, but the layered medium continued to be stretched by the rigid sphere until the occurrence of the jump-out instability. Brittle- and ductile-like mode of surface separation observed after full unloading

led to the development of a surface detachment map based on the maximum surface separation and substrate plasticity parameter. The dependence of the mode of surface separation (detachment) on the maximum surface separation was influenced by the plasticity parameter. This can be explained by considering the competing effects of the adhesion (attractive) surface force and the residual stress at the layer/substrate interface induced by the adjacent plastic zone in the substrate, both of which increased with the maximum surface separation. With the increase of the maximum surface separation, the unloading process exhibited more ductile- or brittle-like behavior for high or low values of the plasticity parameter, respectively. The pull-off force decreased with increasing layer-to-substrate elastic modulus ratio, while the separation force demonstrated an opposite trend, which was explained in terms of the effective Tabor parameter. Plastic deformation decreased significantly with the increase of the layer stiffness and the maximum equivalent plastic strain shifted from the layer/substrate interface below the edge of the residual pile-up (neck) to the substrate below the center of the contact region, indicating a decreasing propensity for interfacial delamination with increasing layer stiffness. Substrate plasticity intensified and surface separation exhibited more ductile-like behavior with decreasing layer thickness. Incremental plasticity (ratcheting) in the substrate was found to be the most likely steady-state deformation mechanism. Subsequent approach cycles produced a larger (smaller) adhesion force was larger and smaller (larger) critical surface separation for jump-in compared to the first cycle for low (high) β values. This trend was attributed to the residual impression (permanent pile-up) produced in the first cycle.

A bilinear cohesive zone law, characterized by a cohesive strength and work of adhesion, that allowed for crack initiation and growth along the film/substrate interface was used in a finite element analysis of adhesive contact between a rigid sphere and an elastic-plastic layered medium. The unloading response was found to include five sequential stages: elastic recovery, interface damage (crack) initiation, damage evolution (delamination), film bending, and abrupt surface separation (jump-out), with plastic deformation in the substrate occurring only during damage initiation. Complete crack closure was prevented by plastic deformation in the substrate. A residual cohesive zone, formed after full unloading (jump-out), produced residual tensile stresses at the front of the crack tip that induced a downward deflection of the elastic film. For a low-strength substrate, interface delamination was not observed during unloading, while for a substrate of intermediate strength, damage (crack) initiation and failure (delamination) at the interface occurred during unloading, leading to the formation of a residual crack upon the occurrence of jump-out. For a high-strength substrate, deformation during loading was essentially elastic and the interface crack formed during unloading exhibited almost complete closure upon jump-out. The cohesive strength exhibited a significant effect on both loading and unloading behavior. Unstable crack initiation was only observed for a high cohesive strength. This trend was interpreted in terms of a dimensionless parameter representing the layered medium-to-interface stiffness ratio. Following surface jump-out, crack closure and the crack-tip opening displacement increased with decreasing cohesive strength due to the enhancement of cohesive zone closure and the increase of the critical surface separation for interfacial failure, respectively. The presence of an interfacial defect smaller than a critical size did not affect the loading-unloading behavior; however, beyond this critical size, the critical separation at the instant of the jump-in and jump-out instability increased linearly with the defect size.

Two sets of constitutive equations were developed for asperities exhibiting smooth and abrupt contact. Rough surface contact demonstrated a three-stage behavior with decreasing mean surface separation: (1) zero contact area, (2) nonlinear and rapid increase in contact area due to the jump-in instabilities occurring at the asperity level (particularly for surfaces characterized by high values of the Tabor parameter μ), and (3) linear increase in contact area (Hertz-like behavior) independent of μ. The strength of adhesion decreased with increasing surface roughness and generally increased with μ, approaching asymptotically to the value predicted for elastic spheres by the JKR contact model, implying a negligible surface roughness effect for $\mu \gg 1$. However, for $\mu \ll 1$, the strength of adhesion approached asymptotically to a very low value, which increased with decreasing surface roughness. The adhesion parameter θ proposed by Fuller and Tabor was shown to govern the strength of adhesion of surfaces characterized by a high μ value (i.e., low θ and/or high surface roughness). A new adhesion parameter ζ, defined as the ratio of surface roughness to the equilibrium interatomic distance, was proven to describe the strength of adhesion of rough surfaces with a low μ value. Differences between θ and ζ parameters were interpreted in terms of the effective surface separation, defined as the sum of the effective distance range of the adhesion force and the elastic deformation of an asperity due to adhesion. It was shown that the strength of adhesion can be characterized over the entire range of the Tabor parameter by a general adhesion parameter ξ, defined as the ratio of the surface roughness to the effective surface separation, with θ and ζ representing asymptotic values in the high- and low-range of the Tabor parameter, respectively.

In summary, the contribution of the present dissertation in contact mechanics is the additional fundamental understanding of elastic-plastic deformation during loading and unloading and the role of surface adhesion in the contact behavior of both smooth and rough surfaces. Among the main findings summarized in this chapter, the most important results of this work are the first derivation ever of an analytical solution of the critical condition for adhesion-induced contact instabilities and the introduction of a new adhesion parameter that characterizes the strength of adhesion between rough surfaces. In addition, numerical and analytical results of comprehensive adhesion contact studies yielded further insight into contact mechanics, fretting contact behavior, and the mechanical response of layered media to single and repetitive adhesive contact.

Bibliography

ABAQUS User's Manual, version 6.7.2, 2008. ABAQUS Inc., Rhode Island, USA.

Anderson, T.L., 1995. *Fracture Mechanics: Fundamentals and Applications*, second ed., CRC Press, Boca Raton, FL.

Attard, P., Parker, J.L., 1992. Deformation and adhesion of elastic bodies in contact. Phys. Rev. A 46, 7959–7971.

Bagchi, A., Evans, A.G., 1996. The mechanics and physics of thin film decohesion and its measurement. Interface Sci. 3, 169–193.

Barthel, E., and Perriot, A., 2007. Adhesive Contact of a Coated Elastic Substrate. J. Phys. D: Appl. Phys., 40, 1059–1067.

Berthoud, P., Baumberger, T., 1998. Shear stiffness of a solid–solid multi-contact interface. Proceedings: Mathematical, Physical and Engineering Sciences 454 (1974), 1615–1634.

Bhattacharya, A.K., Nix, W.D., 1988. Finite element simulation of indentation experiments. Int. J. Solids. Struct. 24, 881–891.

Biwa, S., Storåkers, B., 1995. An analysis of fully plastic Brinell indentation. J. Mech. Phys. Solids 43, 1303–1333.

Borri-Brunetto, M., Carpinteri, A., Chiaia, B., 1999. Scaling phenomena due to fractal contact in concrete and rock fractures. Int. J. Fracture 95, 221–238.

Boussinesq, J., 1885.Application des potentiels à l' étude de l' équilibre et du mouvement des solides elastiques. Gauthier-Villars, Paris, France.

Bradley, R.S., 1932. The cohesive force between solid surfaces and the surface energy of solids. Phil. Mag. 13, 853–862.

Brizmer, V., Kligerman, Y., Etsion, I., 2007. Elastic-plastic spherical contact under combined normal and tangential loading in full stick. Tribol. Lett. 25 (1), 61-70.

Carpick, R. W., Ogletree, D. F., and Salmeron, M., 1999. A General Equation for Fitting Contact Area and Friction vs. Load Measurements. J. Colloid Interface Sci., 211, 395–400.

Cattaneo, C., 1938. Sul contatto di due corpi elastici: Distribuzione locale deglisforzi. Rc Accad Naz Lincei 27, 474–478.

Ciavarella, M., Demelio, G., Barber, J.R., Jang, Y.H., 2000. Linear elastic contact of the Weierstrass profile. Proc. R. Soc. Lond. A 456,387–405.

Chai, H., 2003. Fracture mechanics analysis of thin coatings under spherical indentation. Int. J. Fract. 119, 263–285.

Chen, L., Yeap, K.B., Zeng, K.Y., Liu, G.R., 2009, Finite element simulation and experimental determination of interfacial adhesion properties by wedge indentation. Phil. Mag. 89, 1395–1413.

Cowles, B.A., 1996. High cycle fatigue in aircraft gas turbines – an industry perspective. Int. J. Fract. 80, 147–163.

Derjaguin, B.V., Muller, V.M., Toporov, Y.P., 1975. Effect of contact deformations on the adhesion of particles. J. Colloid Interface Sci. 53, 314–326.

Drory, M.D., Hutchinson, J.W., 1996. Measurement of the adhesion of a brittle film on a ductile substrate by indentation. Proc. R. Soc. Lond. A 452, 2319–2341.

Du, Y., Adams, G. G., McGruer, N. E., and Etsion, I., 2008. A Parameter Study of Separation Modes of Adhering Microcontacts. J. Appl. Phys., 103, 064902(1)–064902(9).

Du, Y., Chen, L., McGruer, N.E., Adams, G.G., Etsion, I., 2007. A finite element model of loading and unloading of an asperity contact with adhesion and plasticity. J. Colloid Interface Sci. 312, 522–528.

Eid, H., Joshi, N., McGruer, N. E., and Adams, G. G., 2011. A Model of Contact With Adhesion of a Layered Elastic-Plastic Microsphere With a Rigid Flat Surface. ASME J. Tribol., 133, 031406(1)–031406 (5).

Eriten, M., Polycarpou, A., Bergman, L., 2011. Physics-based modeling of fretting behavior of nominally flat rough surfaces. Int. J. Solids. Struct. 48, 1436–1450.

Eriten, M., Polycarpou, A., Bergman, L., 2011. Surface roughness effect on energy dissipation in fretting contact of nominally flat surfaces. J. Appl. Mech. 78, (021011) 1–8.

Etsion, I., Kligerman, Y., Kadin, Y., 2005. Unloading of an elastic-plastic loaded spherical contact. Int. J. Solid. Struct. 42, 3716-3729

Feng, J.Q., 2000. Contact behavior of spherical elastic particles: a computational study of particle adhesion and deformations. Colloid Surf. A: Physicochem. Eng. Aspects 172, 175–198.

Feng, J. Q., 2001. Adhesive Contact of Elastically Deformable Spheres: A Computational Study of Pull-off Force and Contact Radius. J. Colloid Interface Sci., 238, 318–323.

Fischer-Cripps, A. C., 2011. Nanoindentation. Springer-Verlag, New York, NY

Follansbee, P.S., Sinclair, G.B., 1984. Quasi-static normal indentation of an elasto-plastic half-space by a rigid sphere–I. Analysis. Int. J. Solids. Struct. 20, 81–91.

Fuller, K.N.G., Tabor, D., 1975. The effect of surface roughness on the adhesion of elastic solids. Proc. R. Soc. Lond. A 345, 327–342.

Gao, Y.F., Bower, A.F., 2004. A simple technique for avoiding convergence problems in finite element simulations of crack nucleation and growth on cohesive interfaces. Modelling Simul. Mater. Sci. Eng. 12, 453–463.

Giannakopoulos, A.E., Larsson, P.-L., Vestergaard, R., 1994. Analysis of Vickers indentation. Int. J. Solids. Struct. 31, 2679–2708.

Greenwood, J.A., 1997. Adhesion of elastic spheres. Proc. R. Soc. Lond. A 453, 1277–1297.

Greenwood, J.A., Johnson, K.L., 1998. An alternative to the Maugis model of adhesion between elastic spheres. J. Phys. D: Appl. Phys. 31, 3279–3290.

Greenwood, J.A., Williamson, J.B.P., 1966. Contact of nominally flat surfaces. Proc. R. Soc. Lond. A 295, 300–319

Hardy, C., Baronet, C.N., Tordion, G.V., 1971. The elasto-plastic indentation of a half-space by a rigid sphere. Int. J. Numer. Meth. Eng. 3, 451–462.

Hill, R., 1967. The Mathematical Theory of Plasticity. Oxford University Press, London, pp. 128–149.

Hill, R., Storåkers, B., Zdunek, A.B., 1989. A theoretical study of the Brinell hardness test. Proc. R. Soc. Lond. A 423, 301–330.

Ishlinsky, A.Y., 1944. Axially symmetric problem in plasticity and Brinell's hardness test. Prikl. Mat. Mekh. 8, 201–224.

Israelachvili, J.N., 1992. Intermolecular and Surface Forces. 2nd ed., Academic Press, San Diego, CA.

Jackson, R. L., Streator, J. L., 2006. A multi-scale model for contact between rough surfaces. Wear. 261, 1337-1347

Johnson, K.L., 1955. Surface interaction between elastically loaded bodies under tangential forces. Proc. R. Soc. Lond. A 230 (1183), 531–548.

Johnson, K.L., 1958. A note on the adhesion of elastic solids. Brit. J. Appl. Phys. 9, 199–200.

Johnson, K.L., 1985. Contact Mechanics, Cambridge University Press, Cambridge, England.

Johnson, K.L., Greenwood, J.A., 1997. An adhesion map for the contact of elastic spheres. J. Colloid Interface Sci. 192, 326–333.

Johnson, K.L., Kendall, K., Roberts, A.D., 1971. Surface energy and the contact of elastic solids. Proc. R. Soc. Lond. A 324, 301–313.

Johnson, K. L., and Sridhar, I., 2001. Adhesion Between a Spherical Indenter and an Elastic Solid With a Compliant Elastic Coating. J. Phys. D: Appl. Phys., 34, 683–689.

Kadin, Y., Kligerman, Y., Etsion, I., 2006. Unloading of an elastic-plastic contact of rough surfaces. J. Mech. Phys. Solids. 54, 2652-2674

Kadin, Y., Kligerman, Y., Etsion, I., 2006. Multiple loading-unloading of an elastic-plastic spherical contact. Int. J. Solid. Struct. 43, 7119-7127

Kadin, Y., Kligerman, Y., Etsion, I., 2008a. Loading-unloading of an elastic-plastic adhesive spherical microcontact. J. Colloid Interface Sci. 321, 242–250.

Kadin, Y., Kligerman, Y., Etsion, I., 2008b. Cyclic loading of an elastic-plastic adhesive spherical microcontact. J. Appl. Phys. 104, 073522(1–8).

Kadin, Y., Kligerman, Y., Etsion, I., 2008c. Jump-in induced plastic yield onset of approaching microcontacts in the presence of adhesion. J. Appl. Phys. 103, 013513(1–8).

Kesari, H., Doll, J.C., Pruitt, B.L., Cai., W, Lew, A.J., 2010. Role of surface roughness in hysteresis during adhesive elastic contact. Phil. Mag. Lett. 90, 891–902.

Kesari, H., Lew, A.J., 2011. Effective macroscopic adhesive contact behavior induced by small surface roughness. J. Mech. Phys. Solids 59, 2488–2510.

Kim, K.-S., McMeeking, R.M., Johnson, K.L., 1998. Adhesion, slip, cohesive zones and energy fluxes for elastic spheres in contact. J. Mech. Phys. Solids 46, 243–266.

King, R. B., 1987. Elastic Analysis of Some Punch Problems for a Layered Medium. Int. J. Solids Struct., 23, 1657–1664.

Kogut, L., Etsion, I., 2002, Elastic-plastic contact analysis of a sphere and a rigid flat. J. Appl. Mech. 69, 657-662

Kogut, L., Etsion, I., 2003. Adhesion in elastic-plastic spherical microcontact. J. Colloid Interface Sci. 261, 372–378.

Kogut, L., Komvopoulos, K., 2004. Analysis of the spherical indentation cycle for elastic-perfectly plastic solids. J. Mater. Res. 19, 3641–3653.

Komvopoulos, K., 1988. Finite Element Analysis of a Layered Elastic Solid in Normal Contact With a Rigid Surface. ASME J. Tribol., 110, 477–485.

Komvopoulos, K., 1996. Surface engineering and microtribology for microelectromechanical systems. Wear 200, 305–327.

Komvopoulos, K., 2000. Head-disk interface contact mechanics for ultrahigh density magnetic recording. Wear 238, 1–11.

Komvopoulos, K., 2003. Adhesion and friction forces in microelectromechanical systems: mechanisms, measurement, surface modification techniques, and adhesion theory. J. Adhes. Sci. Technol. 17, 477–517.

Komvopoulos, K., Saka, N., and Suh, N. P., 1986. Plowing Friction in Dry and Lubricated Metal Sliding. J. Tribol. 108, 3, 301–313.

Komvopoulos, K., Saka, N., and Suh, N. P., 1987. The Role of Hard Layers in Lubricated and Dry Sliding. ASME J. Tribol., 109, 223–231.

Komvopoulos, K., Gong, Z.-Q., 2007. Stress analysis of a layered elastic solid in contact with a rough surface exhibiting fractal behavior. Int. J. Solids. Struct. 44, 2109–2129.

Komvopoulos, K., Yan, W., 1998. Three-dimensional elastic-plastic fractal analysis of surface adhesion in microelectromechanical systems. ASME J. Tribol. 120, 808–813.

Komvopoulos, K., Ye, N., 2001. Three-dimensional contact analysis of elastic-plastic layered media with fractal surface topographies. ASME J. Tribol. 123, 632–640.

Kogut, L., Etsion, I., 2002. Elastic-Cplastic contact analysis of a sphere and a rigid flat. J. Appl. Mech. 69 (5), 657-662.

Kral, E.R., Komvopoulos, K., Bogy, D.B., 1993. Elastic-plastic finite element analysis of repeated indentation of a half-space by a rigid sphere. ASME J. Appl. Mech. 60, 829–841.

Kral, E. R., Komvopoulos, K., and Bogy, D. B., 1995a. Finite Element Analysis of Repeated Indentation of an Elastic-Plastic Layered Medium by a Rigid Sphere, Part I: Surface Results. ASME J. Appl. Mech., 62, 20–28.

Kral, E. R., Komvopoulos, K., and Bogy, D. B., 1995b. Finite Element Analysis of Repeated Indentation of an Elastic-Plastic Layered Medium by a Rigid Sphere, Part II: Subsurface Results. ASME J. Appl. Mech., 62, 29–42.

Knapp, J.A., Follstaedt, D.M., Myers, S.M., Barbour, J.C., Friedmann, T.A., 1999. Finite-element modeling of nanoindentation. J. Appl. Phys. 85, 1460–1474.

Lemaitre, J., Chaboche, J. L., 1994. Mechanics of Solid Materials. Cambridge University Press, Cambridge, U.K.

Li, J., and Chou, T.-W., 1997. Elastic Field of a Thin-Film/Substrate System Under an Axisymmetric Loading. Int. J. Solids Struct., 34, 4463–4478.

Li, Q., Kim, K.-S., 2009. Micromechanics of rough surface adhesion: a homogenized projection method. Acta Mechanica Solida Sinica 22, 377–390.

Majumdar, A., Bhushan, B., 1990. Role of fractal geometry in roughness characterization and contact mechanics of surfaces. J. Tribol. 112, 205-216.

Majumdar, A., Bhushan, B., 1991. Fractal model of elastic-plastic contact between rough surfaces. J. Tribol. 113, l-11.

Mandelbrot, B.B., 1983. The Fractal Geometry of Nature. Freeman, New York. 1–83 and 116–118.

Marshall, D.B., Evans, A.G., 1984. Measurement of adherence of residually stressed thin films by indentation. I. Mechanics of interface delamination. J. Appl. Phys. 56, 2632–2638.

Maugis, D., 1992. Adhesion of spheres: the JKR-DMT transition using a Dugdale model. J. Colloid Interface Sci. 150, 243–269.

Maugis, D., Pollock, H. M., 1984. Surface forces, deformation and adherence at metal microcontacts. Acta Metall. 32, 1323–1334.

Majumder, S., McGruer, N. E., Adams, G. A., Zavracky, P. M., Morrison, R. H., Krim, J., 2001. Study of contacts in an electrostatically actuated microswitch. Sensors and Acturators A. 93, 19-26

Marsh, D.M., 1964. Plastic flow in glass. Proc. R. Soc. Lond. A 279, 420–435.

Mesarovic, S.D., Fleck, N.A., 1999. Spherical indentation of elastic-plastic solids. Proc. R. Soc. Lond. A 455, 2707–2728.

Mesarovic, S.D., Johnson, K.L., 2000. Adhesive contact of elastic–plastic spheres. J. Mech. Phys. Solids 48, 2009–2033.

Mindlin, R.D., 1949. Compliance of elastic bodies in contact. J. Appl. Mech. 16 (3), 259-268.

Mindlin, R.D., Mason, W.P., Osmer, T.F., Deresiewicz, H., 1952. Effects of an oscillating tangential force on the contact surfaces of elastic spheres. Proceedings of the First US National Congress of Applied Mechanics 1951, 203-208

Morrow, C., Lovell, M., Ning, X., 2003. A JKR-DMT transition solution for adhesive rough surface contact. J. Phys. D: Appl. Phys. 36, 534–540.

Mukherjee, S., Ali, S.M., Sahoo, P., 2004. An improved elastic-plastic contact model of rough surfaces in the presence of adhesion. Proc. Inst. Mech. Eng., Part J: J. Eng. Tribol. 218, 557–567.

Muller, V.M., Yushchenko, V.S., Derjaguin, B.V., 1980. On the influence of molecular forces on the deformation of an elastic sphere and its sticking to a rigid plane. J. Colloid Interface Sci. 77, 91–101.

O'Sullivan, T. C., and King, R. B., 1988. Sliding Contact Stress Field Due to a Spherical Indenter on a Layered Elastic Half-Space. ASME J. Tribol., 110, 235–240.

Park, Y.J., Pharr, G.M., 2004. Nanoindentation with spherical indenters: finite element studies of deformation in the elastic–plastic transition regime. Thin Solid Films 447/448, 246–250.

Pethica, J. B., Sutton, A.P., 1988. On the stability of a tip and flat at very small separations. J. Vac. Sci. Technol. A 6, 2490–2494.

Perriot, A., and Barthel, E., 2004. Elastic Contact to a Coated Half-Space: Effective Elastic Modulus and Real Penetration. J. Mater. Res., 19, 600–608.

Persson, B.N.J., Bucher, F., Chiaia, B., 2002. Elastic contact between randomly rough surfaces: comparison of theory with numerical results. Phys. Rev. B 65, (184106) 1–7.

Sahoo, P., Chowdhury, S.K.R., 1996. A fractal analysis of adhesion at the contact between rough solids. Proc. Inst. Mech. Eng., Part J: J. Eng. Tribol. 210, 269–279.

Samuels, L.E., Mulhearn, T.O., 1957. An experimental investigation of the deformed zone associated with indentation hardness impressions. J. Mech. Phys. Solids 5, 125–134.

Sergici, A. O., Adams, G. G., and Müftü, S., 2006. Adhesion in the Contact of a Spherical Indenter With a Layered Elastic Half-Space. J. Mech. Phys. Solids, 54, 1843–1861.

Smallwood, S.A., Eapen, K.C., Patton, S.T., Zabinski, J.S., 2006. Performance results of MEMS coated with a conformal DLC. Wear 260, 1179–1189.

Song, J., Srolovitz, D.J., 2006. Adhesion effects in material transfer in mechanical contacts. Acta Mater. 54, 5305–5312.

Song, Z., and Komvopoulos, K., 2011. Adhesion-Induced Instabilities in Elastic and Elastic-Plastic Contacts During Single and Repetitive Normal Loading. J. Mech. Phys. Solids, 59, 884–897.

Song, Z., Komvopoulos, K., 2012. Adhesive contact of a rigid sphere with a hard elastic film on an elastic-plastic substrate. ASME J. Appl. Mech. (accepted)

Song, Z., Komvopoulos, K., 2012. Spherical indentation of an elastic-plastic half-space: deformation map and evolution of plasticity. (Submitted)

Sridhar, I., Johnson, K. L., and Fleck, N. A., 1997. Adhesion Mechanics of the Surface Force Apparatus. J. Phys. D: Appl. Phys., 30, 1710–1719.

Sridhar, I., and Sivashanker, S., 2003. On the Adhesion Mechanics of Multi-Layer Elastic Systems. Surf. Coat. Technol., 167, 181–187.

Tabor, D., 1951. The Hardness of Metals, Clarendon Press, Oxford, England.

Tabor, D., 1977. Surface forces and surface interactions. J. Colloid Interface Sci. 58, 2–13.

Timoshenko, S.P., Goodier, J.N., 1970. Theory of Elasticity. 3rd ed., McGraw-Hill, New York, NY.

Tvergaard, V., Hutchinson, J.W., 1994. Toughness of an interface along a thin ductile layer joining elastic solids. Phil. Mag. A 70, 641–656.

Tvergaard, V., Hutchinson, J.W., 1996. Effect of strain-dependent cohesive zone model on predictions of crack growth resistance. Int. J. Solids Struct. 33, 3297–3308.

Wang, S., Komvopoulos, K., 1994a. A fractal theory of the interfacial temperature distribution in the slow sliding regime: Part I – elastic contact and heat transfer analysis. J. Tribol. 116, 812–823.

Wang, S., Komvopoulos, K., 1994b. A fractal theory of the interfacial temperature distribution in the slow sliding regime: Part II – multiple domains, elastoplastic contacts and applications. J. Tribol. 116, 824–832.

Wang, X.-D., Shen, Z.-X., Zhang, J.-L., Jiao, H.-F., Cheng, X.-B., Chen, L.-Y., and Wang, Z.-S., 2010. Submicrometer Aluminum Spheres' Adhesion to Planar Silicon Substrates. Langmuir, 26, 13903–13906.

Wu, J.-J., 2008. Easy-to-Implement Equations for Determining Adhesive Contact Parameters with the Accuracy of Numerical Simulations. Tribol. Lett., 30, 99–105.

Wu, Y.-C., Adams, G.G., 2009. Plastic yield conditions for adhesive contacts between a rigid sphere and an elastic half-space. J. Tribol. 131, 011403(1–7).

Xia, S.M., Gao, Y.F., Bower, A.F., Lev, L.C., Cheng, Y.-T., 2007. Delamination mechanism maps for a strong elastic coating on an elastic-plastic substrate subjected to contact loading. Int. J. Solids Struct. 44, 3685–3699.

Yang, J., Komvopoulos, K., 2005. A mechanics approach to static friction of elastic–plastic fractal surfaces. J. Tribol. 127, 315–324.

Yan, W., Komvopoulos, K., 1998. Contact analysis of elastic-plastic fractal surfaces. J. Appl. Phys. 84, 3617-3624

Yan, S. L., Li, L. Y., 2003. Finite element analysis of cyclic indentation of an elastic-perfectly plastic half-space by a rigid sphere. Proc. Inst. Mech. Engrs. 217, 505-515

Ye, N., Komvopoulos, K., 2003. Indentation analysis of elastic-plastic homogeneous and layered media: criteria for determining the real material hardness. ASME J. Tribol. 125, 685–691.

Yin, X., Komvopoulos, K., 2010. An adhesive wear model of fractal surfaces in normal contact. Int. J. Solids. Struct. 47, 912-921

Yu, N., Polycarpou, A.A., 2004. Adhesive contact based on the Lenard-Jones potential: a correction to the value of the equilibrium distance as used in the potential. J. Colloid Interface Sci. 278, 428–435.

Zhao, Y.-P., Wang, L.S., Yu, T.X., 2003. Mechanics of adhesion in MEMS – a review. J. Adhesion Sci. Technol. 17, 519-546.

Zait, Y., Kligerman, Y., Etsion, I., 2010. Unloading of an elastic-plastic spherical contact under stick contact condition. Int. J. Solid. Struct. 47, 990-997

Appendix A: Surface traction distribution due to the Lennard-Jones potential

For two-atom interaction described by a potential of the form

$$V(r) = -\frac{C}{r^n}\ , \tag{A1}$$

where r is the atom-to-atom distance, the interfacial energy per unit area of two planar surfaces is given by (Israelachvili, 1992)

$$V(x) = -\frac{2\pi C\rho_1\rho_2}{(n-2)(n-3)(n-4)x^{n-4}} \tag{A2}$$

where x is the distance between the planar surfaces and ρ_1, ρ_2 are the atomic densities of the two planar surfaces, respectively.

The L-J interatomic potential can be written as

$$V(r) = 4D\left[\left(\frac{\sigma}{r}\right)^{12} - \left(\frac{\sigma}{r}\right)^{6}\right] = -\frac{C_1}{r^6} + \frac{C_2}{r^{12}} = V_1(r) + V_2(r) \tag{A3}$$

where D is the minimum potential, σ is the zero potential distance, $C_1 = 4D\sigma^6$, and $C_2 = 4D\sigma^{12}$.

Using Eqs. (A2) and (A3) and setting n = 6 and 12 in V_1 and V_2, respectively, the interfacial energy per unit area is expressed as

$$V(x) = V_1(x) + V_2(x) = \frac{\pi D\rho_1\rho_2}{3}\left[\frac{\sigma^{12}}{30x^8} - \frac{\sigma^6}{x^2}\right] \tag{A4}$$

The surface traction $p(x)$ due to the L-J potential can then be obtained as the first derivative of Eq. (A4), i.e.,

$$p(x) = \frac{2\pi D\rho_1\rho_2}{3}\left[\frac{\sigma^6}{x^3} - \frac{2\sigma^{12}}{15x^9}\right] \tag{A5}$$

The surface distance at equilibrium ε is the solution of $p(x) = 0$ and is given by

$$\varepsilon = \left(\frac{2}{15}\right)^{1/6} \sigma \tag{A6}$$

Substitution of Eq. (A6) into Eq. (A5) yields

$$p(x) = 5\pi D\varepsilon^3 \rho_1 \rho_2 \left[\left(\frac{\varepsilon}{x}\right)^3 - \left(\frac{\varepsilon}{x}\right)^9\right] \tag{A7}$$

The work of adhesion $\Delta\gamma$ is given by

$$\Delta\gamma = \int_{\varepsilon}^{\infty} p(x)dx = \frac{15}{8}\pi D\varepsilon^4 \rho_1 \rho_2 \tag{A8}$$

Hence, from Eqs. (A7) and (A.8), it follows that

$$p(x) = \frac{8\Delta\gamma}{3\varepsilon}\left[\left(\frac{\varepsilon}{x}\right)^3 - \left(\frac{\varepsilon}{x}\right)^9\right] \tag{A9}$$

A similar derivation of the surface traction due to the interatomic L-J potential has been reported by Yu and Polycarpou (2004).

Appendix B: Contact area at maximum adhesion force derived from the JKR theory

In the JKR theory, the Hertzian equation of the contact radius a, modified to include the effect of surface energy, is given by (Johnson et al., 1971)

$$a = \left[\frac{3R}{4E^*}\left[P + 3\pi R\Delta\gamma + \{6\pi R\Delta\gamma P + (3\pi R\Delta\gamma)^2\}^{1/2}\right]\right]^{1/3} \quad \text{(B1)}$$

Substitution of $P = -(3/2)\pi R\Delta\gamma$ into Eq. (B1) leads to the following equation of the contact radius at the instant of $P_{\max}$:

$$a = \left[\frac{9\pi R^2\Delta\gamma}{8E^*}\right]^{1/3} \quad \text{(B2)}$$

Using the same normalization scheme, i.e., $\bar{a} = a/(\varepsilon R)^{1/2}$, Eq. (B2) can be written in dimensionless form as follows

$$\bar{a} = \left(\frac{9\pi}{8}\right)^{1/3}\mu^{1/2} \quad \text{(B3)}$$

The contact radius given by Eq. (B3) consists of regions with compressive and tensile surface tractions, whereas in Eq. (8.6b) the contact radius is defined as the region of compressive surface traction. Therefore, for consistency, it is necessary to determine the contact region under compressive traction in the JKR solution. In the JKR theory, the effect of adhesion on Hertzian contact is included by balancing the external work with the surface energy and the elastic strain energy. The JKR model accounts for the effects of contact pressure and adhesion only within the contact area. The general solution of the contact pressure $p(r)$ can be obtained as the superposition of a compressive contact stress distribution due to the applied normal (compressive) force P_1 and an adhesive (tensile) contact stress distribution due to a tensile force P_2 applied by a rigid punch over the same contact radius (Eq. (B1)). Consequently, $p(r)$ is expressed as (Johnson, 1958)

$$p(r) = \frac{3P_1}{2\pi a^2}\left[1 - \left(\frac{r}{a}\right)^2\right]^{1/2} - \frac{P_2}{2\pi a^2}\left[1 - \left(\frac{r}{a}\right)^2\right]^{-1/2} \quad \text{(B4)}$$

where r is the radial distance from the center of contact.

The Hertzian contact load P_1 and the repulsive load P_2 at the instant of $P_{\max}$ are given by

$$P_1 = \frac{4E^*}{3R}a^3 \quad \text{(B5)}$$

$$P_2 = P_1 + \frac{3}{2}\pi R\Delta\gamma = \frac{4E^*}{3R}a^3 + \frac{3}{2}\pi R\Delta\gamma \quad \text{(B6)}$$

Substitution of Eqs. (B5) and (B6) into Eq. (B4) and use of the normalization $\bar{a} = a/(\varepsilon R)^{1/2}$ leads to the following equation of the normal stress distribution:

$$p(r) = \frac{2E^* a}{\pi R\left[1-\left(\frac{r}{a}\right)^2\right]^{1/2}}\left[\frac{2}{3} - \left(\frac{r}{a}\right)^2 - \frac{3\pi}{8\bar{a}^3}\left(\frac{R\Delta\gamma^{1/2}}{E^{*2}\varepsilon^3}\right)\right] \tag{B7}$$

Substitution of Eq. (B3) into Eq. (B7) yields,

$$p(r) = \frac{2E^* a}{\pi R\left[1-\left(\frac{r}{a}\right)^2\right]^{1/2}}\left[\frac{1}{3} - \left(\frac{r}{a}\right)^2\right] \tag{B8}$$

The contact radius a_c corresponding to the region of compressive surface traction, obtained by setting Eq. (B8) equal to zero, is given by $a_c = a/\sqrt{3}$. Hence, using Eq. (B3), the dimensionless contact radius $\bar{a}_c$ can be expressed as

$$\bar{a}_c = \frac{1}{\sqrt{3}}\bar{a} = \frac{1}{\sqrt{3}}\left(\frac{9\pi}{8}\right)^{1/3}\mu^{1/2} \approx 0.88\mu^{1/2} \tag{B9}$$